A Study of Indentation Cracking in Brittle Materials Using Cohesive Zone Finite Elements

A Dissertation Presented for the
Doctor of Philosophy
Degree
The University of Tennessee, Knoxville

Kurt E. Johanns
May 2014

DEDICATION

This work is dedicated to my family: grandparents, parents, sisters, aunts, uncles, and even in-laws. I have received nothing but support from them my entire life. Above all, this would not be possible without the love and sacrifice of my wife, Sheena, and son, Erik. You have allowed me to pursue a dream that I did not think was possible, and I thank you from the bottom of my heart.

ACKNOWLEDGEMENTS

I've had the pleasure of working with a large number of people in my graduate school career and each and every one have contributed in some way:

G. M. Pharr: I am a better person because of you. Thank you.

E. G. Herbert and P. Sudharshan Phani: My experience at UT would have been extremely different without your friendship. I'm always up for discussions and forced lunches no matter where we might be in the world.

A. A. Wereszczak: I would not have even thought grad school was possible if it were not for you (though I'm still deciding if that is a good or bad thing). Just say when you need to mow your lawn, and I'll have "the boy" there ASAP!

I am grateful for receiving the Helmut N. Friedlander Fellowship from AMETEK.

C. Melcher, staff, and students at Scintillation Materials Research Center at the University of Tennessee.

Y. F. Gao and J. Landes for serving on my committee, teaching, and the helpful discussions on modeling and fracture mechanics.

The National Science Foundation (grant number CMMI 0926798).

The University of Tennessee faculty and staff, especially Carla Lawrence.

C. J. Rawn and the ASM Materials Camp.

NSF REU Program, Center for Materials Processing at UT, and UT for undergraduate research.

E. P. George and staff at the alloy behavior and development group at Oak Ridge National Laboratory.

G. Duscher and the electron microscopy group at Oak Ridge National Lab.

O. Kraft, R. Monig, and A. Sedlmayr at the Karlsruhe Institute for Technology.

Fellow grad students at the University of Tennessee.

S. Johanns: Thank you for encouragement and sticking with me in tough times.

ABSTRACT

Cohesive zone finite element simulations of pyramidal indentation cracking in brittle materials have been carried out in order to: (1) critically examine indentation cracking models that relate fracture toughness to indentation data; (2) determine the underlying physical mechanisms of indentation crack growth from a continuum view and their relationship to material properties; (3) explore the influence of indenter geometry on crack extension; and (4) provide a platform from which future simulations can add more complex material behavior as well as guidance for experimental measurements of fracture toughness. Standard fracture toughness geometries in addition to simplified indentation geometries were simulated in order to assess the advantages and limitations of using cohesive zone finite element simulations to study indentation cracking in brittle materials. Simulation results were found to be consistent with linear-elastic fracture mechanics when crack lengths approximately 10 times larger than process zone sizes. Results from Vickers indentation cracking simulations showed deviations from standard models and additional material dependencies not considered in therein. A transition in cracking behavior from *median* type cracks to *Palmqvist* type cracks was observed as the ratio of elastic modulus to hardness increased and plasticity played a more prominent role in the deformation response. Separate stress intensity factor solutions were derived for the two cracking regimes by applying simple scaling relationships and observations from the finite elements. Simulations of different indenter geometries were found to correlate well with the stress intensity factors. In addition, the indentation cracking response could be tailored to a specific behavior by changing the indenter centerline-to-face angle. Cohesive zone finite element simulations were found to be well suited to exploring, improving, and studying the materials science of indentation cracking.

TABLE OF CONTENTS

CHAPTER I Introduction 1
References 13
Appendix 1.1 16
CHAPTER II An Evaluation of the Advantages and Limitations in Simulating Indentation Cracking with Cohesive Zone Finite Elements 21
Abstract 22
2.1. Introduction 23
2.2. A Continuum View of Indentation Cracking 25
2.3. The Cohesive Zone Model 28
2.4. Indentation Cracking and Cohesive Zone Models 31
2.5. Finite Element Modeling 32
2.6. Results and Discussion 36
2.7. Conclusions 44
References 46
Appendix 2.1 49
CHAPTER III Simulating Wedge Indentation Cracking with 2D Cohesive Zone Finite Elements 64
Abstract 65
3.1. Introduction 66
3.2. The Lawn, Evans, and Marshall Model in 2D and 3D 69
3.3. Finite Element Simulations 74
3.4. Results 77
3.5. Discussion 83
3.6. Conclusions 89
References 92
Appendix 3.1 94
CHAPTER IV Simulating Vickers Indentation Cracking in Brittle Materials with Cohesive Zone Finite Elements 114
Abstract 115
4.1. Introduction 116
4.2. Finite Element Simulations 119
4.3. Results 123
4.4. Discussion 129
4.5. Conclusions 134
References 136
Appendix 4.1 139
CHAPTER V A Model for the Stress Intensity Factor of an Indentation Crack in the Median Cracking Regime 159
Abstract 160
5.1. Introduction 161
5.2. Stress Intensity Factor for an Indentation Crack in the Median Regime 162
5.3. Estimation of Fracture Toughness 168

5.4. Conclusions....169
References....170
Appendix 5.1....171
CHAPTER VI A Model for the Stress Intensity Factor of an Indentation Crack in the Palmqvist Cracking Regime....181
Abstract....182
6.1. Introduction....183
6.2. Stress Intensity Factor on Loading....185
6.3. Stress Intensity Factor on Unloading....189
6.4. Conclusions....191
References....192
Appendix 6.1....193
CHAPTER VII Exploring Indenter Geometry Effects in Indentation Cracking with Cohesive Zone Finite Elements....203
Abstract....204
7.1. Introduction....205
7.2. Finite Element Simulations....207
7.3. Results....209
7.4. Discussion....213
7.5. Conclusions....218
References....220
Appendix 7.1....221
CHAPTER VIII Summary and Conclusions....238
APPENDIX....243
VITA....257

LIST OF TABLES

Table 2.1. Material and cohesive element input properties in the finite element simulations. 50
Table 3.1. Material, indenter, and cohesive element input properties in the finite element simulations. 95
Table 5.1. Finite element curve fits to coefficients A and B in Eq. 5.6 for a Vickers indenter. 172
Table 7.1. Material, indenter, and cohesive element input properties in the finite element simulations. 222

LIST OF FIGURES

Figure 1.1. The various crack geometries observed during indentation with the Vickers pyramidal indenter. 17
Figure 1.2. Median crack in glass beneath a Vickers indenter showing crack develop during loading (a), at maximum load (b), partially unloaded (c), and after complete removal of load (d). Crack is only visible at the surface during the unloading portion of the cycle. 18
Figure 1.3. Harding's indentation fracture toughness measurements compared to standard fracture toughness tests for a number of ceramic materials. 19
Figure 1.4. Half-Penny crack geometry observed in cohesive finite element simulations of Vickers indentation cracking. Notice the similarities in loaded and unloaded crack geometries between the simulations and the experimental results in Fig. 1.2. 20
Figure 2.1. A continuum picture of indentation cracking in elastic-plastic materials: (a) geometrically self-similar contact by elastic-plastic deformation where the size of the contact scales with the applied load and hardness; (b) the formation of a stable flaw nucleated by plastic deformation; (c) the short-crack regime where the process zone dominates crack behavior; and (d) steady-state crack growth where process zone effects are insignificant and the crack length scales according to the LEFM analysis. 51
Figure 2.2. Schematic of the cohesive zone model of a crack tip: (a) the traction-separation constitutive behavior; and (b) a magnified view of a crack-tip in a CCT specimen showing the process zone geometry. Points A, B, C, and D in (a) correspond to the locations identified in (b). 52
Figure 2.3. CCT cohesive finite element mesh and boundary conditions: (a) overall mesh; (b) magnified view of the refined region under deformation. Displacements in the horizontal direction in the deformed mesh have been exaggerated. A similar mesh was used for the 2D wedge simulations. 53
Figure 2.4. 3D Berkovich indentation cohesive finite element mesh and boundary conditions: (a) isometric view; (b) top-down view.. 54
Figure 2.5. Finite element simulation of a CCT specimen using cohesive elements: (a) overview of the CCT geometry with crack opening displacements exaggerated for display purposes; (b) magnified view of the crack tip showing the stresses in the cohesive zone; and (c) measured cohesive zone sizes for comparison to Dugdale's prediction. 55
Figure 2.6. Input and output traction-separation curves for a single cohesive finite element in the CCT and 2D wedge simulation. The use of viscous regularization did not result in element overloading. Note that in calculating G_c using Eq. 2.4 the input critical separation distance must be doubled to account for the mirror symmetry used in the model. 56
Figure 2.7. Apparent fracture toughness measured from finite elements simulations of a CCT specimen where the size of the cohesive zone is controlled by the maximum cohesive strength. An apparent decrease in

fracture toughness occurs when the size of the cohesive zone is on the order of the size of the crack. 57
Figure 2.8. Results from the simulation of 2D wedge indentation cracking in an E/Y=20 brittle material with a fracture toughness of 1.0 MPa $m^{1/2}$ and a σ_c/Y of 0.15: (a) self-similar elastic-plastic regime where the maximum tensile stress occurs at the elastic-plastic boundary; (b) formation of a stable process zone; (c) short-crack regime; and (d) steady-state crack geometry. Blue, white, and red shaded regions represent the plastic zone, process zone, and traction-free crack, respectively. 58
Figure 2.9. The square-root of crack length as a function of applied load for 2D indentation cracking simulations with a 60^o wedge indenter for two materials with different E/Y ratios (E=100 GPa, v=0.25, K_{Ic}=1.0 MPa $m^{1/2}$, σ_c=1 GPa). After the threshold load for cracking and the short-crack regime, the rate of crack growth, $d\sqrt{c}/dP$, reaches a constant, steady-state. 59
Figure 2.10. Results from FE simulations of Vickers indentation cracking: (a) isometric view of the Vickers indentation model showing crack planes aligned with indenter edges and faces (cracking only occurred on planes aligned with edges), and (b) and (c) crack morphologies as a function of load on a given plane for materials with E/Y=10 and E/Y=100, respectively. Note that the crack morphology evolution is controlled by the elastic-plastic properties of the material. Cracks are highlighted in red and plastic zones are in blue. 60
Figure 2.11. Results from FE simulations of Berkovich indentation cracking: (a) isometric view of the Berkovich indentation model showing crack planes aligned with indenter edges and faces (cracks did not extend to the face of the indenter), and (b) and (c) crack morphologies as a function of load on a given plane for materials with E/Y=10 and E/Y=100 respectively. Cracks are highlighted in red and plastic zones are in blue. 61
Figure 2.12. Results from Berkovich indentation simulations where only one set of planes (corner and face) were allowed to crack: (a) and (b) crack morphologies for materials with E/Y ratios of 10 and 100, respectively. In this case, cracks extend to the face side of the indenter on both loading and unloading. The crack is highlighted in red and the plastic zone is in blue. 62
Figure 2.13. Sectioned indents in an annealed soda-lime glass made with sharp three-sided indenters: (a) Tandon's experimental observation of quarter-penny cracks with a cube-corner indenter (micrograph used with permission), and (b) a similarly sectioned FE simulation in a glass-like material having the same modulus and hardness with a 40^o centerline-to-face angle indenter. The crack is highlighted in red and the plastic zone is in blue. 63
Figure 3.1. Idealized schematic of the 2D wedge indentation cross-sectional geometry examined in this study. 96

Figure 3.2. Hill's expanding cavity result for the radius of the plastic zone, *b*, with respect to the radius of the expanding cavity, *r*, for 2D and 3D (open circles). Dashed lines are power-law fits to Hill's model. The resulting fit exponents are not unique, but depend on the range of the fit. 97
Figure 3.3. The cohesive finite element simulation geometry (not to scale)..... 98
Figure 3.4. Influence of compliance effects on crack growth due to the finite sample size in the simulations. The expected linear relationship between the square-root of crack lengths and applied load breaks down as the crack length becomes a significant fraction of the sample size. 99
Figure 3.5. Crack growth rates, $d\sqrt{c}/dP$, as a function of applied load showing the artifact of the process zone in the short crack regime. Slight slope in data at large loads is a result of compliance effects due to finite sample sizes. 100
Figure 3.6. Square roots of crack lengths plotted as a function of load for various values of *E/Y*. Increasing *E/Y* results in increased crack growth rates.. 101
Figure 3.7. Square roots of crack lengths plotted as a function of load for various indenter angles. Increasing the indenter angle results in increased crack growth rates. 102
Figure 3.8. The effect of Poisson's ratio on crack growth rates as a function of material properties. Significant changes occur and Poisson's ratio cannot be neglected..... 103
Figure 3.9. Simulation crack growth rates plotted as a function of the LEM parameter..... 104
Figure 3.10. Plots of (a) hardness and (b) the ratio of plastic zone depth to contact dimension as a function of load for given materials showing that expected scaling relationships are maintained in the presence of crack growth. 105
Figure 3.11. Crack mouth opening displacement rates with respect to load plotted as a function of indenter angle and hardness. Linear relationship suggests that crack mouth opening displacements scales with the size of the contact..... 106
Figure 3.12. Normalized wedge indentation hardness, *H/E*, compared to normalized expanding cavity pressure, p_{EC}/E. Deviations occur at small values of *E/Y*. 107
Figure 3.13. Wedge indentation constraint factor, *H/Y*, and expanding cavity model constraint factor, p_{EC}/Y, plotted as a function of *E/Y*. Deviations occur at large values of *E/Y* due to a transition in deformation types that is not accounted for in the radially symmetric expanding cavity model..... 108
Figure 3.14. Ratio of the contact dimension to the plastic zone depth for wedge indenters of various angles and Hill's expanding cavity model prediction as a function of *E/H*..... 109
Figure 3.15. Estimating the elastic stresses by a vertical point line-load and a horizontal line-load. 110

Figure 3.16. Stresses acting normal to the crack plane measured from finite element simulations of indentation with a 65° wedge indenter in an elastic and elastic-perfectly plastic material (*E/Y* = 20). 111
Figure 3.17. Thin rigid wedge stress intensity factor solution used in the analysis of 2D wedge indentation cracking. 112
Figure 3.18. All of the simulation results of crack growth rates plotted as a function of Eq. 3.17. 113
Figure 4.1. Top-down schematic of the Vickers indentation geometry. 140
Figure 4.2. Subsurface view of the Vickers indentation cracking geometry. 141
Figure 4.3. Sink-in/pile-up surface deformation geometries. 142
Figure 4.4. Finite element results of Vickers indentation crack lengths showing the effects of the process zone size on crack growth. 143
Figure 4.5. Elastic contact: (a) Vickers indentation median crack after complete unloading; and (b) contours of crack opening stresses in a Boussinesq contact. 144
Figure 4.6. Example finite element mesh (a) and Vickers indentation crack geometries for E/Y ratios of 12.5, 25, and 200: at maximum load (b, c, and d); and complete unload (e, f, and g).. 145
Figure 4.7. Idealized Vickers indentation crack geometries resulting from the finite element simulations: (a) median cracking; (b) Palmqvist cracking at small loads; and (c) Palmqvist cracking at larger loads. 146
Figure 4.8. Plastic zone contours for various values of *E/Y* and corresponding points of crack initiation.. 147
Figure 4.9. Vickers indentation cracking simulation results plotted against the LEM prediction. 148
Figure 4.10. Simulation results from Vickers indentation as a function of Poisson's ratio. 149
Figure 4.11. Minimum values of the ratio of crack length to contact size in the median cracking regime. The minimum ratio is limited by influences of the process zone.. 150
Figure 4.12. Finite element results plotted against the LEM model and individual experimental results. 151
Figure 4.13. Scaling behavior of surface and subsurface crack lengths as a function of *E/H*. 152
Figure 4.14. The ratio of indentation hardness to Hill's expanding cavity pressure as a function of material properties. 153
Figure 4.15. Indentation constraint factor plotted against the predicted value from Hill's expanding cavity model. 154
Figure 4.16. Surface deformation behavior as function of material properties showing a transition from sink-in to pile-up at an *E/H* of ~30.. 155
Figure 4.17. Finite element plastic zone geometries compared to the LEM prediction. 156
Figure 4.18. Comparison between finite element results and the LEM model without the use of Hill's expanding cavity model. 157

Figure 4.19. Errors in predicted fracture toughness between the LEM model and finite element results. 158
Figure 5.1a. Selvadurai and Singh's rigid disk stress intensity factor geometry used to represent indentation cracking in the median regime. 173
Figure 5.1b. Top-down view of the Vickers indentation crack geometry. 174
Figure 5.2. Simulation results of unloaded crack opening displacements of a Vickers median crack. 175
Figure 5.3. Vickers indentation cracking results in the median regime plotted as a function of the rigid disk stress intensity factor solution. 176
Figure 5.4. Sink-in/pile-up surface deformation geometries. 177
Figure 5.5. Finite element results of contact depth to total indenter displacement: (a) the entire *E/H* range examined; and (b) results from the median cracking regime showing logarithmic behavior. 178
Figure 5.6. Correlations between: (a) sink-in/pile-up and the rigid disk stress intensity factor solution; and (b) indentation cracking parameters and the natural log of *E/H*. 179
Figure 5.7. Comparison between fracture toughness predictions from the LEM model and the median cracking model derived from finite elements. 180
Figure 6.1. An idealized subsurface Palmqvist indentation cracking geometry during Vickers indentation. 194
Figure 6.2. Crack length versus load for Palmqvist cracks during loading. 195
Figure 6.3. Normalized loads and crack lengths for Palmqvist cracks during loading (Poisson's ratio = 0.10). 196
Figure 6.4. Unloaded surface crack lengths of Vickers indentation cracking simulations in the Palmqvist regime. 197
Figure 6.5. Normalized loads and crack lengths for Palmqvist cracks after complete unload. 198
Figure 6.6. Stress Intensity factor geometries 24.5 (a) and 24.6 (a) from the stress analysis of cracks handbook. 199
Figure 6.7. Schematics of the stress intensity factor geometries used to describe indentation cracking. 200
Figure 6.8. Comparison between the finite element results and the stress intensity factor model for loading given by Eq. 6.10. 201
Figure 6.9. Predicted scaling behavior of non-dimensional crack lengths *c* and *l* as well as non-dimensional plastic zone size, *b*, in the Palmqvist regime. Finite element results have been superimposed on the plot. 202
Figure 7.1. Harding's experimental results on crack lengths measurements from Vickers and Berkovich indentations at the same load in a number of brittle materials. 223
Figure 7.2. Example finite element model of a multi-sided pyramidal indenter: (a) top down view of a 5-sided indenter; and (b) resulting quarter-penny cracks occurring on planes aligned with indenter corners. 224
Figure 7.3. The non-dimensional cracking parameter, $K_{Ic}c^{3/2}/P_{max}$, plotted as a function of *E/H* (semi-log scale) for materials in the median indentation cracking regime. 225

Figure 7.4. Berkovich results versus Vickers results for materials with a constant fracture toughness.. 226
Figure 7.5. Normalized crack lengths plotted as a function of normalized load for Vickers and Berkovich indenters in the Palmqvist regime. 227
Figure 7.6. The non-dimensional cracking parameter plotted as a function of the number of cracks for pyramidal indenters having different sides..... 228
Figure 7.7. Indentation cracking geometries observed in simulations of a 3-sided indenter having a centerline-to-face angle of 45°: finite element model (a); geometries at maximum load for *E/Y* ratios of 50 and 12.5, respectively (b,c); and unloaded geometries (d,e).. 229
Figure 7.8. Indentation cracking geometries observed in simulations of a 3-sided indenter having a centerline-to-face angle of 55°: finite element model (a); geometries at maximum load for *E/Y* ratios of 50 and 10, respectively (b,c); and unloaded geometries (d,e)... 230
Figure 7.9. Indentation cracking geometries observed in simulations of a 3-sided indenter having a centerline-to-face angle of 75°: finite element model (a); geometries at maximum load for *E/Y* ratios of 50 and 12.5, respectively (b,c); and unloaded geometries (d,e)... 231
Figure 7.10. The non-dimensional cracking parameter plotted as a function of *E/H* for 3-sided indenters having different centerline-to-face angles. 232
Figure 7.11. Equivalent contact area outlines for 70.3° cone, Vickers, and Berkovich indenters. 233
Figure 7.12. Ouchterlony's stress intensity factor model compared to results from indentation cracking simulations having different numbers of cracks. 234
Figure 7.13. The entire simulation dataset in the median cracking regime plotted as a function of Eq. 7.5. 235
Figure 7.14. The entire simulation dataset in the Palmqvist regime plotted as a function of Eq. 7.6. 236
Figure 7.15. Harding's experimental cube-corner indentation cracking results plotted along with the finite element results..... 237

LIST OF VARIABLES

Important Variables (in order of appearance)	*Symbol*
Fracture Toughness	K_{Ic}
Hardness	H
Elastic Modulus	E
Surface Crack Length	c
Maximum Applied load on the Indenter	P_{max}
Poisson's Ratio	v
Yield Strength	Y
Applied Load on the Indenter	P
Projected Contact Size	a
Critical Flaw Size	c^*
Cohesive Strength	σ_c
Critical Cohesive Separation	δ_c
Fracture Energy	G_c
Plane-Strain Elastic Modulus	E'
Process Zone Size	ρ
Applied Stress on CCT Specimen	σ_{app}
Cohesive Element Stiffness	S
Cohesive Element Viscosity	μ
Indenter Centerline-to-Face Angle	θ
Indenter Displacement into Surface	h
Indenter Contact Displacement	hc
Crack Mouth Opening Displacement (CMOD)	δ_m
Plastic Zone Radius	b
Hill's Expanding Cavity Pressure	P_{EC}
Hill's Expanding Cavity Radius	r
2D Wedge Crack Growth Rate	$d\sqrt{c}/dP$
Mode I Stress Intensity Factor	K_I
Non-Dimensional Crack Length	$\hat{c}$
Non-Dimensional Load	$\hat{P}$
Ouchterlony's SIF Modifying Factor	$k(n)$

CHAPTER I

INTRODUCTION

A search for the term “indentation cracking” in the materials science literature yields a list of publications that numbers into the thousands. These papers examine metals, ceramics, polymers, and unique biological materials ranging from bulk samples to thin-films and even nano-particles. The papers generally deal with the relationship between fracture properties and cracks that develop during indentation in brittle materials (see, for example, the various crack geometries observed experimentally in Fig. 1.1). However, it is not always clear as to how “indentation cracking” became such a ubiquitous phrase or why its application has been used, in some cases, without regard for the assumptions and conditions inherent to the models describing the phenomenon. To answer those questions, a brief review of indentation testing is required as well as some historical perspective on the development of indentation cracking. This dissertation follows most of the literature in focusing almost exclusively on pyramidal type indenters and illuminates the complexities of indentation testing as well as highlighting some of the controversies existing in the indentation cracking literature.

The main goal of this work is to add a level of understanding to the indentation cracking problem by identifying the physical mechanisms underlying crack growth during indentation testing of bulk samples and their relationship to specific material properties such as elastic moduli, yield strength, and fracture toughness. Although elements of fracture mechanics are used in this dissertation, the focus is on the materials science of indentation cracking. In addition, a critical examination of the assumptions and ideas behind the more prominent indentation cracking models is carried out to examine their validity and applicability. To that end, numerical finite element modeling is used to examine the problem in three thrusts: (1) examining the applicability of cohesive finite elements to simulate indentation cracking in brittle ceramic-like materials, (2) developing an understanding of the physical mechanisms underlying crack growth in the simplified geometry of two-dimensional wedge indentation, and (3) extending the analysis to examine three-dimensional pyramidal indentation

cracking over a wide range of material properties and indenter geometries. More discussion of each approach and the outcomes is provided following a short literature review.

The response and reliability of an engineering component is dictated by the mechanical properties of the material comprising that component. In that regard, properties such as elastic moduli, yield strength, fatigue parameters, and fracture toughness have become important inputs in predictive modeling analyses. There are a number of standardized tests (e.g., tensile testing for yield strength and elastic modulus and the compact tension testing for fracture toughness) that are used to assess these mechanical properties. However, these tests often require and sample a large amount of material and can be expensive due to machining costs. Thus, when the length scale of the material in question is small or conventional testing costs become prohibitive, an alternative technique such as indentation may be used to measure mechanical properties.

Indentation testing is a technique in which a spherical or pyramidal indenter, typically made of diamond, is pushed into a target material. The displacement incurred by the material as well as the projected contact area is measured as a function of the applied load on the indenter resulting in a hardness, a measure of the resistance to plastic deformation. The advantages of such a non-destructive test include multiple sampling in a much smaller volume of material than would be required for a tensile test and the ability to make the measurement directly on the material in the engineering component. Disadvantages include the fact that the test geometry results in a stress condition that is complicated and does not lend itself to straightforward analyses. It is often difficult to describe how the force applied on the indenter is transferred to the physical mechanisms active during indentation. In addition, the outcomes of an indentation test are often not direct inputs into reliability models. A large focus on current indentation research is on describing the relationship between uniaxial properties and indentation results.

Fracture toughness, K_{Ic}, entered indentation testing when surface cracks were observed during post-test examination of indentation sites in brittle materials. While Hertz [1] may have been the first to observe and report the phenomenon of indentation fracture, Palmqvist, working in WC-Co composites, was the first to indirectly relate the toughness of a material to the sum of the lengths of surface cracks emanating from a residual impression of a Vickers indenter for a given applied load [2]. His results showed that crack lengths scaled linearly with the applied load. Palmqvist was not only able to show that the load required to reach 300μm of crack length increased for increasing percentages of Co in the WC-Co composites (increases in Co content result in increases in toughness), but was also able to identify experimental errors when working with relatively small loads [3, 4]. These surface cracks are recognized today as Palmqvist cracks or, more commonly, radial cracks. However, their subsurface geometry at the time was unknown. Other researches took Palmqvist's work on WC-Co to the next level by identifying experimental artifacts such as surface condition and by directly relating toughness to indentation results [5-9].

The era from 1970 to 1980 saw contributions to the understanding of indentation cracking that attempted to add fracture mechanics analyses. Lawn and co-workers, their work predominantly featured in the 1975 issues of the Journal of Materials Science, made key observations that would ultimately lead to the development of a significant model describing the driving forces behind indentation cracking. Glass became the prototypical material as in-situ observations of crack initiation and propagation were aided by the transparent material. Marshall and Lawn used glass to provide details on crack morphology during loading and unloading of a Vickers indenter as shown in Fig. 1.2 [10]. Lawn and Swain [11] considered the contribution of the tensile components from the elastic indentation stress field (a Boussinesq stress field) as a means by which fracture mechanics could be applied to indentation cracks that appeared to extend beneath the indenter on planes perpendicular to the surface, but parallel

to the indent diagonals. These types of cracks became known as median cracks and appeared during the loading half of the indentation cycle [12]. Lawn and Wilshaw and Lawn and Swain et al. [13] also identified lateral cracks (those running parallel to the surface) that propagated on the unloading half of the indentation cycle.

Hardness, *H*, entered the description as the contact pressure in the elastic stress field equations and provided the magnitude of the tensile stresses acting on the crack in the fracture mechanics analysis. The elastic modulus of the material, *E*, entered the equations as a result of the relationship between fracture toughness and the strain energy release rate in linear elastic fracture mechanics. It was quickly recognized that the ratio of the elastic modulus to the hardness was an important parameter, but the physical significance was not well understood.

Lawn and Fuller [14] made the observation that residual stresses due to the irreversible deformation caused by indentation played a major role in deciding the final crack geometry. Lawn and Fuller also observed that median cracks would tend to grow and break through to the surface to take on a geometry that is commonly known today as the half-penny crack. They showed that the lengths of surface traces of these cracks, *c*, scaled with the maximum applied load, P_{max}, raised to the power of *2/3,* which held for a wide range of indenter angles. At this point during the development of indentation cracking theory, scaling arguments and empirical evidence [15, 16] were used to relate the four most apparent variables in the problem: elastic modulus, hardness, applied load, and resulting crack lengths.

Palmqvist noted that working with low loads led to errors in comparing the toughness of different WC-Co composites. This was presumably due to a critical load below which surface traces of cracks were not visible. This so-called crack threshold load is often ignored in most of the literature as the focus was on the equilibrium propagation of cracks, but there were attempts to describe the crack initiation [17-19]. Two different views have been taken in the initiation process:

(1) crack propagation occurs from existing flaws within the material once the stress intensity factor on the flaw reaches the fracture toughness, and (2) crack nucleation occurs by the mechanisms and interactions of plastic deformation specific to the material during indentation. As length scales move to smaller regimes and material processing minimizes defects in materials such as single crystal silicon, it is expected that the likelihood of finding a flaw decreases and the second viewpoint would describe the nucleation process. However, in both cases the process by which nucleation of a crack occurs is specific to a material and is likely not describable from a continuum view. Crack nucleation is briefly discussed in this work in how it relates to the use of cohesive finite elements; however it is not the primary focus since the use of cohesive finite elements may be an inappropriate technique for simulating indentation crack nucleation.

Lawn, Evans, and Marshall (LEM) developed a model that considered the driving forces and factors affecting the propagation of a half-penny shaped crack during indentation [20]. A description of the model is provided here as it is the source of both the widespread use and the controversy surrounding the use of indentation to measure toughness. Many authors have revisited the derivation [21, 22], and a detailed description of each step is provided in a later chapter. Development of an indentation fracture toughness model required a long time (decades) due to the fact that it is fundamentally different from standard fracture toughness testing. Applied loads or stresses in standard tests are directly related through linear-elasticity to the stress intensity factor. However, in indentation cracking, the load applied on the indenter acts to plastically deform the material, which in turn drives crack growth. The challenge is then to determine the relationship between material properties, applied load on the indenter, and the stress intensity factor. Doing so requires an assumption about the material behavior beneath the indenter. LEM suggested that the elastic contact stresses and the residual stresses due to plasticity are two separate contributions to the stress intensity factor at the crack tip during the loading half of the indentation cycle, while the residual stress acts alone upon complete unloading of the

indenter. LEM utilized the principal of superposition of stress intensity factors to find the net result.

LEM assumed that the residual component to the stress intensity factor stemmed from the material having to accommodate the volume of material plastically deformed by the indentation. The plastic volume is accommodated elastically and creates a tensile residual stress acting on the crack. In the limit that the crack is large compared to the size of the indentation, the crack can be considered a point-force loaded half-penny crack. LEM assumed that Hill's expanding cavity model [23] accurately reflects the physics of indentation and used it to link the geometry of the indentation to the ratio of the materials' elastic modulus to hardness.

LEM derived the elastic component by integrating the Boussinesq contact field along the crack length and found that the stress intensity factor scales with load and crack length in the same manner as the residual component. LEM argued that the residual component would greatly outweigh the contributions of the elastic component due to the significant crack growth observed during the unloading of the indenter. Anstis et al. [24] summarized the contributions of the two components into one equation by empirically fitting the results of indenting a number of ceramic materials with a Vickers indenter. The combination of modeling and experiments resulted in the following relationship between fracture toughness, material properties, and indentation data:

$$K_{Ic} = 0.016\sqrt{\frac{E}{H}}\frac{P_{\max}}{c^{3/2}}. \qquad (1.1)$$

From the above equation, it is easy to see how the use of indentation cracking spread rapidly, especially with the emergence of instrumented indentation techniques and the ability to measure modulus, hardness, and crack lengths in one convenient experiment.

It must be brought to attention here that there are a number of works in the literature that suggest there may be other material dependencies [25] or length scale issues [26] not captured in the LEM model. Past researchers have

developed equations dealing with the lead coefficient and the E/H exponent. A detailed review of such works was compiled by Ponton and Rawlings [27, 28].

A detailed analysis of in-situ indentation cracking observations in some glasses and ceramics was conducted by Cook and Pharr [29]. They found that there was no generalized crack morphology between materials. Radial crack extension was observed both on loading and unloading, where previously thought to grow only on unloading. In addition, Cook and Pharr provided evidence that radial cracks may coalesce into the half-penny crack geometry on loading. Again, the importance of their work was that there may be extra material dependencies not considered in the existing indentation cracking models.

In a detailed examination of the ability of the LEM model to measure fracture toughness over a wide range of brittle materials, Harding showed a significant amount of error between standard fracture toughness measurements and indentation cracking [30]. Harding's results are shown in Fig. 1.3. While his experiments utilized a different indenter geometry than the Vickers pyramid, his work again pointed to missing material dependencies in the LEM model.

There have been a few efforts toward numerically simulating indentation cracking with the development of more powerful and economical computation tools (e.g. the finite element method). Several authors have utilized finite elements with a unique constitutive behavior that allows for material degradation under an applied tensile stress [31-33]. These models have been shown to capture the behavior observed in experiments, but lack a description of the underlying physics behind the crack driving forces. Others have used numerical techniques to "calibrate" the LEM equation, arriving at values for the coefficient for different indenter geometries [34, 35]. Lee and co-authors [36] have shown that cohesive zone finite element simulations of Vickers indentation cracking can help to add understanding to the physics behind indentation cracking and pointed out that properties not considered in the LEM derivation such as Poisson's ratio have an important role. Lee also showed remarkably similar half-penny crack geometries as those observed by Lawn and co-workers (see Fig. 1.4). Feng and

co-authors, working on the indentation problem, have recently derived a solution to the elastic-plastic indentation stress field [37]. While this work does not consider indentation cracking, their results are of interest as the stress field may be used in the fracture mechanics.

Measuring fracture toughness from indentation cracking is more complicated than standard fracture toughness testing because one must relate the load applied to the indenter to the crack driving force. This relationship is not straightforward because it is dependent on both the elastic and plastic properties of the material. Furthermore, the lack of a general crack morphology confuses the issue. While indentation cracking models exist, the assumptions made in their derivation may be prone to errors and may underestimate material dependencies. There is also controversy concerning the appropriateness of these models in measuring fracture toughness [38]. Numerical simulations have proven useful in aiding the understanding of complex elastic-plastic problems and appear to capture the important elements of indentation cracking. From recent results, it is expected that more refined simulations over a wide range of materials may provide answers to some outstanding questions in the literature.

Descriptions of indentation cracking in the past have relied on empirical observations from experiments and assumptions of material behavior during the indentation process. In order to circumvent these problems and provide a fresh view of indentation cracking, this dissertation utilizes numerical crack growth simulations in the form of cohesive finite elements with the finite element package ABAQUS [39]. Elastic-perfectly plastic materials described by isotropic elastic moduli and a yield strength are used in the modeling. In addition, the cohesive element constitutive behavior is formulated in such as way that the materials herein are considered brittle, i.e., crack extension can be described by linear-elastic fracture mechanics. Contact is simulated with rigid indenters on frictionless surfaces and planar cracks are forced to emanate from indenter corners. Note however, that though the cracks form on median planes aligned with indenter corners, their morphology and size is determined from the

indentation processes specific to the indenter geometry and material properties. This study is limited to the examination of the median/radial crack system; lateral or other secondary crack systems are not considered.

The work herein is split into six chapters that critically examine indentation cracking with cohesive zone finite element modeling, each one building upon previous chapters. Chapter II shows that cohesive finite element simulations not only capture experimental observations of indentation cracking, but are indeed appropriate for modeling crack growth in the case of brittle materials. Chapter II includes the modeling of a standard fracture toughness test specimen, the development of a framework for incorporating cohesive element constitutive behavior into the finite element indentation simulations, and the construction of two-dimensional and three-dimensional finite element indentation meshes. Each step is made ensuring that conditions are valid for linear elastic fracture mechanics analyses. One major conclusion arising from this work is that cohesive finite elements are not applicable to describing crack initiation during indentation, stemming from the fact that initiation events during elastic-plastic indentation with pyramidal indenters are highly dependent on the cohesive element constitutive behavior, while crack extension once the cracks are well developed is only sensitive to the magnitude of fracture toughness. The result is a critical crack length that must be exceeded before linear-elastic fracture mechanics are valid.

In order to separate material responses and geometrical effects, Chapter III of this work includes the derivation and critical examination of the LEM model in the case of two-dimensional (2D) plane-strain wedge indentation. Both the geometry of the indenter and the crack are simplified in 2D. In addition, 2D simulations lend themselves to highly accurate, computationally efficient calculations that cover a wide sample space. The results in this chapter highlight discrepancies between material behavior in the finite elements simulations and the assumed behavior in the LEM model. For example, Hill's expanding cavity model does not appropriately capture the indentation plastic zone geometry. It is

also shown that a simple stress intensity factor solution combined with a non-dimensional scaling argument accurately describes crack extension over the range of materials and indenters angles examined. While examining the advantages and disadvantages of the LEM model is the primary result, the 2D simulations provide input toward understanding their three-dimensional counterparts that may have been overlooked otherwise.

Chapter IV, and crux of this dissertation, incorporates the observations and results from the previous sections and focuses on simulating indentation cracking in brittle materials beneath the four-sided pyramidal Vickers indenter. Critically examining indentation cracking models as well as identifying the differences between materials that exhibit Palmqvist versus half-penny crack geometries is of primary importance. Two common themes emerged from this work: First, the transition in indentation behavior from elastically dominated deformation to plastically dominated deformation with increasing ratio of elastic modulus to hardness (*E/H*) plays an important role in the indentation cracking behavior. Second, more ceramic-like materials (*E/H* < 30) tend to exhibit *median* type cracking while more metallic-like materials (*E/H* > 30) tend to exhibit *Palmqvist* or *Radial* type cracking (see Fig. 1.1). The most important result from this section is that material dependencies not considered, namely material pile-up and sink-in at the contact periphery, in existing indentation cracking models play a considerable role in crack extension and morphology. The lack of a general crack morphology as observed by Cook and Pharr was confirmed and can be attributed to the transition in deformation mode.

Chapters V and VI attempt to correlate the observations and data from the Vickers indentation cracking simulations with stress intensity factor solutions [40]. *Median* type cracking is approximated with a rigid wedge stress intensity factor solution in Chapter V, where the driving force arises from elastic resistance to the expansion of the wedge. Chapter VI utilizes a stress-based stress intensity factor solution to describe *Palmqvist* type cracking where elastic effects are minimal and plasticity dominates. The solutions are not meant to be strict

analytical derivations of indentation stress intensity factors, but take advantage of new observations of indentation cracking derived from the simulations.

Finally, Chapter VII moves away from examining the effect of material properties and evaluates the influence of indenter geometry on indentation cracking. Cohesive zone finite element simulations of the Berkovich indenter, an indenter having a triangular base as opposed to the square base of the Vickers indenter, are used to explain observations by Harding [22] and Dukino and Swain [41], wherein Berkovich indentation gives rise to longer cracks than Vickers indentation at the same load for a given material. It is also shown that indenter geometry can be tailored to force a specific indentation cracking response, which in turn allows for greater accuracy in measuring fracture toughness.

Ultimately, this dissertation provides evidence as to why existing indentation crack models are not well suited to measuring fracture toughness in all cases. New formulas derived from physical observations from the finite element simulations for calculating fracture toughness that are not dependent on assumptions of material behavior are introduced and shown to more accurately measure fracture toughness over a wider range of materials than the LEM model and other models of indentation cracking.

References

1. Hertz, H., *Miscellaneous papers [microform] / by Heinrich Hertz ... with an introduction by Philipp Leonard ; authorised English translation by D.E. Jones ... and G.A. Schott*. Landmarks of science. 1896, London ; New York :: Macmillan.
2. Palmqvist, S., Jernkontorets Ann., 1957. **141**: p. 300-307.
3. Palmqvist, S., Arch. Eisenhuettw., 1962. **33**(629-633).
4. Palmqvist, S., Jernkontorets Ann., 1963. **147**: p. 107-110.
5. Exner, E., J. Pickens, and J. Gurland, *A comparison of indentation crack resistance and fracture toughness of five WC-Co alloys.* Metallurgical and Materials Transactions A, 1978. **9**(5): p. 736-738.
6. Ogilvy, I.M., C.M. Perrott, and J.W. Suiter, *On the indentation fracture of cemented carbide part 1 -- Survey of operative fracture modes.* Wear, 1977. **43**(2): p. 239-252.
7. Perrott, C.M., *On the indentation fracture of cemented carbide II -- the nature of surface fracture toughness.* Wear, 1978. **47**(1): p. 81-91.
8. Peters, C.T., *The relationship between Palmqvist indentation toughness and bulk fracture toughness for some WC-Co cemented carbides.* Journal of Materials Science, 1979. **14**(7): p. 1619-1623.
9. Exner, H.E., *The Influence of Sample Preparation on Palmqvist's Method for Toughness Testing of Cemented Carbides.* Transactions of the Mettallurgical Society of AIME, 1969. **245**: p. 677-683.
10. Marshall, D.B. and B.R. Lawn, *Residual stress effects in sharp contact cracking.* Journal of Materials Science, 1979. **14**(8): p. 2001-2012.
11. Lawn, B.R. and M.V. Swain, *Microfracture beneath point indentations in brittle solids.* Journal of Materials Science, 1975. **10**(1): p. 113-122.
12. Lawn, B. and R. Wilshaw, *Indentation fracture: principles and applications.* Journal of Materials Science, 1975. **10**(6): p. 1049-1081.
13. Lawn, B.R., M.V. Swain, and K. Phillips, *On the mode of chipping fracture in brittle solids.* Journal of Materials Science, 1975. **10**(7): p. 1236-1239.
14. Lawn, B.R. and E.R. Fuller, *Equilibrium penny-like cracks in indentation fracture.* Journal of Materials Science, 1975. **10**(12): p. 2016-2024.
15. Evans, A.G. and E.A. Charles, *Fracture Toughness Determinations by Indentation.* Journal of the American Ceramic Society, 1976. **59**(7-8): p. 371-372.
16. Evans, A.G. and T.R. Wilshaw, *Quasi-static solid particle damage in brittle solids--I. Observations analysis and implications.* Acta Metallurgica, 1976. **24**(10): p. 939-956.
17. Hagan, J.T., *Micromechanics of crack nucleation during indentations.* Journal of Materials Science, 1979. **14**(12): p. 2975-2980.
18. Lawn, B.R. and A.G. Evans, *A model for crack initiation in elastic/plastic indentation fields.* Journal of Materials Science, 1977. **12**(11): p. 2195-2199.

19. Lankford, J. and D.L. Davidson, *The crack-initiation threshold in ceramic materials subject to elastic/plastic indentation.* Journal of Materials Science, 1979. **14**(7): p. 1662-1668.
20. Lawn, B.R., A.G. Evans, and D.B. Marshall, *Elastic-Plastic Indentation Damage in Ceramics - the Median-Radial Crack System.* Journal of the American Ceramic Society, 1980. **63**(9-10): p. 574-581.
21. Jang, J.-i. and G.M. Pharr, *Influence of indenter angle on cracking in Si and Ge during nanoindentation.* Acta Materialia, 2008. **56**(16): p. 4458-4469.
22. Harding, D.S., *Craking in Brittle Materials During Low-Load Indentation and its Relation to Fracture Toughness.* PhD Thesis, Rice University, 1995.
23. Hill, R., *The mathematical theory of plasticity*. 2004, Oxford: Clarendon Press.
24. Anstis, G.R., et al., *A Critical Evaluation of Indentation Techniques for Measuring Fracture Toughness: I, Direct Crack Measurements.* Journal of the American Ceramic Society, 1981. **64**(9): p. 533-538.
25. Tanaka, K., *Elastic/plastic indentation hardness and indentation fracture toughness: The inclusion core model.* Journal of Materials Science, 1987. **22**(4): p. 1501-1508.
26. Niihara, K., R. Morena, and D.P.H. Hasselman, *Evaluation of K_{Ic} of brittle solids by the indentation method with low crack-to-indent ratios.* Journal of Materials Science Letters, 1982. **1**(1): p. 13-16.
27. Ponton, C.B. and R.D. Rawlings, *Vickers indentation fracture toughness test Part 1 Review of literature and formulation of standardised indentation toughness equations.* Materials Science and Technology, 1989. **5**: p. 865-872.
28. Ponton, C.B. and R.D. Rawlings, *Vickers indentation fracture toughness test Part 2 Application and critical evaluation of standardised indentation toughness equations.* Materials Science and Technology, 1989. **5**: p. 961-976.
29. Cook, R.F. and G.M. Pharr, *Direct Observation and Analysis of Indentation Cracking in Glasses and Ceramics.* Journal of the American Ceramic Society, 1990. **73**(4): p. 787-817.
30. Harding, D.S., G.M. Pharr, and W.C. Oliver, *Cracking during nanoindentation and its use in the measurement of fracture toughness*. 1994. Medium: ED; Size: 6 p.
31. Zhang, W. and G. Subhash, *An elastic-plastic-cracking model for finite element analysis of indentation cracking in brittle materials.* International Journal of Solids and Structures, 2001. **38**(34-35): p. 5893-5913.
32. Muchtar, A., L.C. Lim, and K.H. Lee, *Finite element analysis of vickers indentation cracking processes in brittle solids using elements exhibiting cohesive post-failure behaviour.* Journal of Materials Science, 2003. **38**(2): p. 235-243.

33. Wan, H., et al., *A plastic damage model for finite element analysis of cracking of silicon under indentation.* Journal of Materials Research, 2010. **25**(11): p. 2224-2237.
34. Leonardi, A., et al., *Analytical Approaches to Stress Intensity Factor Evaluation for Indentation Cracks.* Journal of the American Ceramic Society, 2009. **92**(5): p. 1093-1097.
35. Leonardi, A., et al., *Numerical analysis of brittle materials fractured by sharp indenters.* Engineering Fracture Mechanics, 2010. **77**(2): p. 264-276.
36. Lee, J.H., et al., *Cohesive interface simulations of indentation cracking as a fracture toughness measurement method for brittle materials.* Acta Materialia, 2012. **60**(15): p. 5448-5467.
37. Feng, G., et al., *An analytical expression for the stress field around an elastoplastic indentation/contact.* Acta Materialia, 2007. **55**(9): p. 2929-2938.
38. Quinn, G.D. and R.C. Bradt, *On the Vickers Indentation Fracture Toughness Test.* Journal of the American Ceramic Society, 2007. **90**(3): p. 673-680.
39. Simulia, *ABAQUS User's Manual*. 2008: Simulia Co.
40. Tada, H., P.C. Paris, and G.R. Irwin, *The stress analysis of cracks handbook*. 1973: Del Research Corp.
41. Dukino, R.D. and M.V. Swain, *Comparative Measurement of Indentation Fracture Toughness with Berkovich and Vickers Indenters.* Journal of the American Ceramic Society, 1992. **75**(12): p. 3299-3304.

APPENDIX 1.1.

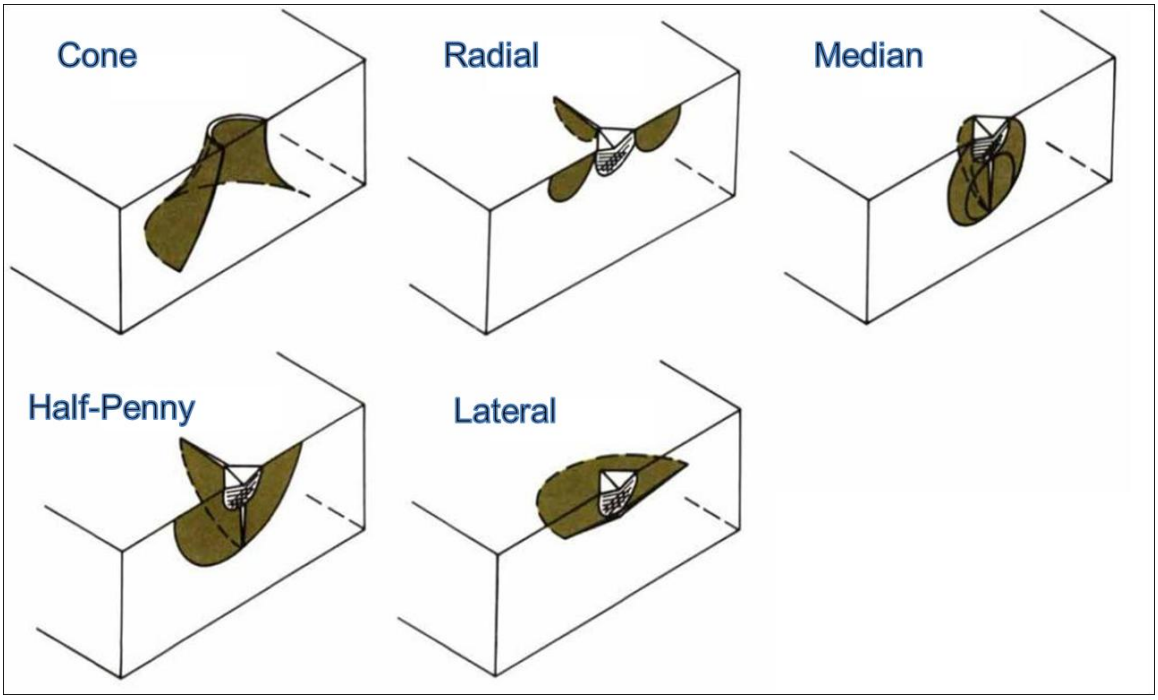


Figure 1.1. The various crack geometries observed during indentation with the Vickers pyramidal indenter.

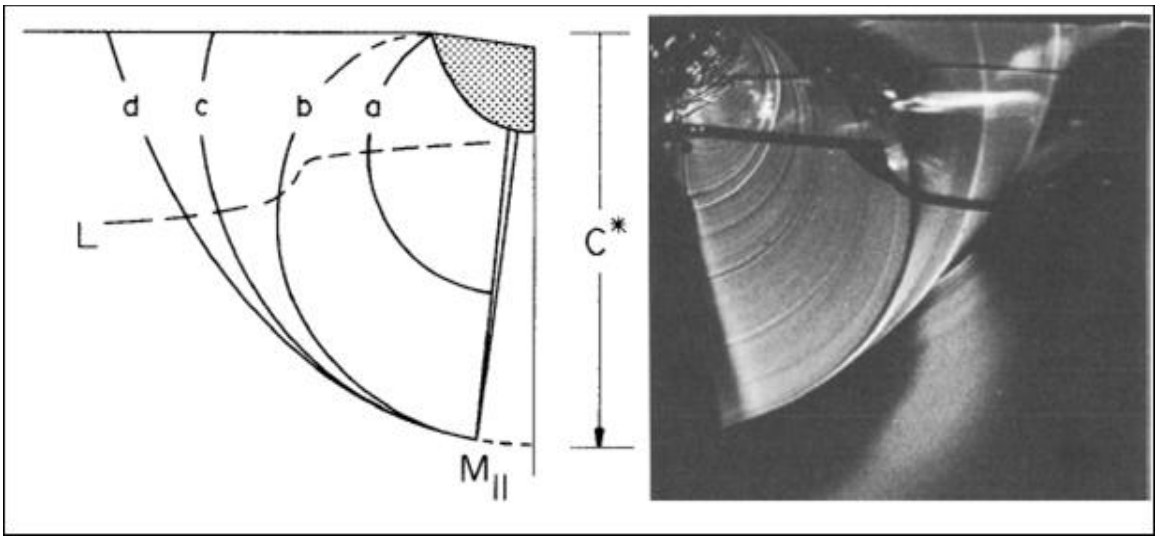


Figure 1.2. Median crack in glass beneath a Vickers indenter showing crack development: (a) during loading, (b) at maximum load, (c) partially unloaded, and (d) after complete removal of load. The crack is visible at the surface only during the unloading portion of the cycle.

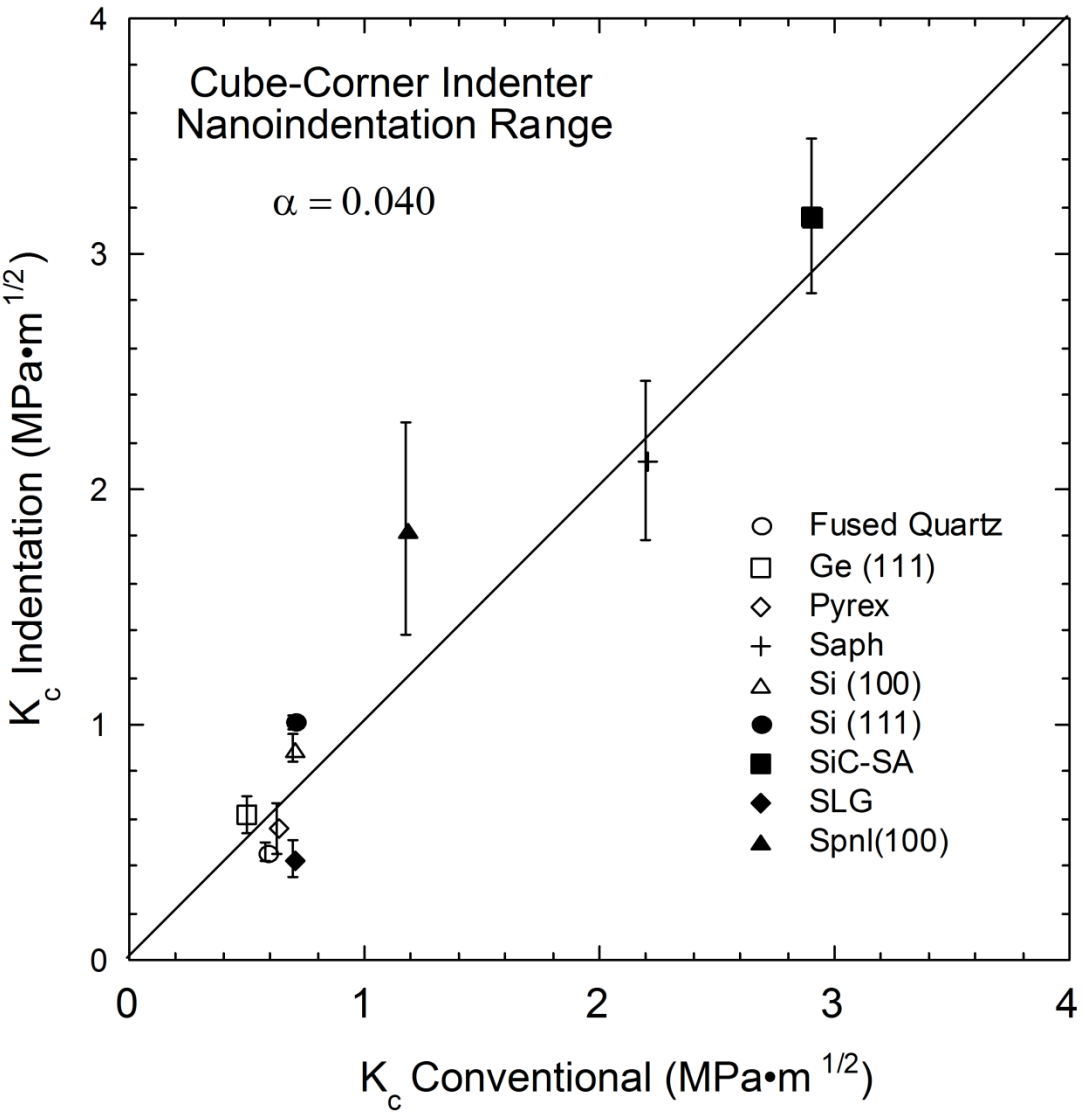


Figure 1.3. Harding's indentation fracture toughness measurements compared to standard fracture toughness tests for a number of ceramic materials.

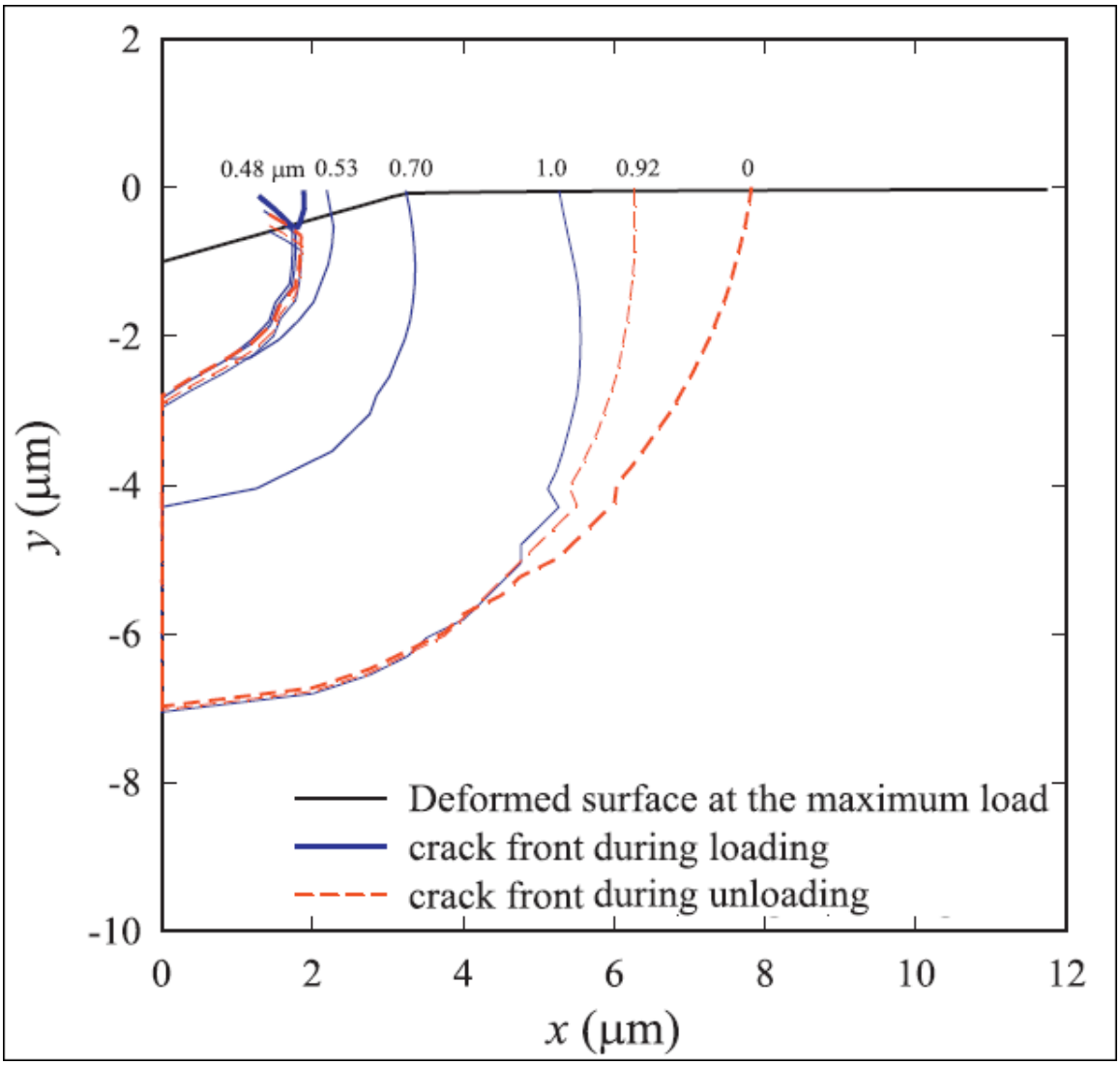


Figure 1.4. Half-Penny crack geometry observed in cohesive finite element simulations of Vickers indentation cracking. Notice the similarities in loaded and unloaded crack geometries between the simulations and the experimental results in Fig. 1.2.

CHAPTER II

AN EVALUATION OF THE ADVANTAGES AND LIMITATIONS IN SIMULATING INDENTATION CRACKING WITH COHESIVE ZONE FINITE ELEMENTS

Abstract

A cohesive zone model is applied to a finite element scheme to simulate indentation cracking in brittle materials. Limitations of using the cohesive zone model to study indentation cracking are determined from simulations of a standard fracture toughness specimen and a two-dimensional indentation cracking problem wherein the morphology of the crack and the geometry of the indenter are simplified. It is found that the principles of linear-elastic fracture mechanics are valid for cracks that are long in comparison to the size of the cohesive zone. Vickers and Berkovich pyramidal indentation crack morphologies (3D) are also investigated and found to be controlled by the ratio of elastic modulus to yield strength (*E/Y*), with median type cracking dominating at low ratios (e.g., *E/Y=10*) and Palmqvist type cracking at higher ratios (e.g., *E/Y=100*). The results show that cohesive finite element simulations of indentation cracking can indeed be used to critically examine the complex relationships between crack morphology, material properties, indenter geometry, and indentation test measurements, provided the crack length is long in comparison to the cohesive zone size.

2.1. Introduction

Indentation testing provides a means to assess the mechanical properties of a material when standard testing techniques may not be applicable, e.g., a limited volume of material or when high spatial resolution is required. The number of mechanical properties that can be measured (elastic modulus, hardness, residual stress, etc.), combined with the ease-of-use and availability of indentation testing equipment, has made indentation testing ubiquitous [1-4]. However, closed-form analyses of indentation contact are usually possible only when the contact is elastic [5-9]. Elastic-plastic loading conditions require models that relate material properties to measured loads and displacements [1, 10, 11], and because of test complexities and assumptions inherent to such models, it is often difficult to know when the results from an indentation test are accurately representative of the mechanical properties of the material [12-14].

Numerical approximations, e.g., finite element techniques, have proven to be an integral part of understanding the physical processes involved during elastic-plastic indentation and their relationship to material properties [15, 16]. In addition, results from numerical simulations have both identified the limits of applicability and extended the accuracy of models used for property estimation [17]. A natural progression in the understanding of indentation testing would be to extend elastic-plastic numerical simulations to include more complicated physical processes, such as cracking, in order to critically examine models that relate indentation test results to material properties like fracture toughness [18, 19].

Indentation cracking in brittle materials occurs during both the loading and unloading of the indenter due to the compressive and tensile stress states associated with elastic-plastic indentation testing [7, 20, 21]. The morphology and size of such cracks is dependent on material properties, indenter geometry, and the applied indentation load. For example, the median/radial crack system is often observed during indentation with the Vickers, Berkovich, and cube corner pyramidal indenters. While median dominated cracking is observed in materials

such as glasses, radial or Palmqvist dominated cracking is seen in others such as tungsten carbide [22, 23]. Thus, relating indentation crack length measurements to fracture toughness is further complicated by a lack of knowledge of the general behavior in crack development from material to material [20]. It is complexities like these that limit the accuracy and applicability of current indentation methods to measuring toughness. Thus, numerical techniques for solving cracking problems can help to provide an understanding of the physical processes controlling indentation cracking and improve modeling capabilities [24].

The cohesive zone model, a traction-separation based constitutive behavior that is often used as a phenomenological representation of crack-tip processes, has been successfully used to model crack growth in numerical simulations for various test configurations including standard fracture toughness samples as well as indentation testing [25-28]. A common theme emerging from the use of the cohesive zone model is the importance of the size of the cohesive zone with respect to the crack length and loading conditions [29]. The primary purpose of this work is to explore the utility of cohesive zone modeling in indentation fracture, and to examine the advantages and limitations of its use in the measurement of fracture toughness by indentation cracking methods. In a parallel work [30], we investigated the relationship between crack size and material parameters under four-sided pyramidal indentations. Because of the computational expense in these three-dimensional problems, we experienced limitations when trying to ensure a very small cohesive zone size. A systematic investigation along this line, as well as the crack initiation problem when the cohesive zone size plays a critical role, is easier to understand in two-dimensional simulations, which is the primary focus here.

We begin the development with a continuum description of indentation cracking and the relationship between material properties, indentation geometry, and the cohesive zone model with an emphasis on the effect of the cohesive zone size on the observed results. A robust finite element procedure that

includes median/radial cracking in indentation simulations is then developed by applying the cohesive zone model. Simulations of cracking during the loading of elastic-plastic materials with a 2D wedge, Vickers, and Berkovich indenter geometries are carried out and used to explore the differences between median/radial cracking and Palmqvist cracking and how they can be explained by differences in material properties and indenter geometry. The intent of this work is not to develop relationships between indentation data and material properties, but to examine the applicability and limitations of the cohesive zone model in simulating indentation cracking in brittle materials. Follow on papers will apply the methods to indentation with conical and pyramidal indenters. The three specific items addressed herein are:

(1) to critically examine the conditions under which cohesive zone modeling can be used to accurately simulate indentation cracking.
(2) to examine the relationship between applied indentation load and crack development as a 2D crack is nucleated and progresses into a long crack.
(3) to assess whether the methods properly predict the cracking behavior in 3D with pyramidal indenters.

2.2. A Continuum View of Indentation Cracking

For simplicity, we begin with a development of the physical mechanisms underlying crack nucleation and subsequent growth during indentation with a rigid two-dimensional (2D) wedge indenter in a brittle, isotropic elastic-perfectly plastic material. Developing these ideas for the 2D wedge eliminates the need to visualize the complicated geometry of pyramidal indentation cracking. In addition, we focus solely on the median/radial crack geometry, with the assumption that cracks grow on specific planes perpendicular to the material surface and aligned with the sharp indenter edges, as observed in experiments. Such planes are also associated with the location of the maximum tensile stress (discussed below). In 2D, the median/radial crack geometry becomes a 2D through-crack, further simplifying the indentation cracking description. The

development, illustrated schematically in Fig. 2.1, involves several sequential processes: elastic-plastic indentation without cracking followed by stable flaw formation, and ending with the steady-state crack geometry. During this process, the geometry evolves from a geometrically self-similar contact to one where the crack length and contact size scale with different dependencies on the applied load.

First, we consider indentation without cracking, as seen in Fig. 2.1a, such that the only relevant length scale is the size of the contact. Indentation in elastic-perfectly plastic materials with wedge, conical, and pyramidal indenters results in geometrically self-similar contact, i.e., the state of stress and strain is independent of the size of the indentation. For an isotropic, elastic-perfectly plastic material, the resulting indentation stress state is only a function of the indenter geometry, the elastic modulus, E, Poisson's ratio, v, and yield strength, Y. The hardness, H, of the material is defined by the applied load, P, and the projected contact dimension, a, and is given by:

$$H = \frac{P}{2a}. \tag{2.1}$$

For 2D problems, the applied load has units of force/length and scales with the projected contact dimension such that the hardness is a constant for the geometrically self-similar indent. There are then two elements pertinent to the indentation cracking problem associated with the indentation conditions: (1) the state of stress and strain is fixed from the onset of indentation, and (2) the magnitudes of the stresses and strains are limited by the yield strength of the material and decay away from the contact. The maximum tensile stress is located at the elastic-plastic boundary on the indentation axis and has a magnitude less than the yield strength of the material, usually on the order of $Y/2$ or less [9].

Now consider the formation of a stable flaw within the context of the geometrically similar indentation, as pictured in Fig. 2.1b. Crack initiation and stable crack propagation will only occur when the flaw size is commensurate with

the local stresses generated by the indentation geometry such that the stress intensity factor acting on the flaw is equal to the critical stress intensity factor of the brittle material. In the elastic-plastic continuum picture, this flaw cannot be generated at the theoretical strength because plasticity limits the magnitude of the maximum tensile stress to stresses well below this value. There are then two ways by which this critical flaw size can be achieved: (1) a pre-existing distribution of flaw sizes exists in the material, so that as the indentation size increases with increasing load, a flaw of appropriate size and orientation is encountered; or (2) material-specific physical processes caused by plastic deformation during indentation are responsible for the creation and growth of a flaw until it has reached the critical size needed for brittle crack extension, e.g., the mechanism proposed by Hagan and Swain [31] where the intersection of slip bands generates a stress concentration sufficient to nucleate a crack. In either case, the critical flaw is not necessarily present in the highly stressed zone near the indenter tip at the instance of first contact, and a finite load is required to initiate the crack. This so-called "threshold load" is a function of the elastic-plastic and fracture properties of the material. Lawn and Evans [32] derived a relationship between the critical flaw size, c^*, hardness, and fracture toughness, K_{Ic}, as:

$$c^* \propto \left(\frac{K_{Ic}}{H} \right)^2 . \tag{2.2}$$

Since this critical flaw size scales as the square of the ratio of the fracture toughness to the hardness (or yield strength), it represents an additional length scale in the problem that plays an important role in simulating indentation fracture with cohesive zone concepts.

With the initiation of a critical flaw, the indentation crack increases in size with increasing load, as seen in Figs. 2.1c and 2.1d. With the onset of cracking, there is a loss of geometric similarity, i.e., the contact dimension and crack length scale differently with load; however the contact size continues to scale with hardness. Initially, in the short crack regime, the crack process zone is a

significant fraction of the crack length and the crack tip process zone dominates the criteria for crack extension (Fig. 2.1c). A steady-state crack geometry, i.e., the state at which crack lengths and indenter loads are related through linear-elastic fracture mechanics (LEFM), occurs only when the size of the crack tip process zone is insignificant when compared to the total crack geometry (Fig. 2.1d). Process zone remnants during the initial stable flaw formation are closed by the advancing plastic zone in the steady-state regime, and depending on the size of the contact, the compressive stresses in the plastic zone can also close previously cracked material (Fig. 2.1d). Fracture processes are often irreversible so crack healing is not permitted. The steady-state indentation crack grows into a decreasing stress field in an infinite half-space with a driving force that is proportional to the indenter load, because of geometric similarity, such that the stress intensity factor has a similar form to that of a crack loaded with a point-force at the mouth [33-35]:

$$K_I \propto \frac{P}{\sqrt{c}}. \tag{2.3}$$

The exact relationship between the stress intensity factor, the applied load, and the crack length has not yet been solved for the case of 2D wedge elastic-perfectly plastic indentation due to the complexity of relating the crack driving force to material and indenter properties. Unloading of the indenter can, in principle, cause further crack growth as the compressive stresses in the elastic field are reduced. This growth is driven by the residual stresses produced by formation of the plastic zone.

2.3. The Cohesive Zone Model

Cohesive zone models have been successfully used to simulate crack-tip processes and crack growth for a wide arrange of material behaviors and loading conditions [27]. The cohesive zone model uses a traction-separation constitutive relationship that is a phenomenological description of the crack-tip processes involved in energy dissipation during crack growth. For the assumed brittle

cracking behavior herein, the length scale associated with crack-tip processes needs to be minimized in order to maintain consistency with LEFM concepts. Here, we describe the constitutive behavior of the cohesive zone model with a focus on the size of the process zone in relationship to the crack length. Note also that the terms “cohesive zone” and “process zone” are used interchangeably since they both describe the zone in which energy is dissipated at the crack-tip during crack extension.

We adopt a bi-linear traction separation relationship, as illustrated in Fig. 2.2a and only account for mode I loading conditions, fully noting that cohesive zones are able to take on many forms and can be used to describe mixed-mode constitutive behavior [36]. Crack separations or crack opening displacements, δ, are elastic upon initial separation and are linearly related to the normal stress, σ, needed to cause the separation through the parameter S (a measure of elastic stiffness), while negative separations are not allowed in the cohesive zone model. Crack separations beyond the point at which the stress is equal to the maximum cohesive strength, σ_c, cause permanent damage, and the cohesive strength decreases as further separations occur up to a critical cohesive displacement, δ_c, after which all stresses are taken to be traction-free. The constitutive behavior does not allow for the healing of cracks. The fracture energy, G, during the separation process is given by the area beneath the traction-separation curve:

$$G = \frac{1}{2}\sigma_c \delta_c. \tag{2.4}$$

It is evident from Fig. 2.2a that a length scale is automatically added to the problem in the form of a critical separation for complete decohesion, δ_c. However, the relevant length scale to be considered is the physical size of the cohesive zone at the tip of a crack, which is typically much greater than the magnitude of the critical separation [29].

Now consider a far-field loaded crack with a crack tip that is bridged by a process zone, as pictured in Fig. 2.2b of a magnified view of a crack-tip in a

center-cracked tension (CCT) specimen. The stresses to the left of the process zone must be elastic and increase as the crack opening displacements increase at the mouth of the crack. In the crack to the right of the process zone, stresses must be traction-free. The length of the process zone, ρ, is defined from the portion of the crack that is between these two regions and in which the stresses vary from zero to the maximum cohesive strength. We choose here to define the crack length, c, as the length of the traction-free zone, noting that the definition of the crack length is relatively arbitrary as one could choose the crack length to include the cohesive zone length (e.g., Irwin's plastic zone correction [33]). This has a negligible effect on the results presented here.

In applying the cohesive zone model, we assume that the mode I plane-strain fracture toughness, K_{Ic}, is determined by brittle fracture processes such that the critical energy release rate is equal to the energy release rate in the cohesive zone, i.e., energy dissipative processes outside of the cohesive zone model do not influence fracture toughness. Of course for a ductile material, the plastic zone developed at the crack tip will influence fracture toughness. Crack extension occurs when the strain energy released is equal to the critical strain energy release rate, G_c, which, according to LEFM, is related to K_{Ic} and the plane-strain elastic modulus, $E'=E/(1-\nu^2)$, by:

$$K_{Ic} = \sqrt{G_c E'}. \tag{2.5}$$

The size of the process zone is dependent on the far-field loading conditions that determine the crack opening displacements, the fracture toughness of the material, and the maximum cohesive strength in the cohesive zone model. A common way to estimate the size of the process zone, ρ, is $\rho=E\delta_c/\sigma_c$. This follows from the work of Dugdale [33], who found that the size of the process zone, ρ, in a CCT specimen with a cohesive strength of σ_c can be estimated by:

$$\rho = \frac{\pi}{8}\left(\frac{K_{Ic}}{\sigma_c}\right)^2. \tag{2.6}$$

Elastic-plastic materials cannot support stress singularities, and therefore the maximum cohesive strength is finite resulting in a finite cohesive zone size. The size of the process zone relative to the crack length would then place a limit on the application of LEFM solutions when cohesive zone models are used to simulate brittle fracture problems. It is apparent from Eq. 2.6 that maximizing the critical cohesive strength minimizes the size of the process zone and thus minimizes the size effect.

2.4. Indentation Cracking and Cohesive Zone Models

We now consider the interplay between the elastic-perfectly plastic indentation stress field described in section 2.2 and the constitutive behavior of the cohesive zone model described in section 2.3. For elastic-plastic indentation, the tensile stresses on the crack plane are limited by plastic deformation to be no more than approximately the yield strength of the material. Thus, cracks must form either from a pre-existing flaw or be generated by plastic deformation processes, neither of which is explicitly included in the modeling approach. Thus, initial crack formation in the simulations performed here cannot accurately describe real crack nucleation processes during indentation, and the initial stages of cracking in the simulations are not meaningful. However, once the crack is well formed and its behavior is dominated by crack propagation mechanisms rather than crack formation mechanisms, the cohesive zone model does provide an accurate description provided the energetics of crack propagation are appropriately modeled. Specifically, the area under the traction-separation curve must be consistent with the fracture toughness of the material. In this case, the propagation behavior is not sensitive to the specific values used for the cohesive zone strength and maximum opening separation [30].

These observations lead to the conclusion that the relationship between indenter loads, fracture toughness, and crack lengths must be made when the influence of the cohesive zone is minimized, i.e., in the limit of long crack lengths with respect to the cohesive zone size.

2.5. Finite Element Modeling

The finite element (FE) software package ABAQUS/Standard [37] was used to develop a robust procedure to apply the cohesive zone concepts described in the previous sections to critically examine indentation cracking. Three separate loading geometries were examined. First, a model of a CCT fracture toughness specimen was developed to identify the limitations of cohesive zone finite elements. Second, with an appreciation for the effects of cohesive zones on crack growth from the CCT simulations, 2D wedge indentation was examined to show how cohesive elements can be used to describe the indentation cracking problem. Finally, a limited number of 3D FE simulations of Vickers and Berkovich indentation cracking were undertaken to compare to experimental observations from the literature.

ABAQUS bi-linear traction-separation based cohesive elements (COH2D4) were employed in all simulations, obviating the need for user-defined materials or elements. A MAXS criterion was used for the onset of debonding, and an input energy was used for crack nucleation. Such elements, with an initial separation of zero, were placed on planes of prospective crack growth, specifically, planes that contain the maximum tensile stress corresponding to the sharp edges of the indenter. Cracks were allowed to grow to the shape and length dictated by the material properties and loading conditions, but were constrained to remain within the defined crack plane.

The cohesive element constitutive behavior was prescribed by four material properties: the mode-I critical energy release rate, the maximum cohesive strength, the initial stiffness, and the viscosity. Definitions, descriptions, and selection of each property can be found in the ABAQUS documentation [37]. The critical energy release rate determines the area beneath the traction-separation curve and is related to fracture toughness through LEFM (Eq. 2.5). The maximum cohesive strength was set equal to $\sim Y/6$ since the maximum tensile stress observed at the elastic-plastic boundary for a given material and loading condition was typically $\sim Y/5$. Note that a choice of the theoretical atomic

debonding strength as the cohesive strength will not lead to crack initiation or growth because the stresses near the crack tip are severely limited by plasticity. Both the mode II and III strain energy release rates and maximum cohesive (shear) strengths were set well above the mode I parameters so that these modes had no influence on the problem. The values used for material properties in the simulations have been summarized in Table I.

Both the initial stiffness, *S*, the property relating the elastic crack opening displacements and stresses, and viscosity, a parameter that forces a positive tangent stiffness matrix during stiffness degradation [37], are phenomenological parameters that facilitate convergence in the FE method when using cohesive elements and may introduce undesirable artifacts. Gao and Bower [38] provided a detailed explanation of the use of viscous regularization with the cohesive zone model (note that the simulations utilized the default ABAQUS viscous regularization technique and not the one proposed by Gao and Bower). The initial stiffness introduces an artificial compliance into the problem because the cohesive element separates elastically before reaching the maximum cohesive strength, adding displacements that would not occur in the absence of the cohesive element. Thus, an infinite initial stiffness is ideally what is needed to minimize the additional compliance. However, the FE simulation will not converge unless a finite value is employed due to the discontinuity between the initial separation and the maximum cohesive strength. Based on the results of Gao and Bower [38] and over the course of developing the FE simulations, it was found that an initial stiffness set two orders of magnitude greater than the elastic modulus (ABAQUS assigns a fictitious finite thickness to the cohesive elements in order to define the initial stiffness in units of elastic moduli [37]) combined with a viscosity parameter of 1×10^{-6} (units of 1/time) and time increments of 0.001 for a total step time of 1.000 resulted in compliances that deviated less than 1% from the ideal compliance.

Three separate sets of FE simulations were undertaken. First, a 2D elastically isotropic CCT specimen having an initial crack length of 2*c* loaded by a

uniform tensile stress, σ, was modeled in order to quantify possible cohesive zone size effects on crack growth. The quarter-symmetry model consisted of 41000 elements (CPE4), meshed such that the elements were concentrated at the crack tip and along the crack path. Details of the overall mesh and refined region have been provided in Fig. 2.3a and Fig. 2.3b respectively. Symmetric boundary conditions were applied to the top and left side surfaces, while a displacement control boundary condition was applied to the right surface where the loads are applied. The crack was constrained to reside entirely within the refined region of the mesh. The fracture toughness was held constant while the cohesive strength was varied, effectively changing the size of the cohesive zone. Both the size of the cohesive zone and the critical stress for crack extension were measured as a function of the maximum cohesive strength. The critical stress was then used to calculate an apparent fracture toughness that was compared to the input value.

Second, a 2D model of an isotropic elastic-perfectly plastic half-space indented with a rigid wedge with a centerline-to-face angle of 60^o was modeled. The purpose of the 2D wedge model was to simplify the indentation and crack geometries by eliminating edge/face effects and median/radial behavior in 3D cases. The half-symmetry model consisting of 41000 elements (CPE4) was meshed such that a higher density of elements was found near the contact and along the prospective crack path. A single crack plane was placed on the indentation axis, perpendicular to the surface of the material. The same mesh as the CCT mesh shown in Fig. 2.3 was used in the 2D wedge simulations. The indenter was driven into the material vertically downward along the axis of symmetry with the crack forming on the same plane. No crack was included at the beginning of the simulations; rather, the crack was allowed to form according to the conditions dictated by the traction-separation law. A symmetric boundary condition was used on the left side while the bottom of the model was fixed (see Fig. 2.3). Displacement controlled boundary conditions were applied to the rigid indenter, which was only free to move in the indentation direction. Frictionless

contact was assumed between the indenter and the contact surface. In these simulations, all material properties except the yield strength were held constant. Loads and crack lengths were measured to see if the behavior was consistent with LEFM concepts of a crack growing into a decaying stress field.

Finally, a limited number of3D models of rigid pyramidal indenters indenting an isotropic elastic-perfectly plastic half-space were simulated in light of the results from the CCT and 2D wedge simulations. Crack planes were placed perpendicular to the free surface and aligned with the edges of the indenter. In addition, a second group of crack planes was placed on planes perpendicular to the center of the faces in order to see if cracking would occur there. The symmetry of the indenters was used to minimize the number of elements required in the simulation. Eight-fold and six-fold symmetries were used for the four-sided (Vickers) and three-sided (Berkovich) models, respectively. More than 60,000 full integration elements (C3D6 and C3D8) were employed with the mesh being denser near the contact and prospective crack paths. Isometric and top-down views of the six-fold symmetry Berkovich indentation mesh are provided in Fig. 2.4a and Fig. 2.4b respectively. Symmetric boundary conditions were applied to both sides of the model while the bottom was held fixed. Displacement control boundary conditions were applied to the rigid indenter, which was only free to move in the indentation direction. Frictionless contact was assumed between the indenter and the upper surface. A similar mesh with eight-fold symmetry was used in the case of the Vickers indentation simulations. The goal of the 3D pyramidal indentation was to observe crack morphologies as a function of material properties, and to that end the assumed fracture toughness was held constant while the yield strength was varied. Results are presented in terms of crack geometry as a function of applied load.

2.6. Results and Discussion

Results from the FE simulation of a brittle, elastic CCT specimen (E=100 GPa, v=0.25, K_{Ic}=1.46 MPa $m^{1/2}$) are shown in Fig. 2.5 with a focus on the geometry of the process zone with respect to the far-field tensile stress. Assumed cohesive strengths ranged from 0.4 GPa to 2.0 GPa, effectively changing the size of the process zone (Eq. 2.6). The CCT geometry under an applied stress, σ_{app}, is shown in Fig. 2.5a with the crack opening displacements exaggerated for display purposes. A magnified view of the stresses inside the process zone is presented in Fig. 2.5b. The separations inside the process zone are unique to the loading condition. Here, we choose to define the size of the process zone as the distance measured from the point at which the cohesive elements are traction free to the point where irreversible deformation begins (i.e., separations greater than the separation at the maximum cohesive strength). Process zone sizes, plotted in Fig. 2.5c as a function of the applied tensile stress, were found to be in excellent agreement with Dugdale's prediction from Eq. 2.6.

A traction-separation profile for a single cohesive element in the CCT simulation is shown in Fig. 2.6. The results exhibit a good match between the input and output constitutive behavior, i.e., the use of viscous regularization did not result in an overloading of the cohesive element. A similar traction-separation profile has been supplied in the case of the 2D wedge simulation in Fig. 2.6 for convenience. While the behavior of only one element has been shown, inspection of other cohesive elements showed similar results. The area beneath the initial rise in the traction-separation curve is ~1% of the debonding area in both types of simulations, an important result that ensures the compliance of the model is minimally affected by the addition of cohesive elements.

Failure by unstable crack growth occurred in the CCT FE simulations when the applied stress satisfied the conditions for crack growth in the cohesive zone model. The applied stress at failure, σ_{app}^{*}, did not necessarily occur when the stress intensity factor reached the input fracture toughness, K_{Ic}^{input} (calculated

from Eq. 2.5), since we are dealing with a cohesive crack instead of an ideal Griffith crack. It was observed that the applied stress at failure decreased as the size of the process zone increased. In order to quantitatively describe the effect of the process zone on crack extension, an apparent fracture toughness, K_{Ic}^{app}, was calculated from the stress intensity factor solution for a CCT specimen:

$$K_{Ic}^{app} = \sigma_{app}^{*}\sqrt{\pi c}. \tag{2.7}$$

The resulting effect of the size of the process zone on fracture toughness is shown in Fig. 2.7, with the resulting apparent fracture toughness from the CCT specimen plotted as a function of the size of the process zone, ρ, relative to the crack length, c. The apparent fracture toughness was found to be consistently lower than the input fracture toughness, and the discrepancy increased with increasing size of the process zone. Only when the size of the process zone tends toward zero does the apparent fracture toughness approach the input value. Dugdale, in a similar manner to Irwin's plastic zone correction, corrected the CCT fracture toughness solution by adding the size of the process zone to the length of the crack, that is:

$$K_{Ic}^{app} = \sigma_{app}^{*}\sqrt{\pi c + \frac{\pi^2}{8}\left(\frac{K_{Ic}}{\sigma_c}\right)^2}. \tag{2.8}$$

Here, the size of the process zone from Eq. 2.6 has been combined with Eq. 2.7. Dugdale's correction to the apparent fracture toughness from the FE simulation is plotted in Fig. 2.7 along with the uncorrected data. Clearly, the use of Eq. 2.8 results in an apparent fracture toughness nearly the same as the input fracture toughness (within computation accuracy). It should be noted, however, that Dugdale's correction applies to the CCT geometry only, and no such simple representations can be easily found for different loading conditions and geometries.

The results of the CCT simulations have two important ramifications for indentation cracking simulations with the cohesive zone model. First, accurate determination of the relationship between material properties, indenter geometry,

applied load, and crack length must be made under the condition that the size of process zone is insignificant relative to the size of the crack. Inasmuch as the behavior in Fig. 2.7 is general to all cohesive zone simulations, the apparent fracture toughness is within ~95% of the input fracture toughness when the size of the process zone is less than ~10% of the size of the crack. Second, because the indentation crack starts from zero length in the simulations, the process zone size and crack length require a finite load to develop into a steady-state geometry (see Fig. 2.1d). The initial crack sizes and geometries upon first contact (i.e., the flaw formation regime in Fig. 2.1b) are not only dependent on the input fracture toughness, but also on the parameters of the cohesive zone model along with the local stress state. The length scale represented by the parameter $(K_{Ic}/\sigma_c)^2$ in comparison to the crack length will determine whether valid connections between model results and input material properties are determined. Clearly, Eq. 2.8 reduces to the LEFM solution in the limit that this length scale is small relative to the crack length.

FE Simulation results for a 60^o rigid 2D wedge indenting an elastic-perfectly plastic material with an modulus to yield strength ratio (E/Y) of 20, a fracture toughness of 1.41 MPa $m^{1/2}$, and a σ_c/Y of 0.15, properties similar to many ceramic-like materials, are shown in Fig. 2.8. The resulting deformation geometry, plastic zone, and crack length as a function of applied load (load here refers to a force per unit area in 2D) are all shown. Figures 2.8a-d correspond to the elastic-plastic, stable flaw formation, short crack, and steady-state regimes, respectively (see section 2, Fig. 2.1). The magnitude and location of the maximum tensile stress in the crack opening direction are shown in Fig. 2.8a. Ignoring numerical artifacts at very small displacements when only a few elements are in contact, there are initially two competing processes acting at the elastic-plastic boundary that determine when the crack first initiates (i.e., when the first cohesive element becomes traction free). The constant tensile stress at the elastic-plastic boundary acts as a separating mechanism; however, stresses inside the plastic zone are compressive and act as a closing mechanism (the

cohesive elements do not “heal” but they can close). While separation of cohesive elements begins immediately, successive displacements of the indenter increase the size of the plastic zone and close the cohesive elements just inside the plastic zone. The opening of cohesive elements at the elastic-plastic boundary scales with the indenter displacement due to geometric similarity, or equivalently, from a dimensional argument. Thus, it is eventually large enough to initiate a crack. Once a crack is initiated, the increase in crack length is greater than the increase in the size of the plastic zone for a given increase in applied load. However, the plastic zone continues to close the crack at the end near the surface. Additionally, the size of the process zone, initially zero, plateaus as the crack tip moves away from the plastic zone and becomes a smaller and smaller fraction of the crack length. The observations from the 2D FE simulation help to show that the crack initiation process is not a function of fracture toughness, but rather strongly depends on the critical cohesive strength and the traction-free separation, which are probably not representative of the real physical mechanisms by which a crack nucleates.

Adding the constant of proportionality to Eq. 2.3 and taking the derivative of the square-root of the crack length with respect to load, the 2D wedge indentation crack should stably increase with applied load if the assumptions of LEFM are met according to:

$$\frac{d\sqrt{c}}{dP} = \frac{\alpha}{K_{Ic}}, \tag{2.9}$$

where α is a scaling factor (unknown in the case of 2D wedge indentation) that depends on the relationship between material properties, the applied load, P, and the crack driving force. While the indenter load, acting in a direction parallel to the crack growth direction, is not the crack driving force, the crack driving forces must scale with the applied load. The square-root of the crack length as a function of load is plotted in Fig. 2.9 for two materials with E/Y ratios of 20 and 33 (E=100 GPa, v=0.25, K_{Ic}=1.41 MPa m$^{1/2}$, σ_c=1 GPa). The locations of the four regimes in Fig. 2.5 are highlighted for the E/Y=20 curve. In both materials, once

the threshold load for cracking has been reached, the initial rate at which the crack grows is large, but slowly decreases until a steady-state is achieved and the rate of increase of the square-root of crack length is linear with load. This is consistent with Eq. 2.9 and the CCT observations that the apparent fracture toughness increases as the ratio of the crack length to process zone increases until finally converging to the input toughness. The size of the process zone in the 2D wedge simulations was ~0.7 μm, which is slightly greater than the Dugdale prediction of ~0.4 μm (Eq. 2.6). Unloading of the indenter did not produce further crack growth in the case of the 2D wedge.

The data in Fig. 2.9 fits well to a linear fit in the long crack regime showing that the 2D wedge crack has reached a steady-state geometry that can be described by LEFM (Eq. 2.9). The values of α/K_{Ic} from the fits were found to be ~0.24 $\mu m^{3/2}$ mN^{-1} and ~0.45 $\mu m^{3/2}$ mN^{-1} for E/Y ratios of 20 and 33 respectively, showing a clear dependence on the elastic-plastic properties of the material, where more plastic-like materials (e.g., E/Y=33) create a larger driving force for crack growth. Unfortunately, there is no fracture mechanics solution for the 2D wedge indentation crack problem and therefore the predicted values of α are unknown. In addition, 2D contact problems suffer from calculation cell size dependencies that may affect the magnitude of α because of the logarithmic decay of the remote stress fields [6]. That being said, Eq. 2.9 appears to be a valid description of the indentation crack problem in the limit of large crack to process zone size ratios, consistent with the observations from the CCT specimen. The results represented in Fig. 2.9 can be used to critically examine indentation cracking models in 2D as described in more detail in Chapter III.

3D pyramidal indentation during loading and unloading was simulated to: (1) examine the difference between the Vickers (4-sided) and Berkovich (3-sided) indenter geometries, (2) rationalize the difference between median/radial and Palmqvist type cracking, and (3) confirm that the simulation results are consistent with experimental observations. Results are presented for two brittle, elastic-perfectly plastic materials (E=100 GPa, v=0.25, K_{Ic}=1.41 MPa $m^{1/2}$, σ_c=0.3 GPa),

the only difference being the ratio of elastic modulus to yield strength, namely E/Y=10 and E/Y=100. The two materials can be thought of as representing the elastic-plastic limits of ceramic-like materials, i.e., deformation will be dominated by elasticity in the E/Y=10 material, while the E/Y=100 material will be more metallic-like with a greater degree of plasticity. The authors refer readers to Tabor's seminal book on indentation hardness [4] for more detailed discussion on the influence of material properties on indentation behavior.

Vickers indentation crack morphologies as a function of load are shown in Fig. 2.10. Of the crack planes considered in the model, only those aligned with the indenter edges produced cracks, as seen in Fig. 2.10a. Figure 2.10b shows the resulting crack geometry of one such plane as a function of load for the E/Y=10 material. At all times during loading, median cracking dominates the crack geometry, and this is maintained up to the maximum load. Upon unloading, the median crack extends radially at the surface forming the classic half-penny morphology. Vickers indentation crack geometries in the E/Y=100 material are shown in Fig. 2.10c. In contrast to the results from the E/Y=10 material, cracking begins near the surface at the indenter edges to produce surface oriented Palmqvist type cracks. Further loading causes the crack to extend downward into the material but avoiding the compressive stresses inside the plastic zone. Upon unloading, the crack again extends radially at the surface producing half-penny cracks aligned with the four edges of the Vickers indenter. The observed differences in crack geometries between the two materials can be rationalized from the transition of the maximum tensile stress from a position on the axis of indentation in the E/Y=10 material to a position near the surface in the E/Y=100 material. This transition is associated with an increase in plasticity at the surface region for larger values of E/Y.

Berkovich indentation cracking morphologies as a function of load are presented in Fig. 2.11. As with the Vickers indenter, cracking only occurred on planes aligned with the edges of the Berkovich indenter as seen in Fig. 2.11a. The crack geometries observed at the maximum load, and upon unloading are

shown in Figs. 2.11b and 2.11c for the *E/Y*=10 and *E/Y*=100 materials, respectively. The results are consistent with the observations from the Vickers indenter with one caveat: cracks do not propagate to the face side of the indenter, ultimately leading to a configuration of three quarter-penny cracks aligned with the three edges of the indenter. The consistency with the Vickers indenter can be understood from the equivalent depth-to-projected areas of the two indenters (i.e., the indentation strains are similar) and thus similar deformation behavior. In other words, the two indenters have equivalent cone angles, and the indentation strain is determined from the ratio of *E/Y* and the indenter angle [6].

The lack of face-side cracking in the Berkovich indenter simulations can be understood from the symmetry of the indenter. Three independent cracks intersect at the axis of the indentation and therefore cannot propagate through to the face of the indenter. Also, because of the symmetry imposed in the FE simulations, each of the three cracks form in a symmetric manner such that one crack cannot preferentially grow at the expense of others. In experiments, one crack could preferentially form first and thus break the symmetry allowing for propagation to the face side. In order to show that face-side cracking can exist, crack geometries of Berkovich indents where only one edge plane (and one face plane) was allowed to crack are shown in Fig. 2.12. As in Fig. 2.11, the *E/Y*=10 material, seen in Fig. 2.12a, is dominated by median cracking on loading and the *E/Y*=100 material, seen in Fig. 2.12b, has components of Palmqvist cracking on loading. The major difference is that the crack extends to the face side of the indenter on both loading and unloading. It is conceivable that these types of crack morphologies in three-sided indentation may be observed experimentally due to a number of factors including asymmetry of the indenter or preferential growth of one crack at the expense of another.

Three important conclusions can be drawn from the 3D indentation cracking simulations:

(1) First and foremost, the way in which we have utilized the cohesive finite elements gives rise to indentation crack geometries very similar to those observed in experiments, pointing to the value of using the cohesive zone approach to describe the propagation of indentation cracks and evolution of indentation crack geometries.
(2) There is a strong dependence of crack geometry on material properties. Half-penny crack geometries tend to occur in more ceramic-like materials (E/Y~10) while Palmqvist geometries occur in more metallic-like materials (E/Y~100). This change in crack geometry with an increasing E/Y ratio may have a significant role in the relationship between crack lengths, loads, and material properties.
(3) The development of indentation crack geometries for a 4-sided Vickers indenter and a 3-sided Berkovich indenter is quite different due to the lack mirror symmetry for the 3-sided indenter.

Ultimately, the results from these FE simulations of indentation cracking are of value only if they are consistent with experimental observations. The results to this point have been presented for two fictitious materials, but they support observations in the literature for why some materials exhibit median/radial cracking and others form surface oriented Palmqvist cracks. To more directly compare to experimental observations, we also present results from a simulation on a real glass-like material having an E/Y ratio of 25 and a fracture toughness of ~1 MPa $m^{1/2}$, in order to compare to testing in a similar material with a cube-corner indenter [39]. The cube-corner indenter has a centerline-to-face angle of 35^{o}; however, convergence is often difficult in simulations of sharp indenters and the smallest possible angle achieved in these results was 40^{o}. Figure 2.13 shows the experimental observations [39] alongside the FE results. The extremely similar final crack morphologies demonstrate that the cohesive zone FE approach does indeed properly capture the indentation cracking behavior. This result further strengthens the idea that FE simulations of

indentation cracking applying the cohesive zone model can be used to critically examine the relationships between material properties, indenter geometry, and indenter loads and displacements.

2.7. Conclusions

Cohesive zone finite element techniques were used to model indentation cracking. Simulations were performed to examine a standard fracture toughness specimen, 2D wedge indentation cracking, and 3D pyramidal indentation cracking with Vickers and Berkovich indenters. The following observations were made:

(1) The fundamental assumptions of LEFM are valid when simulating crack growth with the cohesive zone model in the limit that the size of the process zone is small compared to the size of the crack. From results of CCT specimen simulations, the apparent fracture toughness is within ~95% of the input fracture toughness when the size of the process zone is less than ~10% the size of the crack.

(2) Observations from 2D wedge indentation cracking simulations show that the effects of the cohesive zone model are consistent with observations from simulations of a standard fracture toughness geometry. In addition, the crack length scales according to the simple relationship of a crack growing into a decreasing stress field, where the driving force is proportional to the applied indentation load.

(3) Vickers (four-sided pyramid) indentation cracking models exhibit the commonly observed half-penny crack geometry, while Berkovich (three-sided pyramid) indentation results in a quarter-penny geometry due to the symmetry of the indenter. Both indenters show crack growth during loading and unloading.

(4) The geometry of the indentation crack has a dependence on the elastic-plastic properties of the material. Median dominated crack growth occurs

in materials with low *E/Y* ratios, whereas Palmqvist dominated cracking occurs as the ratio of *E/Y* increases toward that of metallic materials.

Finally, the ability to simulate indentation cracking with cohesive finite elements provides a tool by which indentation cracking models (e.g., the LEM model [18]) can be critically analyzed for elastic-plastic materials. In addition, the complicated crack driving force can be related to material properties, indenter geometry, and indentation parameters such as load and displacement. The predictive capability of indentation cracking models could be greatly improved with such knowledge.

References

1. W.C. Oliver and G.M. Pharr: Measurement of hardness and elastic modulus by instrumented indentation: Advances in understanding and refinements to methodology. *Journal of Materials Research*. **19**, 3 (2004).
2. A. Gouldstone, N. Chollacoop, M. Dao, J. Li, A.M. Minor and Y.-L. Shen: Indentation across size scales and disciplines: Recent developments in experimentation and modeling. *Acta Mater*. **55**, 4015 (2007).
3. M.R. VanLandingham, J.S. Villarrubia, W.F. Guthrie and G.F. Meyers: Nanoindentation of polymers: an overview. *Macromolecular Symposia*. **167**, 15 (2001).
4. D. Tabor, *The Hardness of metals*. 1951, Oxford: Clarendon Pr.
5. I.N. Sneddon: The relation between load and penetration in the axisymmetric boussinesq problem for a punch of arbitrary profile. *International Journal of Engineering Science*. **3**, 47 (1965).
6. K.L. Johnson, *Contact Mechanics*. 1987: Cambridge University Press.
7. S.S. Chiang, D.B. Marshall and A.G. Evans: The response of solids to elastic/plastic indentation. I. Stresses and residual stresses. *J. Appl. Phys.* **53**, 298 (1982).
8. E.H. Yoffe: Elastic stress fields caused by indenting brittle materials. *Philosophical Magazine A*. **46**, 617 (1982).
9. G. Feng, S. Qu, Y. Huang and W.D. Nix: An analytical expression for the stress field around an elastoplastic indentation/contact. *Acta Mater*. **55**, 2929 (2007).
10. Y.-T. Cheng and C.-M. Cheng: Relationships between hardness, elastic modulus, and the work of indentation. *Appl Phys Lett*. **73**, 614 (1998).
11. J.S. Field and M.V. Swain: A simple predictive model for spherical indentation. *Journal of Materials Research*. **8**, 297 (1993).
12. Y.-T. Cheng and C.-M. Cheng: Can stress–strain relationships be obtained from indentation curves using conical and pyramidal indenters? *Journal of Materials Research*. **14**, 3493 (1999).
13. X. Chen, N. Ogasawara, M. Zhao and N. Chiba: On the uniqueness of measuring elastoplastic properties from indentation: The indistinguishable mystical materials. *J Mech Phys Solids*. **55**, 1618 (2007).
14. J. Menčík and M.V. Swain: Errors associated with depth-sensing microindentation tests. *Journal of Materials Research*. **10**, 1491 (1995).
15. A.E. Giannakopoulos, P.L. Larsson and R. Vestergaard: Analysis of Vickers indentation. *International Journal of Solids and Structures*. **31**, 2679 (1994).
16. P.L. Larsson, A.E. Giannakopoulos, E. SÖderlund, D.J. Rowcliffe and R. Vestergaard: Analysis of Berkovich indentation. *International Journal of Solids and Structures*. **33**, 221 (1996).
17. A. Bolshakov and G.M. Pharr: Influences of pileup on the measurement of mechanical properties by load and depth sensing indentation techniques. *Journal of Materials Research*. **13**, 1049 (1998).

18. B.R. Lawn, A.G. Evans and D.B. Marshall: Elastic-Plastic Indentation Damage in Ceramics - the Median-Radial Crack System. *J Am Ceram Soc*. **63**, 574 (1980).
19. C.B. Ponton and R.D. Rawlings: Vickers indentation fracture toughness test Part 1 Review of literature and formulation of standardised indentation toughness equations. *Materials Science and Technology*. **5**, 865 (1989).
20. R.F. Cook and G.M. Pharr: Direct Observation and Analysis of Indentation Cracking in Glasses and Ceramics. *J Am Ceram Soc*. **73**, 787 (1990).
21. B. Lawn and R. Wilshaw: Indentation fracture: principles and applications. *Journal of Materials Science*. **10**, 1049 (1975).
22. J. Lankford: Indentation microfracture in the Palmqvist crack regime: implications for fracture toughness evaluation by the indentation method. *Journal of Materials Science Letters*. **1**, 493 (1982).
23. M.T. Laugier: Palmqvist indentation toughness in WC-Co composites. *Journal of Materials Science Letters*. **6**, 897 (1987).
24. A. Leonardi, F. Furgiuele, R.J.K. Wood and S. Syngellakis: Numerical analysis of brittle materials fractured by sharp indenters. *Engineering Fracture Mechanics*. **77**, 264 (2010).
25. A. Muchtar, L.C. Lim and K.H. Lee: Finite element analysis of vickers indentation cracking processes in brittle solids using elements exhibiting cohesive post-failure behaviour. *Journal of Materials Science*. **38**, 235 (2003).
26. W. Zhang and G. Subhash: An elastic-plastic-cracking model for finite element analysis of indentation cracking in brittle materials. *International Journal of Solids and Structures*. **38**, 5893 (2001).
27. A. Cornec, I. Scheider and K.-H. Schwalbe: On the practical application of the cohesive model. *Engineering Fracture Mechanics*. **70**, 1963 (2003).
28. H. Wan, Y. Shen, Q. Chen and Y. Chen: A plastic damage model for finite element analysis of cracking of silicon under indentation. *Journal of Materials Research*. **25**, 2224 (2010).
29. G. Bao and Z. Suo: Remarks on Crack-Bridging Concepts. *Applied Mechanics Reviews*. **45**, 355 (1992).
30. J.H. Lee, Y.F. Gao, K.E. Johanns and G.M. Pharr: Cohesive interface simulations of indentation cracking as a fracture toughness measurement method for brittle materials. *Acta Mater*. **60**, 5448 (2012).
31. J.T. Hagan and M.V. Swain: The origin of median and lateral cracks around plastic indents in brittle materials. *Journal of Physics D: Applied Physics*. **11**, 2091 (1978).
32. B.R. Lawn and A.G. Evans: A model for crack initiation in elastic/plastic indentation fields. *Journal of Materials Science*. **12**, 2195 (1977).
33. T.L. Anderson, *Fracture Mechanics: Fundamentals and Applications*. 2005: Taylor & Francis.
34. H. Tada, P.C. Paris and G.R. Irwin, *The stress analysis of cracks handbook*. 1973: Del Research Corp.
35. B.R. Lawn, *Fracture of Brittle Solids*. 1993: Cambridge University Press.

36. M. Ortiz and A. Pandolfi: Finite-deformation irreversible cohesive elements for three-dimensional crack-propagation analysis. *International Journal for Numerical Methods in Engineering*. **44**, 1267 (1999).
37. Simulia, *ABAQUS User's Manual*. 2008: Simulia Co.
38. Y.F. Gao and A.F. Bower: A simple technique for avoiding convergence problems in finite element simulations of crack nucleation and growth on cohesive interfaces. *Model Simul Mater Sc*. **12**, 453 (2004).
39. R. Tandon: A technique for measuring stresses in small spatial regions using cube-corner indentation: Application to tempered glass plates. *Journal of the European Ceramic Society*. **27**, 2407 (2007).

APPENDIX 2.1.

Table 2.1. Material and cohesive element inputs in the finite element simulations.

Simulation	**E** (GPa)	**Y** (GPa)	**v**	**σ_c** (GPa)	**G** (GPa μm)	**S** (GPa)	**μ** (s^{-1})	**CE length to ρ ratio**
2D CCT	100	N/A	0.25	0.4-2.0	1.0×10^{-2}	1.0×10^{4}	1.0×10^{-6}	~ 0.1
2D Wedge	100	3.0, 5.0	0.25	1.0	9.375×10^{-3}	1.0×10^{4}	1.0×10^{-6}	~ 0.1
3D Indenter	100	1.0, 10.0	0.25	0.3	9.375×10^{-3}	1.0×10^{4}	1.0×10^{-6}	~ 0.2

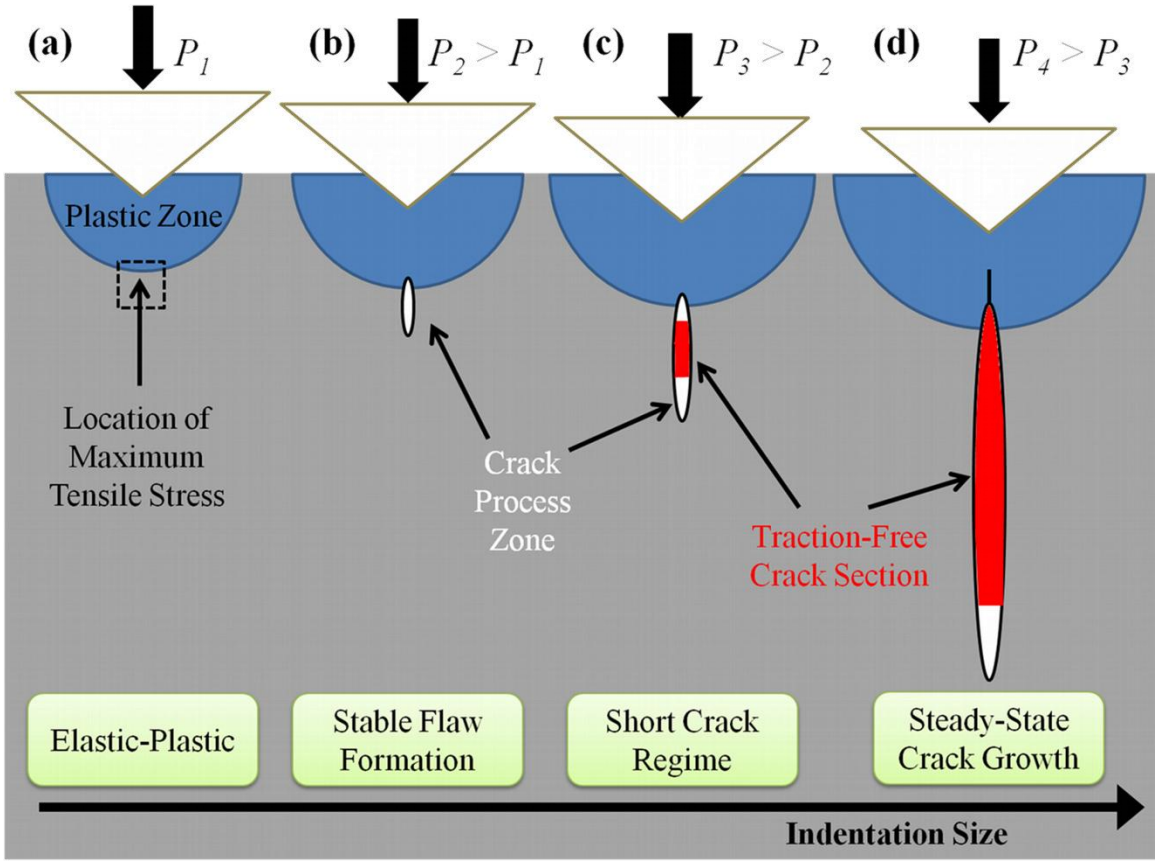


Figure 2.1. A continuum picture of indentation cracking in elastic-plastic materials: (a) geometrically self-similar contact by elastic-plastic deformation where the size of the contact scales with the applied load and hardness; (b) the formation of a stable flaw nucleated by plastic deformation; (c) the short-crack regime where the process zone dominates crack behavior; and (d) steady-state crack growth where process zone effects are insignificant and the crack length scales according to the LEFM analysis.

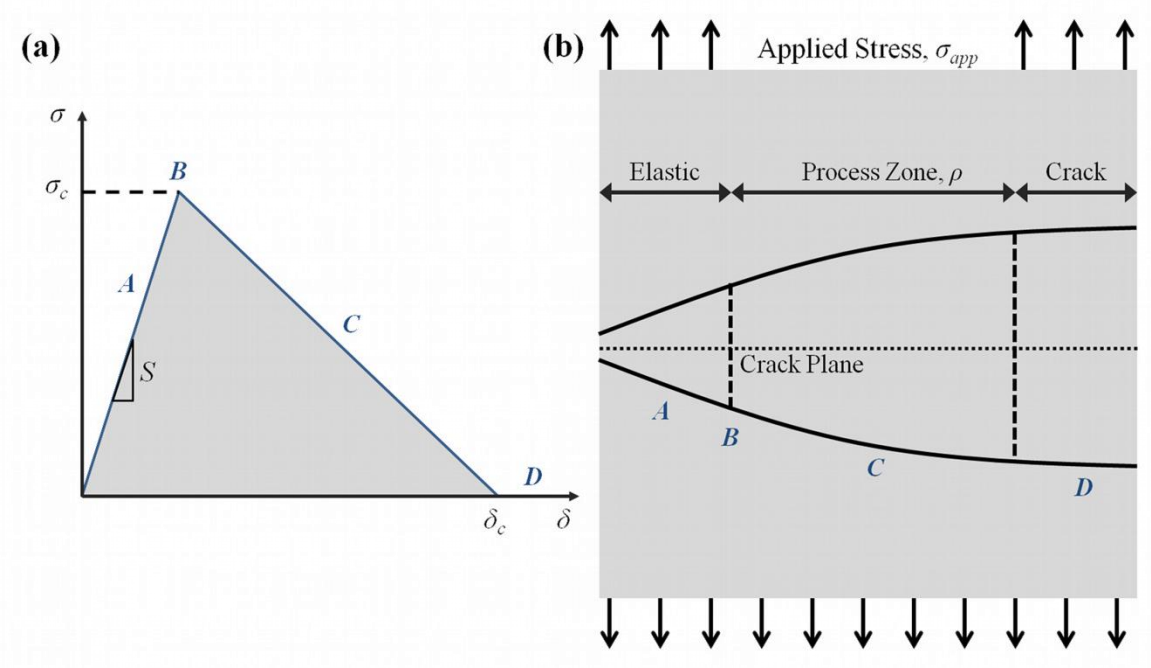


Figure 2.2. Schematic representation of the cohesive zone model of a crack tip: (a) the traction-separation constitutive behavior; and (b) a magnified view of a crack-tip in a CCT specimen showing the process zone geometry. Points A, B, C, and D in (a) correspond to the locations identified in (b).

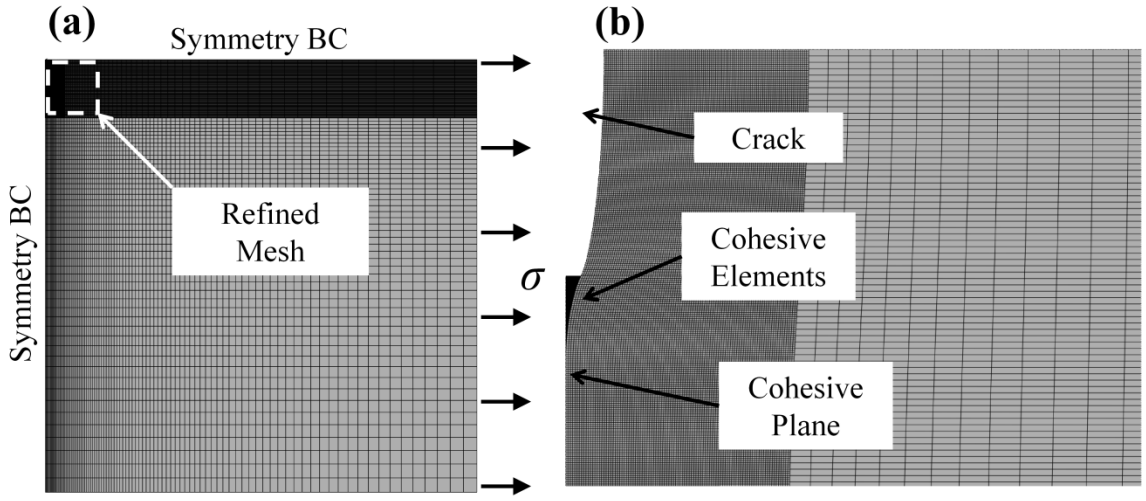


Figure 2.3. CCT cohesive finite element mesh and boundary conditions: (a) overall mesh; (b) magnified view of the refined region under deformation. Displacements in the horizontal direction in the deformed mesh have been exaggerated. A similar mesh was used for the 2D wedge simulations.

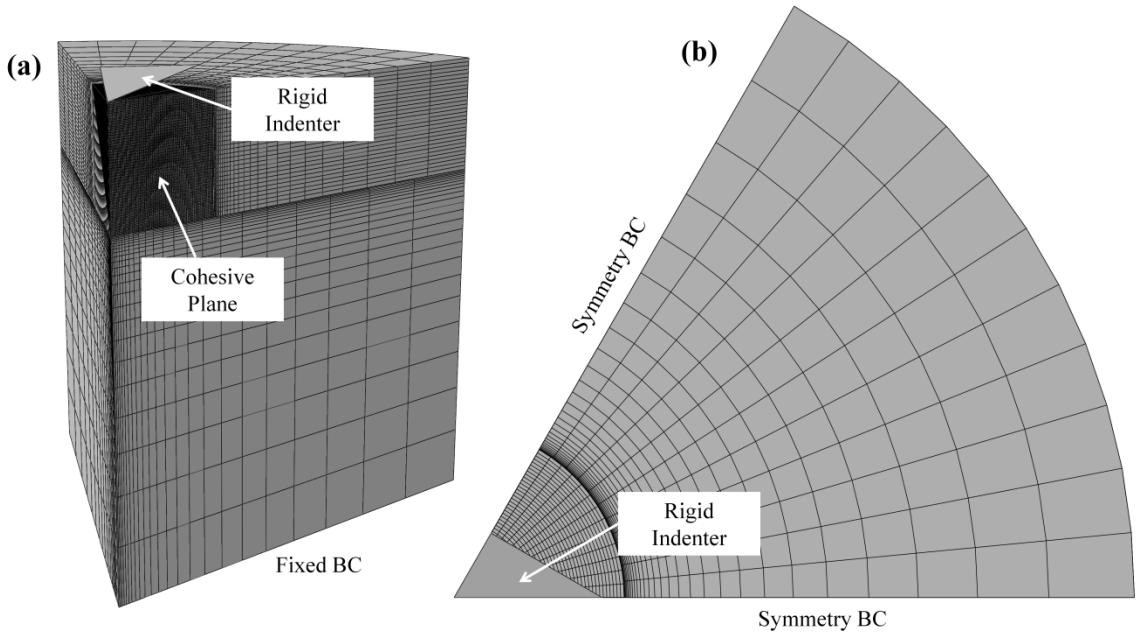


Figure 2.4. 3D Berkovich indentation cohesive finite element mesh and boundary conditions: (a) isometric view; (b) top-down view.

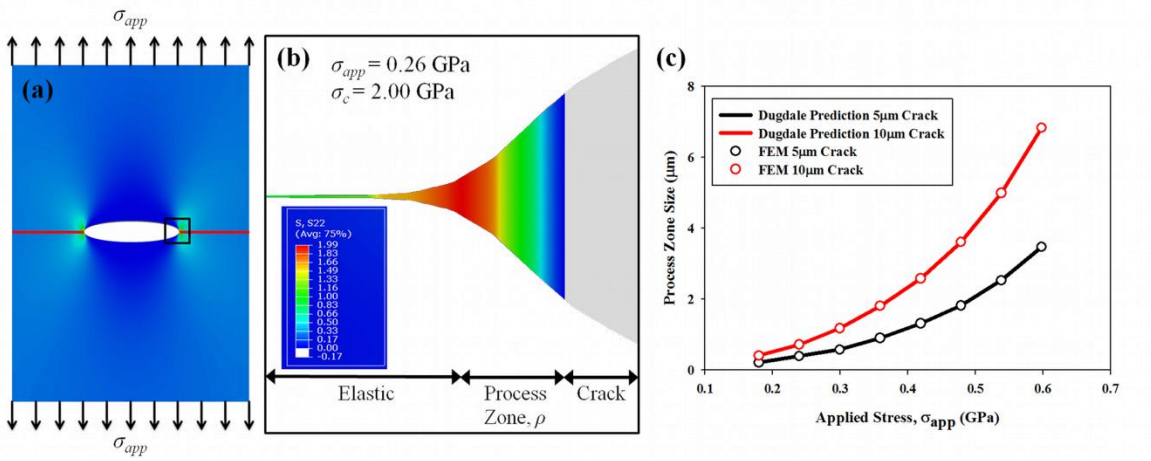


Figure 2.5. Finite element simulation of a CCT specimen using cohesive elements: (a) overview of the CCT geometry with crack opening displacements exaggerated for display purposes; (b) magnified view of the crack tip showing the stresses in the cohesive zone; and (c) measured cohesive zone sizes for comparison to Dugdale's prediction.

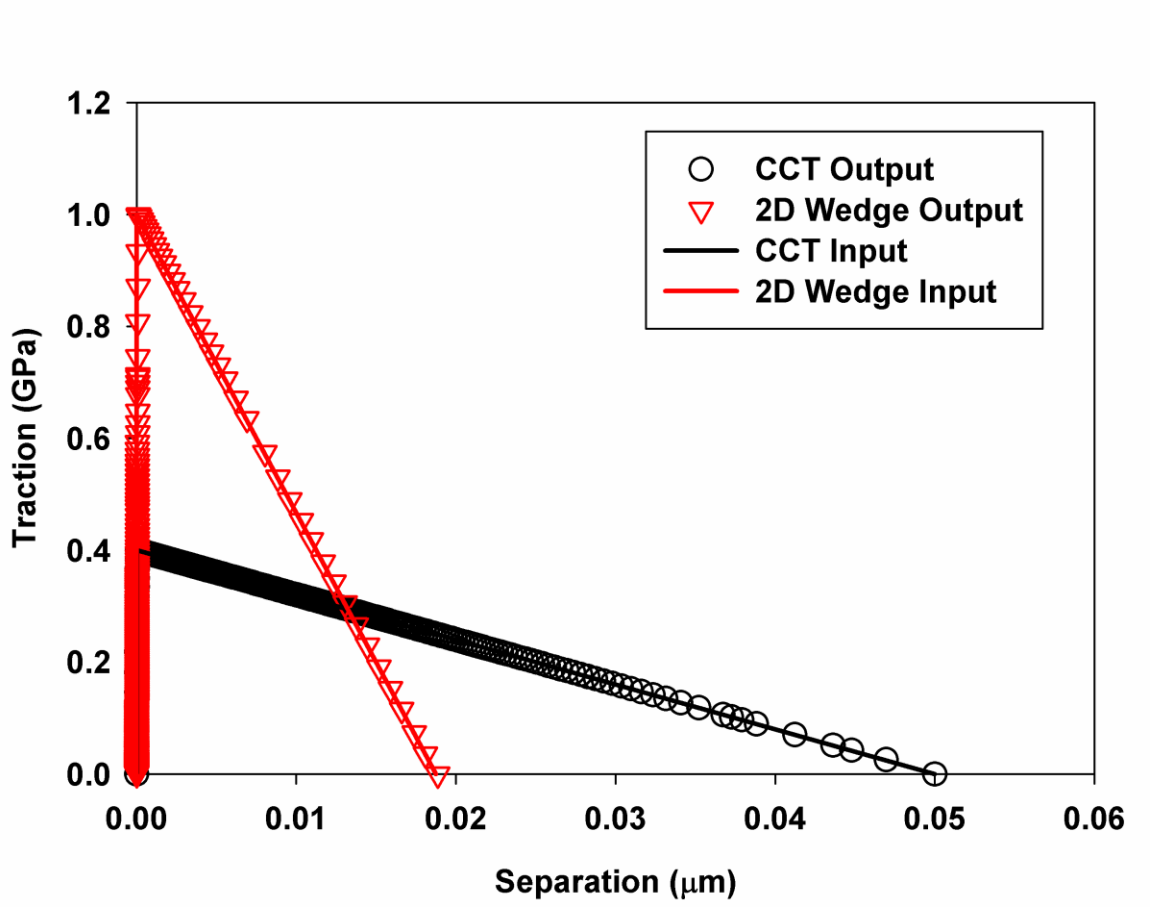


Figure 2.6. Input and output traction-separation curves for a single cohesive finite element in the CCT and 2D wedge simulation. The use of viscous regularization did not result in element overloading. Note that in calculating G_c using Eq. 2.4 the input critical separation distance must be doubled to account for the mirror symmetry used in the model.

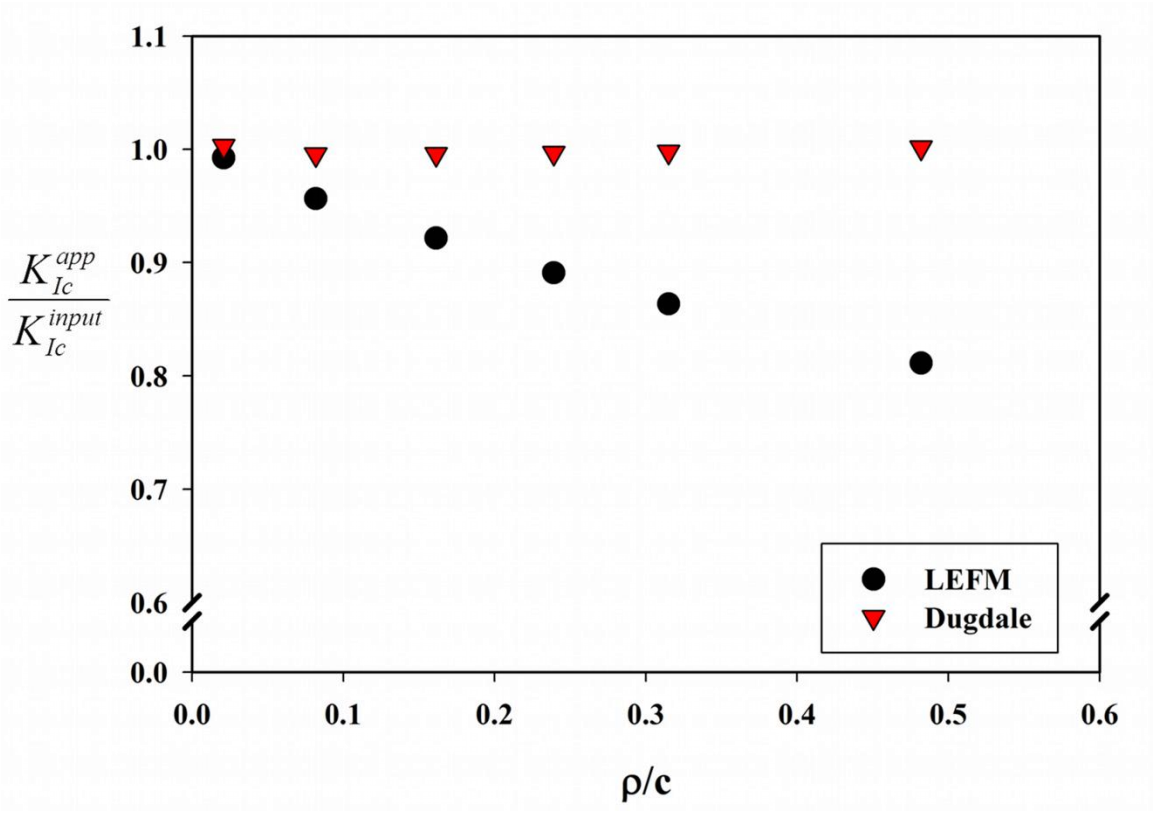


Figure 2.7. Apparent fracture toughness measured from finite elements simulations of a CCT specimen where the size of the cohesive zone is controlled by the maximum cohesive strength. An apparent decrease in fracture toughness occurs when the size of the cohesive zone, ρ, is on the order of the size of the crack, c.

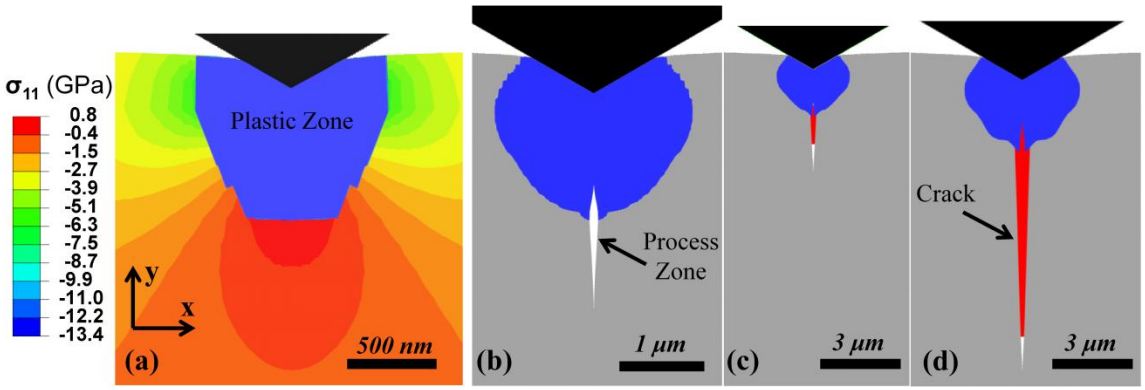


Figure 2.8. Results from the simulation of 2D wedge indentation cracking in an E/Y=20 brittle material with a fracture toughness of 1.0 MPa $m^{1/2}$ and a σ_c/Y of 0.15: (a) self-similar elastic-plastic regime where the maximum tensile stress occurs at the elastic-plastic boundary; (b) formation of a stable process zone; (c) short-crack regime; and (d) steady-state crack geometry. Blue, white, and red shaded regions represent the plastic zone, process zone, and traction-free crack, respectively.

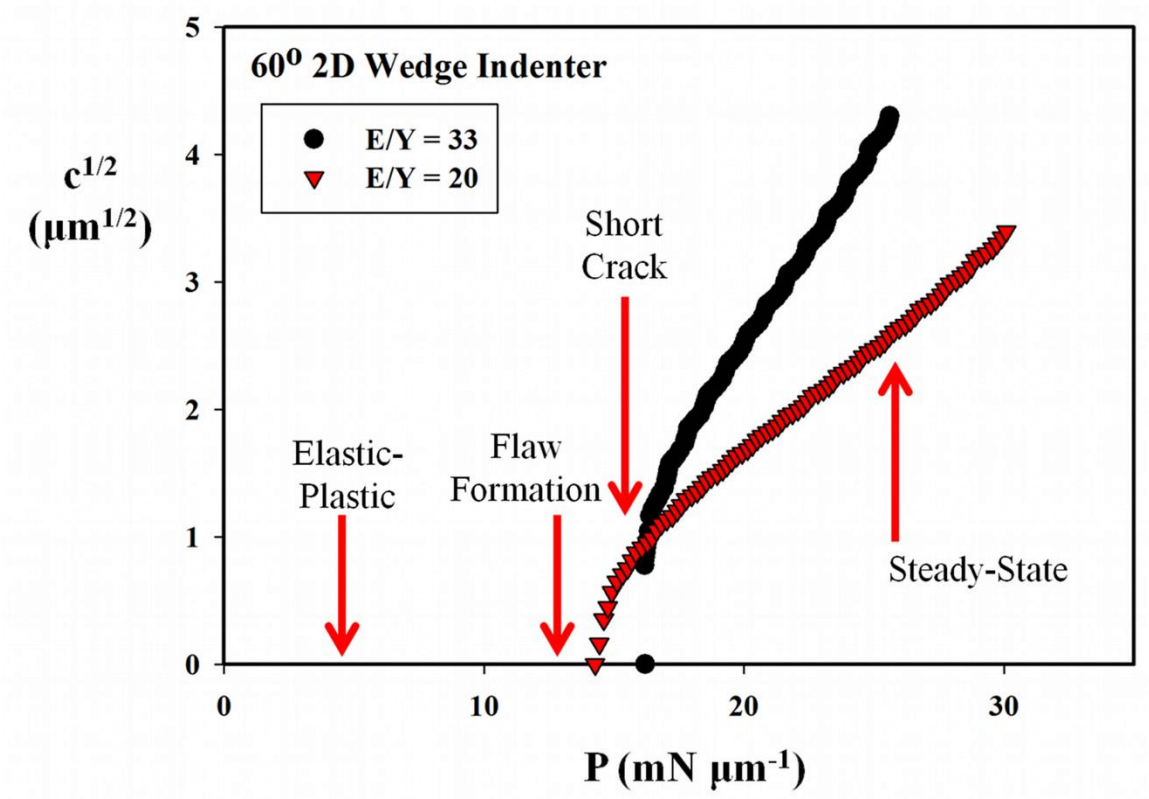


Figure 2.9. The square-root of crack length as a function of applied load for 2D indentation cracking simulations with a 60° wedge indenter for two materials with different *E/Y* ratios (*E*=100 GPa, *v*=0.25, K_{Ic}=1.0 MPa $m^{1/2}$, σ_c=1 GPa). After the threshold load for cracking and the short-crack regime, the rate of crack growth, $d\sqrt{c}/dP$, reaches a constant, steady-state.

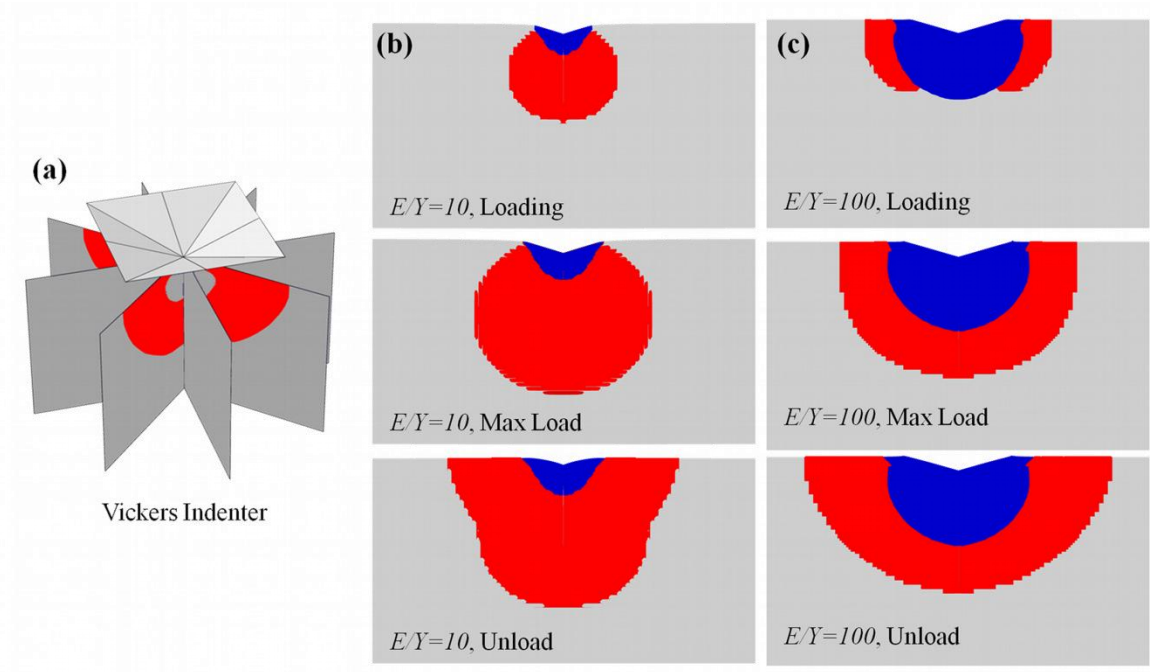


Figure 2.10. Results from FE simulations of Vickers indentation cracking: (a) isometric view of the Vickers indentation model showing crack planes aligned with indenter edges and faces (cracking only occurred on planes aligned with edges), and (b) and (c) crack morphologies as a function of load on a given plane for materials with E/Y=10 and E/Y=100, respectively. Note that the crack morphology evolution is controlled by the elastic-plastic properties of the material. Cracks are highlighted in red and plastic zones are in blue.

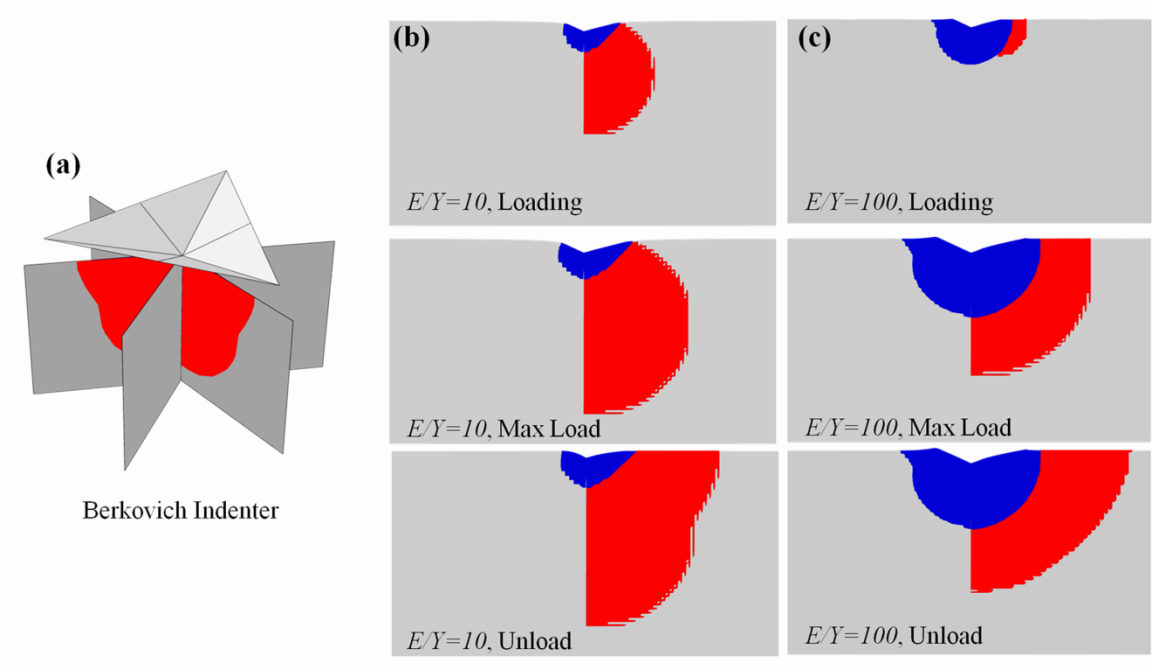


Figure 2.11. Results from FE simulations of Berkovich indentation cracking: (a) isometric view of the Berkovich indentation model showing crack planes aligned with indenter edges and faces (cracks did not extend to the face of the indenter), and (b) and (c) crack morphologies as a function of load on a given plane for materials with *E/Y*=10 and *E/Y*=100 respectively. Cracks are highlighted in red and plastic zones are in blue.

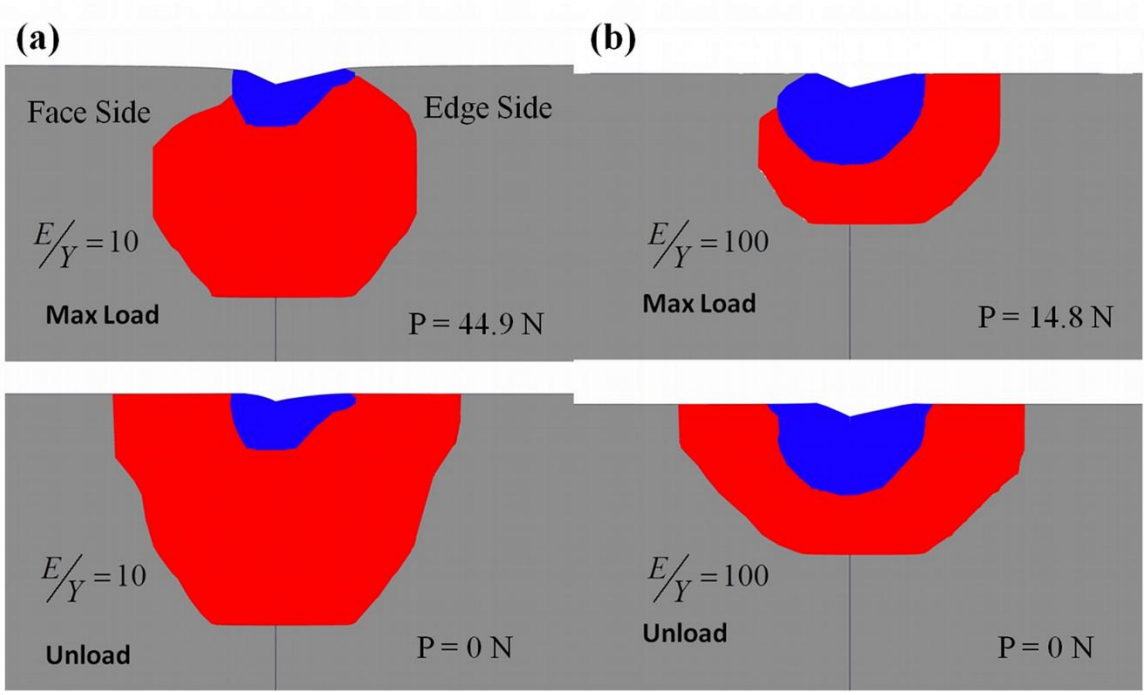


Figure 2.12. Results from Berkovich indentation simulations where only one set of planes (corner and face) were allowed to crack: (a) and (b) crack morphologies for materials with *E/Y* ratios of 10 and 100, respectively. In this case, cracks extend to the face side of the indenter on both loading and unloading. The crack is highlighted in red and the plastic zone is in blue.

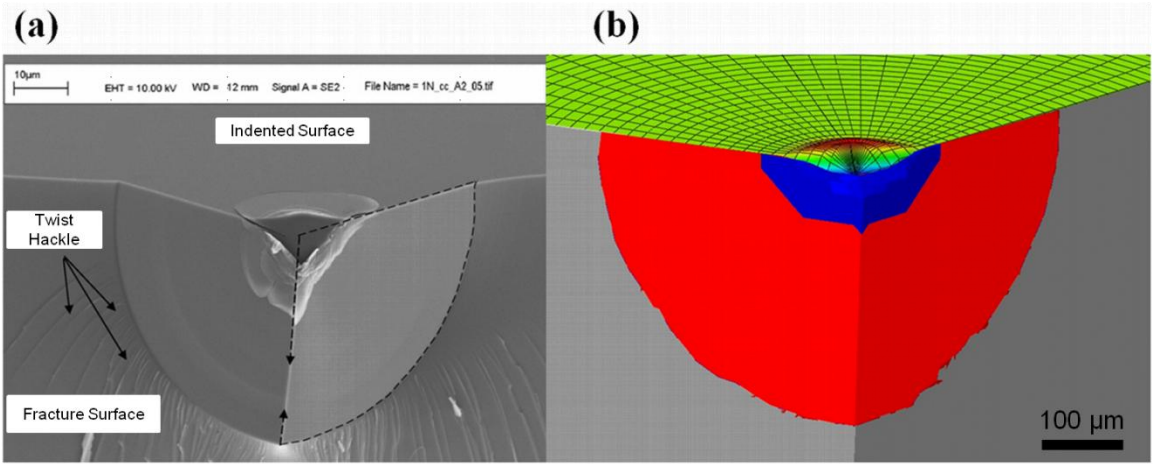


Figure 2.13. Sectioned indents in an annealed soda-lime glass made with sharp three-sided indenters: (a) Tandon's experimental observation of quarter-penny cracks with a cube-corner indenter (micrograph used with permission), and (b) a similarly sectioned FE simulation in a glass-like material having the same modulus and hardness with a 40° centerline-to-face angle indenter. The crack is highlighted in red and the plastic zone is in blue.

CHAPTER III

SIMULATING WEDGE INDENTATION CRACKING WITH 2D COHESIVE ZONE FINITE ELEMENTS

Abstract

Cohesive zone finite element simulations of two-dimensional wedge indentation cracking have been carried out in order to critically analyze the seminal indentation cracking model proposed by Lawn, Evans, and Marshall (LEM). Results are presented to show individual effects of material properties and indenter geometry on crack growth and quantitative comparisons are made to predictions from the LEM model. Deviations between simulation results and the LEM model are discussed in terms of their reliance on Hill's expanding cavity model to approximate elastic-plastic indentation conditions. In light of observations from the simulations, a model is developed that combines a simple displacement-controlled stress intensity factor solution with a crack mouth opening displacement scaling argument. Model predictions are found to be in excellent agreement with simulation results over a wide range of material properties and indenter angles. The results are a methodology for evaluating fracture toughness with wedge indenters and insights into indentation cracking analyses of more complex indentation geometries.

3.1. Introduction

Indentation testing is a technique for assessing the mechanical properties of materials when standard mechanical testing techniques that may require complex specimen geometries or large volumes of material become impractical. Additionally, the high degree of spatial resolution and improved statistics offered by indentation testing support material characterization, especially as materials are increasingly tailored for engineering applications at scales on the order of a nanometer. However, such advantages come at the expense of introducing a non-uniform state of stress that necessitates complex analyses [1-4]. Identification of relationships between material properties and indentation test results and the application of those relationships in exploring specific material physics affecting mechanical behavior as a function of the wide range of length scales available drives the development of indentation analyses. Results from such vigorous analyses and tests are valuable to the materials processing community where knowledge of the interplay between microstructure and properties is critical.

One seminal indentation analysis is the Lawn, Evans, and Marshall (LEM) model of indentation cracking, wherein fracture toughness is related to elastic-plastic material properties, indenter geometry, and measured loads and crack lengths [5, 6]. In their analysis, crack extension is driven by a force resulting from the residual produced during elastic-plastic indentation [7]. The LEM model relies on a number of assumptions in order to avoid numerical analyses, which at the time of development would have been computationally expensive or impossible and difficult to evaluate over a wide range of material behavior. For example, the key to connecting the indentation geometry and crack driving force in the LEM model is the use of Hill's expanding cavity model [8]. While the result is a simple methodology for evaluating fracture toughness, it is conceivable that such assumptions may limit the applicability of the LEM indentation cracking model and furthermore may not properly incorporate some important material dependencies.

Numerical modeling techniques (e.g., the finite element method) are capable of solving nonlinear elastic-plastic problems and have been instrumental in developing indentation analyses where analytical solutions are only available under purely elastic conditions [9]. These techniques continually improve with advances in technology that reduce computational expense and increase accuracy. The finite element method allows for the development of indentation analyses that require fewer assumptions, in addition to providing an opportunity to examine the physical mechanisms behind indentation behavior from a continuum viewpoint. Simulating elastic-plastic indentation with finite elements is relatively straightforward and has been successfully accomplished for a number of indentation geometries [10, 11]. However, simulations requiring additional physical processes often require specialized elements or user defined material behavior. For example, the cohesive zone model and its related cohesive element is one common technique for introducing cracking into a finite element framework. It has been shown that cohesive finite elements are amenable to simulating indentation cracking in brittle materials when care is taken to eliminate artifacts resulting from the application of the cohesive zone model [12-15]. Considerable importance in cohesive finite element simulations is placed on the geometry of the crack with respect to the overall model loading conditions and geometry.

Originally, the LEM model was developed for the conical indentation geometry and the median/radial crack system commonly observed in indentation of brittle materials with pyramidal indenters [5]. In this work, we will use finite element simulations to explore the problem of indentation cracking in brittle materials during two-dimensional (2D) wedge indentation and a median through-crack in order to build an understanding of the physical mechanisms that control crack extension without the complications that arise from three-dimensional (3D) geometric effects. "Brittle" in this work describes a material wherein crack extension occurs when the mode-I stress intensity factor at a crack tip is equal to the linear-elastic plane strain fracture toughness, K_{Ic}. The wedge simplifies the

geometry of the problem by eliminating the 3D nature of the pyramidal indenters (e.g., the 4 corners of a Vickers indenter) and the complex crack geometries found beneath pyramidal indentations in brittle materials.

An idealized 2D plane strain wedge indentation cracking geometry, exaggerated for visualization purposes, is schematically shown in Fig. 3.1. A wedge indenter, having a half-included angle θ, penetrates an elastic-plastic material to a contact depth of h_c and a contact dimension a. The applied load, P, required for penetration has units of force per unit length in the 2D contact formulation. Because the wedge comes to a point at the apex, a zone of plastic deformation, characterized by a radius of b, initiates upon first contact and expands with increasing load depending on the elastic-plastic properties of the material. The presence of a median through-crack, having a length c, breaks the overall geometric self-similarity of the problem as the crack length has a different scaling relationship than the contact dimension with respect to the applied load. The crack extends along the indentation axis, and the crack mouth and associated crack mouth opening displacement, δ_m, occur at the boundary between the elastically and plastically deformed material (elastic-plastic boundary). This simple 2D geometry lends itself to numerical analyses with a limited number of assumptions.

Here, we present a detailed derivation of the LEM model and provide results and analyses of cohesive finite element simulations for the case of 2D wedge indentation cracking in brittle materials with a focus on four specific goals:

1) to identify the important material properties and test variables that influence crack growth;
2) to directly compare simulation results with the LEM model in order to critically examine the assumptions of indentation cracking behavior;
3) to develop an understanding of the physics controlling crack extension during wedge indentation to gain insights into pyramidal indentation cracking; and

4) to introduce a model that limits the need for assumptions of material behavior that may reduce the applicability of wedge indentation fracture toughness testing.

3.2. The Lawn, Evans, and Marshall Indentation Cracking Model in 2D and 3D

The Lawn, Evans, and Marshall (LEM) model for indentation cracking is the result of a culmination of analyses and observations that centered on understanding the material properties and testing conditions that influenced crack growth. In their model, they divide contributions to crack growth into residual and elastic components, represented by the plasticity and elasticity of the indentation process [5]. Here, we present a detailed derivation of the three-dimensional (3D) case in order to show the corresponding model for the two-dimensional (2D) plane strain wedge indentation case. The following describes the steps involved in estimating the *force*, F, acting on the crack mouth during the indentation process. An effort is made to maintain Poisson's ratio dependencies and constants of proportionality, terms that were ignored for simplification in the original LEM derivation [5]. Inherent to the LEM model is the assumption that scaling relationships are maintained throughout the indentation and are not broken by the presence of crack growth. Differences between 3D and 2D nomenclature are highlighted where appropriate, while equation numbers are labeled with an 'a' or 'b' for 3D and 2D, respectively.

The model starts with a hemispherical volume (3D) or hemicylindrical volume (2D) of material characterized by a radius b that is extracted from the surface of an infinite half-space and deformed under the assumption of constant volume plasticity by a conical (3D) or wedge (2D) indenter having an included half-angle of θ to a characteristic indent contact dimension given by a. LEM calculate a volumetric strain as the volume of the indent, V_I, divided by the volume of the original undeformed material, henceforth referred to as the volume

of the plastic zone, V_{PZ}, where b is the radius of the plastic zone. The volumetric strain is written as:

$$\frac{V_I}{V_{PZ}} = \frac{1}{2}\frac{a^3}{b^3}\cot\theta, \tag{3.1a}$$

$$\frac{V_I}{V_{PZ}} = \frac{2}{\pi}\frac{a^2}{b^2}\cot\theta. \tag{3.1b}$$

Because of the constant volume deformation assumption, the deformed volume is now larger than the original hole from which it was extracted. LEM use the volumetric strain to calculate a stress required to restore the plastic zone into the original hole. In 3D, this stress is assumed to be hydrostatic and is calculated from isotropic elastic moduli and the volumetric strain, while the equivalent stress required under 2D plane strain conditions is a radial stress. The hydrostatic pressure, p, and radial stress, σ_r, for elastically isotropic materials are given by:

$$p = \frac{E}{6(1-2\upsilon)}\frac{a^3}{b^3}\cot\theta, \tag{3.2a}$$

$$\sigma_r = \frac{E}{(1+\nu)(1-2\upsilon)}\frac{2}{\pi}\frac{a^2}{b^2}\cot\theta, \tag{3.2b}$$

where E and v are the elastic modulus and Poisson's ratio, respectively. The indentation hardness, H, which is then used for substituting a^2 in Eq. 3.2, is defined as the applied load, P, divided by the projected area under contact, given by:

$$H = \frac{P}{\pi a^2}, \tag{3.3a}$$

$$H = \frac{P}{2a}. \tag{3.3b}$$

In the case of geometrically self-similar indenter geometries like a cone or wedge, hardness is a constant and can be thought of as the mean pressure a material can support for a given material and indenter angle. It is not clear,

however, if the presence of crack growth invalidates the constant hardness assumption.

The crack driving force, *F*, acting on the crack due to the indentation plastic zone is found by assuming the pressure (3D) or radial stress (2D) is constant within the plastic zone and integrating over the diametral area of the plastic zone. The resulting force is given by:

$$F = \frac{1}{12(1-2\nu)}\frac{a}{b}\frac{E}{H}P\cot\theta, \tag{3.4a}$$

$$F = \frac{1}{\pi(1+\nu)(1-2\nu)}\frac{a}{b}\frac{E}{H}P\cot\theta. \tag{3.4b}$$

In order to eliminate the radius of the plastic zone, a dimension that is not readily measureable experimentally, LEM ingeniously make use of Hill's expanding cavity (3D) and expanding cylinder (2D) models [8]. In these models, a cavity with radius, *r*, in an elastic-plastic material is subjected to an expanding pressure, p_{EC}. After yielding, an increase in the pressure results in the radial expansion of both the cavity and the surrounding plastic zone. Under the condition of an expanding cavity in an infinite medium, the ratio of plastic zone radius to cavity radius, *b/r*, is fixed for a given material and is only a function of the applied pressure, which has obvious parallels to the indentation problem. The relationship between material properties and expanding cavity geometry in an infinite medium is given by:

$$(1-\nu)\frac{p_{EC}}{E} = \frac{6\ln(b/r)+2}{9(b/r)^3}, \tag{3.5a}$$

$$(5-4\nu)\frac{p_{EC}}{E} = \frac{2\ln(b/r)+1}{(b/r)^2}. \tag{3.5b}$$

In order to connect the expanding cavity model and indentation geometries, LEM make the assumption that the indentation hardness is equivalent to the expanding cavity pressure and that the volume of the cavity is equal to the volume of the indent. LEM apply power-law fits to the *b/r* ratio over a range of E/p_{EC} ratios common to brittle materials for simplification. Power-law fits

to Eq. 3.5 are shown in Fig. 3.2, where the *b/r* ratio is plotted as a function of material properties. The resulting fit exponents are ~1/2 and ~1/3 for 3D and 2D, respectively, for the range given. Note from Fig. 3.2 that resulting fit exponents are not unique, but rather depend on the range chosen for fitting. That being said, the resulting *a/b* ratio, given the LEM model assumptions, can be written as:

$$\frac{a}{b} = \frac{4^{1/3}(1-\nu)^{1/2}}{0.55}\left(\frac{E}{H}\right)^{-1/2}\cot^{-1/3}\theta, \tag{3.6a}$$

$$\frac{a}{b} = \frac{\sqrt{\pi}}{1.44}(5-4\nu)^{2/3}\left(\frac{E}{H}\right)^{-2/3}\cot^{-1/2}\theta. \tag{3.6b}$$

The stress intensity factor is found by assuming that the crack driving force, *F*, acts as a point-loaded half-penny crack (3D) or a point-loaded through crack (2D). This assumption necessitates a crack length, *c*, that is much larger than the plastic zone radius. The stress intensity factors, K_I, for these geometries are found in Fett and Munz (3D) and Tada (2D) [16] and are given by:

$$K_I = \frac{1.144F}{(\pi c)^{3/2}}, \tag{3.7a}$$

$$K_I = \frac{2.6F}{(\pi c)^{1/2}}. \tag{3.7b}$$

Under the condition of equilibrium crack growth, the mode-I plane strain fracture toughness, K_{Ic}, can be found by combining Eqs. 3.4, 3.6, and 3.7, and is given by:

$$K_{Ic} = 0.049\frac{(1-\nu)^{1/2}}{(1-2\nu)}\left(\frac{E}{H}\right)^{1/2}\frac{P}{c^{3/2}}\cot^{2/3}\theta, \tag{3.8a}$$

$$K_{Ic} = 0.57\frac{(5-4\nu)^{2/3}}{(1+\nu)(1-2\nu)}\left(\frac{E}{H}\right)^{1/3}\frac{P}{\sqrt{c}}\cot^{1/2}\theta. \tag{3.8b}$$

Note here that this is only the residual component of the fracture toughness. LEM consider an elastic contribution to the stress intensity factor that can be represented by the Boussinesq stress field and is proportional to $P/c^{3/2}$ in 3D. The corresponding term in 2D would result from the Flamant solution for a

line load and would be proportional to $P/\sqrt{c}$. Note however, that the 3D Boussinesq and 2D Flamant stress fields are compressive at the surface of the sample and along the indentation axis, respectively [2]. These positions also correspond to the locations where crack lengths are measured. Neither stress field then, in theory, will contribute to crack extension at these locations, though the compressive stresses may suppress crack growth until removal of the load, depending on the magnitude of the stress. Thus, the unloaded crack length at the surface (3D) and along the indentation axis (2D) is then determined strictly from the residual component, and can be described by Eq. 3.8 if the LEM model accurately predicts indentation cracking relationships. Influences and the importance of the elastic component in the case of the 2D wedge will be discussed later.

In summarizing the LEM model, it is helpful to set aside the details of the derivation and look at the broad impact of predicted material dependencies that affect indentation cracking. The *E/H* dependency arises from the use of Hill's expanding cavity model, and, for a fixed load and indenter angle, a material with a greater *E/H* ratio will have a greater crack driving force compared to a material with a smaller *E/H* ratio. In other words, for the same fracture toughness, materials that have a more metallic-like behavior (large *E/H*) will crack more than more ceramic-like materials (low *E/H*) under the same test conditions. This is not readily apparent experimentally because it is hard to realize metallic and ceramic materials with the same fracture toughness. Poisson's ratio dependencies arise from both Hill's expanding cavity model and the relationship between stress and strain in Eq. 3.2. While the dependencies are complex, the LEM model predicts a singularity for incompressible materials (i.e., Poisson's ratio equal to 0.5). The indenter angle contribution to the crack driving force is greater for sharper indenters, which is a direct result of the indent volume to contact dimension relationship. All of these material dependencies are only valid if scaling relationships are maintained constant during crack growth. Comparisons between cohesive finite element simulations of 2D wedge indentation cracking to

the LEM model will be made in light of these predicted material and indenter dependencies.

3.3. Finite Element Simulations

Cohesive Finite element (FE) simulations of 2D wedge indentation cracking were carried out using the FE software package ABAQUS [17]. A detailed description of the 2D wedge indentation cracking simulation procedure can be found in Chapter II, but a summary is provided here for completeness that refers to the model schematic provided in Fig. 3.3. Frictionless contact between a rigid wedge indenter having an included half-angle of θ and a 2D plane strain quarter-space having a finite size was used for the simulations. The finite quarter-space size played an important role in 2D indentation cracking simulations as will be shown in detail later. 4-node plane strain elements were used with a refined mesh in the regions of contact and crack growth. The constitutive behavior was limited to isotropic elastic-perfectly plastic materials characterized by an elastic modulus, E, Poisson's ratio, v, and yield strength, Y. Cracking behavior was modeled with specialized cohesive finite elements having inputs of fracture energy, G, maximum cohesive strength, σ_c, and a stabilizing viscosity, η. A detailed explanation of cohesive elements and their use can be found elsewhere [12, 18-20]. Because we are simulating crack growth in brittle materials, fracture toughness was related to fracture energy through linear-elastic fracture mechanics (LEFM) by:

$$K_{Ic} = \sqrt{EG \Big/ \left(1 - \nu^2\right)}. \tag{3.9}$$

The cohesive elements initially had a zero thickness (i.e., initial crack opening displacements are zero) and were positioned along the indentation axis. These elements were allowed to fail under mode-I loading conditions and thus the crack opening displacements were perpendicular to the loading axis. Cracking was constrained within the indentation plane for simplicity, noting that

this plane contained the maximum tensile stress in the absence of cracking, which consistently occurred at the elastic-plastic boundary. Although cracks could close due to compressive stresses, crack healing was not allowed in the cohesive element formulation. The use of the cohesive zone model introduces a length scale into the problem and thus units become important. The ranges and units of the simulation inputs explored in this work are summarized in Table 1.

For 2D crack extension problems, it is expected that the crack driving parameters (e.g., loads, stresses, or displacements) should scale with the square-root of the crack length [21]. However, there are two important details in simulating indentation cracking with 2D cohesive finite elements that may alter the expected behavior. First, a finite sample size must be accounted for due to the fact that an increase in compliance accelerates crack growth as the crack length becomes a greater portion of the sample size (see, for example, the polynomial in the compact tension fracture toughness specimen testing that is a function of crack length and specimen width [21]). The contribution to crack growth from compliance effects is mitigated as the sample size tends toward infinity. Figure 3.4 shows the results of the square root of crack length as a function of applied load for simulations conducted using $E/Y=33.3$, Poisson's ratio = 0.025, fracture toughness = 1.0 MPa $m^{1/2}$, an indenter angle of 65°, for sample sizes of 100 µm, 200 µm, 500 µm, and 1000 µm. Based on the results from Fig. 3.4, analyses and results are presented when crack lengths are less than 50 µm for sample sizes of 1000 µm in order to avoid compliance effects in finite sample sizes.

Second, deviations from expected behavior can also occur due to artifacts introduced in applications of cohesive zone model, which arise from an additional length scale represented by the size of the process zone [21, 22]. The process zone is a phenomenological region at the crack tip that accommodates the energy dissipation required for crack extension. Effects of the process zone size on indentation cracking simulations with cohesive finite elements have been discussed elsewhere, however, an example is shown in Fig. 3.5 where $\sqrt{c}$ is

plotted as a function of applied load. The results in Fig. 3.5 are for a 65° indenter and a material with an *E/Y* ratio, Poisson's ratio, and fracture toughness of 20, 0.25, and 1.0 MPa $m^{1/2}$, respectively. The different curves are from changing the cohesive strength, σ_c, which in turn alters the size of the process zone. The effect of changing the cohesive strength is to alter the load at which crack nucleation occurs. However, crack lengths and loads converge in all three cases once the crack length is long in comparison to the size of the process zone. Thus, simple LEFM analyses must be carried out when the length of the crack is much larger than the size of the process zone. In Chapter II, it has been shown that cohesive zone concepts and LEFM are equivalent, for brittle materials, when the length of the crack is greater than ~10 times the size of the process zone. Further discussion of the cohesive zone model and similar crack bridging ideas can be found in the literature [22]. The size of the process zone, ρ, is only exactly known in cases of simple crack loading geometries [21] (e.g., the center cracked tension specimen), but can be reasonably estimated by:

$$\rho = \frac{\pi}{8}\left(\frac{K_{Ic}}{\sigma_c}\right)^2. \tag{3.10}$$

In the FE results presented here, we chose to fix the elastic modulus, *E*, fracture energy, *G*, and the cohesive element strength, σ_c, to values of 100 GPa, 0.01 GPa um, and 0.75 GPa, respectively, which resulted in relatively constant process zone sizes that ranged from 0.70 μm to 0.85 μm depending on Poisson's ratio (see Eq. 3.9).

These two limitations give rise to bounds between which a simple LEFM solution may be applied to the results; namely crack lengths greater than ~10ρ and less than 50 μm for a sample size of 1000 μm. In addition, over the course of the investigation, it was realized that the crack growth rate with respect to load, $d\sqrt{c}/dP$, within these limits was more appropriate for making final comparison to the LEM model. The reason being, that the nucleation of a crack during cohesive FE simulations is extremely dependent on material properties, indenter

geometry, and the specific cohesive element parameters used in the simulation (see Fig. 3.5).

Measurements from FE simulations can often be user-dependent and are therefore described here for completeness with reference to the wedge indentation cracking geometry shown in Fig. 3.1. Hardness, H, is defined in Eq. 3.3b, where the contact dimension, a, was measured as the horizontal distance from the indentation axis to the edge of contact. The load, P, was taken as the reaction force in the indentation direction acting on the rigid indenter, which, in this formulation, was maintained in displacement control. The crack length, c, was measured from the point of maximum crack opening displacement, which occurred at or near the elastic-plastic boundary, to the last traction-free cohesive element. The reason for defining the crack length in this way versus defining the length from the initial point of contact will become apparent when results are compared to a specific stress intensity factor solution. The crack growth rate, $d\sqrt{c}/dP$, was measured by taking a linear fit to a plot of $\sqrt{c}$ vs. P for crack lengths greater than 10ρ and less than 50 μm. Crack mouth opening displacement, δ_m, was taken as the maximum crack opening displacement, which consistently occurred at or near the elastic-plastic boundary. The remaining parameters required for evaluating the LEM model (i.e., the elastic moduli and indenter angle) were all inputs in the FE simulations.

3.4. Results

The goal of this work is to make detailed comparisons between cohesive finite element simulations of wedge indentation cracking results and the model proposed by Lawn, Evans, and Marshall (LEM) in addition to highlighting the physical mechanisms that control crack extension. To that end, a short list of general observations that are independent of material properties and indenter geometry is warranted here, as it helps in understanding the results:

- Crack growth occurred only during loading of the indenter. Unloading of the indenter resulted in an elastic recovery that depended on material properties and indenter angle that had negligible effect on crack length.
- The range of materials and indenter geometries examined in this study covered the transition from sink-in to pile-up types of deformation commonly observed in indentation testing. However, no change in crack growth behavior was noticed between these two states of deformation.
- The depth and magnitude of crack mouth opening displacements were strongly correlated with the size and geometry the plastic zone.

In light of these observations, qualitative comparisons of material and indenter dependencies of the LEM model will be made first, followed by direct quantitative comparisons. Resulting load and geometry relationships are examined in order to comment on scaling parameters implicit in the LEM model. Based on the observation that crack growth does not occur on unloading, reported loads, crack lengths, and crack growth rates are quantities measured during loading.

Figure 3.6 shows FE simulation results for $\sqrt{c}$ as a function of load for several E/Y ratios. The indenter angle, fracture toughness, and Poisson's ratio were fixed at 65°, 1.0 MPa $\sqrt{m}$, and 0.25, respectively. It is evident from the figure that increasing the ratio of E/Y (and thus the ratio of elastic modulus to hardness) results in a greater crack growth rate, $d\sqrt{c}/dP$, which is qualitatively consistent with the LEM model as shown in Eq. 3.8b. Also evident from Fig. 3.6 is the fact that absolute values of loads and crack lengths are history dependent based on the process zone and nucleation of a crack. As mentioned previously, this result is not intuitive in that one typically associates increases in plasticity (i.e., lower yield strength) with increases in fracture toughness. In these simulations, however, fracture toughness is independent of the elastic modulus to yield strength ratio and is a constant for the results shown in Fig. 3.6. This may be a feature unique to the 2D wedge indentation cracking problem. Tensile

stresses occur in standard fracture toughness specimens under elastic conditions due to their geometry. In 2D wedge indentation, however, elastic stresses acting on the crack plane are compressive and generation of a plastic zone is the only way to produce tensile stresses. While the magnitude of these tensile stresses depends on the magnitude of yield strength, for a given load, the size of the plastic zone is greater for materials with greater *E/Y* ratios. It is the plastic nature of indentation that gives rise to crack growth forces.

Figure 3.7 shows FE simulation results for loads and square-root of crack lengths as a function of indenter angle for fixed values of *E/Y*, fracture toughness, and Poisson's ratio of 33, 1.0 MPa √m, and 0.25, respectively. The results are also qualitatively consistent with the LEM model in that as the wedge becomes sharper the indenter angle decreases crack growth rates are greater. Sharper indenters displace more volume than blunter indenters for a given contact size from a constant volume of plastic deformation viewpoint and the LEM crack driving force stems from the material accommodating this displaced volume.

In exploring the effect of Poisson's ratio on indentation cracking, we choose to report crack growth rates, $d\sqrt{c}/dP$, as they highlight the magnitude of the contribution of Poisson's ratio, something that was neglected in the original derivation of the LEM model. Figure 3.8 shows FE simulation results for crack growth rates as a function of the ratio E/HK_{Ic} for materials with different Poisson's ratios and an indenter with a half included angle of 65°. Note that we use E/HK_{Ic} for plotting because while fracture energy was held fixed for all simulations, fracture toughness changed with Poisson's ratio according to Eq. 3.9. Crack growth rates increase for increasing values of E/HK_{Ic} and Poisson's ratio, which is again qualitatively consistent with the LEM model. In addition, crack growth rates can differ by ~20% between materials with Poisson's ratios of 0.1 and 0.4, for everything else held constant. The apparent linear dependence of crack growth rates on E/HK_{Ic}, as shown in Fig. 3.8, will be discussed later.

Although the results are qualitatively consistent the LEM model, the predicted relationship between crack length and fracture toughness has not been corroborated. In order to make direct comparisons to FE simulation data, Eq. 3.8b can be rewritten in terms of crack growth rates as:

$$\frac{d\sqrt{c}}{dP} = \frac{2.6(5-4\nu)^{2/3}}{\pi(1+\nu)(1-2\nu)} \frac{1}{K_{Ic}} \left(\frac{E}{H}\right)^{1/3} \cot^{1/2}\theta. \tag{3.11}$$

Crack growth rates from the FE simulations are shown in Fig. 3.9 plotted against the functional form of Eq. 3.11. Elastic modulus, *E*, and fracture energy *G*, are fixed quantities in Fig. 3.9, while other parameters like Poisson's ratio, yield strength, and indenter angle are varied. It is evident from both the lack of correlation and non-zero intercepts in Fig. 3.9 that the LEM model does not capture the exact material property and indenter geometry dependencies. This lack of correlation becomes the crux of the problem and potential sources of error will be discussed later in terms of the assumptions made in the LEM model derivation.

A key concept of the LEM model is that the presence of crack growth does not break the scaling relationships between the applied load, contact dimension, and plastic zone geometry. The presence of a crack destroys the self-similarity of the overall geometry because the crack length, *c*, scales as the load squared while the contact dimension, *a*, scales as the load to the first power. Here, results based on scaling relationships are presented to show that the FE simulations are in good agreement with the assumption that the presence of crack growth does not invalidate geometric self-similarity of the plasticity. Furthermore, the following results provide a different viewpoint of the crack driving force wherein the indenter creates a zone of plastic deformation, which in turn may control crack growth through crack opening displacements at the elastic-plastic boundary.

In order to evaluate the assumption that important scaling relationships are not invalidated in the presence of a crack and crack growth, hardness, *H*, and the ratio of plastic zone depths to contact dimension, *b/a*, are plotted as a

function of load in Fig. 3.10a and Fig. 3.10b, respectively. The results are for *E/Y* values of 20 and 50, indenter angles of 55° and 65°, Poisson's ratio of 0.25, and a fracture toughness of 1.0 MPa $m^{1/2}$. These quantities should be, and indeed are, constant with load if the scaling relationships are maintained in the presence of crack growth. This is an important result because it is not obvious that the presence of a crack does not destroy the scaling relationships.

Over the course of the investigation, it was recognized that the crack mouth opening displacement (CMOD) may be a parameter that helps elucidate the scaling issue in addition to the hardness and plastic zone size. The CMOD may be thought of as the link between the two mechanisms of permanent deformation (i.e., plasticity and cracking) as it occurs at the elastic-plastic boundary, and thus may be indicative of which mechanism is controlling the problem. The concept of geometrically self-similar indentation argues that all displacements in the problem will scale with each other for an indenter that is geometrically self-similar. This is only valid for CMOD if it is controlled solely by the elastic-plastic contact, and not by influences from the process zone and crack growth. Stated differently, the plastic zone controls the CMOD and plasticity is not affected by the presence of a crack. In this problem, the contact dimension, *a*, and the contact depth, h_c, are related by the geometry of the indenter through $a=h_c\tan\theta$. Given that, the crack mouth opening displacement, δ_m, can be written in terms of the contact depth, which in turn is related to the material hardness, *H*, and indenter angle, θ, through:

$$\delta_m \propto h_c \propto \frac{P}{H}\cot\theta. \tag{3.12}$$

Maintaining consistency of measurements from the finite element simulations, the rate of change of the CMOD with respect to load can be written as:

$$\frac{d\delta_m}{dP} \propto \frac{\cot\theta}{H}. \tag{3.13}$$

Equation 3.13 is valid for a given material and indenter geometry, but it might be expected that the constant of proportionality would change as a function

of material properties. However, unlike the contact depth, which changes with E/Y as material pile-up occurs at the contact periphery, CMOD is unique in the case of 2D wedge indentation as it occurs on the indentation axis at the elastic-plastic boundary and is highly constrained by the symmetry of the problem. The nature of deformation at this position has been shown to be relatively insensitive to changes in material properties and indenter angles [23]. In order to examine the validity of Eq. 3.13, CMOD rates with respect to load are plotted as a function of $\cot\theta/H$ in Fig. 3.11 for different indenter angles and different ratios of E/Y. Clearly, the finite elements simulations bear out the expected relationship under the assumption of geometric self-similarity of the plasticity. Fitting the data in Fig. 3.11 gives rise to a constant of proportionality between the crack mouth opening displacement rate, $d\delta_m/dP$, and $\cot\theta/H$ of ~0.167. One might consider estimating the constant of proportionality with a model that assumes a rigid-plastic type of deformation wherein the expansion of the plastic zone upon increased loading results in expansion of the crack mouth. However, the purpose of FE simulations in this work is to obviate the need for any assumptions of material behavior.

The result from this finding is that the plastic zone not only maintains geometric-self similarity, but also acts as a bridging mechanism between the indenter and the crack mouth. The applied load on the indenter induces plastic deformation in the material, which in turn promotes increases in crack mouth opening displacement. These displacements scale with the applied load and may be thought of as the driving force for crack growth. It is important to reiterate here that plastic deformation at the crack mouth is constrained to move perpendicular to the crack plane in the case of the wedge indentation crack, which may explain the lack of a modulus dependence on the scaling. Plastic deformation at the mouth of a surface crack, like the half-penny shaped crack commonly observed beneath pyramidal indenters, may have a different scaling relationship than Eq. 3.13 due to changes in sink-in and pile-up at that location with changes in the E/H ratio (i.e., material is not constrained to move in only one direction).

3.5. Discussion

It is obvious from the lack of correlation between FE simulation results and the predicted behavior of the Lawn, Evans, and Marshall (LEM) indentation cracking model shown in Fig. 3.9 that there is some flaw in estimating the crack driving force. Fundamentally, the LEM model relies on Hill's expanding cavity (EC) model to make the connection between indentation geometry and material properties. The most apparent discrepancy is the presence of a free surface in the case of indentation compared with a radially symmetric geometry in the EC model. A model with such symmetry cannot capture the transition from sink-in to pile-up that is known to exist in indentation testing. In this section, we will compare the EC model with 2D wedge indentation finite element simulation results. For simplicity and a more direct comparison, finite element simulation results are presented in the absence of cracking. Three directly comparable details will be examined:

1. The equivalence between indentation hardness and expanding cavity pressure.
2. The constraint factor, defined as ratio of indentation hardness (or EC pressure) to yield strength.
3. The ratio of the contact dimension to the plastic zone radius.

The LEM model assumes that the pressure in the EC model, p_{EC}, is equivalent to the indentation hardness. For comparison, the indentation hardness, in the absence of cracking, normalized with respect to the elastic modulus for materials with the same *E/Y* ratios, a fixed Poisson's ratio of 0.25, and the 55° and 70.3° indenters, the lower and upper angles explored in this study, is plotted in Fig. 3.12 against the normalized EC pressure, where the normalized EC pressure, p_{EC}, for the 2D case is given by [8]:

$$\frac{p_{EC}}{E} = \frac{Y}{\sqrt{3}E}\left[1 + \ln\left(\frac{\sqrt{3}E}{4Y}\right)\right]. \tag{3.14}$$

It is apparent from Fig. 3.12 that there is a deviation from equivalence as *E/Y* decreases, toward more ceramic-like materials, possibly due to the fact that Hill neglects terms in the derivation of Eq. 3.14 on the order of *Yv/Er* for simplification. The magnitude of *Yv/Er* is negligible in metallic materials, for which the EC model was intended. This deviation is exaggerated as the indenter geometry moves toward more acute angles and thus further away from the radial symmetry imposed in the EC model.

The indentation constraint factor, defined as *H/Y*, in the absence of cracking and expanding cavity constraint factor, p_{EC}/Y, calculated from Eq. 3.14 are plotted as a function of *E/Y* in Fig. 3.13 for a fixed Poisson's ratio of 0.25 and the 55° and 70.3° indenters. Indentation constraint factors plateau to a value that is dependent on indenter angle, while the EC model monotonically increases. Though not explicitly used in the LEM model, differences in constraint factors between indentation and the expanding cavity model help to demonstrate the fact that that the expanding cavity model does not accurately capture the physics of indentation. It is also interesting to note that the hardness-pressure equivalence works well at large values of E/H, but not at low values, while the opposite holds for constraint factor.

The ratio of contact dimension, *a*, to plastic zone radius, *b*, in the absence of cracking for a fixed Poisson's ratio of 0.25 and the 55°, 60°, 65°, and 70.3° indenter angles is plotted as a function of *E/H* in Fig. 3.14. Plastic zone radii were measured from the point of initial contact to the length of the plastic zone along the indentation axis, the same definition as in the LEM model. The plastic zone was identified as those elements having plastic strains greater than 1e-4. The EC radius, *r*, in Hill's model is related the contact dimension, *a*, through the LEM assumption that the volume of the cavity is equal to the volume of the indent. Notice that the finite elements predict a nearly constant *a/b* ratio that, to a first approximation, is independent of indenter angle. Furthermore, the EC model prediction does not appropriately predict the simulation results over the *E/H*

range examined. Similar discrepancies with the EC model have been observed by Chen and Bull in the case of conical indenters.

While all three details examined with FE simulations show inconsistencies with the EC model, the most damning to the LEM model is the discrepancy between indentation plastic zone geometries and EC model geometries shown in Fig. 3.14. The LEM model relies heavily on the EC model prediction and the *E/H* to the power of 1/3 dependency is a direct result. Note here, though, in choosing to estimate the *force* acting on the crack, LEM require a model that relates the indentation geometry to material properties and indenter geometry. In the following, we will develop a model based on the observations from FE simulations that assumes *displacements*, stemming from the plasticity of the contact, control crack extension. It will be shown that relying on displacements does not require a model of the indentation geometry, but rather relies on the fact that geometric self-similarity of the plastic zone is maintained.

Three main observations lead to the development of a model for wedge indentation cracking: (1) the expanding cavity model cannot accurately describe the physics and geometry of wedge indentation; (2) the plastic zone acts as a bridging mechanism between the indenter and the crack mouth; and (3) crack mouth opening displacements scale with the applied load in the same way as the contact size. These observations provide a different approach to the indentation cracking problem from the LEM model, where the crack driving mechanism is a *force* resulting from the plastic nature of the contact. While both viewpoints are equivalent from a fracture mechanics standpoint, the LEM model requires a number of assumptions to connect the indentation geometry to the crack driving force. The following discussion will incorporate the observations from the finite element simulations into a model that includes material properties, indenter geometry, applied loads, and measured crack lengths.

The elastic component of the stress intensity factor solution cannot be neglected since the crack length is determined during the loading portion of the indentation cycle while unloading does not result in further crack growth. In other

words, the stresses acting on the crack plane due to contact may play a role in crack growth. While the LEM derivation utilizes the 2D Flamant solution for line contact to estimate the elastic stress intensity factor contribution, it may not be exactly appropriate for a wedge indenter as it does not take into account forces acting tangential to the surface due to the wedge nature of the indenter. In order to analytically estimate the elastic component we choose to use the Flamant solution for a vertical 2D line-load having a force *P* and a double line-load with force *Pcotθ* separated by the contact dimension, *a*, acting at the surface of the sample to account for any wedging forces due to the indenter. The separation of the double line-load is arbitrary, but is chosen here based on the relationship between hardness and load given in Eq. 3.3b. We choose this configuration for convenience, noting that there are other possible ways to estimate the elastic stresses for wedge indentation. The stress acting on the crack plane, σ_x, as a function of depth below the surface, *y*, due to this type of elastic loading condition can be written as [2]:

$$\sigma_x = \frac{2H}{\pi}\left[\frac{-a}{y} + \frac{4a^4 \cot\theta}{\left(a^2 + y^2\right)^2}\right]. \tag{3.15}$$

Notice that the two components to Eq. 3.15 have different signs. Compressive stresses due to the vertical line-load dominate at deep depths (the first term) while tensile stresses due to the horizontal double force dominate at shallow depths and increases with sharper indenter angles (the second term). The two components in Eq. 3.15 and their sum are plotted in Fig. 3.15 for an indenter angle of 65°. The elastic stresses decay to zero at deep depths, and at a *y/a* ratio of 3, the approximate location of the elastic-plastic boundary in the finite element simulations, the stresses are compressive and have a magnitude of *~0.2H* for an indenter angle of 65°. These compressive elastic stresses will not contribute to crack growth, but will inhibit crack growth until removal of the load. However, the addition of plasticity to the indentation problem results in dramatic deviations from the elastic stress field. In the absence of a crack, stresses acting on the indentation axis in the *x* direction are tensile at the elastic-

plastic boundary. The stresses acting on the crack plane as measured from a non-cracking finite element simulation for an elastic material and one with an *E/Y* of 20 and Poisson's ratio of 0.25 under contact with an indenter having an angle of 65° are shown in Fig. 3.16. The elastic component from the finite elements corresponds well with the prediction from Eq. 3.15 and is nearly negligible compared to the elastic-plastic stresses at full load, suggesting that removal of the elastic stresses upon unloading will not contribute to further crack growth. This was consistently observed over the range of materials examined in this study. Furthermore, unloading of the indenter does not result in crack growth even in materials with low values of *E/Y*. All these observations provide evidence that the residual component of the stress intensity factor dominates the problem, even during loading.

In estimating the residual component of the stress intensity factor, one could choose to use the elastic-plastic indentation stress field over the prospective crack length. However, there is no analytical solution for stress field under elastic-plastic wedge indentation and would therefore inconveniently require numerical integration. Alternatively, we choose to model the residual stress intensity factor from a crack mouth opening displacement viewpoint as described above. One such solution can be found in Tada 3.11 in the form of a rigid wedge of constant thickness opening a through crack in an infinite body [16], as shown in Fig. 3.17. While this solution neglects the presence of a free surface and is not exactly the same as the indentation geometry, the parallel between wedge thickness and crack mouth opening displacement is of primary interest. In this solution, crack length is defined as the length of the crack from the point of the rigid wedge to the crack tip, similar to the way crack lengths were measured in the indentation cracking simulations. The stress intensity, K_I, factor for this geometry is given by:

$$K_I = \frac{E\delta_m}{\left(1-\nu^2\right)\sqrt{2\pi c}}. \tag{3.16}$$

Taking the derivative of the square-root of crack length with respect to load and assuming equilibrium crack growth, the crack growth rate can be expressed as:

$$\frac{d\sqrt{c}}{dP} = \frac{1}{\sqrt{2\pi}K_{Ic}} \frac{E}{\left(1-\nu^2\right)} \frac{d\delta_m}{dP}. \tag{3.17}$$

The CMOD rate with respect to load can be replaced by the geometric self-similar observations previously described. The crack growth rate can now be written as:

$$\frac{d\sqrt{c}}{dP} = \frac{\alpha}{K_{Ic}} \frac{E}{H} \frac{\cot\theta}{\left(1-\nu^2\right)}, \tag{3.18}$$

where *α* is a constant of proportionality. Notice that this solution includes both Poisson's ratio and *E/H* dependencies that naturally arise from the both the LEFM solution and scaling relationship of the crack mouth opening displacements. Figure 3.18 shows crack growth rates for all of the simulations described above plotted against the functional form of Eq. 3.18. Note that data in Fig. 3.18 contains the all of the simulations and that Eq. 3.18 very appropriately describes the behavior over a wide range of indenter angles, Poisson's ratios, yield strengths, and fracture toughnesses.

The value of the constant of proportionality in Eq. 3.18 was found to be ~0.02, as estimated from a linear fit to the data shown in Fig. 3.18. This value differs by a factor of ~3 from the value that would be predicted by substituting the CMOD rate constant of proportionality of 0.167 from Fig. 3.11 into Eq. 3.17, possibly due to the presence of the free surface and the fact that the wedge indentation geometry is not exactly the geometry of the stress intensity factor solution chosen for the analysis. Note here that the material dependencies arise from a completely different set of physics then the LEM model.

While this analysis incorporates material properties, indenter geometry, loads, and crack lengths into one simple description of wedge indentation cracking behavior, differences are expected for the case of pyramidal indentation such as the four-sided Vickers indenter and the median/radial crack system. The presence of a tensile elastic component in addition to observations of crack

growth on loading and unloading complicates analyses. However, the insight gained from this work lends itself to describing the crack driving mechanisms in 3D indentation geometries.

Integrating Eq. 3.18 with respect to load and assuming that crack nucleation loads are negligible, fracture toughness may be estimated from experimental measurements of wedge indentation cracks through:

$$K_{Ic} = 0.02 \frac{E^*}{H} \frac{P}{\sqrt{c}} \cot\theta. \tag{3.19}$$

Eq. 3.19 is convenient from an instrumented indentation view as the reduced indentation modulus, E^*, and the hardness, H, are readily measurable from existing indentation analyses [1]. Note that Eq. 3.19 does not include compliance effects due to finite sample sizes, so crack lengths must be small compared to thickness of the sample. Also, the development of Eq. 3.19 is for materials that do not exhibit any material size effects (i.e., materials where hardness may be a function of indenter displacement). Whichever technique is used to measure crack lengths, it is recommended that a wide range of loads be used and attention needs to be paid to the alignment of the wedge. Crack lengths measured at the edges of samples may have different dependencies than the one described by Eq. 3.19 due to a state of plane stress at the edge, similar to cracks a the edge of compact tension specimen.

3.6. Conclusions

In this chapter we have developed the Lawn, Evans, and Marshall (LEM) model of indentation cracking for the simplified case of 2D plane strain wedge indentation. Finite element simulations, where crack growth was incorporated via the cohesive zone model, were then used to critically examine material property and indenter geometry dependencies on crack growth for comparison with the LEM model. Although qualitatively matching, the LEM model was found to be lacking in predicting exact material behavior due to discrepancies between Hill's expanding cavity model and wedge indentation for the range of materials and

indenter angles simulated in this study. These results, combined with observations of the physical mechanisms controlling crack growth from the finite element simulations, led to the development of a wedge indentation cracking model that utilizes a simple stress intensity factor solution and invokes geometric self-similarity of crack mouth opening displacements occurring at the elastic-plastic boundary. The results can be summarized as follows:

1) While the LEM model of indentation cracking incorporates the correct elements, reliance on Hill's expanding cavity model limits the applicability of the solution.
2) Hill's 2D expanding cavity model does not accurately capture the physics and geometry of the wedge indentation problem over the range of materials and indenter angles examined in this study.
3) Scaling relationships between contact dimensions, plastic zone sizes, and indenter loads are maintained in the presence of crack growth. Furthermore, the crack mouth opening displacement, which occurs at the elastic-plastic boundary, scales as $P\cot\theta/H$.
4) The plastic zone can be considered as a bridging mechanism between the indenter and the crack mouth. In the 2D wedge simulations, accommodation of plastic deformation resulted in increased crack mouth opening displacement at the elastic-plastic boundary.
5) In the 2D wedge indentation geometry, the residual component of the stress intensity factor is responsible for crack growth during loading and the elastic component is negligible. Thus, crack growth does not occur during unloading.
6) A simple LEFM solution combined with a crack mouth opening displacement scaling argument results in a model that captures crack length dependencies on material properties (E, H, v, and K_{Ic}) as well as indentation parameters (angle and load).

The resulting observations from this work can be used to help understand experimental relationships between wedge indentation cracking and material properties. In addition, these observations combined with cohesive finite element simulations of more complex indentation cracking geometries (e.g., the median/radial crack system beneath pyramidal Vickers or Berkovich indenters) can be used to critically examine other indentation cracking models as well as answer some outstanding questions in the indentation cracking literature. That being said, the results herein are based on numerical simulations of continuum concepts. Individual material physics may play a role not observed in this study.

References

1. Oliver, W.C. and G.M. Pharr, *Measurement of hardness and elastic modulus by instrumented indentation: Advances in understanding and refinements to methodology.* Journal of Materials Research, 2004. **19**(01): p. 3-20.
2. Johnson, K.L., *Contact Mechanics*. 1987: Cambridge University Press.
3. Tabor, D., *The Hardness of metals*. 1951, Oxford: Clarendon Pr.
4. Fischer-Cripps, A.C., *Introduction to Contact Mechanics*. 2000: Springer-Verlag.
5. Lawn, B.R., A.G. Evans, and D.B. Marshall, *Elastic-Plastic Indentation Damage in Ceramics - the Median-Radial Crack System.* Journal of the American Ceramic Society, 1980. **63**(9-10): p. 574-581.
6. Anstis, G.R., et al., *A Critical Evaluation of Indentation Techniques for Measuring Fracture Toughness: I, Direct Crack Measurements.* Journal of the American Ceramic Society, 1981. **64**(9): p. 533-538.
7. Marshall, D.B. and B.R. Lawn, *Residual stress effects in sharp contact cracking.* Journal of Materials Science, 1979. **14**(8): p. 2001-2012.
8. Hill, R., *The mathematical theory of plasticity*. 2004, Oxford: Clarendon Press.
9. Sneddon, I.N., *The relation between load and penetration in the axisymmetric boussinesq problem for a punch of arbitrary profile.* International Journal of Engineering Science, 1965. **3**(1): p. 47-57.
10. Giannakopoulos, A.E., P.L. Larsson, and R. Vestergaard, *Analysis of Vickers indentation.* International Journal of Solids and Structures, 1994. **31**(19): p. 2679-2708.
11. Larsson, P.L., et al., *Analysis of Berkovich indentation.* International Journal of Solids and Structures, 1996. **33**(2): p. 221-248.
12. Lee, J.H., et al., *Cohesive interface simulations of indentation cracking as a fracture toughness measurement method for brittle materials.* Acta Materialia, 2012. **60**(15): p. 5448-5467.
13. Wan, H., et al., *A plastic damage model for finite element analysis of cracking of silicon under indentation.* Journal of Materials Research, 2010. **25**(11): p. 2224-2237.
14. Muchtar, A., L.C. Lim, and K.H. Lee, *Finite element analysis of vickers indentation cracking processes in brittle solids using elements exhibiting cohesive post-failure behaviour.* Journal of Materials Science, 2003. **38**(2): p. 235-243.
15. Zhang, W. and G. Subhash, *An elastic-plastic-cracking model for finite element analysis of indentation cracking in brittle materials.* International Journal of Solids and Structures, 2001. **38**(34-35): p. 5893-5913.
16. Tada, H., P.C. Paris, and G.R. Irwin, *The stress analysis of cracks handbook*. 1973: Del Research Corp.
17. Simulia, *ABAQUS User's Manual*. 2008: Simulia Co.

18. Gao, Y.F. and A.F. Bower, *A simple technique for avoiding convergence problems in finite element simulations of crack nucleation and growth on cohesive interfaces.* Modelling and Simulation in Materials Science and Engineering, 2004. **12**(3): p. 453-463.
19. Tomar, V., J. Zhai, and M. Zhou, *Bounds for element size in a variable stiffness cohesive finite element model.* International Journal for Numerical Methods in Engineering, 2004. **61**(11): p. 1894-1920.
20. Cornec, A., I. Scheider, and K.-H. Schwalbe, *On the practical application of the cohesive model.* Engineering Fracture Mechanics, 2003. **70**(14): p. 1963-1987.
21. Anderson, T.L., *Fracture Mechanics: Fundamentals and Applications*. 2005: Taylor & Francis.
22. Bao, G. and Z. Suo, *Remarks on Crack-Bridging Concepts.* Applied Mechanics Reviews, 1992. **45**(8): p. 355-366.
23. Hirst, W. and Howse, M. G. J. W., *THe Indentation of Materials by Wedges*. Proceedings of the Royal Society of London A, 1969. 311: p. 429-444.

APPENDIX 3.1.

Table 3.1. Material, indenter, and cohesive element inputs in the finite element simulations.

Simulation Input	Range of Values
Elastic Modulus to Yield Strength Ratio	10 - 50
Poisson's Ratio , v	0.10, 0.25, 0.40
Indenter Angle, θ (degrees)	55, 60, 65, 70.3
Cohesive Element Strength, σ_c (GPa)	0.75
Fracture Energy, G (GPa um)	1E-2
Fracture Toughness, K_{Ic} (MPa $\sqrt{}$m)	1.0 – 1.1
Cohesive Element Viscosity, η (1/s)	1E-6

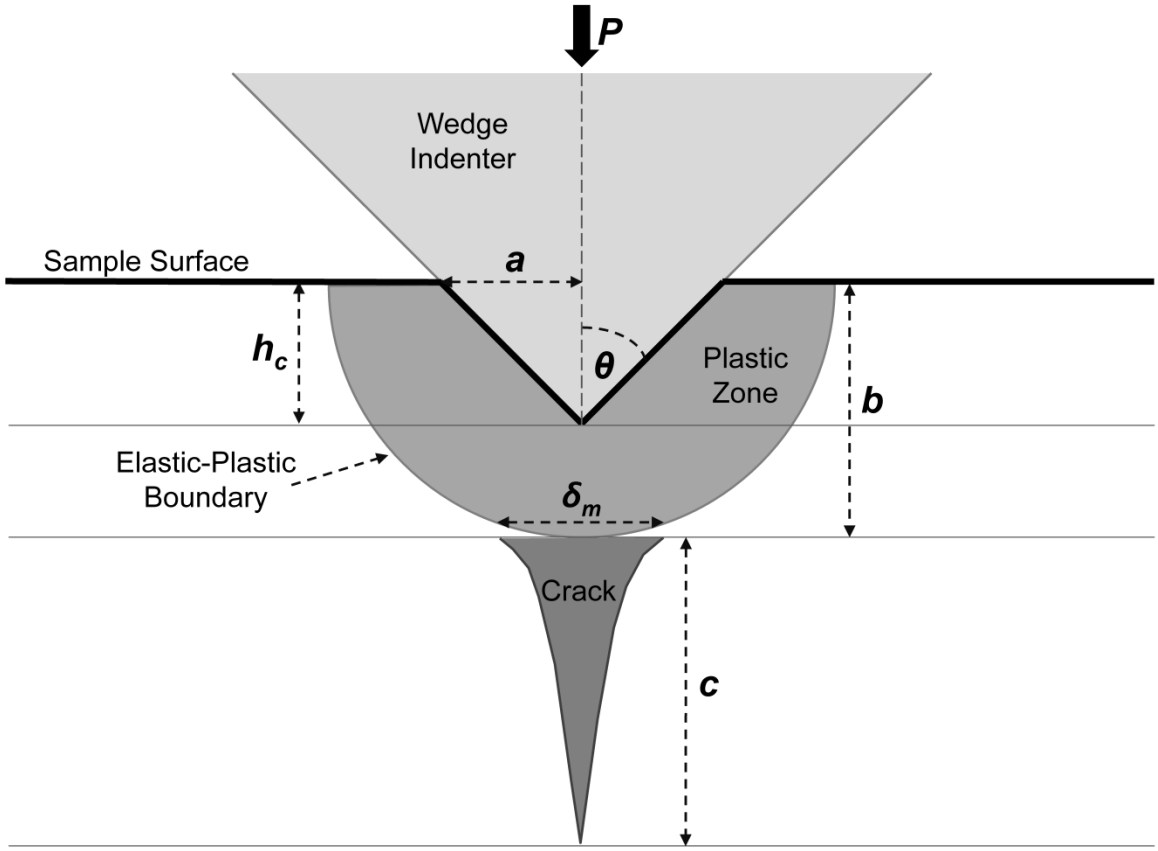


Figure 3.1. Idealized schematic of the 2D wedge indentation cross-sectional geometry examined in this study.

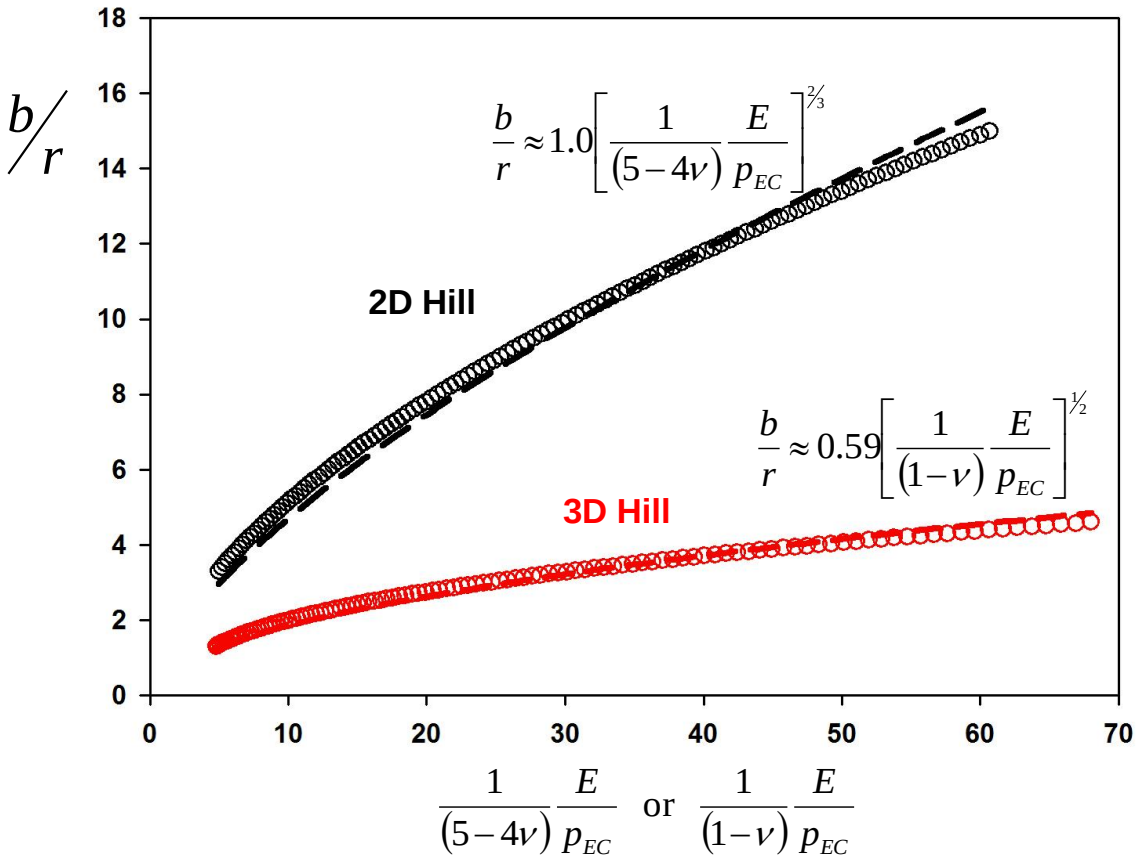


Figure 3.2. Hill's expanding cavity result for the radius of the plastic zone, b, with respect to the radius of the expanding cavity, r, for 2D and 3D (open circles). Dashed lines are power-law fits to Hill's model. The resulting fit exponents are not unique, but depend on the range of the fit.

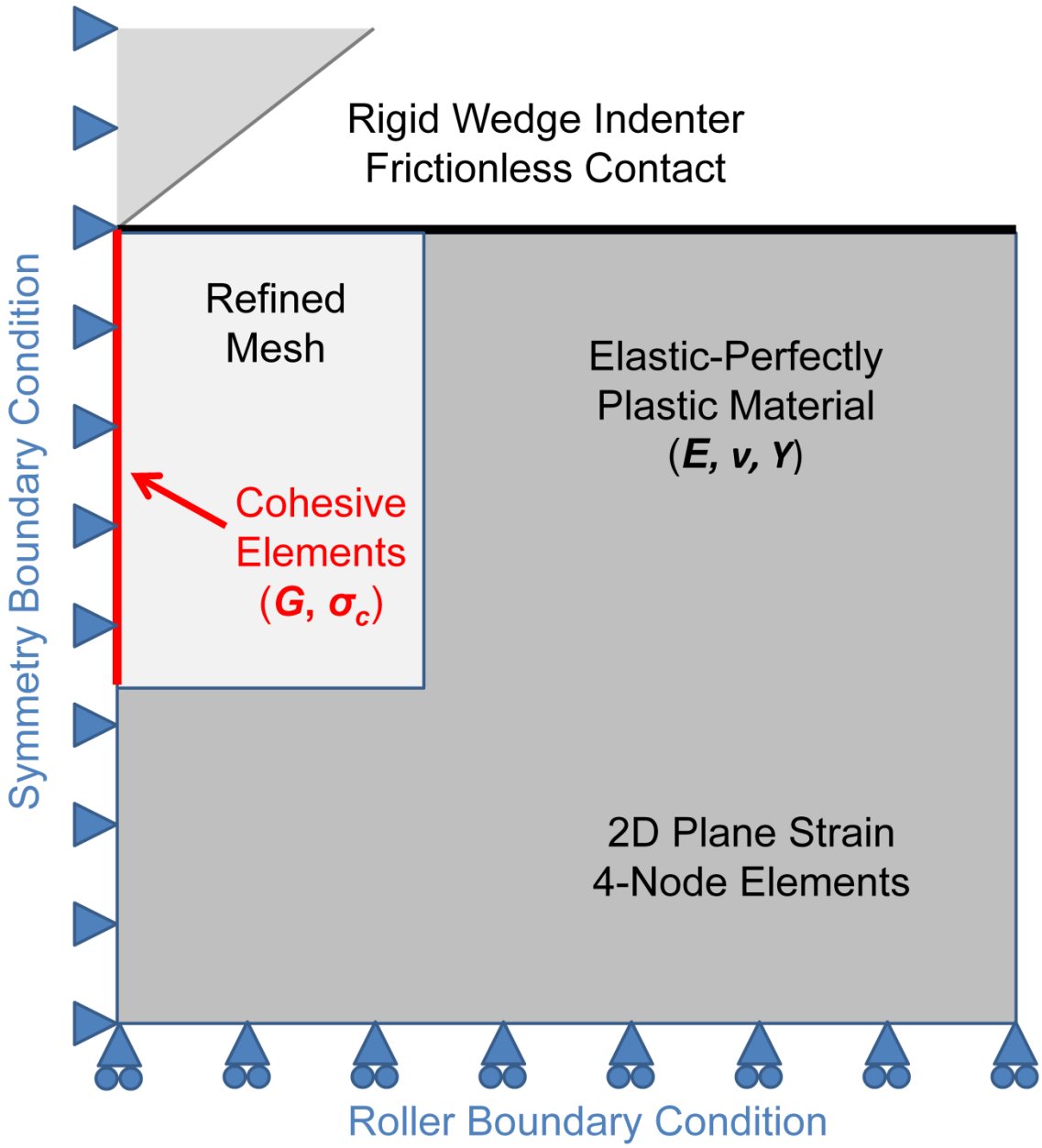


Figure 3.3. The cohesive finite element simulation geometry (not to scale).

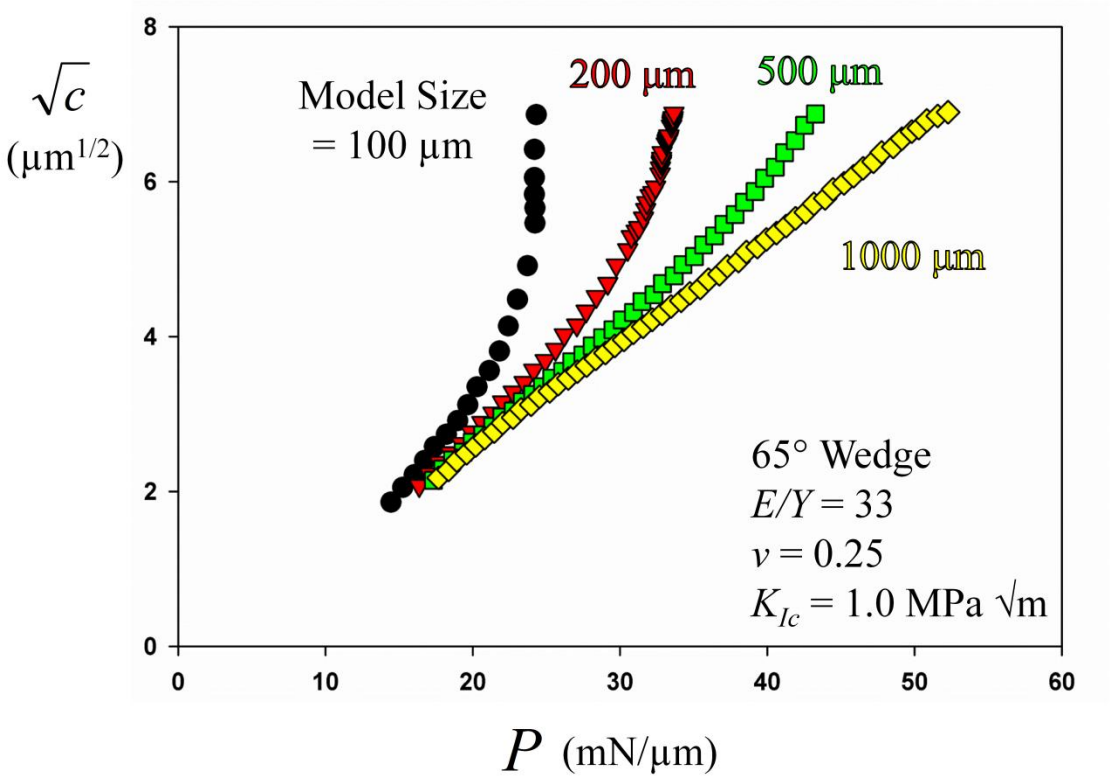


Figure 3.4. Influence of compliance effects on crack growth due to the finite sample size in the simulations. The expected linear relationship between the square-root of crack lengths and applied load breaks down as the crack length becomes a significant fraction of the sample size.

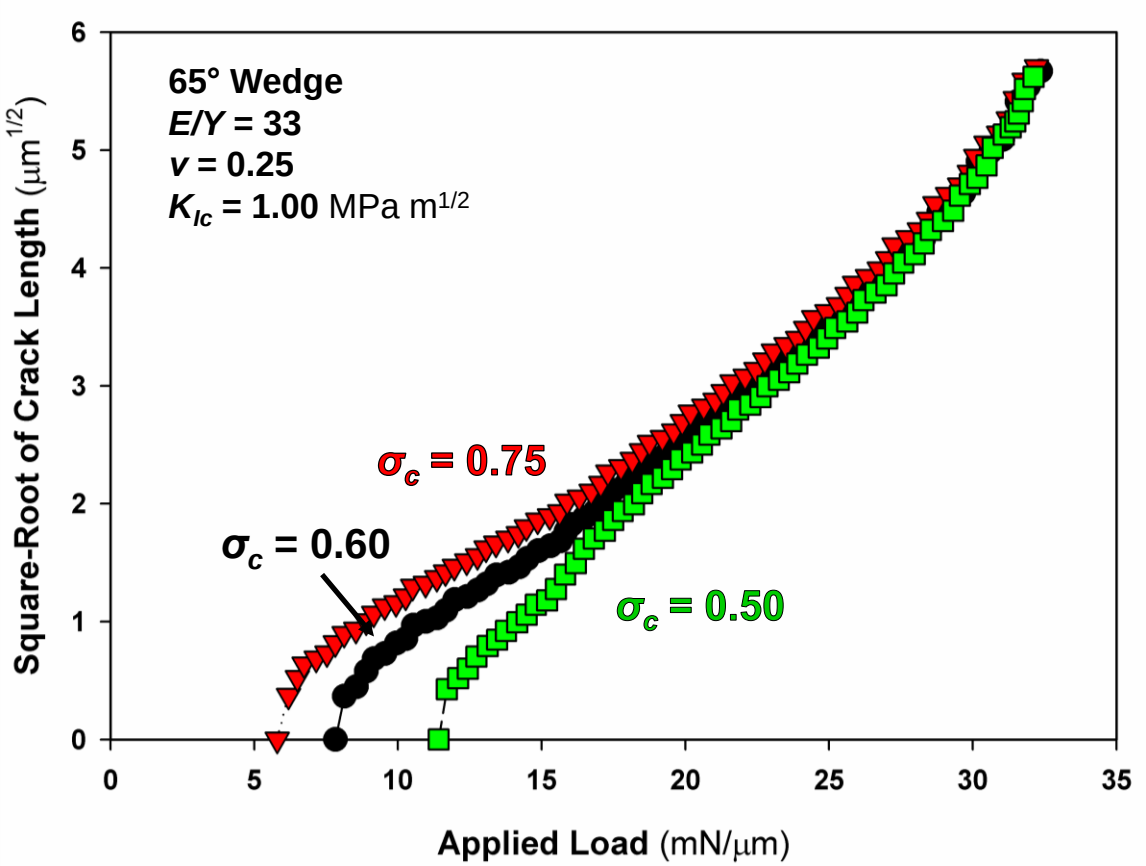


Figure 3.5. Crack growth rates, $d\sqrt{c}/dP$, as a function of applied load showing the artifact of the process zone in the short crack regime. Slight slope in data at large loads is a result of compliance effects due to finite sample sizes.

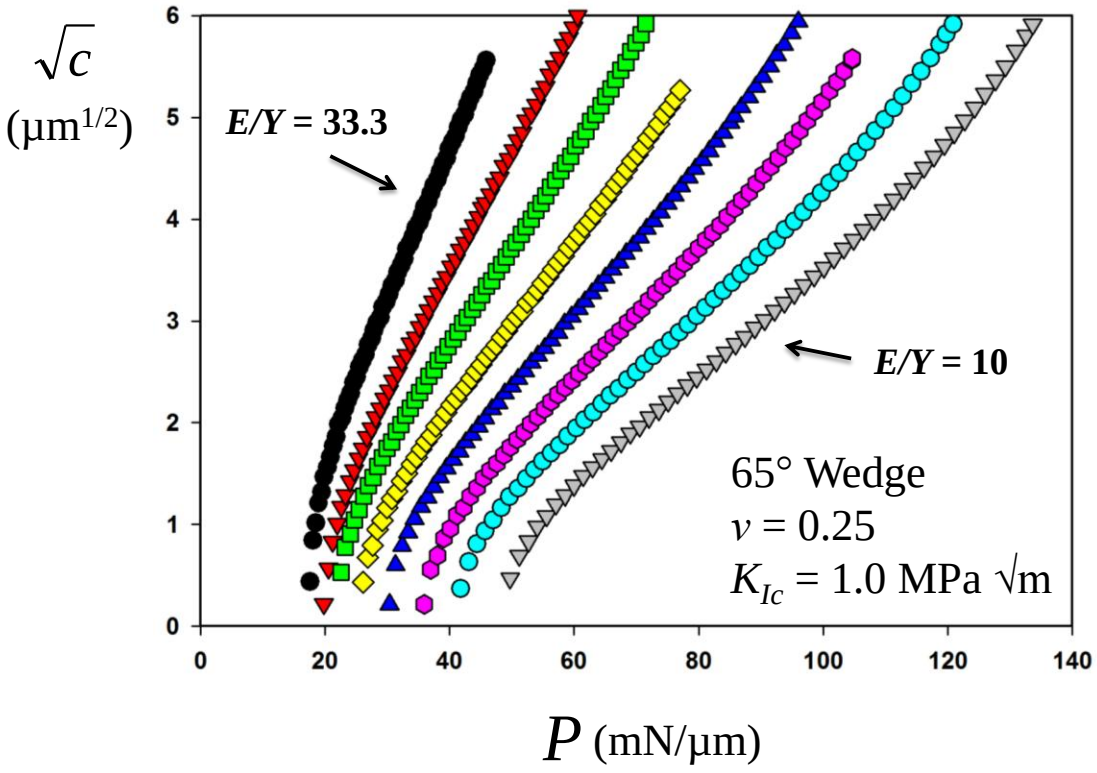


Figure 3.6. Square roots of crack lengths plotted as a function of load for various values of *E/Y*. Increasing *E/Y* results in increased crack growth rates.

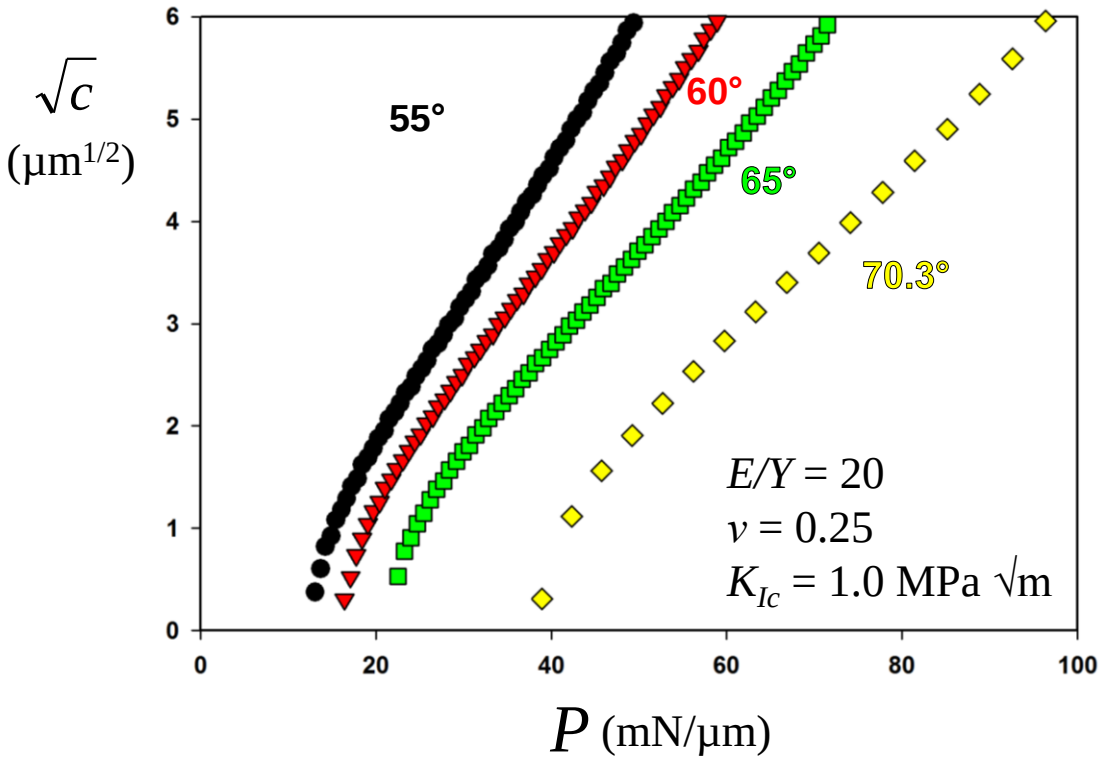


Figure 3.7. Square roots of crack lengths plotted as a function of load for various indenter angles. Increasing the indenter angle results in increased crack growth rates.

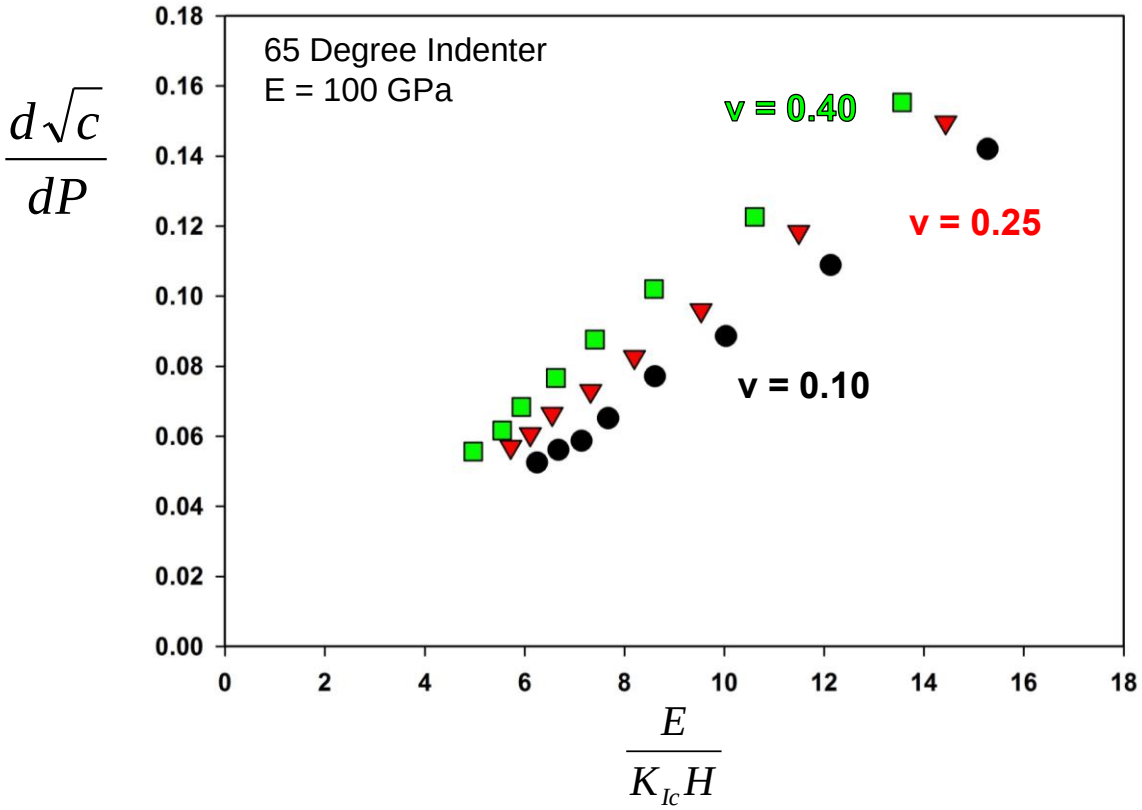


Figure 3.8. The effect of Poisson's ratio on crack growth rates as a function of material properties. Significant changes occur and Poisson's ratio cannot be neglected.

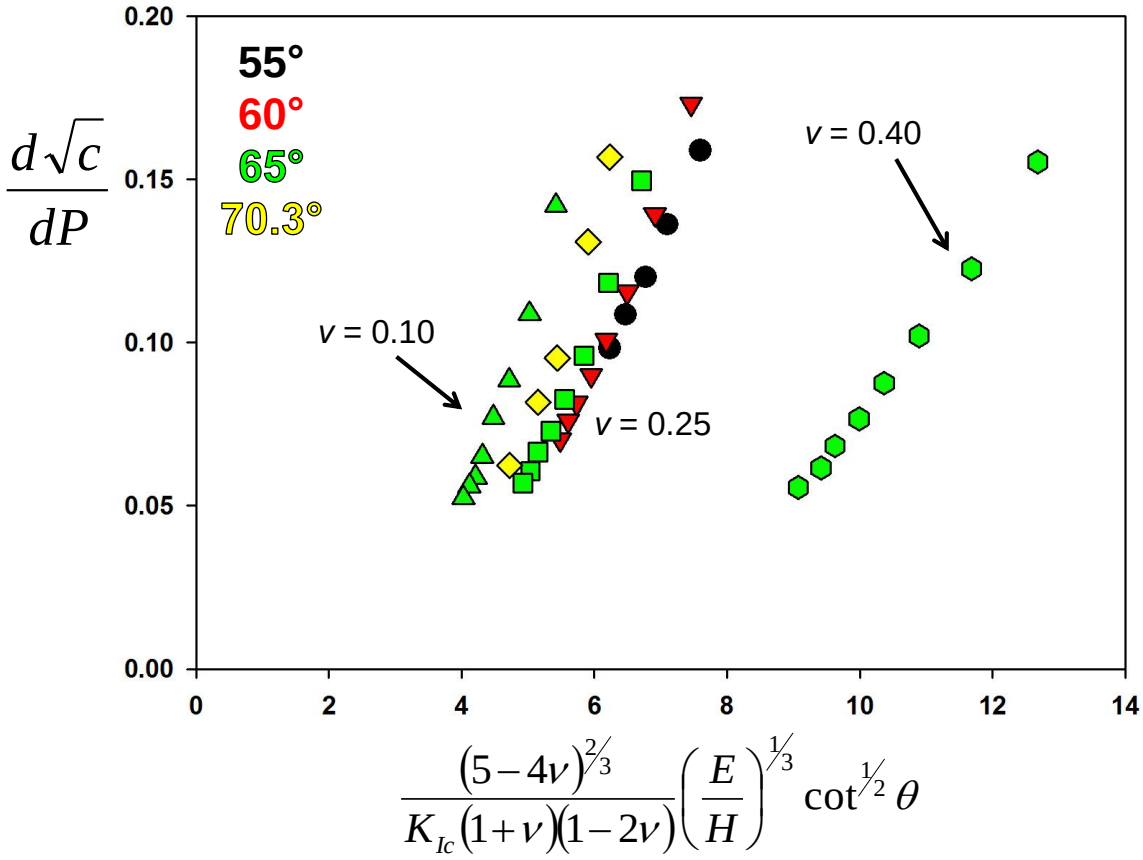


Figure 3.9. Simulation crack growth rates plotted as a function of the LEM parameter.

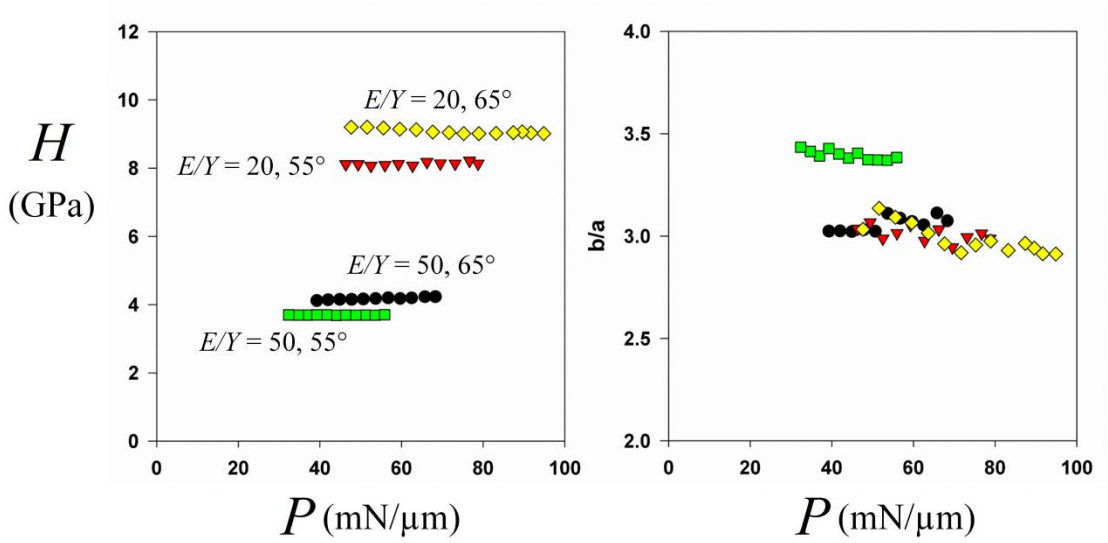


Figure 3.10. Plots of (a) hardness and (b) the ratio of plastic zone depth to contact dimension as a function of load for given materials showing that expected scaling relationships are maintained in the presence of crack growth.

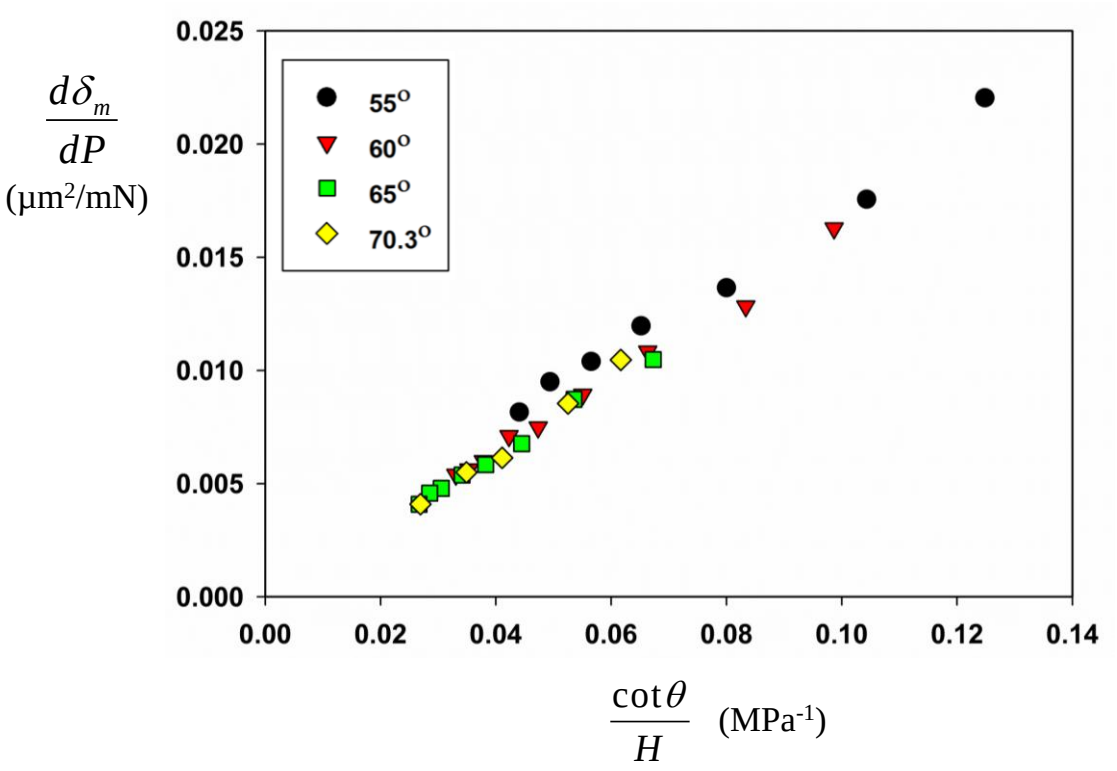


Figure 3.11. Crack mouth opening displacement rates with respect to load plotted as a function of indenter angle and hardness. Linear relationship suggests that crack mouth opening displacements scales with the size of the contact.

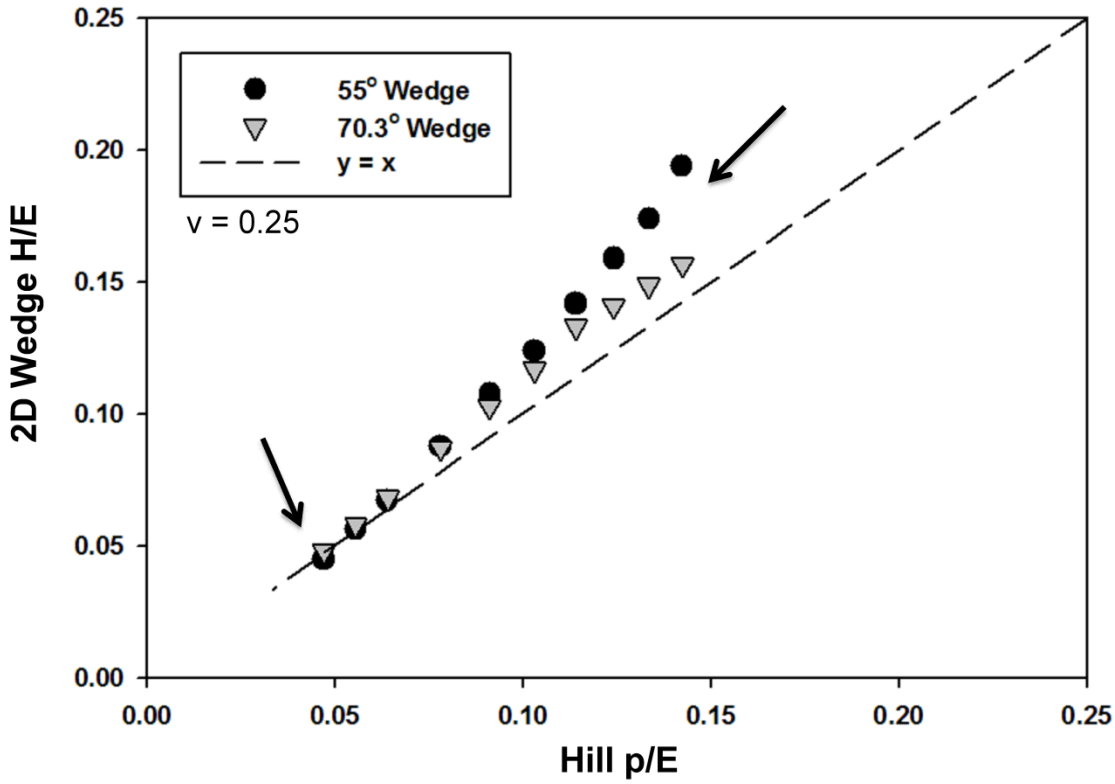


Figure 3.12. Normalized wedge indentation hardness, *H/E*, compared to normalized expanding cavity pressure, p_{EC}/E. Deviations occur at small values of *E/Y*.

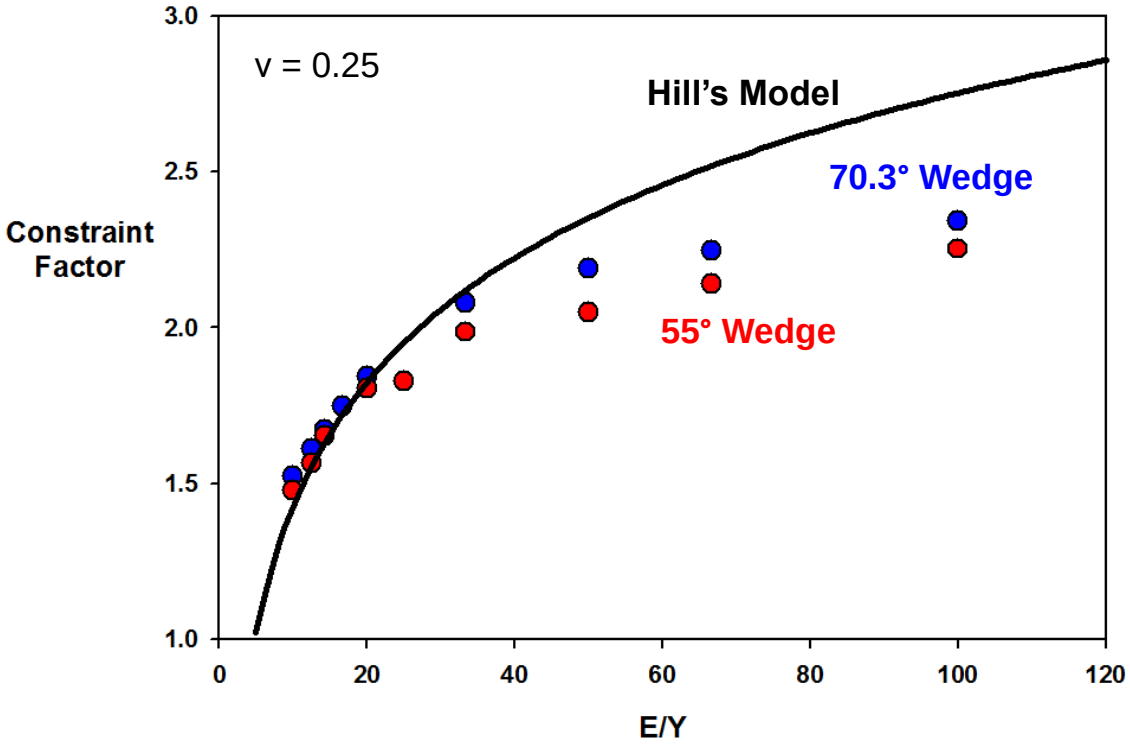


Figure 3.13. Wedge indentation constraint factor, *H/Y*, and expanding cavity model constraint factor, p_{EC}/Y, plotted as a function of *E/Y*. Deviations occur at large values of *E/Y* due to a transition in deformation types that is not accounted for in the radially symmetric expanding cavity model.

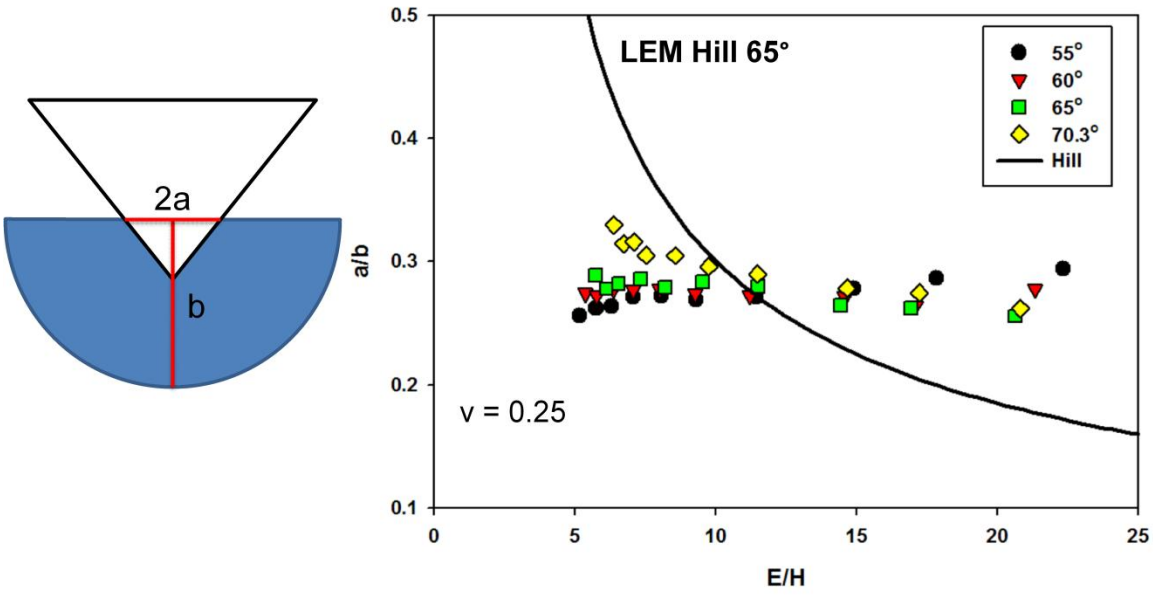


Figure 3.14. Ratio of the contact dimension to the plastic zone depth for wedge indenters of various angles and Hill's expanding cavity model prediction as a function of *E/H*.

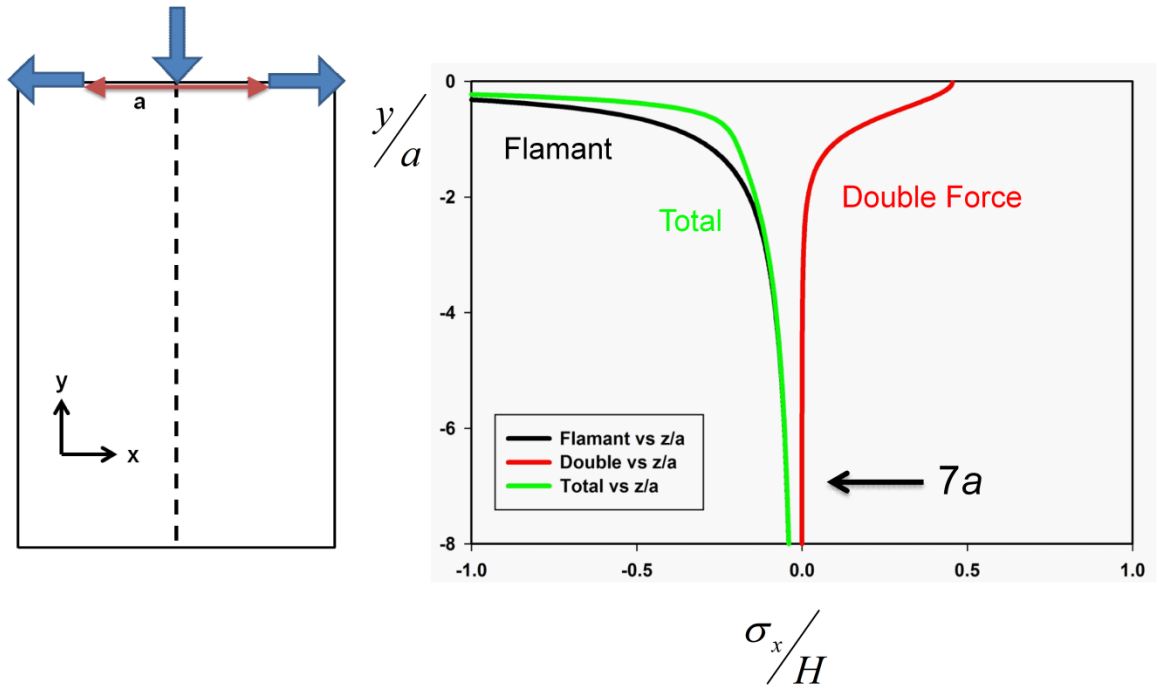


Figure 3.15. Estimating the elastic stresses by a vertical point line-load and a horizontal line-load (Eq. 3.15) for a 65° wedge indenter.

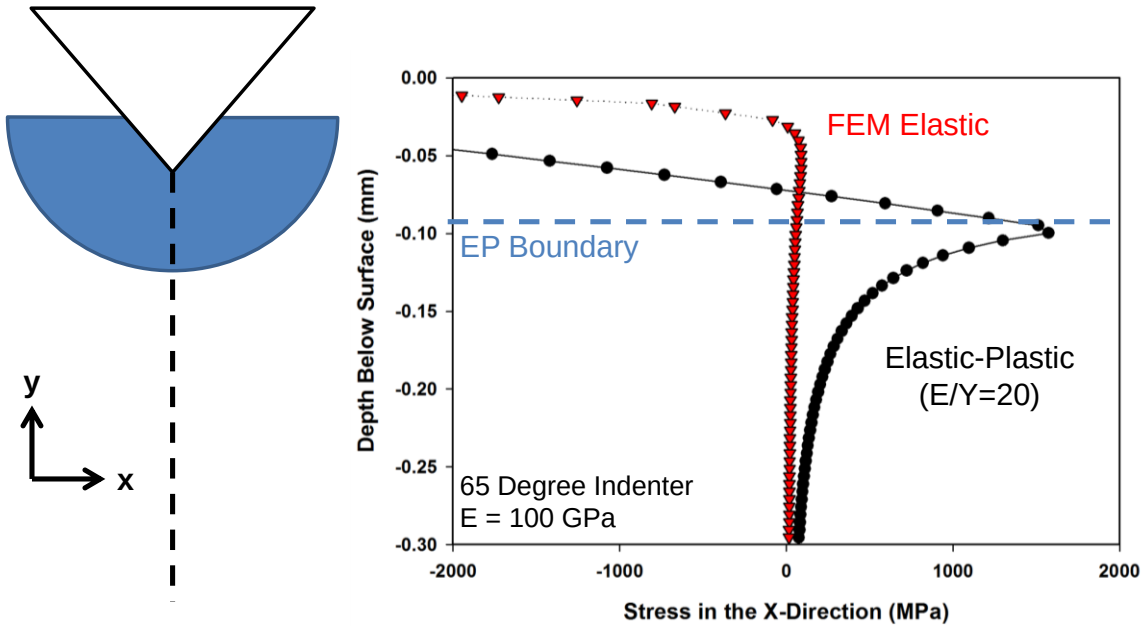
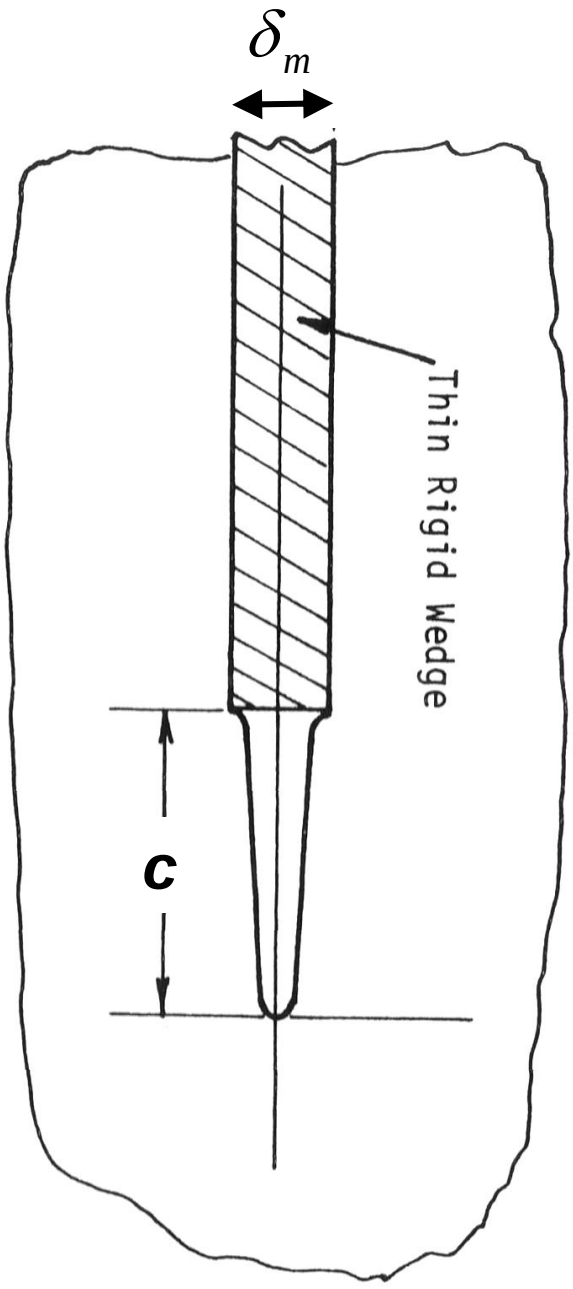


Figure 3.16. Stresses acting normal to the crack plane measured from finite element simulations of indentation with a 65°wedge indenter in an elastic and elastic-perfectly plastic (*E/Y* = 20) material.



$$K_I = \frac{E\delta_m}{\left(1-\nu^2\right)\sqrt{2\pi c}}$$

Figure 3.17. Thin rigid wedge stress intensity factor solution used in the analysis of 2D wedge indentation cracking.

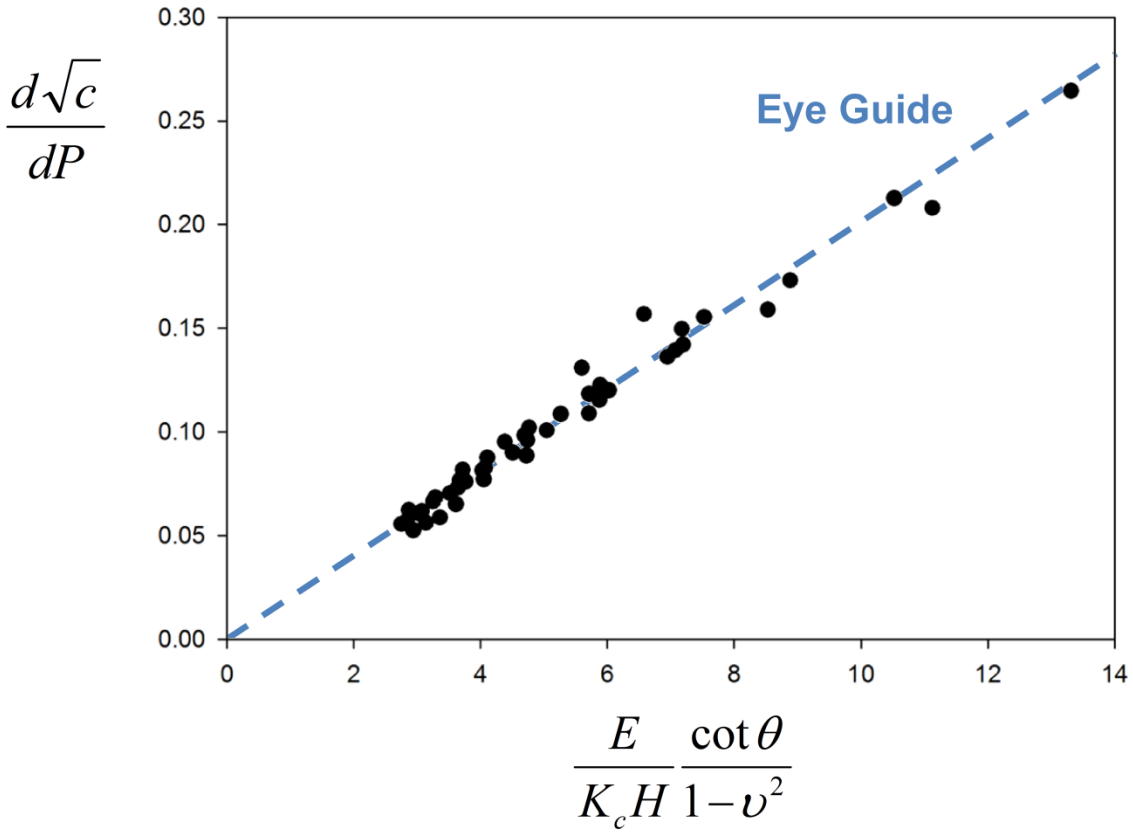


Figure 3.18. All of the simulation results of crack growth rates plotted as a function of Eq. 3.17.

CHAPTER IV

SIMULATING VICKERS INDENTATION CRACKING IN BRITTLE MATERIALS WITH COHESIVE ZONE FINITE ELEMENTS

Abstract

Three-dimensional cohesive zone simulations of the four-sided pyramidal Vickers indentation cracking geometry in elastic-perfectly plastic brittle materials have been carried out using the finite element software package ABAQUS. The Lawn, Evans, and Marshall indentation cracking model was critically examined with respect to the assumptions of material behavior and crack morphology during contact. Two important conclusions were drawn from the Vickers simulations: (1) The Lawn, Evans, and Marshall model is accurate over a small range of the ratio of elastic modulus to hardness, a range where indentation behavior is consistent with Hill's expanding cavity model, but deviates significantly outside of this limited range; and (2) there was a dramatic change in indentation cracking behavior as the ratio of elastic modulus to hardness moved from more ceramic-like materials toward metallic-like materials. Materials with lower values of elastic modulus to hardness, where elastic deformation dominated, exhibited *median* like cracking behavior where surface cracking was only evident upon unloading of the indenter. More metallic-like materials, where plasticity dominated deformation, exhibited *Palmqvist* type cracking where surface crack extension occurred on loading and unloading. This transition in indentation cracking behavior was consistent with experimental observations in glass (*median*) and tungsten carbide (*Palmqvist*). To the best of our knowledge, this was the first report of the change in cracking behavior being linked to the way in which a material accommodates deformation during the indentation process.

4.1. Introduction

Indentation of brittle materials such as glasses or ceramics with the pyramidal Vickers indenter is unique in that both controlled elastic-plastic deformation and stable crack growth are observed simultaneously. These phenomena provide opportunities to observe the competition and interaction of plastic deformation and crack growth mechanisms. In addition, indentation allows for examining mechanical behavior over length scales from nanometers to millimeters without the need for the, often complex or unfeasible, specimen geometries of more standardized tests. However, despite these advantages and the abundance of literature on the topic, the application of indentation fracture toughness techniques has been controversial [1-4]. The controversy stems from complexities associated with highly non-uniform elastic-plastic stress fields, individual material physics, and the need for models relating fracture toughness to indentation test data.

There is no direct relationship between the load applied to the indenter, crack length, and fracture toughness as exists for standard linear-elastic fracture toughness specimens [5, 6]. Indentation cracking may be unique in that both elastic and plastic deformation produces the crack driving force, as exhibited by crack extension during loading and unloading of the indenter [7]. In addition, until the work in transparent materials [8, 9], the only information on crack development during the indentation cycle came from observations of surface crack lengths or post-mortem analyses. Further complication includes the observation that different materials may exhibit different crack geometries such as the median/radial (often termed half-penny) or Palmqvist systems. Thus, the first models of indentation cracking were empirically based and tended to rely on experimental observations and assumptions of material behavior [10].

The Lawn, Evans, and Marshall (LEM) model of indentation cracking was the culmination of many years of experimental observations and collection of test data [7]. Their model elegantly links elastic-plastic deformation induced by the indenter to crack extension through a number of assumptions of material

behavior. There are a number of reviews and derivations of the LEM model, so only the critical parts will be highlighted in this section and a detailed examination is provided later. LEM choose to model the crack as a centrally point-loaded half-penny crack, where the driving force is composed of both elastic and residual contributions. The elastic component is modeled from a Boussinesq stress field [11], but is dominated by the residual component arising from the plastic accommodation of the indented volume of material. An integral part of their model comes from linking the elastic-plastic indentation material response and Hill's expanding cavity model [12]. This assumption gives a simple relationship between indentation hardness, H, elastic modulus, E, fracture toughness, K_{Ic}, and indentation test data of applied load, P_{max}, and crack length, c. Anstis et al. [13] experimentally calibrated the LEM model for a Vickers indenter with a number of brittle materials and arrived at the following equation:

$$K_{Ic} = 0.016\left(\frac{E}{H}\right)^{1/2}\frac{P_{\max}}{c^{3/2}}. \tag{4.1}$$

The ability to measure hardness and elastic modulus with instrumented indentation testing combined with the simplicity of Eq. 4.1 resulted in the extensive use of indentation fracture toughness measurements. That being said, there are a number of studies that highlight discrepancies between measurements from indentation cracking and standard fracture toughness tests. Ponton and Rawlings [2, 3] generated an extensive review of indentation cracking models which showed that making the selection of which model to use was often arbitrary and confusing. Nihaara [14] noted that measurements deviate when the ratio of contact size to crack length is small. Other authors have pointed out that the scaling relationship between load and crack length may be dependent on crack geometry [15]. For example, Palmqvist surface crack lengths have been observed to scale linearly with the maximum applied load [16]. Furthermore, some have pointed toward different or additional material dependencies not captured in the LEM model, e.g., the original LEM derivation ignores Poisson's ratio effects [17]. These concerns have caused some to

question the accuracy of indentation cracking models, while others go as far as to say the indentation cracking test should never be used [1]. Thus, despite its simplicity, the application of the LEM model for measuring fracture toughness is extremely controversial.

All of the above being said, critically examining the LEM model and the assumptions therein is often difficult due to experimental challenges of varying material properties over large enough ranges. Specifically, most brittle ceramic materials lie in a narrow range of E/H between 15 and 25. Differences in individual material microstructures and physics, such as grain size or the mechanism by which plastic deformation is accommodated, may further complicate experimental attempts at reconciling differences between the LEM model and standard fracture toughness tests.

Numerical simulations have provided insights into indentation testing over a wide range of material properties while simultaneously minimizing the need for assumptions of material behavior. In the past, these advantages would have come at the cost of computationally expensive calculations, but developments in technology have greatly reduced the requirements. There are a number of works that have shown that cohesive zone finite element simulations accurately reflect experimental observations of indentation cracking and that they can be used to model indentation of brittle materials [17-20]. Two-dimensional (2D) cohesive zone finite element simulations of wedge indentation cracking were used in Chapter III of this dissertation to critically examine the LEM model and showed that a simple rigid-wedge crack mouth opening displacement model well-described the fracture mechanics. Lee et al. [17] were the first to show a strong Poisson's ratio dependence on median/radial crack growth during Vickers indentation of brittle materials that has been previously ignored.

The current work is not meant to be a review of the literature but rather to provide both a fresh view of indentation cracking from a continuum mechanics view. This work is driven on the premise that, when used appropriately, numerical simulations provide an opportunity to extend the understanding of the

physical mechanisms underlying elastic-plastic indentation. In this case, cohesive zone finite element simulations are utilized to obviate the need for assumptions of material behavior under the complex elastic-plastic and cracking conditions observed during the indentation of brittle materials with pyramidal indenters.

The investigation begins by reporting results of simulations of indentation cracking and describing the discrepancies and matches with the LEM model in terms of the assumptions therein. The work then quickly gains complexity by using these results in combination with previous results of 2D wedge indentation cracking simulations to examine the physical mechanisms underlying crack growth. In addition to a strong Poisson's ratio dependence, it will be shown that the transition from elastically dominated deformation to plastically dominated deformation with increasing values of *E/H*, manifested as material sink-in or pile-up at the contact periphery, plays a significant role in crack driving forces. This transition also results in a change in both crack morphology and fracture mechanics, consistent with experimental observations of half-penny and Palmqvist crack geometries. We conclude that the transition results in different material dependencies than those predicted from Hill's expanding cavity model, and this has important consequences for the LEM analysis. Finally, comments based on the results in this work will be made on the appropriateness of measuring fracture toughness from Vickers indentation cracks.

4.2. Finite Element Simulations

The finite element software package ABAQUS v6 [21] was used for simulating Vickers indentation cracking with cohesive zone finite elements. Two separate types of simulations were performed during this investigation. First, three-dimensional cohesive finite element simulations were used to simulate cracking in brittle materials under contact with the pyramidal Vickers indenter and its conical equivalent. Second, axisymmetric conical indentation analyses in the absence cracking were run in order to aid the critical examination of the

assumptions in the LEM model. In all cases, contact was simulated with rigid indenters under frictionless conditions, and material models were limited to elastic-perfectly plastic materials described by an elastic modulus, E, Poisson's ratio, v, and yield strength, Y. The yield criterion was determined from J_2 flow theory. The simulations take advantage of the fact that geometrically self-similar indentation is dictated by the ratio of E/Y [22] (see Chapter I). Extensive details on the application of cohesive finite elements in indentation simulations and the Vickers indentation cracking meshes can be found in Johanns et al. [20] and Lee et al. [17] as well as previous chapters in this dissertation, but details pertinent to this study are highlighted below.

Measurements from FE simulations are described here for completeness with reference to the indentation cracking geometry shown in Figs. 4.1, 4.2, and 4.3. These figures are an idealized top-down view, a subsurface view sectioned along the corners of the contact, and a detailed view of material sink-in and pile-up at the contact periphery, respectively. The contact dimension, a, was measured as the horizontal distance from the indentation axis to the edge of contact at full load, where edge of contact refers to the corner on a Vickers indenter. Load, P, was taken as the reaction force in the indentation direction acting on the rigid indenter, which, in this formulation, was maintained in displacement control. Indentation hardness, H, is given by $P/2a^2$ and $P/\pi a^2$ for a Vickers and conical indenter, respectively. Note here that this is not the traditional method of measuring hardness where the contact area is measured after unloading the indenter, a measurement that is not possible or at best arbitrary in the finite element simulations. The discrepancy between the two measurements of hardness can be large when there is a significant amount of elastic recovery on unloading. The surface crack length, c, and the subsurface median crack length, m, were measured from the initial point of contact to the last traction-free cohesive element in the respective direction. The plastic zone length at the surface, b_{surf}, and the plastic zone depth, b_{depth}, were measured from the initial point of contact to a point in the material with an equivalent plastic

strain of $1x10^{-4}$. The contact depth, h_c, is affected by material sink-in or pile-up and was measured as the vertical distance from the tip of the indenter to the edge of contact full load while total indenter displacement, h, was the displacement of the indenter tip into the material from the original point of contact.

Eight-node linear brick elements (C3D8) in the bulk and six-node linear triangular prism elements (C3D6) on the indentation axis composed a one-eighth symmetric model of Vickers indentation cracking (refer to Fig. 2.4 in Chapter II for picture of mesh). ABAQUS traction-separation based cohesive elements were employed in all simulations, obviating the need for user-defined materials or elements. Such elements, with an initial separation of zero, were placed on planes of prospective crack growth, specifically, planes that contain the maximum tensile stress corresponding to the sharp edges of the indenter. Cracks were allowed to grow to the shape and length dictated by the material properties and loading conditions, but were constrained to remain within the defined crack plane. Table I gives the ranges of material properties simulated. In order to maximize consistency between simulations, a cohesive strength, σ_c, of 0.30 GPa, a stiffness of $1x10^6$ GPa, and a viscosity of $1x10^{-6}$ were used in all simulations. Details of the importance of these variables in cohesive zone simulations and calculations of process zone sizes can be found in Johanns et al [20].

The cohesive zone model plays an integral role in these simulations and it has been shown that the use of cohesive elements can create artifacts, especially when simulating brittle materials. Many of these artifacts have been pointed out previously. However, here we detail one of the more important effects, namely the influence of the process zone size with respect to the crack length. The process zone size, ρ, can be estimated from the following equation [6]:

$$\rho \approx \frac{\pi}{8}\frac{K_{Ic}^2}{\sigma_c^2}. \qquad (4.2)$$

Johanns et al. [20] have shown that a crack can be accurately analyzed with linear-elastic fracture mechanics when the crack length is approximately 10 times the process zone size or greater. Crack lengths below this criterion exhibit an artificially increased toughness, an effect that is also observed in the Vickers indentation cracking simulations. Figure 4.4 shows the result of simulations of Vickers indentation of a material with an elastic modulus of 100 GPa, yield strength of 2 GPa, Poisson's ratio of 0.10, and a fracture toughness, K_{Ic}, of 1.41 MPa √m, a combination of material properties that results in a half-penny crack. The dimensionless parameter $K_{Ic}c^{3/2}/P_{max}$, for surface crack lengths, and $K_{Ic}m^{3/2}/P_{max}$, for median crack lengths is plotted as a function of the ratio of crack length to process zone size at the state of full unload. Notice that once the crack length has become at least 10 times the process zone size, a steady state has been reached and the dimensionless crack length is nearly a constant. Note here that the ratio of crack length to process zone size did not affect the geometry of the crack, and simulations of other material property combinations resulted in similar behavior. All further results are presented from simulations where the crack length is at least 10 times the process zone size.

Axisymmetric conical indenter simulations were carried out using a 70.3° included half-angle indenter, which is gives rise to an equivalent contact area in a Vickers indenter for a given contact depth. Four-node axisymmetric elements (CAX4) were used with an increased mesh density near the contact and region of the plastic zone. The calculation cell size was large enough to ensure boundary effects were negligible and contact sizes were large enough such that measurements of hardness and plastic zone lengths were independent of element size effects. Conical indenter simulations included the same materials described in the Vickers indenter simulations, but without the fracture properties required for cohesive element simulations.

4.3. Results

The main goal of this chapter is to critically examine the Lawn, Evans, and Marshall (LEM) model of indentation cracking with results from cohesive zone finite element (FE) simulations in an effort to comment on the controversial nature of using this model to measure fracture toughness. To that end, results from FE simulations will first be described in terms of crack development and morphology as a function of material properties. Discussion of crack initiation will be limited to location as a function of material properties as initiation events are not well described by the cohesive zone formulation in this work [20]. Second, the results will be directly compared to the LEM model and consistencies and discrepancies will be highlighted in terms of the assumptions inherent to the LEM model. It will be shown that the Hill's spherically symmetric expanding cavity model does not accurately capture indentation behavior, primarily due to the transition from material sink-in to material pile-up at the face of the indenter as material properties move from elastic to elastic-plastic to nearly perfectly-plastic. This same transition also results in changes to both crack geometry from median to Palmqvist and in the fracture mechanics that govern the relationships between maximum load, material properties and crack length.

The description of crack morphology and growth begins with a material with an infinite yield strength, wherein there is no plasticity. While such results are not directly applicable to experimental testing where plasticity occurs upon contact with a Vickers indenter, there are a number of important observations that aid the understanding of indentation cracking. Plasticity was required for crack initiation and growth in the case of 2D wedge contact because the elastic contact stresses are compressive on the prospective crack plane. However, stresses on median crack planes in three-dimensional (3D) elastic contact are both tensile or compressive depending on position relative to the contact. Crack initiation began close to the point of contact on the indentation axis and quickly developed into two sub-surface, penny-like, median cracks aligned with the corners of the Vickers indenter. This crack geometry did not change with

increasing load or elastic modulus, but was dependent on Poisson's ratio. Increasing Poisson's ratio served to reduce the crack size (e.g., the crack depth *m* in Fig. 4.2) for a given load and it was increasingly difficult to generate a crack as Poisson's ratio approached 0.50. This result could be explained by the Boussinesq contact solution to a point force on an elastic body [11]. The hoop stresses, σ_θ, stresses perpendicular to the crack planes, are given by:

$$\sigma_\theta = \frac{P(1-2\nu)}{2\pi}\left[\frac{-1}{x^2} + \frac{z}{x^2\sqrt{x^2+z^2}} + \frac{z}{\left(x^2+z^2\right)^{3/2}}\right], \tag{4.3}$$

where *P* is the applied load, *v* is Poisson's ratio, *x* is the radial direction, and *z* is the depth into the surface of the material.

The FE elastic crack geometry is shown in Fig. 4.5a, and the stress field described by Eq. 4.3 is shown in Fig. 4.5b for a Poisson's ratio of 0.25. The elastic Vickers crack geometry was amazingly approximated by the location and shape of tensile stress contours in Fig. 4.5b even though the Boussinesq solution describes a point force. In a similar manner, Lawn has shown that cone crack growth in hard, brittle materials follows solutions to spherical contact stress fields [23]. Given these observations, further examination of Eq. 4.3 shows that crack opening stresses decay to zero as Poisson's ratio approaches 0.5, which explains the decreased crack size with increasing Poisson's ratio for a given load. One last note of interest in the elastic case is the shape of the deformed surface at load is sunk-in (see Fig. 4.3) as expected from an elastic contact.

Unloading of the indenter during the elastic contact simulation did not result in further crack growth and the final crack geometry never breached the surface no matter how large of a load was applied in the FE simulations. This result has two important ramifications: (1) crack growth at the surface outside of the contact requires plastic deformation and the residual component of the crack driving force plays a strong role in surface crack growth as noted by LEM [7]; and (2) although there is no plasticity, the elastic contact has a finite value of hardness because it is defined here by the contact area at the applied load.

Thus, the ratio of *E/H* for indentation of an elastic material is not zero, but the value of the dimensionless cracking parameter, $K_{Ic}c^{3/2}/P_{max}$, is zero due to the absence of a surface crack.

Results from FE simulation of material with elastic-perfectly plastic behavior will be described in the following with descriptions of crack growth as the ratio of *E/Y* increases, i.e., plasticity begins to play a stronger role in the contact response. Conversion between input values of *E/Y* and resulting values of *E/H* will be provided with the numerical results of crack lengths in the next section. The addition of a yield strength to the constitutive behavior of the material results in crack growth upon unloading and cracks that are visible at the surface. At low values of *E/Y*, less than ~100, two subsurface, penny-like, median cracks aligned with the corners of the Vickers indenter develop in a manner similar to the elastic contact simulation results. No surface cracking is visible during loading. In addition, with reference to Fig. 4.3, material is sunk-in around the indenter in this regime of *E/Y*.

Upon unloading the indenter, crack extension occurs at the penny-like crack-front close to the surface, but not at the crack-front directly beneath the indenter. The crack extends up to the surface upon complete unloading of the indenter such that the final crack geometry is a half-penny crack, i.e., in terms of Fig. 4.2, surface crack length *c* increases and depth crack length *m* does not increase (*m* slightly changes from the fully loaded value due to elastic recovery). This series of crack extension events is remarkably similar to the experimental observations of Lawn and co-workers in transparent materials like glass that have *E/Y* ratios within the range described above [24]. The relative amount of surface extension from a given maximum load depended on the value of *E/Y*, where lower values of *E/Y* resulted in less extension than those materials with greater values of *E/Y*.

A transition in cracking behavior occurred when the *E/Y* ratio was approximately 100. At these values of *E/Y* cracks initiated at the surface just outside of the contact at the corners of the indenter during loading. Material in

this regime of *E/Y* tended to pile-up around the indenter as plastic deformation is prominent (see Fig. 4.3). These four cracks developed into the classic Palmqvist or radial geometry with crack extension occurring radially away from the contact as well as below the surface with increased loading. With even further loading, two Palmqvist cracks growing on the same plane would coalesce to form a half-penny crack that continued to extend along the entire crack front with applied load. Similar observations were made by Cook and Pharr during in-situ measurements of indentation crack growth during loading and unloading [4]. Upon unloading, cracks extension occurs at the surface, but not at the subsurface front, similar to the low *E/Y* regime. Crack extension on unloading occurred independent of whether or not the Palmqvist crack developed into the half-penny geometry. Furthermore, Palmqvist only geometries were observed when crack lengths were greater than ten times the size of the process zone.

The crack geometries described above are shown in Fig. 4.6 alongside an example 3D finite element mesh with highlighted crack planes (Fig. 4.6a). Crack geometries at maximum load for *E/Y* ratios of 12.5, 25, and 200 in Fig. 4.6b, c, and d, respectively. Corresponding unloaded crack geometries are shown in Fig. 4.6e, f, and g. The elastic constraint at the surface dominates during loading at *E/Y* ratios below 100. This elastic constraint is significantly less at *E/Y* ratios greater than 100, resulting in surface crack propagation during loading. It will be shown later that this closely coincides with the plastic zone breaching the surface as the contact becomes dominated by plasticity.

Idealized schematics of completely unloaded subsurface indentation cracking geometries for the low *E/Y* (<100) regime and high *E/Y* (>100) regimes are pictured in Fig. 4.7. The half-penny and Palmqvist geometries are shown in Fig. 4.7a and Fig. 4.7bc, respectively. An important outcome of the simulations was that the magnitude of fracture toughness did not influence crack geometry/development. However, the maximum applied load required to reach a given crack length scaled with the magnitude of fracture toughness. Measurements of surface crack lengths, *c*, from a view along the indentation axis

normal to the surface would not discriminate between the two types of cracking; a point that will be important when estimating fracture toughness from indentation techniques.

The *load* for crack initiation is a complicated function of the magnitude of fracture toughness, *E/Y*, Poisson's ratio, and other cohesive element variables [20]. As such, this work is not concerned with simulating indentation cracking threshold loads. However, the *location* of crack initiation in the cohesive FE simulations can help explain the difference in cracking between the low and high *E/Y* regimes. Cracks initiated in the simulations at the location of the maximum tensile stress on the prospective crack plane. This location scaled with the size of the contact with geometric self-similarity. The location of the maximum tensile stress at full load from conical indentation simulations without cracking changed with the value of *E/Y* and are shown in Fig. 4.8. The contours shown in Fig. 4.8 correspond to the outline of the plastic zone (defined by $1x10^{-4}$ plastic strain) for each of the values of *E/Y* shown in the figure. The location of the maximum tensile consistently occurred outside of the plastic zone. The point of initiation was located on the indentation axis for low *E/Y* materials and transitioned toward the surface as the ratio of *E/Y* reached 100. Similar results could be found from an analytical solution to the stress field beneath a conical indenter in an elastic-plastic material [25, 26]. From this point on, the type of cracking observed in the finite elements will be termed *median* or *Palmqvist* depending on the location of crack initiation, consistent with the terminology found in most of the indentation cracking literature.

We now move from the FE simulation descriptions of Vickers indentation crack morphology/growth to the numerical results of crack lengths as a function of material properties and applied loads with respect to the LEM model. We also choose to switch from using the ratio of *E/Y* to the ratio of *E/H*, a parameter that is more useful experimentally as yield strengths of brittle ceramic-like materials are often difficult to quantify. The transition from *median* cracking to *Palmqvist* cracking observed in the simulations at *E/Y* of ~100 occurred at an *E/H* ratio of

~30. The LEM model indicates the parameter $K_{Ic}c^{3/2}/P_{max}$ should be a constant for a given material through dimensional analysis, and predicts a linear dependence of the non-dimensional parameter with the square-root of *E/H* (Eq. 4.1). Resulting values of $K_{Ic}c^{3/2}/P_{max}$ from the FE simulations with a Poisson's ratio of 0.25 are plotted as a function of the $\sqrt{E/H}$ in Fig. 4.9 alongside the experimentally calibrated LEM prediction [13]. There are a number interesting points in Fig. 4.9: (1) the FE data does not scale linearly with $\sqrt{E/H}$ over the entire regime examined; (2) the LEM model overestimates $K_{Ic}c^{3/2}/P_{max}$ at low values of *E/H* (elastic dominated contacts) as well as high values of *E/H* (plastic dominated contacts); (3) despite points (1) and (2), the FE simulations and LEM model are in relatively good agreement in the range of *E/H* between 15 and 25. Figure 4.9 will be discussed later in terms of the assumptions of the LEM model and the observations from the FE simulations.

The influence of Poisson's ratio on $K_{Ic}c^{3/2}/P_{max}$ as a function of the $\sqrt{E/H}$ is shown in Fig. 4.10 for Poisson's ratios of 0.10, 0.25, and 0.40. Smaller values of Poisson's ratio lead to greater values of $K_{Ic}c^{3/2}/P_{max}$ independent of *E/H*. Lee et. al. were the first to observe this Poisson dependence in similar cohesive FE simulations of Vickers indentation cracking [17]. A derivation of the LEM model in which constants of proportionality as well as Poisson's ratio dependencies are maintained throughout (see chapter II of this dissertation) yields the following relationship:

$$K_{Ic} = 0.049\frac{(1-\nu)^{1/2}}{(1-2\nu)}\left(\frac{E}{H}\right)^{1/2}\frac{P_{\max}}{c^{3/2}}\cot^{2/3}\theta, \qquad (4.4)$$

where θ is the centerline-to-face angle of the indenter. Equation 4.4 differs slightly from other LEM derivations [27, 28] in that Poisson's ratio dependencies in Hill's expanding cavity model are maintained [12]. Equation 4.4 as well as other derivations predicts an increase in $K_{Ic}c^{3/2}/P_{max}$ as Poisson's ratio increases as opposed to the results from these simulations. The magnitude of Poisson's

ratio did not significantly influence the E/H ratio at which the transition from *median* to *Palmqvist* cracking occurred.

It was confirmed that for given *E/H* and Poisson's ratios, but varying *E* and *H*, the resulting value of $K_{Ic}c^{3/2}/P_{max}$ from the FE simulations was consistent in the median cracking regime (low *E/H*) as long as crack lengths were at least ten times greater than the size of the process zone (see Fig. 4.4). There was, however, a small dependence of $K_{Ic}c^{3/2}/P_{max}$ on crack length in the Palmqvist cracking regime. One goal at the onset of this work was to assess Vickers indentation cracking on the ratio of surface crack length, *c*, to the contact size, *a*. However, an outcome of the restriction of the size of the crack with respect to the size of the process zone is the minimum ratio of crack length to contact size, *c/a*, that can be explored in these cohesive zone finite element simulations. Figure 4.11 shows the approximate minimum *c/a* ratio achieved in these simulations as a function of *E/H* that corresponds to a ratio of crack length to process zone size of at least ten. Resulting values of $K_{Ic}c^{3/2}/P_{max}$ from the simulations in Fig. 4.11 are equivalent to those found in tests with greater applied loads. Refer to Fig. 4.4 for results when the process zone size is a significant fraction of the crack length. The minimum ratio was almost always greater than two, the approximate value at which some discrepancies have been observed in the LEM model [14]. Unfortunately, this regime of Vickers indentation cracking could not be explored with the cohesive zone formulation applied in these simulations.

4.4. Discussion

First, the most important and glaring result from the finite element (FE) simulation of Vickers indentation cracking is the transition from median cracking to Palmqvist cracking as the ratio of elastic modulus, *E*, to hardness, *H*, goes above ~30. This transition occurs as the contact behavior transitions from elastically dominated contact to plastically dominated contact. The shape of the deformed surface changes significantly over the range examined in these simulations. A short discussion here on the two regimes of indentation cracking.

Second, results from cohesive zone FE simulations of Vickers indentation cracking show a clear dependence on *E/H* not accounted for in the Lawn, Evans, and Marshall (LEM) model. In light of this discrepancy, we will dissect the LEM model by carefully examining the assumptions of material behavior in its derivation. A similar examination was made of the LEM model for two-dimensional wedge indentation cracking.

Anstis et al. experimentally calibrated the LEM model with a number of brittle materials (see Eq. 4.2) [13]. Note that Anstis et al. measured hardness with the traditional optical technique post-test . Their individual material results along with Harding's data on amorphous silica [28] are shown alongside the FE simulation data for Poisson's ratio of 0.25 in Fig. 4.12. The experimental data points, except for the polycrystalline aluminas (AD90 and AD999) and single crystal sapphire, compare reasonably well with the FE simulation data. This match includes the tungsten carbide (WC) and amorphous silica data at the experimental *E/H* extremes. Tungsten carbide is known to exhibit *Palmqvist* type cracking during Vickers indentation [16, 29-32], which is consistent with the FE results in materials with *E/H* greater than ~30 (WC has an approximate *E/H* of 43 [13]). Experimental results on amorphous silica have significantly lower values of $K_{Ic}c^{3/2}/P_{max}$ than most other materials. This discrepancy has been attributed to local densification beneath the indenter [33], resulting in deviations from expected material behavior, while the FE simulations suggest the lack of crack driving force in amorphous silica stems from the low value of *E/H*, near the elastic limit, and the fact that the median crack has trouble extending to the surface of the material in that regime. Anstis et al.'s limitation in calibration appears to be with the forced square-root dependence on *E/H* from the LEM model.

Deviations from the square-root of *E/H* dependence are obvious in the *Palmqvist* regime where $K_{Ic}c^{3/2}/P_{max}$ is approximately a constant. A closer look at the power law dependence of $K_{Ic}c^{3/2}/P_{max}$ and $K_{Ic}m^{3/2}/P_{max}$ (*c* and *m* correspond to the surface crack length and median crack depth, respectively, as shown in

Fig. 4.2) in the *median* cracking regime is shown in a log-log plot of the FE simulation data in Fig. 4.13. The LEM model predicts a 1/2 power dependence while some other models predict a 2/3 dependence [2]. While the subsurface non-dimensional parameter is well approximated by a power-law description, the surface crack non-dimensional parameter is not.

The LEM model elegantly links the elastic-plastic indentation response of the material to material properties through Hill's expanding cavity in an infinite elastic-perfectly plastic solid model [12]. Hill's model is similar to indentation in that for a given E/Y, pressure and deformed geometry are constants. A detailed discussion on their use of Hill's model is given in Chapter III of this dissertation and therefore this section is dedicated to discrepancies between Hill's model and indentation data from FE simulations of geometrically self-similar indentation without cracking. It will be shown that the transition from elastically dominated deformation to plastically dominated deformation as E/H increases is important to understanding indentation cracking.

First, LEM assume that the hydrostatic pressure required for expanding a cavity in an infinite elastic-perfectly plastic material, p_{EC}, is equivalent to indentation hardness, H (equations for Hill's model can be found in Chapter III). Figure 4.14 shows the ratio of expanding cavity pressure to indentation hardness, p_{EC}/H, plotted as a function of E/H. Each data point represents a material with a fixed value of E/Y. The fact that p_{EC}/H is not unity is not important since the LEM model drops all constants of proportionality, and at low values of E/H, the ratio of p_{EC}/H is nearly constant. However, the magnitude of p_{EC}/H drops as E/H increases, showing that the LEM assumption of the indentation hardness being equal to the expanding cavity pressure is invalid over the range of E/H examined in this study. Material displacements in Hill's model are radial no matter the value of E/Y. Displacements in the indentation geometry, however, transition from radial to cutting with increasing E/H [34, 35].

Second, while not explicitly used in the LEM model, Hill's prediction of the constraint factor, p_{EC}/Y for the expanding cavity model and H/Y for the

indentation geometry, further highlights differences between indentation and assumed material behavior. Constraint factors for each of the geometries are plotted against each other in Fig. 4.15. Again, there is good agreement in the low E/H regime, but significant deviation in the high *E/H* regime begins around an *E/H* of ~30. Indentation constraint factors are nearly constant at a value of *H/Y*=2.6 in the high E/H regime, though the contacts in this regime have not reached rigid-plasticity as there is some elastic recovery on unloading [22].

Examination of pile-up and sink-in of material at the contact periphery provides further evidence that the transition to plastic dominated deformation is important to indentation cracking. The ratio of contact depth, h_c, to total displacement, h, as shown in Fig. 4.3, is plotted as a function of *E/H* in Fig. 4.16. As described in the results section, material is sunk-in at the contact at values of E/H below 30 and piled-up above 30. This also happens to closely correspond to the point at which the plastic zone breaches the surface of the contact (see Fig. 4.8) and the location of crack initiation transitions to the surface upon loading. The pile-up/sink-in parameter, h_c/h, changes rapidly at low values of *E/H* but is nearly constant in the highly plastic regime, similar to the constraint factor.

Third, and arguably the most important assumption in the LEM model, is the ratio of contact size, a, to the radius of the plastic zone, b. The plastic zone in Hill's spherically symmetric model can be described by one value, but the indentation plastic zone is not spherically symmetric due to the free surface. Therefore, the *a/b* ratio for indentation data from the FE simulations is plotted (log-log scale) in Fig. 4.17 as a function of *E/H* for both the plastic zone depth, b_{depth}, and surface length, b_{surf}, as shown in Fig. 4.2. Again, Hill's model accurately describes the indentation data in the range of E/H between 15 and 25, but deviates outside of this regime.

The LEM indentation cracking model can be written without assuming Hill's model to describe the indentation behavior in non-dimensional form as:

$$\frac{K_{Ic}c^{3/2}}{P_{\max}} = \gamma \frac{a}{b}\frac{E}{H}, \tag{4.5}$$

where γ is a constant of proportionality that, if the LEM model is accurate, should be independent of material. The derivation in Chapter III results in a γ equal to 0.0138. Ratios of contact size to plastic zone radius from the FE simulations can be used to directly evaluate the LEM model in light of the discrepancies between indentation behavior and Hill's model. $K_{Ic}c^{3/2}/P_{max}$ is plotted as a function of aE/bH in Fig. 4.18 for Poisson's ratio of 0.25. The LEM model using surface plastic zone sizes is linear in a range of aE/bH that corresponds to the same range of E/H ($15 < E/H < 25$) where Hill's model accurately describes the indentation plastic zone, correlating well with Fig. 4.17. Note, not all of the *Palmqvist* regime is plotted in Fig. 4.18 to show more detail in the *median* regime. However, even taking into account plastic zone geometries resulting from the FE simulations cannot account for the transition from *median* to *Palmqvist* cracking at E/H of ~30. Clearly, estimating the driving force for crack growth through expansion of the plastic zone is not consistent with the FE results over the range of E/H examined.

Estimating fracture toughness with indentation cracking is of primary interest from an engineering perspective. To that end, errors in predicted values of $K_{Ic}c^{3/2}/P_{max}$ from the LEM model compared to the FE results in the *median* cracking regime are plotted in Fig. 4.19 as a function of E/H for Poisson's ratio of 0.25. Errors can be as large as 50%, consistent with experimental observations [3, 36]. Fracture toughness would be underestimated with the LEM model at higher values of E/H, consistent with the observations from Quinn and Bradt in silicon nitride [1].

The LEM model derives its crack driving force from elastic resistance to plastic deformation, which is consistent with the observations from the FE simulations. From this viewpoint, the transition to a nearly constant value of $K_{Ic}c^{3/2}/P_{max}$ even though E/H is increasing, can be thought to occur because the plastic zone has begun to breach the surface of the material during loading can therefore cannot provide continued driving force for crack growth. In addition, the

indentation geometry reaches a steady-state where large changes in *E/H* result in nearly negligible changes in indentation geometry.

There is a high correlation of indentation cracking behavior, both geometry and driving force, to the transition from elastically dominated deformation to plastically dominated deformation. To the best of our knowledge, this is the first time that indentation cracking geometries and driving forces have been correlated to specific changes in plastic flow near the contact. The observations discussed above combined with discrepancies between Hill's expanding cavity model and indentation of geometrically self-similar indenter highlight the need for a different view of indentation cracking. Material flow above and below the surface must be accounted for in a way that is not captured in Hill's expanding cavity model. Such work can be found in following chapters in this dissertation where relationships between indentation cracking data are related to simple stress intensity factor solutions through FE simulation observations.

4.5. Conclusions

Cohesive zone finite element simulations of Vickers indentation cracking of brittle materials were found to be in excellent agreement with many experimental observations. These simulations were used to show that the elastic-plastic properties of a material are extremely influential in determining the relationship between applied load, crack lengths, and fracture toughness. The main conclusions that were drawn from this work are as follows:

1) An *E/H* ratio of ~30 is the point at which a transition occurs in indentation cracking behavior. Cracks initiate subsurface below this value and were termed *median*. *Palmqvist* cracking dominated at values of *E/H* above 30, consistent with experimental observations in tungsten carbide.
2) Material deformation behavior changes rapidly in the low *E/H* (<30) regime, but is nearly independent of changes in *E/H* in the high *E/H* (>30) regime. Evidence for this transition was found in constraint factors and pile-up/sink-in at the contact. Hill's expanding cavity model could not

capture this transition due to its spherical symmetry and forced radial deformation.

3) The Lawn, Evans, and Marshall model of indentation cracking matches reasonably well with the finite element results in the range of *E/H* between 15 and 25. This range happens to be where Hill's expanding cavity model accurately describes indentation behavior. However, the model deviates significantly from the finite element results outside of this range, especially in the *Palmqvist* regime and the extreme low *E/H* regime where elasticity dominates the contact.
4) The loss of crack driving force with *E/H* and subsequent constant value of $K_{Ic}c^{3/2}/P_{max}$ in the *Palmqvist* regime can be thought of as occurring due to plastic deformation piling-up at the contact periphery and a steady-state geometry.
5) The LEM model results in errors in $K_{Ic}c^{3/2}/P_{max}$ of up to 50% in the median cracking regime when compared to the finite element results, consistent with experimental observations.
6) Poisson's ratio, not considered in the original LEM model derivation, plays a significant role in the relationship between crack length, applied load, and fracture toughness.

References

1. Quinn, G.D. and R.C. Bradt, *On the Vickers Indentation Fracture Toughness Test.* Journal of the American Ceramic Society, 2007. **90**(3): p. 673-680.
2. Ponton, C.B. and R.D. Rawlings, *Vickers indentation fracture toughness test Part 1 Review of literature and formulation of standardised indentation toughness equations.* Materials Science and Technology, 1989. **5**: p. 865-872.
3. Ponton, C.B. and R.D. Rawlings, *Vickers indentation fracture toughness test Part 2 Application and critical evaluation of standardised indentation toughness equations.* Materials Science and Technology, 1989. **5**: p. 961-976.
4. Cook, R.F. and G.M. Pharr, *Direct Observation and Analysis of Indentation Cracking in Glasses and Ceramics.* Journal of the American Ceramic Society, 1990. **73**(4): p. 787-817.
5. Tada, H., P.C. Paris, and G.R. Irwin, *The stress analysis of cracks handbook*. 1973: Del Research Corp.
6. Anderson, T.L., *Fracture Mechanics: Fundamentals and Applications*. 2005: Taylor & Francis.
7. Lawn, B.R., A.G. Evans, and D.B. Marshall, *Elastic-Plastic Indentation Damage in Ceramics - the Median-Radial Crack System.* Journal of the American Ceramic Society, 1980. **63**(9-10): p. 574-581.
8. Lawn, B.R. and M.V. Swain, *Microfracture beneath point indentations in brittle solids.* Journal of Materials Science, 1975. **10**(1): p. 113-122.
9. Lawn, B.R. and E.R. Fuller, *Equilibrium penny-like cracks in indentation fracture.* Journal of Materials Science, 1975. **10**(12): p. 2016-2024.
10. Evans, A.G. and E.A. Charles, *Fracture Toughness Determinations by Indentation.* Journal of the American Ceramic Society, 1976. **59**(7-8): p. 371-372.
11. Johnson, K.L., *Contact Mechanics*. 1987: Cambridge University Press.
12. Hill, R., *The mathematical theory of plasticity*. 2004, Oxford: Clarendon Press.
13. Anstis, G.R., et al., *A Critical Evaluation of Indentation Techniques for Measuring Fracture Toughness: I, Direct Crack Measurements.* Journal of the American Ceramic Society, 1981. **64**(9): p. 533-538.
14. Niihara, K., R. Morena, and D.P.H. Hasselman, *Evaluation of K_{Ic} of brittle solids by the indentation method with low crack-to-indent ratios.* Journal of Materials Science Letters, 1982. **1**(1): p. 13-16.
15. Laugier, M.T., *The elastic/plastic indentation of ceramics.* Journal of Materials Science Letters, 1985. **4**(12): p. 1539-1541.
16. Shetty, D.K., et al., *Indentation fracture of WC-Co cermets.* Journal of Materials Science, 1985. **20**(5): p. 1873-1882.

17. Lee, J.H., et al., *Cohesive interface simulations of indentation cracking as a fracture toughness measurement method for brittle materials.* Acta Materialia, 2012. **60**(15): p. 5448-5467.
18. Muchtar, A., L.C. Lim, and K.H. Lee, *Finite element analysis of vickers indentation cracking processes in brittle solids using elements exhibiting cohesive post-failure behaviour.* Journal of Materials Science, 2003. **38**(2): p. 235-243.
19. Zhang, W. and G. Subhash, *An elastic-plastic-cracking model for finite element analysis of indentation cracking in brittle materials.* International Journal of Solids and Structures, 2001. **38**(34-35): p. 5893-5913.
20. Johanns, K.E., et al., *An evaluation of the advantages and limitations in simulating indentation cracking with cohesive zone finite elements.* Modelling and Simulation in Materials Science and Engineering, 2014. **22**(1): p. 015011.
21. Simulia, *ABAQUS User's Manual*. 2008: Simulia Co.
22. Tabor, D., *The Hardness of metals*. 1951, Oxford: Clarendon Pr.
23. Lawn, B.R., *Indentation of Ceramics with Spheres: A Century after Hertz.* Journal of the American Ceramic Society, 1998. **81**(8): p. 1977-1994.
24. Marshall, D.B. and B.R. Lawn, *Residual stress effects in sharp contact cracking.* Journal of Materials Science, 1979. **14**(8): p. 2001-2012.
25. Feng, G., et al., *An analytical expression for the stress field around an elastoplastic indentation/contact.* Acta Materialia, 2007. **55**(9): p. 2929-2938.
26. Feng, G., et al., *A quantitative analysis for the stress field around an elastoplastic indentation/contact.* Journal of Materials Research, 2009. **24**(03): p. 704-718.
27. Jang, J.-i. and G.M. Pharr, *Influence of indenter angle on cracking in Si and Ge during nanoindentation.* Acta Materialia, 2008. **56**(16): p. 4458-4469.
28. Harding, D.S., *Craking in Brittle Materials During Low-Load Indentation and its Relation to Fracture Toughness.* PhD Thesis, Rice University, 1995.
29. Palmqvist, S., Jernkontorets Ann., 1957. **141**: p. 300-307.
30. Perrott, C.M., *On the indentation fracture of cemented carbide II -- the nature of surface fracture toughness.* Wear, 1978. **47**(1): p. 81-91.
31. Lankford, J., *Indentation microfracture in the Palmqvist crack regime: implications for fracture toughness evaluation by the indentation method.* Journal of Materials Science Letters, 1982. **1**(11): p. 493-495.
32. Laugier, M.T., *Palmqvist Crack Extension and the Center-Loaded Penny Crack Analogy.* Journal of the American Ceramic Society, 1985. **68**(2): p. C-51-C-52.
33. Arora, A., et al., *Indentation deformation/fracture of normal and anomalous glasses.* Journal of Non-Crystalline Solids, 1979. **31**(3): p. 415-428.
34. Johnson, K.L., *The correlation of indentation experiments.* Journal of the Mechanics and Physics of Solids, 1970. **18**(2): p. 115-126.

35. Hirst, W. and M.G.J.W. Howse, *The Indentation of Materials by Wedges.* Proceedings of the Royal Society of London. A. Mathematical and Physical Sciences, 1969. **311**(1506): p. 429-444.
36. Pharr, G.M., *Measurement of mechanical properties by ultra-low load indentation.* Materials Science and Engineering A, 1998. **253**(1-2): p. 151-159.

APPENDIX 4.1.

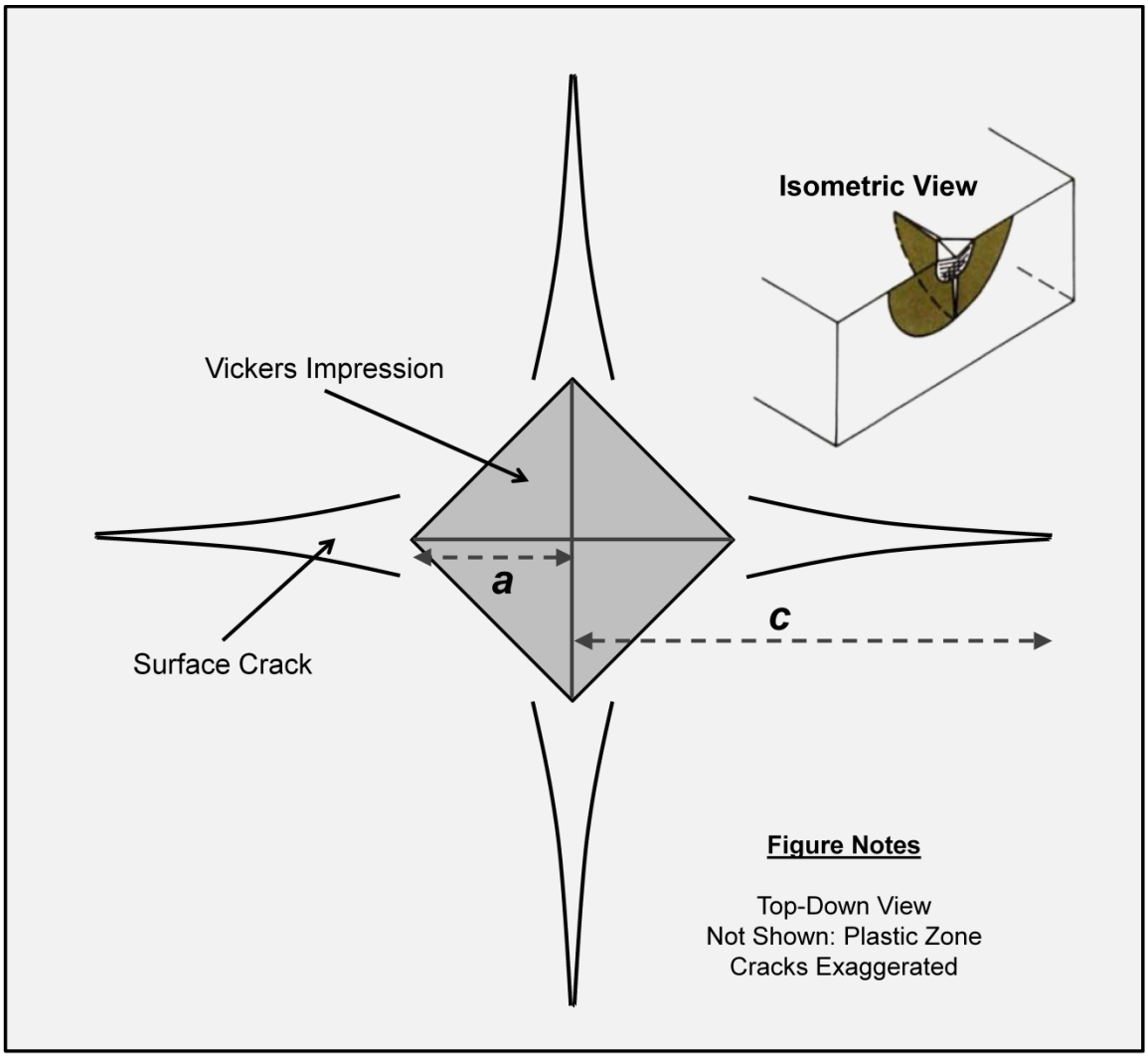


Figure 4.1. Top-down schematic of the Vickers indentation geometry.

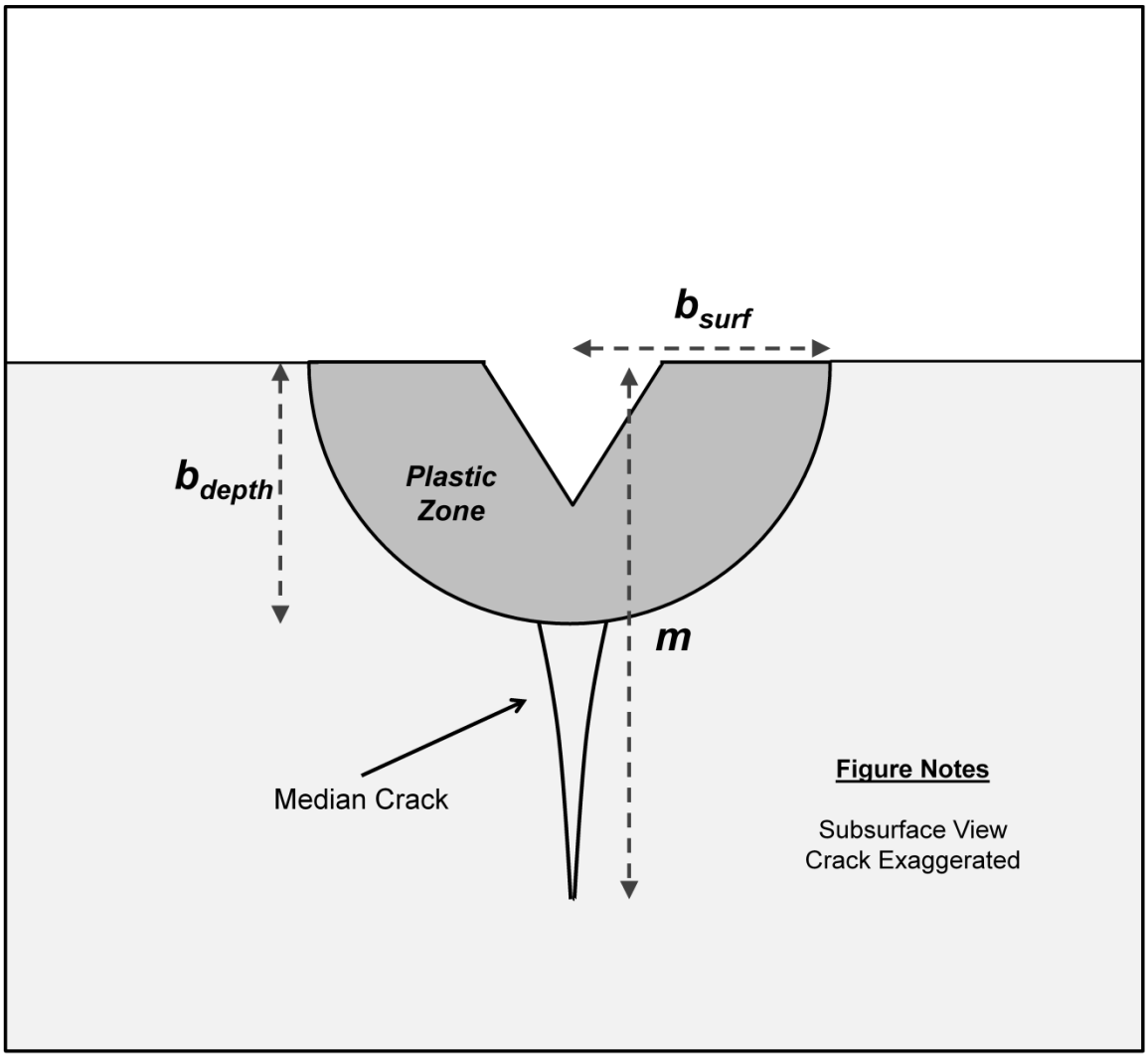


Figure 4.2. Subsurface view of the Vickers indentation cracking geometry.

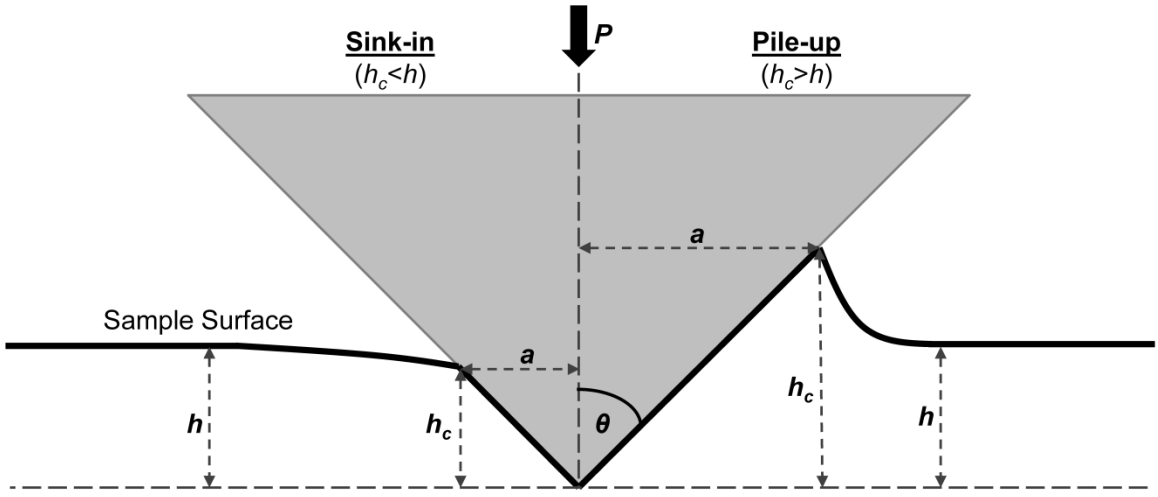


Figure 4.3. Sink-in/pile-up surface deformation geometries.

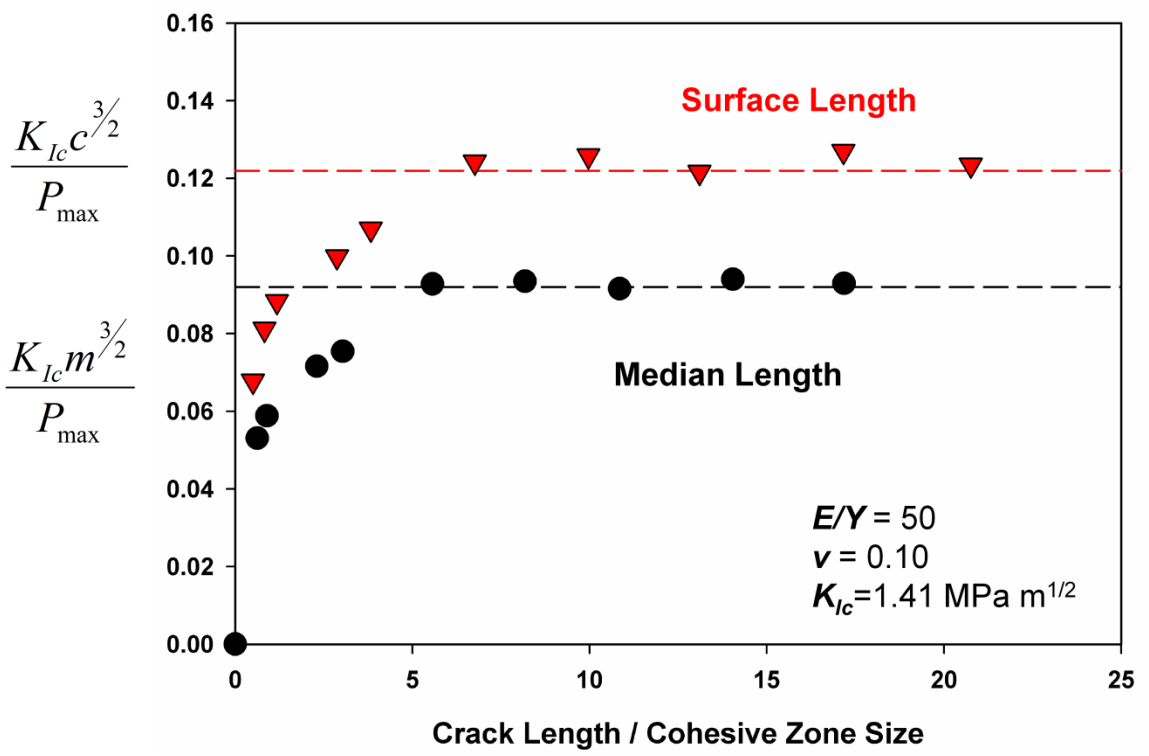


Figure 4.4. Finite element results of Vickers indentation crack lengths showing the effects of the process zone size on crack growth.

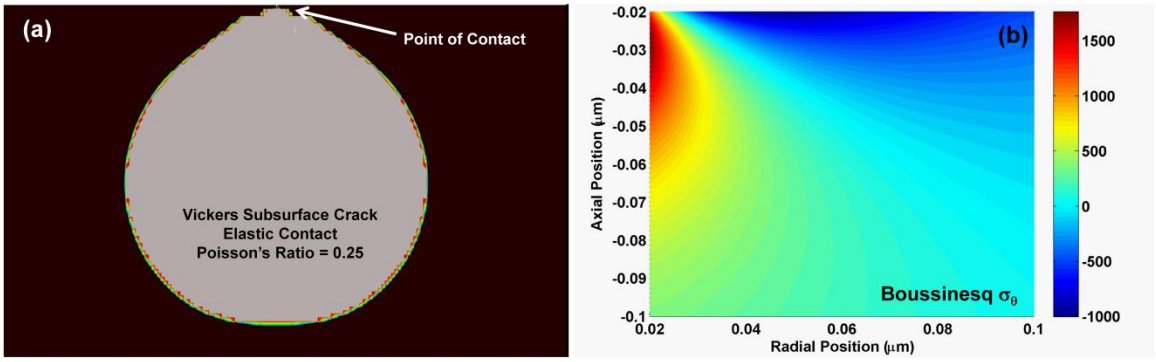


Figure 4.5. Elastic contact: (a) Vickers indentation median crack after complete unloading; and (b) contours of crack opening stresses in a Boussinesq contact.

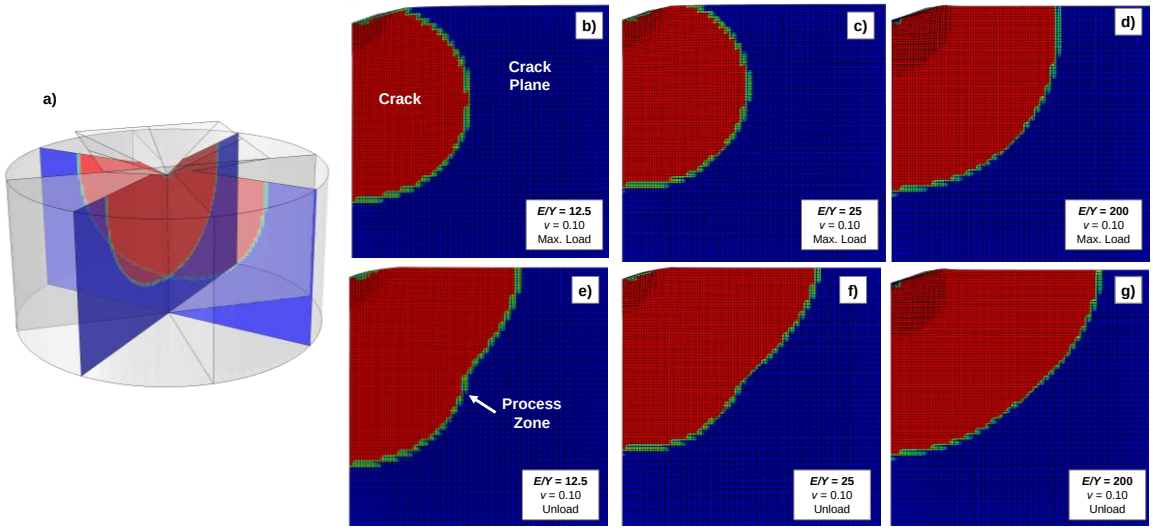


Figure 4.6. Example finite element mesh (a) and Vickers indentation crack geometries for *E/Y* ratios of 12.5, 25, and 200: at maximum load (b, c, and d); and complete unload (e, f, and g).

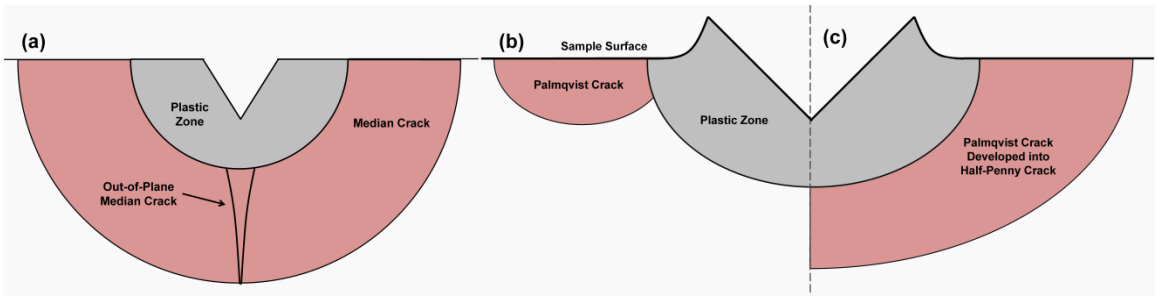


Figure 4.7. Idealized Vickers indentation crack geometries resulting from the finite element simulations: (a) median cracking; (b) Palmqvist cracking at small loads; and (c) Palmqvist cracking at larger loads.

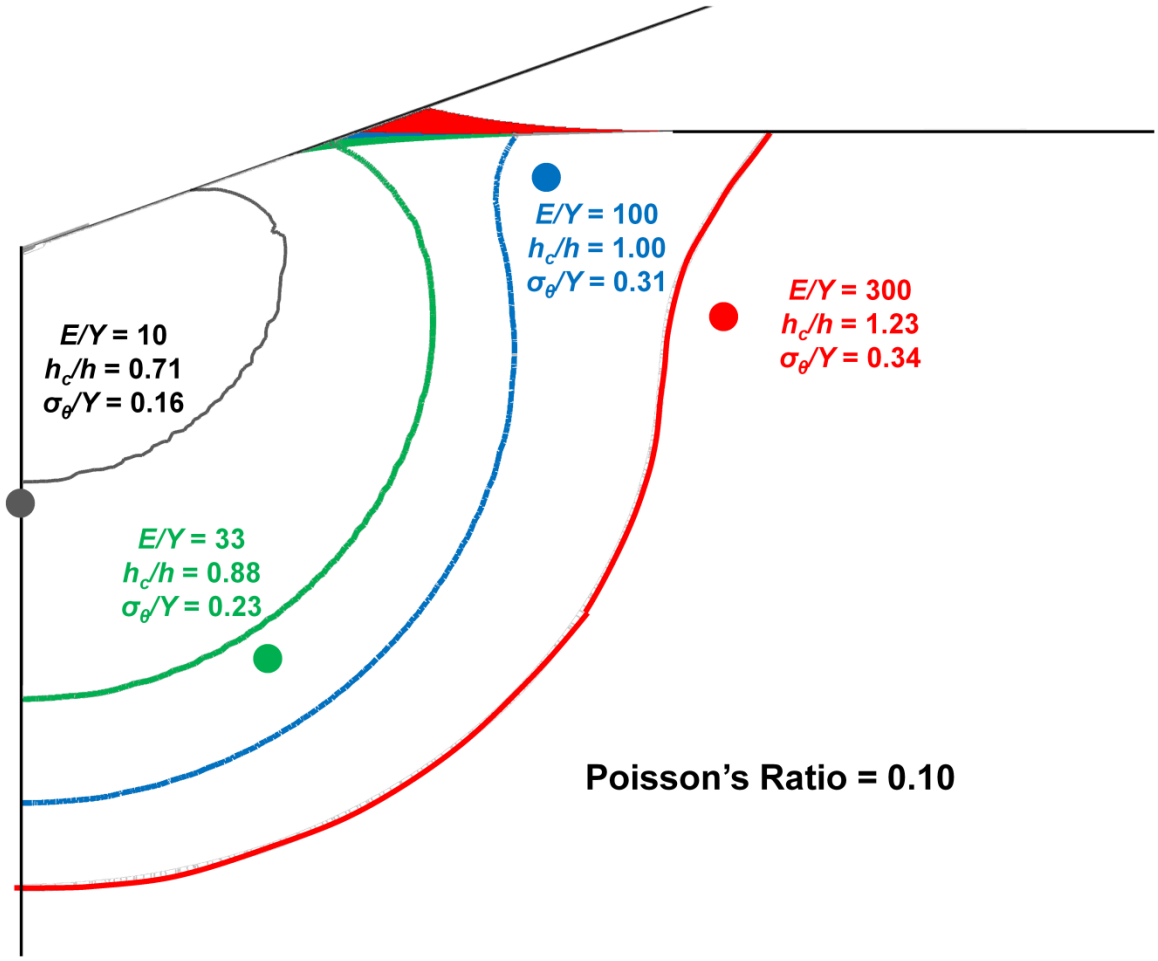


Figure 4.8. Plastic zone contours for various values of *E/Y* and corresponding points of crack initiation.

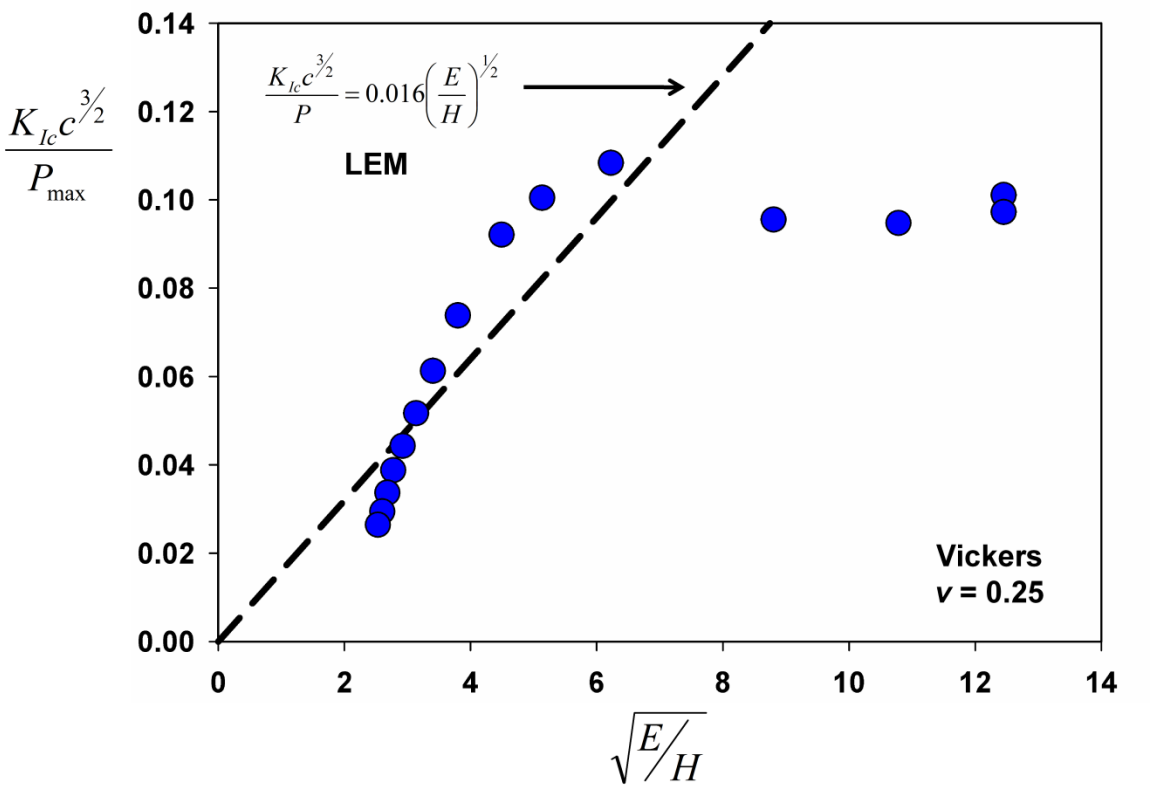


Figure 4.9. Vickers indentation cracking simulation results plotted against the LEM prediction.

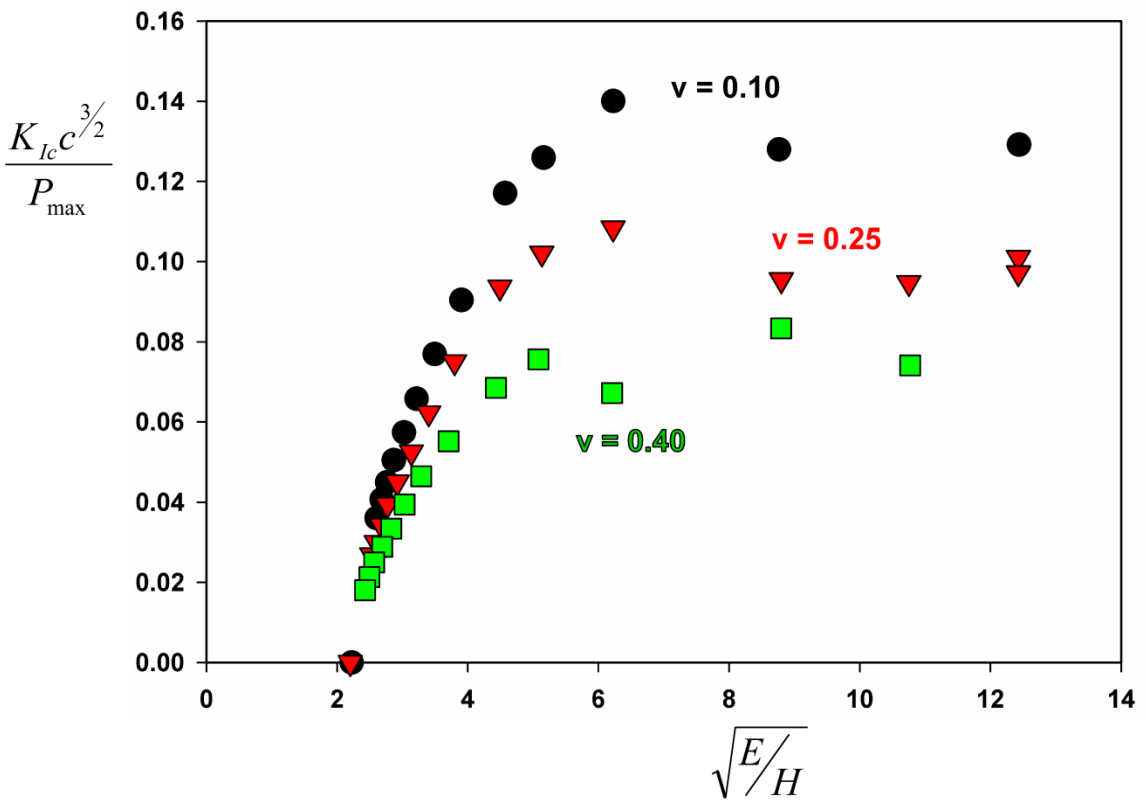


Figure 4.10. Simulation results from Vickers indentation as a function of Poisson's ratio.

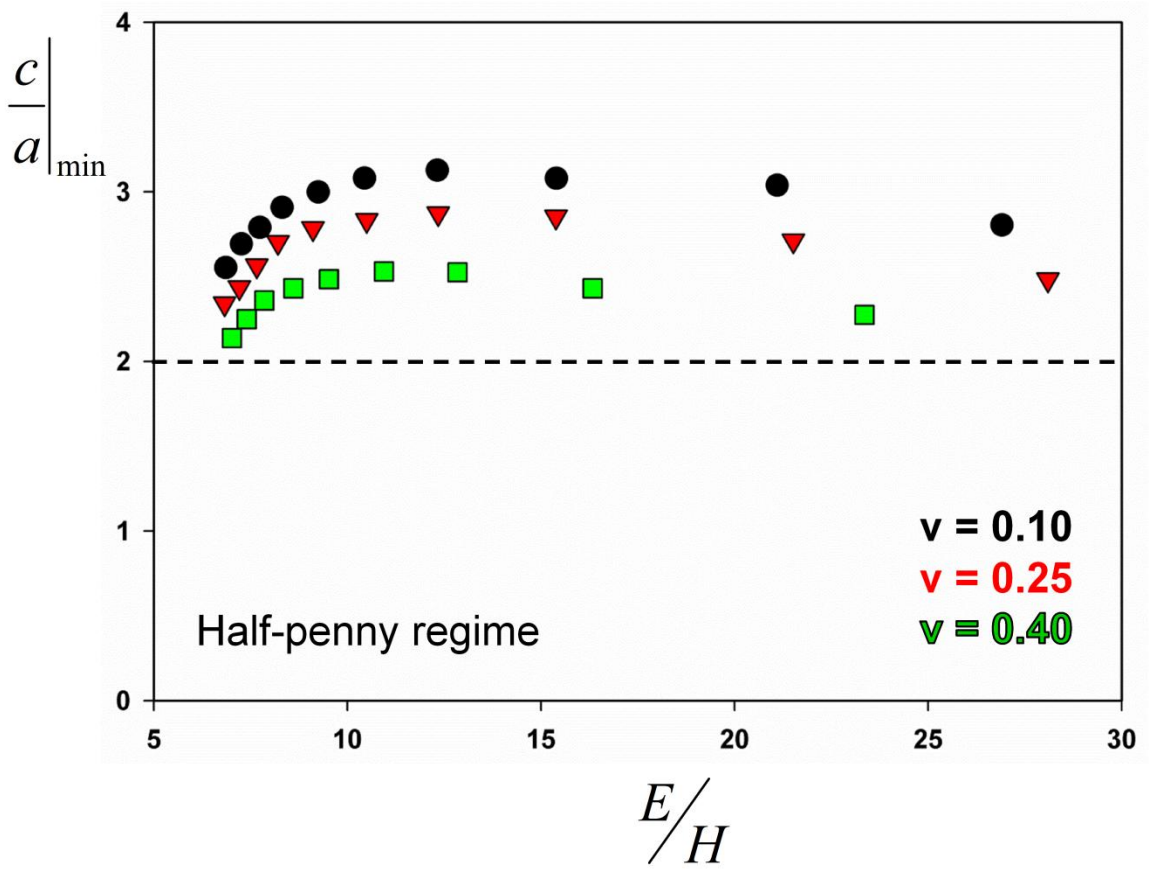


Figure 4.11. Minimum values of the ratio of crack length to contact size in the median cracking regime. The minimum ratio is limited by influences of the process zone.

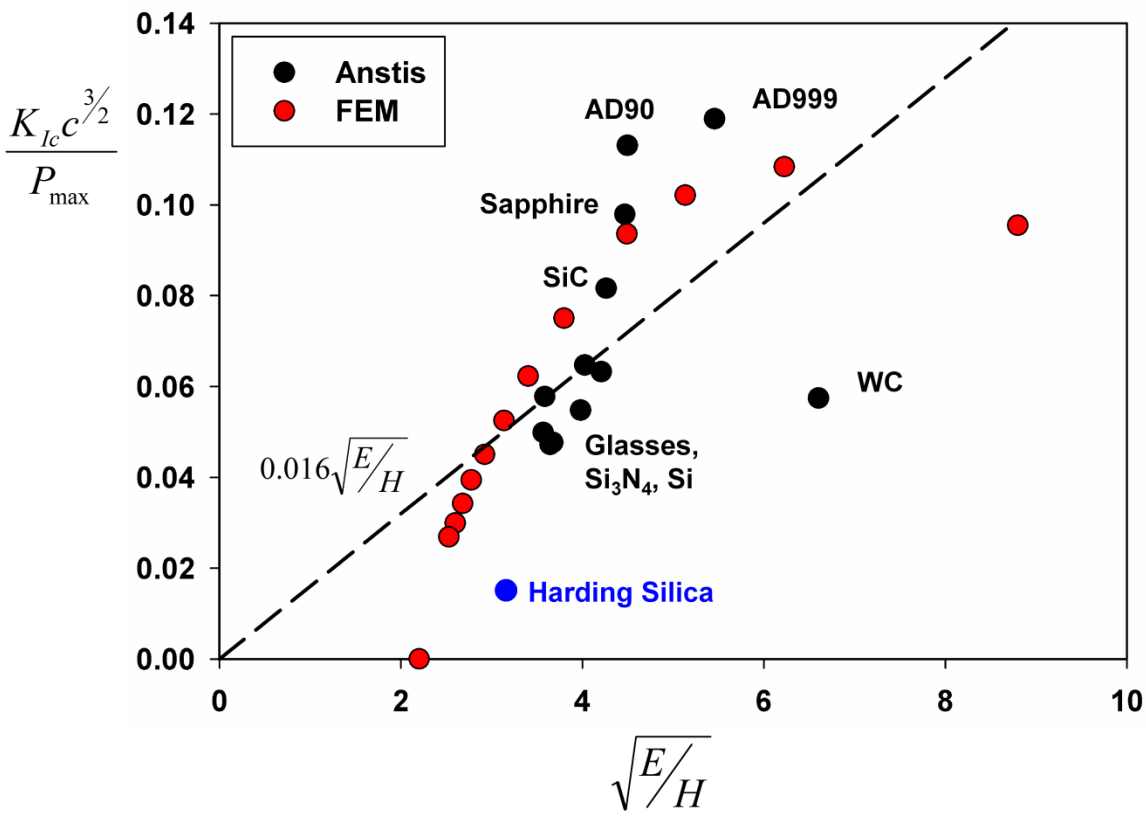


Figure 4.12. Finite element results plotted against the LEM model and individual experimental results.

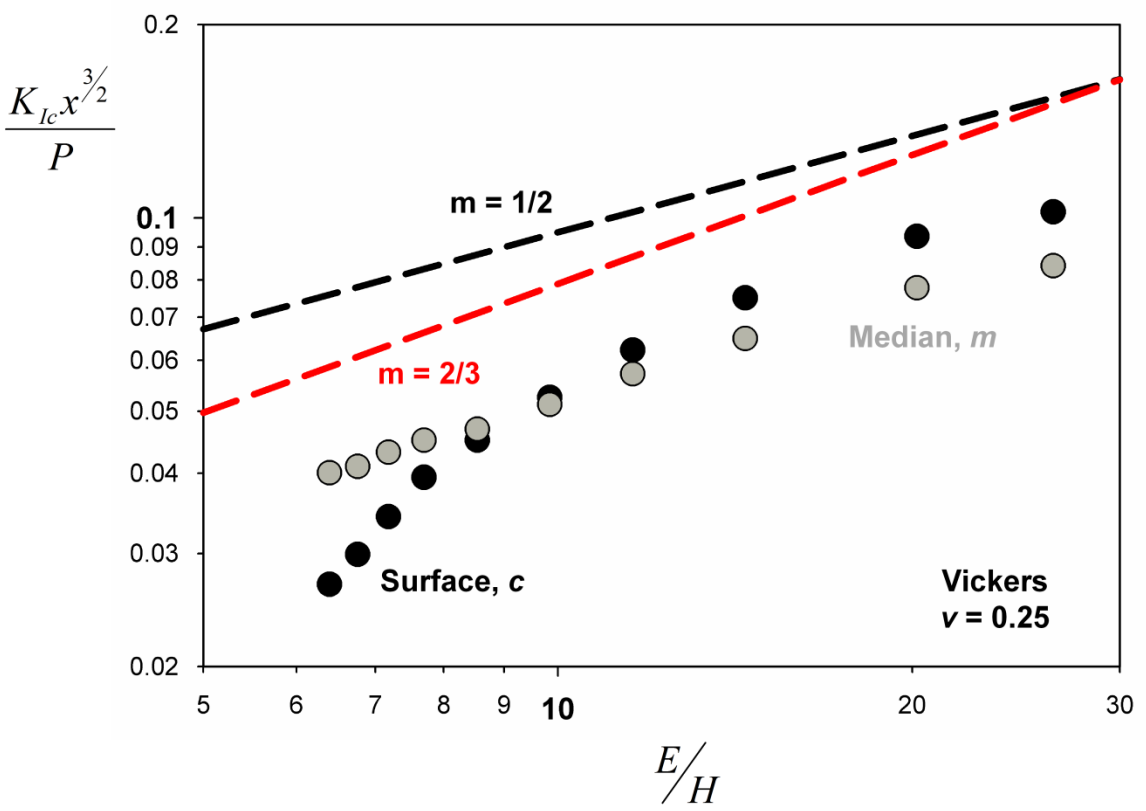


Figure 4.13. Scaling behavior of surface and subsurface crack lengths as a function of *E/H*.

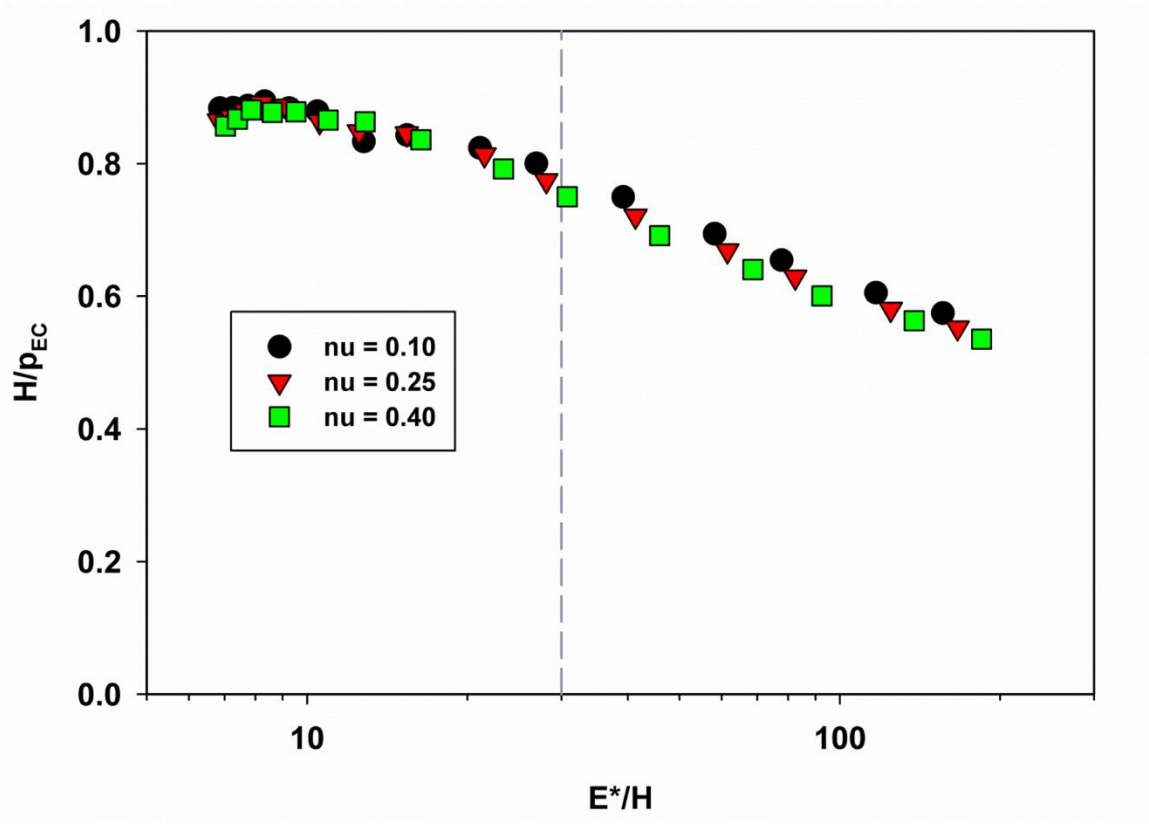


Figure 4.14. The ratio of indentation hardness to Hill's expanding cavity pressure as a function of material properties.

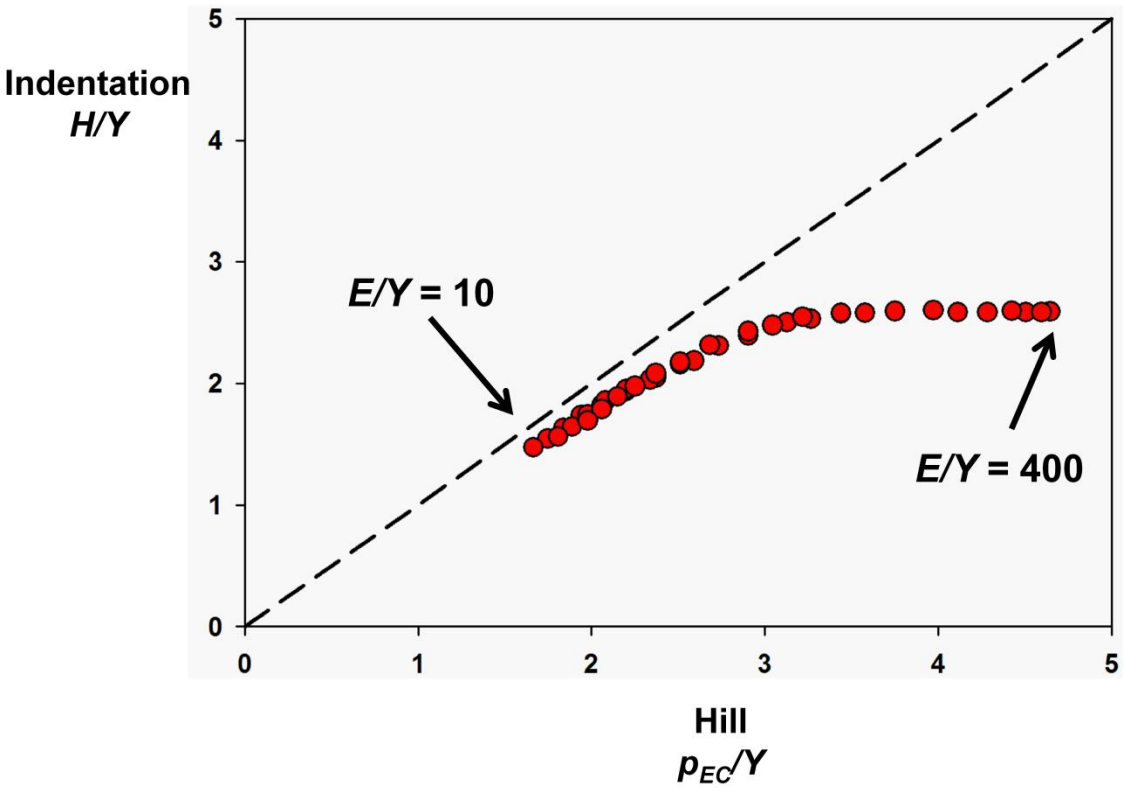


Figure 4.15. Indentation constraint factor plotted against the predicted value from Hill's expanding cavity model.

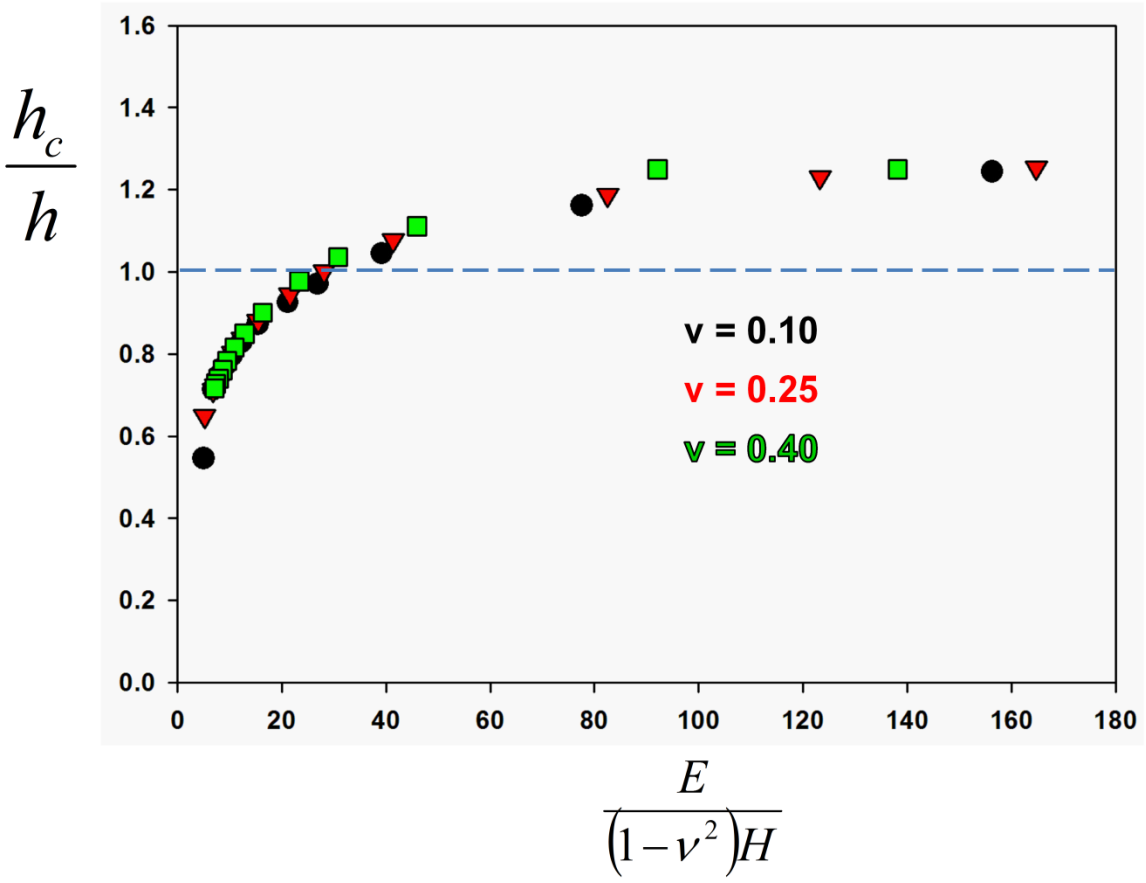


Figure 4.16. Surface deformation behavior as function of material properties showing a transition from sink-in to pile-up at an *E/H* of ~30.

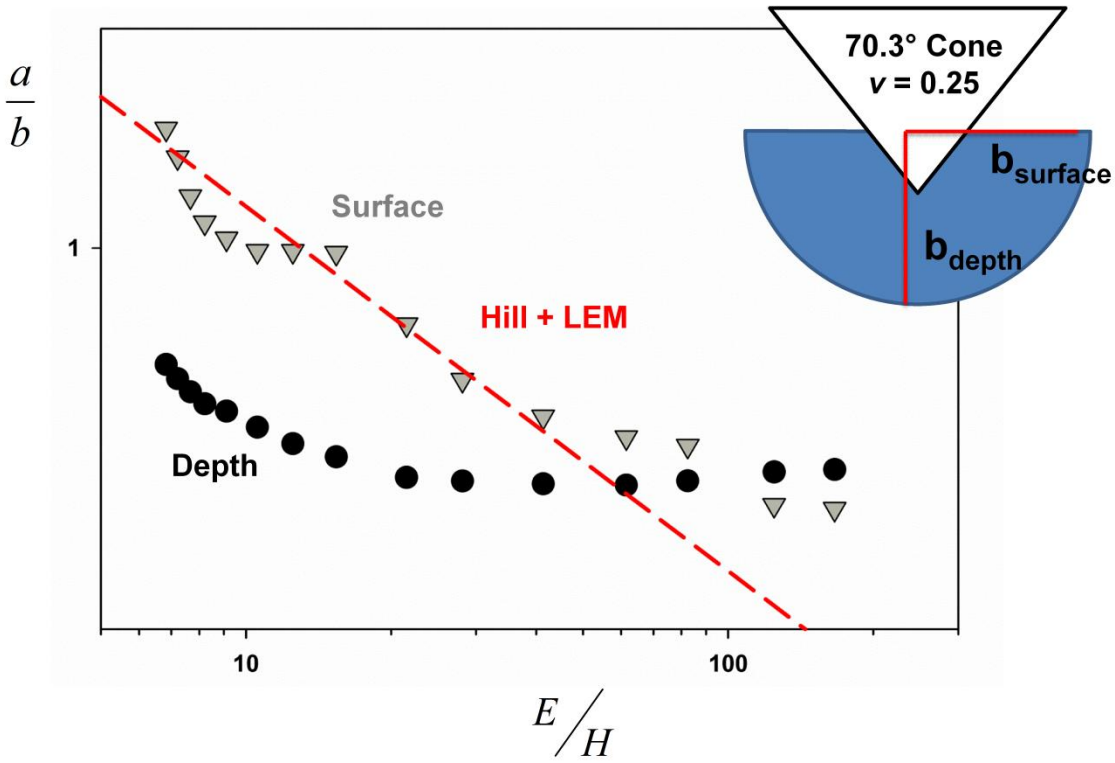


Figure 4.17. Finite element plastic zone geometries compared to the LEM prediction.

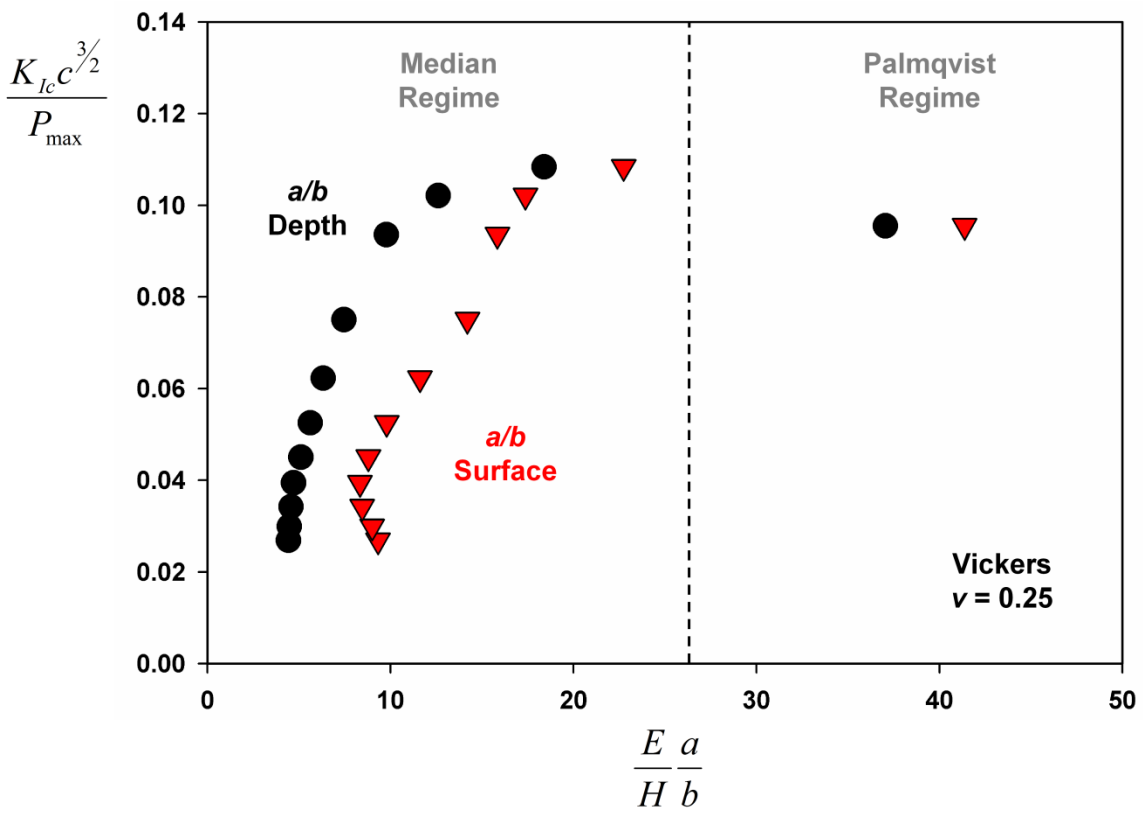


Figure 4.18. Comparison between finite element results and the LEM model without the use of Hill's expanding cavity model.

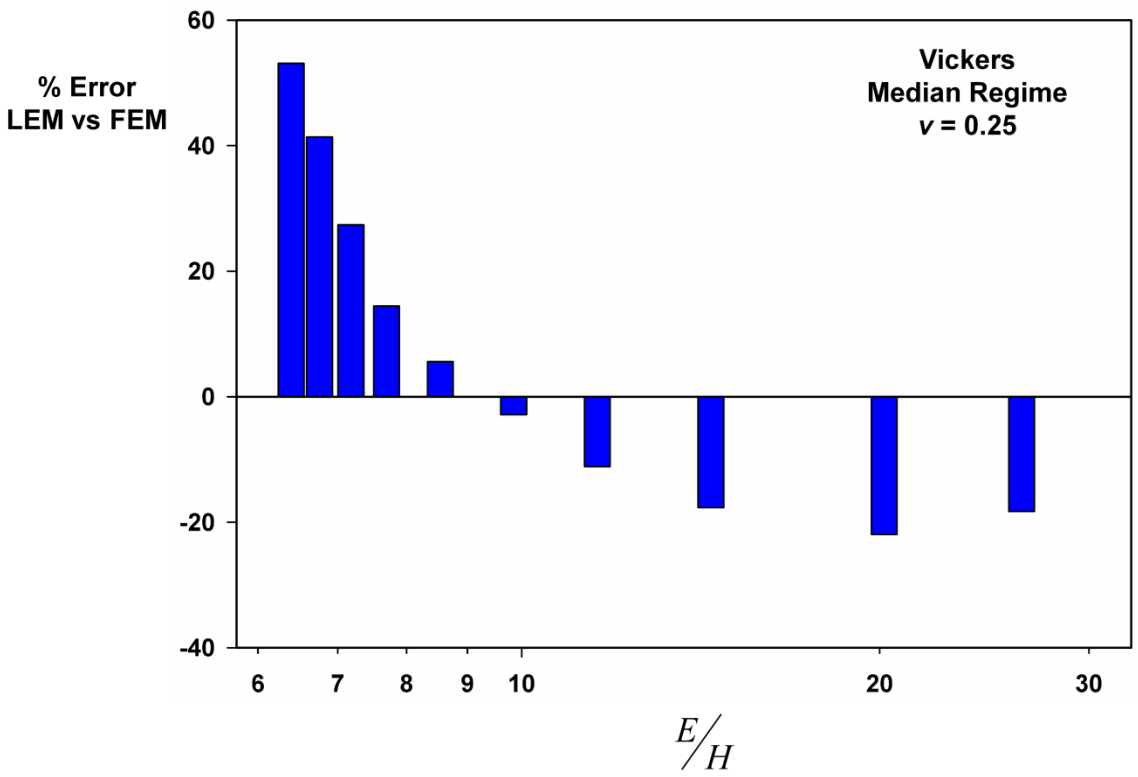


Figure 4.19. Errors in predicted fracture toughness between the LEM model and finite element results.

CHAPTER V

A MODEL FOR THE STRESS INTENSITY FACTOR OF AN INDENTATION CRACK IN THE MEDIAN CRACKING REGIME

Abstract

Observations and numerical data from cohesive zone finite element simulations of Vickers indentation cracking were used to relate material properties, applied loads, and crack lengths to simple stress intensity factor solutions. It was found that a stress intensity factor solution of the expansion of a rigid inclusion, similar to the two-dimensional wedge result found in Chapter III, was able to describe fracture toughness measurements in the *median* cracking regime. However, contrary to the two-dimensional wedge solution, the presence of the free surface needed to be accounted for through material pile-up/sink-in at the contact periphery. Small changes in the ratio of elastic modulus to hardness resulted in significant changes in deformation behavior in the *median* cracking regime giving rise to material behavior not considered in the Lawn, Evans, and Marshall indentation cracking model. While the derived stress intensity factor was accurate in the *median* cracking regime, significant error in fracture toughness was found when the solution was applied to the *Palmqvist* regime.

5.1. Introduction

Estimating fracture toughness with Vickers indentation tests in brittle materials is complicated by the three-dimensional geometry of both the indenter and crack, the lack of a general cracking behavior general to all materials, and the plasticity inherent to indentation. These complications result in a relationship between applied load, crack length, and fracture toughness that is a function of the *elastic-plastic* properties of the material. This is in direct contradiction to standard linear-elastic fracture toughness geometries, where the only constitutive parameter required might be the elastic modulus [1, 2]. Thus, attempts at developing an indentation fracture toughness solution often begin with assumptions of how materials accommodate the deformation that gives rise to crack driving forces. Most notably, Lawn, Evans, and Marshall [3] made use of Hill's expanding cavity model [4] to include the elastic modulus and hardness in indentation fracture toughness estimations. In addition to material behavior, other models have attempted to take into account the difference between the half-penny and Palmqvist crack geometries observed in different materials [5-8]. Ponton and Rawlings have provided a detailed analysis of the more prominent models that have been developed noting that many rely on empirical observations [9, 10].

Cohesive finite element simulations of Vickers indentation cracking, described in previous chapters of this dissertation, have shown that indentation cracking behavior depends on the ratio of the elastic modulus to hardness in a way that is different from the Lawn, Evans, and Marshall prediction as well as other model predictions. In addition, such simulations have shown a Poisson's ratio dependence that has not been previously considered [11]. At low values of the ratio of elastic modulus to hardness, *E/H*, both elasticity and plasticity influence the crack driving force. The result is subsurface median crack growth on loading followed by development into a half-penny geometry on unloading that is visible at the surface. At values of *E/H* greater than ~30 for the Vickers indenter, the cracking behavior transitions to a regime where plasticity dominates

and cracks take on a Palmqvist geometry characterized by crack growth at the surface during loading and unloading. These Palmqvist cracks sometimes propagate further below the surface to form a half-penny geometry with increased loading. This transition in cracking behavior corresponds to the point at which pile-up of material around the indenter begins, i.e., the plastic zone breaches the surface during loading. The deviation from the LEM model is likely, in part, due to the surface morphology outside of the contact. Some of the driving force for crack growth is lost as plastic material flows up the face of the indenter instead of pushing against the elastic region.

The purpose of this chapter is to use observations from the cohesive finite element simulations in combination with known stress intensity factor solutions to develop a relationship between material properties, applied loads, surface crack lengths, and fracture toughness for indentation cracking in the median cracking regime (E/H < ~30) that accounts for many of these observations. A separate model describing the fracture mechanics in the Palmqvist regime will be presented in the next chapter. The development begins with the solution for a two-dimensional (2D) wedge indentation crack from Chapter III and the observation that crack opening displacements at the elastic-plastic boundary play a critical role in crack growth. The model provided herein relates surface crack lengths, applied loads, and material properties after complete unload of the indenter given that cracks are not visible at the surface of opaque materials until completely unloading the indenter.

5.2. Stress Intensity Factor for an Indentation Crack in the Median Regime

The model for the relationship between applied loads, surface crack lengths, and material properties in the case of the two-dimensional (2D) plane-strain wedge indenter was developed based on the observation that the crack opening displacement at the crack mouth, induced by plastic deformation, is the driving force for crack growth. The plastic zone was modeled as a rigid wedge opening a 2D through-crack which expanded in width with increasing load in a

geometrically self-similar manner. The solution was applicable over a wide range of *E/H* in the 2D case because deformation at the crack mouth occurred below the plastic zone and on the indentation axis. Deformation at this subsurface location was limited to one direction (the mode I opening direction) due to plane-strain conditions. Sink-in or pile-up of material at the contact periphery did not influence crack growth, and the free surface only changed the scaling coefficients of the original stress intensity factor solution. The three-dimensional (3D) geometry of the Vickers indentation crack and the fact that cracks exist at the surface outside of the contact necessitates that the free-surface be accounted for in the crack mouth opening displacement model.

Cracks resulting from Vickers indentation in brittle materials are inherently three-dimensional in that the location of the crack front varies with depth. However, from an experimental viewpoint of measuring fracture toughness, we are interested in the stress intensity factor of the crack tip at the surface after complete unload. Thus crack mouth opening displacements and crack lengths are defined at the surface of the residual indentation.

A mode-I stress intensity factor, K_I, solution similar to the 2D rigid wedge becomes the starting point for the 3D Vickers indentation crack in the median crack regime (*E/H* < ~30). Figure 5.1 shows the reference geometries for the derivation. Selvadurai and Singh [12] provide the solution to a penny-shaped crack expanded by a rigid circular disc inclusion under plane strain conditions (Fig. 5.1a):

$$K_I = \frac{E_R \delta_m}{\pi\sqrt{c}}\left[\frac{R}{c} + \frac{1}{\pi}\left(\frac{R}{c}\right)^2 + \left(\frac{1}{\pi^2}+\frac{3}{8}\right)\left(\frac{R}{c}\right)^3 + \left(\frac{2}{3\pi}+\frac{1}{\pi^3}\right)\left(\frac{R}{c}\right)^4 + \left(\frac{23}{24\pi^2}+\frac{15}{64}+\frac{1}{\pi^4}\right)\left(\frac{R}{c}\right)^5 + O\left(\frac{R}{c}\right)^6\right]. \tag{5.1}$$

Here, E_R, is the reduced elastic modulus defined as $E_R=E/(1-\nu^2)$, where E is the elastic modulus and ν is Poisson's ratio. The crack length, c, disk thickness, δ_m, and disk radius R are shown in Fig. 5.1a. Taking only the first

term in their solution in the limit that second order and higher terms are negligible when the crack length is long in comparison to the disk radius yields:

$$K_I = \frac{E_R \delta_m R}{\pi c^{3/2}}. \tag{5.2}$$

As mentioned above, the concept of geometric self-similarity, which results in a constant hardness, was used to convert length scales to applied load and hardness in the case of the 2D wedge indenter. While the same idea can be used in the 3D case, the scaling must alter with changes in the ratio of elastic modulus to hardness (*E/H*) because the surface geometry at the crack mouth is dependent on *E/H* (see Chapter IV, Fig. 4.8). We first assume that the radius of the rigid disk scales with the size of the contact diagonal, *a*, which scales with the maximum load, P_{max}, and hardness, *H*, as:

$$R = a = \sqrt{\frac{P_{max}}{2H}}. \tag{5.3}$$

Substituting Eq. 5.3 into Eq. 5.2 yields:

$$K_I = \frac{E_R \delta_m}{\pi\sqrt{2H}} \frac{\sqrt{P_{max}}}{c^{3/2}}. \tag{5.4}$$

Under the condition of equilibrium crack growth, the stress intensity factor at the tip of the indentation crack at the surface is equal to the fracture toughness, K_{Ic}, of the material. We assume here that the maximum crack opening displacement at the surface, δ_m, is representative of the thickness of the rigid disk (see Fig. 5.1b). The maximum crack opening displacement consistently occurs at the free surface near the elastic-plastic boundary over the range of materials examined in the finite element simulations described in previous sections of this dissertation (See Fig. 5.2). In addition, for a given material, the ratio of $K_{Ic}c^{3/2}/P_{max}$ is a constant in the median cracking regime (See Chapter IV). Rearranging Eq. 5.4 to reflect that result yields a non-dimensional relationship:

$$\frac{K_{Ic}c^{3/2}}{P_{max}} = \frac{E_R\delta_m}{\pi\sqrt{2P_{max}H}}. \quad (5.5)$$

Equation 5.5 is an interesting result as it can be directly evaluated from the cohesive finite element simulations. Based on cohesive zone finite element simulations described in Chapter IV where values of $K_{Ic}c^{3/2}/P_{max}$ have been evaluated by changing the ratio of *E/Y*, Poisson's ratio, and fracture toughness, the left hand side of Eq. 5.5 is plotted against that on the right hand side in Fig. 5.3. Each data point in Fig. 5.3 represents the average value of $K_{Ic}c^{3/2}/P_{max}$ measured from the simulations for a specific value of *E/H* and Poisson's ratio. The linear relationship suggests that both the chosen stress intensity factor solution and the assumptions made leading to Eq. 5.5 are reasonably representative of the indentation cracking geometry. However, the Poisson's ratio dependence in the finite element simulations is not consistent with the predicted behavior from Selvadurai and Singh's solution. Additionally, eliminating the Poisson's ratio dependence in the reduced modulus in Eq. 5.5 does not result in convergence of the three curves shown in Fig. 5.3. The author's cannot directly explain this discrepancy, but offer some points as to where differences may arise:

1. The free surface, not present in Selvadurai and Singh's solution, possibly induces plane-stress conditions.
2. Plastic deformation, and thus the size of the contact, is dependent on Poisson's ratio.
3. Elastic stresses due to contact have a strong Poisson's ratio dependence, e.g., Feng and Nix.
4. Unloading of the indenter and subsequent crack growth is accompanied by elastic recovery that is clearly dependent on Poisson's ratio.

A complete solution to the indentation cracking problem would include resolving the Poisson's ratio dependencies. However, we choose to move forward here ignoring Poisson's ratio in the derivation. Note here, the Poisson

dependencies in 2D plane-strain rigid wedge finite element results matched the stress intensity factor solution while points 1 and 3 above are not factors in the 2D wedge indentation crack geometry.

In theory, crack-opening displacements could be experimentally measured from Vickers indentation crack tests. However, such a measurement, in practice, is difficult and would require careful sample preparation and high-powered microscopy such as a scanning electron microscope. This becomes more improbable noting that most ceramics tend to charge at cracks which would likely result in significant error. It is then appropriate to determine the scaling relationship between the crack mouth opening displacement, applied loads, and materials properties.

In the absence of a free surface, the crack mouth opening displacement, δ_m, would scale with the applied load and hardness in a similar manner to the radius of the rigid disk and $K_{Ic}c^{3/2}/P_{max}$ would scale linearly with E/H. However, the finite element results exhibit a non-linear trend that suggests a slow decay in crack driving forces as E/H increases. After examination of many 2D and 3D indentation cracking simulations, we hypothesize that this decay is due to an increase of material pile-up at the contact periphery as E/H increases, i.e., plastic deformation at the crack mouth is distributed between opening the crack and pile-up of material. Sink-in and pile-up indentation geometries are shown in Fig. 5.4. Material flow takes the path of least resistance, which in the case that material can freely flow to the surface and pile up, is likely to reduce the tendency to open the mouth of the crack. Additional evidence that suggests material pile-up at the contact periphery plays an important role in indentation cracking is that the behavior changes from median cracking to Palmqvist cracking when the plastic zone breaches the surface (i.e., pile-up begins) at a value of E/H of ~30 for the Vickers indenter.

We then propose that the dimensionless term on the right hand side of Eq. 5.5 is a function of the dimensionless ratio of contact depth, h_c, to total indenter displacement into the surface, h, evaluated at maximum load. This ratio, which is

a common measure of the degree of pile-up, can and will be directly measured from the finite element simulations as no analytical solution exists for this parameter. The pile-up parameter, h_c/h, measured from the FE simulations over the entire range of elastic modulus to yield strength, E/Y, including the Palmqvist cracking regime is shown in Fig. 5.5a as a function of E_R/H. Since we are interested in the median cracking regime, pile-up parameters for materials with E/H<30 is plotted in Fig. 5.5b on a semi-log scale to show that h_c/h has a logarithmic trend with E_R/H. Incidentally, Johnson's constraint factor also has a logarithmic trend in a similar range of E/H as being examined in this study [13, 14].

To examine the correlation of the pile-up/sink-in parameter, h_c/h, to indentation cracking behavior, the right hand side of Eq. 5.5, the driving force for cracking, is plotted as a function of h_c/h in Fig. 5.6a. The data in Fig. 5.6a is remarkably linear with h_c/h for all three values of Poisson's ratio. Given the good correlation between the driving force for crack growth in the stress intensity factor solution and h_c/h and the logarithmic behavior with E/H, the non-dimensional cracking parameter $K_{Ic}c^{3/2}/P_{max}$ is plotted as a function of $ln(E_R/H)$ in Fig. 5.6b. Again, good correlation is found between the two parameters shown in Fig. 5.6b with an obvious influence of Poisson's ratio. The "glue" connecting this relationship is physically found in the pile-up/sink-in parameter h_c/h. The resulting relationship can be described by:

$$\frac{K_{Ic}c^{3/2}}{P_{max}} = Aln\left(\frac{E_R}{H} - B\right). \tag{5.6}$$

Admittedly, Eq. 5.6 is not a rigorous analytical derivation and more empirical than not. However, the relationship was developed with significant insight from the finite elements and can be correlated to physical mechanisms like pile-up/sink-in and the idea of a rigid wedge stress intensity factor developed by Selvadurai and Singh [12]. The variable B stems from the fact that surface cracking does not exist in a purely elastic material where the value of E/H is finite based on the way we have defined hardness in this dissertation.

5.3. Estimation of Fracture Toughness

An important step in the process of determining a stress intensity factor solution is the evaluation of the model compared to previous estimations. Fits to constants *A* and *B* to the finite element data for different values of Poisson's ratio are given in Table 1. The value of *B* will be shown to have physical significance related to indenter geometry in a later section of this dissertation.

Lawn, Evans, and Marshall provided an indentation cracking toughness model, described in detail in previous sections of this dissertation, that relied heavily on Hill's expanding cavity model to estimate changes in indentation behavior changes in *E/H*. As we have shown a number of times, Hill's expanding cavity cannot account for free-surface deformation or the transition from sink-in to pile-up that occurs with increasing E/H. Our argument is not based on changes in plastic zone geometry, but rather the amount of plastic deformation at the free surface. Anstis et al. provide an experimentally calibrated form of the Lawn, Evans, and Marshall model for indentation fracture toughness:

$$\frac{K_{Ic}c^{3/2}}{P_{max}} = 0.016\left(\frac{E}{H}\right)^{1/2}. \tag{5.7}$$

Fracture toughness has been estimated from the finite element results using Eqs. 5.6 and 5.7 and percent errors in fracture toughness are plotted as a function of material # (each material has a different *E/H* as labeled in the plot) over both the median and Palmqvist cracking regimes in Fig. 5.7 for Poisson's ratio of 0.25. Two important conclusions can be drawn from Fig. 5.7. First, the physically backed logarithmic model (Eq. 5.6) does a better job at estimating fracture toughness as compared to the Lawn, Evans, and Marshall equation in the median cracking regime; and second, both do not work well after the transition from median cracking to Palmqvist cracking. This deviation is due to a change in both crack development/geometry and indentation behavior. Fracture mechanics in the Palmqvist indentation cracking regime will follow in Chapter VI.

5.4. Conclusions

A model for estimating fracture toughness from Vickers indentation cracking tests in the range of *E/H* from 5 to 30 has been developed. The model is physically based on a rigid-disk opening of a penny-shaped crack stress intensity factor solution developed by Selvadurai and Singh. The radius of the disk was found to scale with the size of the contact, while free surface effects and changes in the pile-up/sink-in ratio with *E/H* needed to be accounted for in determining the scaling of the thickness of the disk. Cohesive finite element results were used to determine the scaling coefficients and the resulting model for indentation fracture toughness was compared to the Lawn, Evans, and Marshall model.

References

1. Anderson, T.L., *Fracture Mechanics: Fundamentals and Applications*. 2005: Taylor & Francis.
2. Tada, H., P.C. Paris, and G.R. Irwin, *The stress analysis of cracks handbook*. 1973: Del Research Corp.
3. Lawn, B.R., A.G. Evans, and D.B. Marshall, *Elastic-Plastic Indentation Damage in Ceramics - the Median-Radial Crack System.* Journal of the American Ceramic Society, 1980. **63**(9-10): p. 574-581.
4. Hill, R., *The mathematical theory of plasticity*. 2004, Oxford: Clarendon Press.
5. Lankford, J., *Indentation microfracture in the Palmqvist crack regime: implications for fracture toughness evaluation by the indentation method.* Journal of Materials Science Letters, 1982. **1**(11): p. 493-495.
6. Niihara, K., *A fracture mechanics analysis of indentation-induced Palmqvist crack in ceramics.* Journal of Materials Science Letters, 1983. **2**(5): p. 221-223.
7. Laugier, M.T., *Palmqvist Crack Extension and the Center-Loaded Penny Crack Analogy.* Journal of the American Ceramic Society, 1985. **68**(2): p. C-51-C-52.
8. Shetty, D.K. and I.G. Wright, *On estimating fracture toughness of cemented carbides from Palmqvist crack sizes.* Journal of Materials Science Letters, 1986. **5**(3): p. 365-368.
9. Ponton, C.B. and R.D. Rawlings, *Vickers indentation fracture toughness test Part 1 Review of literature and formulation of standardised indentation toughness equations.* Materials Science and Technology, 1989. **5**: p. 865-872.
10. Ponton, C.B. and R.D. Rawlings, *Vickers indentation fracture toughness test Part 2 Application and critical evaluation of standardised indentation toughness equations.* Materials Science and Technology, 1989. **5**: p. 961-976.
11. Lee, J.H., et al., *Cohesive interface simulations of indentation cracking as a fracture toughness measurement method for brittle materials.* Acta Materialia, 2012. **60**(15): p. 5448-5467.
12. Selvadurai, A.P.S. and B.M. Singh, *On the expansion of a penny-shaped crack by a rigid circular disc inclusion.* International Journal of Fracture, 1984. **25**(1): p. 69-77.
13. Johnson, K.L., *The correlation of indentation experiments.* Journal of the Mechanics and Physics of Solids, 1970. **18**(2): p. 115-126.
14. Johnson, K.L., *Contact Mechanics*. 1987: Cambridge University Press.

APPENDIX 5.1.

Table 5.1. Finite element curve fits to coefficients *A* and *B* in Eq. 5.6 for a Vickers indenter.

Poisson's Ratio	Coefficient *A*	Coefficient *B*
0.10	0.0394	4.59
0.25	0.0314	4.70
0.40	0.0218	4.91

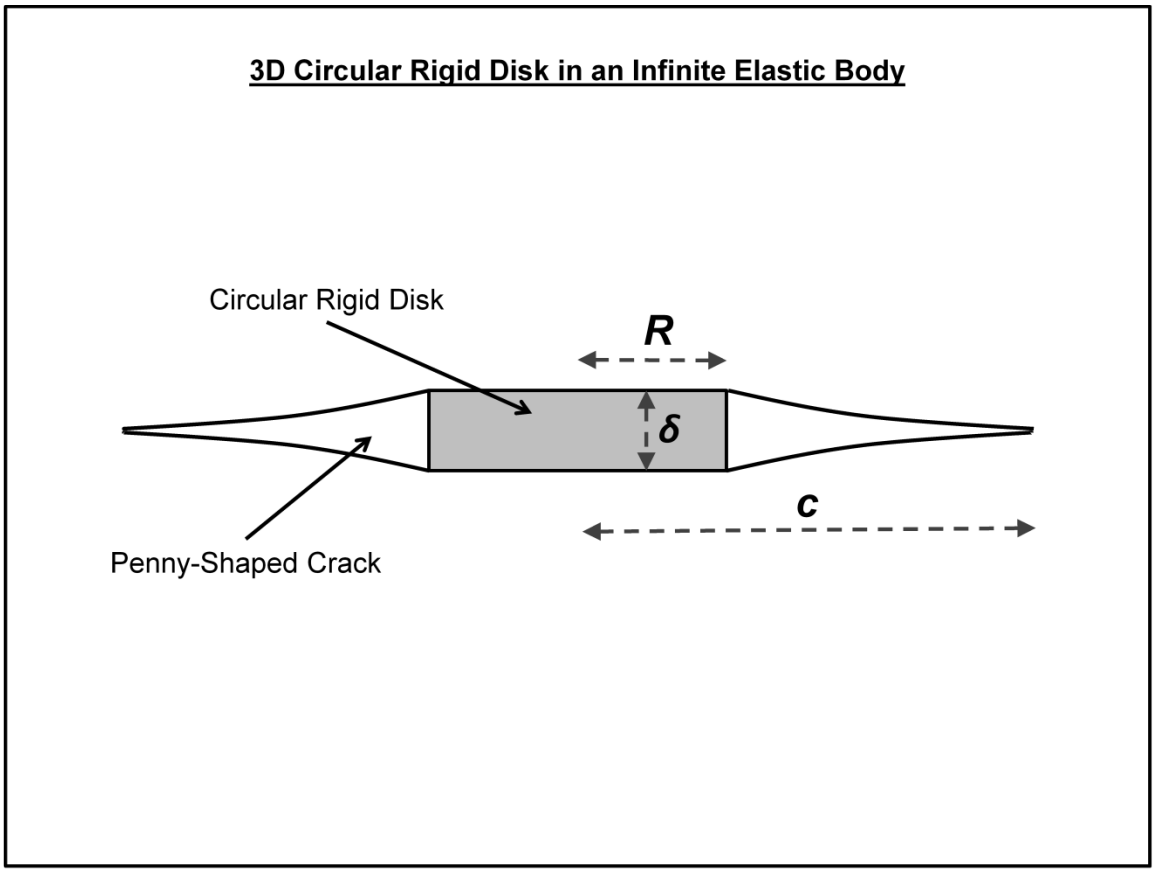


Figure 5.1a. Selvadurai and Singh's rigid disk stress intensity factor geometry used to represent indentation cracking in the median regime.

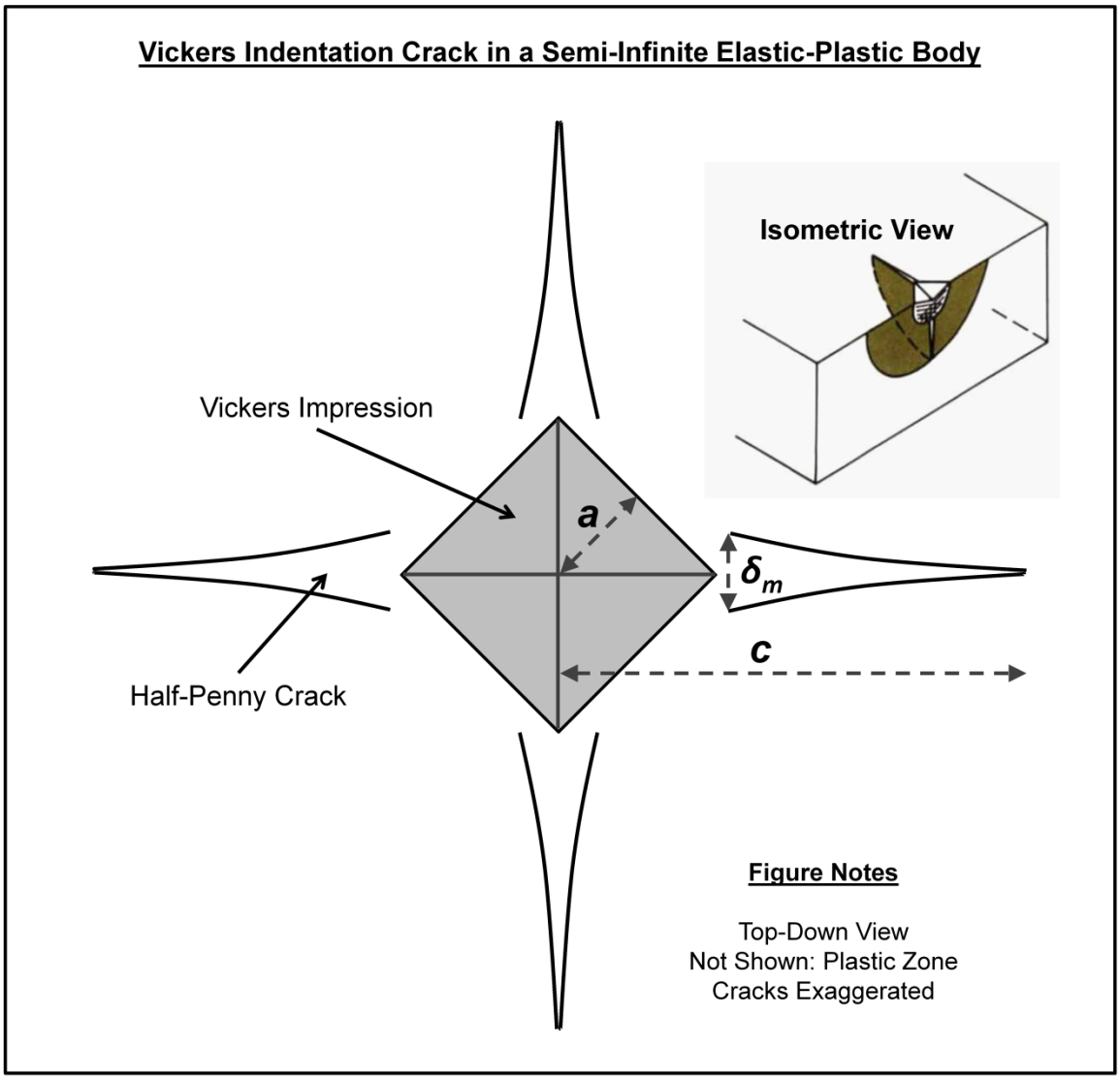


Figure 5.1b. Top-down view of the Vickers indentation crack geometry.

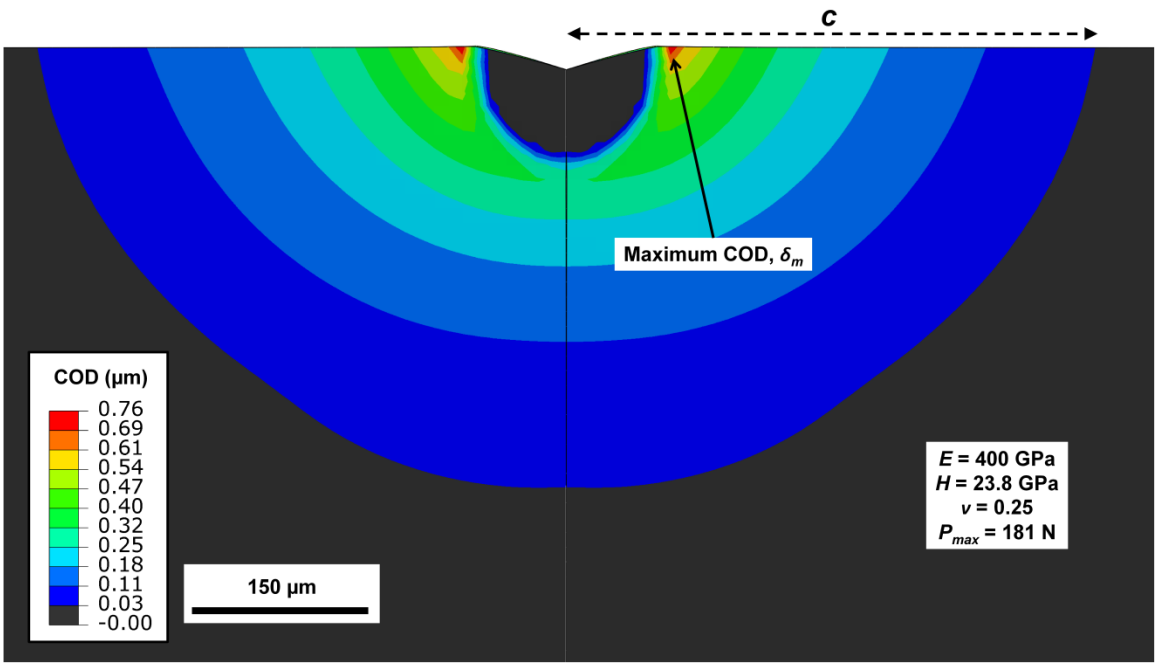


Figure 5.2. Simulation results of unloaded crack opening displacements of a Vickers median crack.

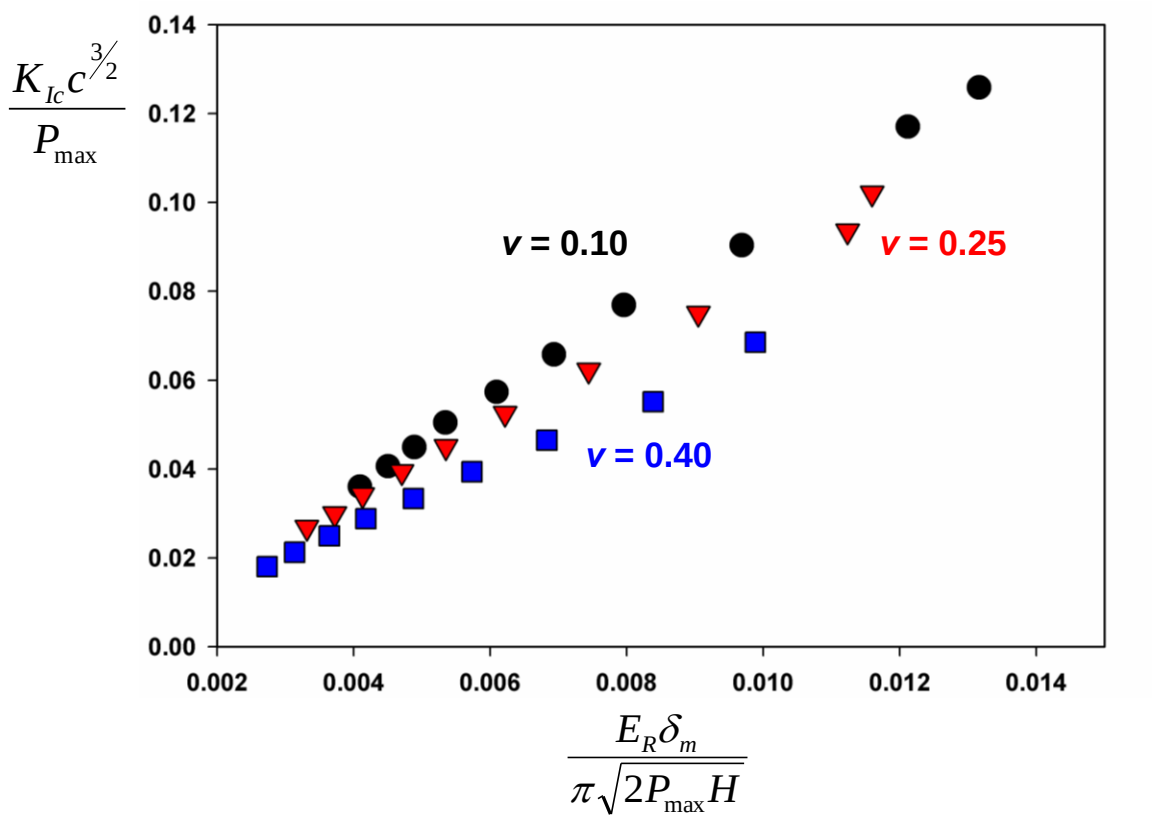


Figure 5.3. Vickers indentation cracking results in the median regime plotted as a function of the rigid disk stress intensity factor solution.

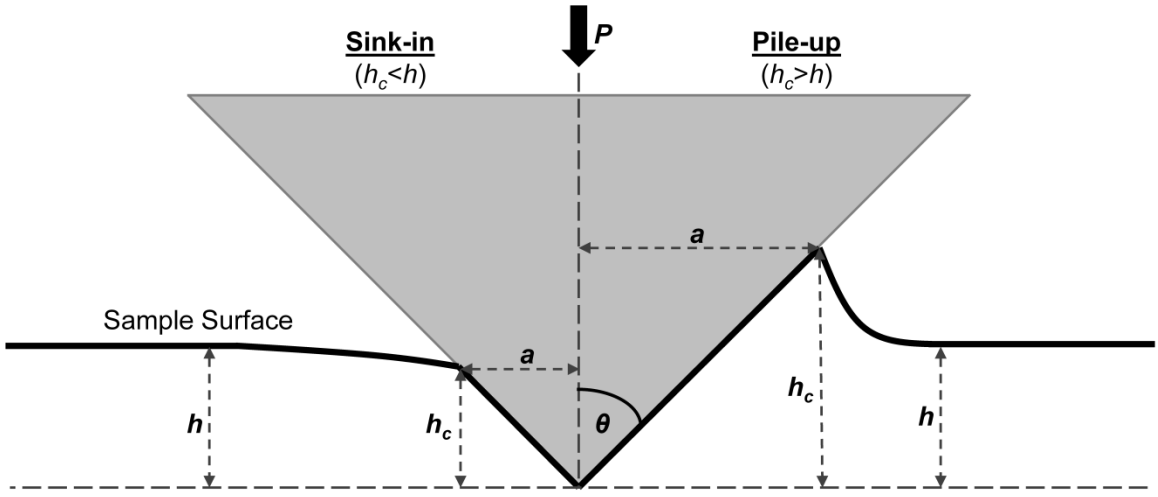


Figure 5.4. Sink-in/pile-up surface deformation geometries.

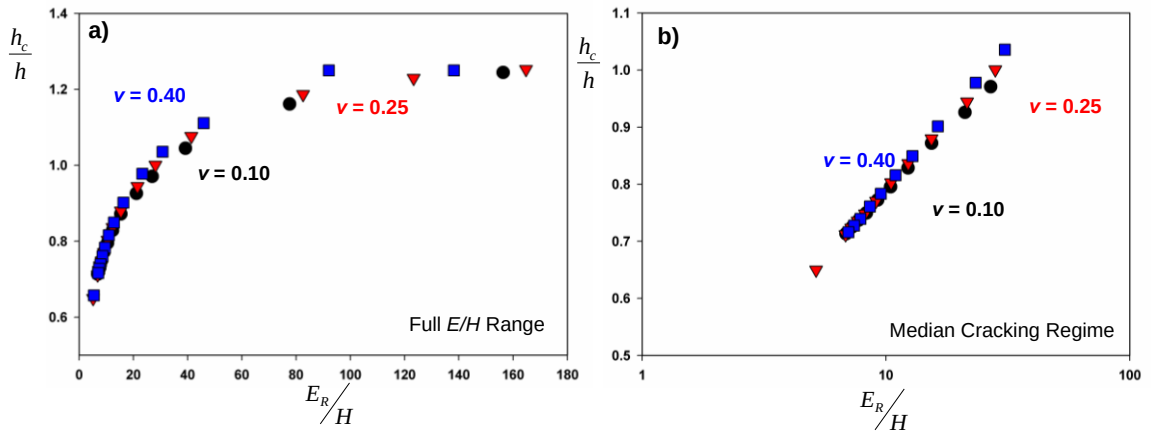


Figure 5.5. Finite element results of contact depth to total indenter displacement: (a) the entire *E/Y* range examined; and (b) results from the median cracking regime showing logarithmic behavior.

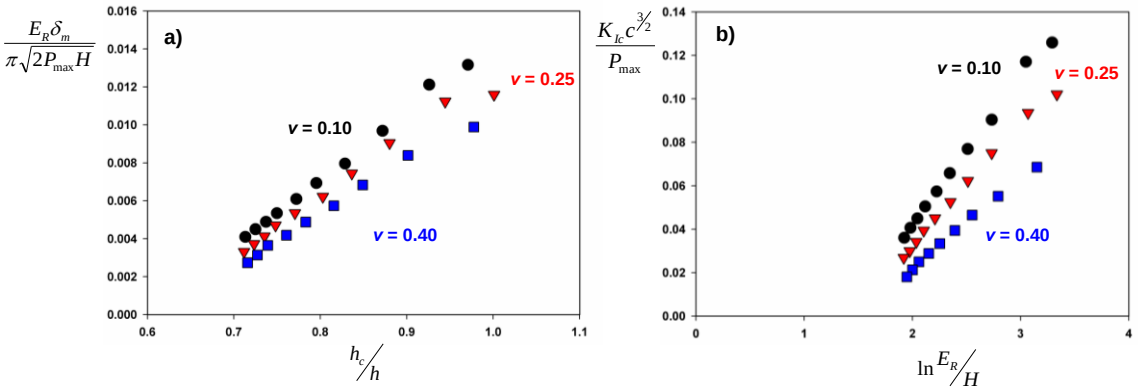


Figure 5.6. Correlations between: (a) sink-in/pile-up and the rigid disk stress intensity factor solution; and (b) indentation cracking parameters and the natural log of E_R/H.

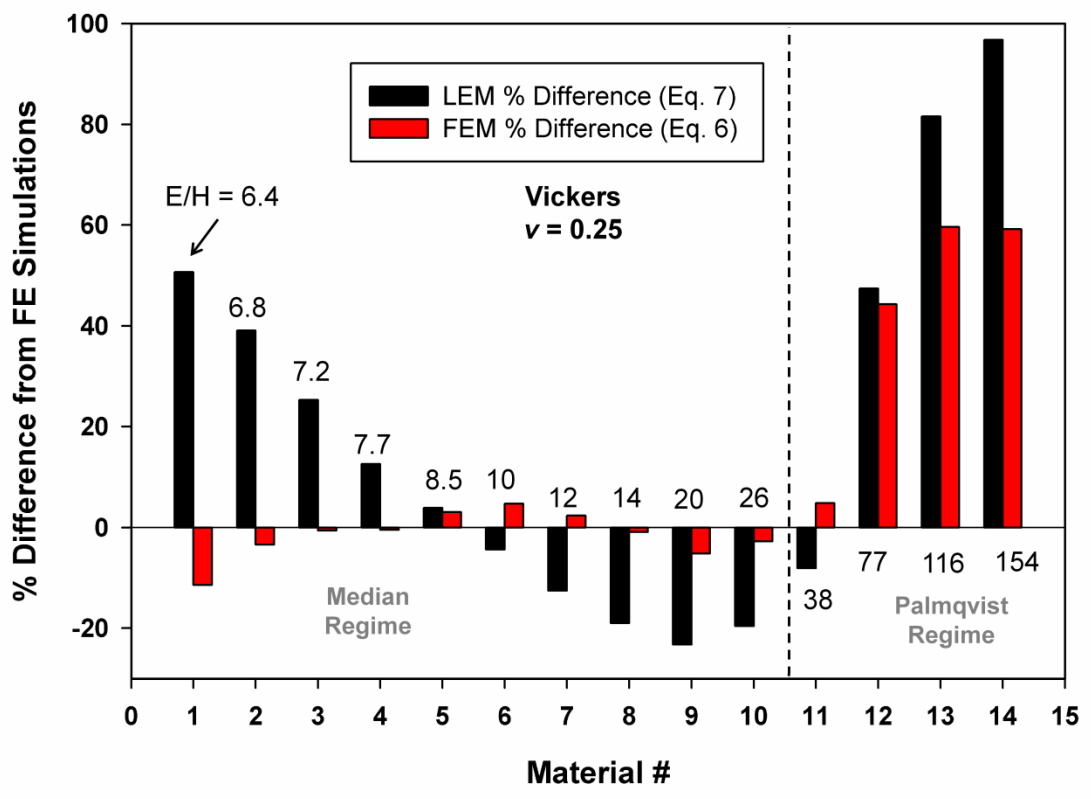


Figure 5.7. Comparison between fracture toughness predictions from the LEM model and the median cracking model derived from finite elements.

CHAPTER VI

A MODEL FOR THE STRESS INTENSITY FACTOR OF AN INDENTATION CRACK IN THE PALMQVIST CRACKING REGIME

Abstract

Observations and numerical data from cohesive zone finite element simulations of Vickers indentation cracking were used to relate material properties, applied loads, and crack lengths to simple stress intensity factor solutions for indentation cracks in the *Palmqvist* regime. Contrary to the rigid inclusion stress intensity factor solution for the *median* cracking regime, a stress-based solution was chosen for the *Palmqvist* regime where large changes in the ratio of elastic modulus to hardness resulted in nearly negligible changes in deformation behavior. The result was a remarkably simple relationship between fracture toughness, applied load, and crack length that was independent of material properties other than Poisson's ratio. Application of the stress intensity factor solution herein to measuring fracture toughness is only valid when plastic deformation dominates the materials response to indentation, such as the case of cube-corner indentation.

6.1. Introduction

Results from cohesive finite element simulations of indentation cracking with a Vickers indenter exhibit two regimes of indentation cracking, viz., a median cracking regime wherein both elastic and plastic strains are important and a Palmqvist cracking regime dominated by plastic deformation and cracking at the surface. This transition in cracking behavior follows the transition from elastic sink-in at the contact periphery to plastic pile-up as the ratio of elastic modulus to hardness increases. The crossover point from the median regime to the Palmqvist regime occurs when pile-up begins, i.e., the plastic zone breaches the surface at the contact periphery (see Fig. 4.8), which occurs at an elastic modulus to hardness ratio of ~30 for a Vickers indenter. At this point, the stress intensity factor solution for the median regime developed in the previous section breaks down and its use results in large errors in fracture toughness measurements in the Palmqvist regime. Given that, the intent of this chapter of the dissertation is to develop a semi-analytical expression for the stress intensity factor of an indentation crack in the Palmqvist regime based on observations and data from the cohesive finite element simulations. As in other parts of this dissertation, development of stress intensity factors and analysis of simulations are confined to linear-elastic fracture mechanics.

Surface cracks are present during loading in the Palmqvist cracking regime unlike the median cracking regime where surface cracks only appear upon unloading. The geometry of the Palmqvist indentation crack has been described in detail in previous chapters, but is pictured in Fig. 6.1 for convenience. The development of a stress intensity factor solution for an indentation crack in the Palmqvist regime begins with the formulation for stable cracks in equilibrium with an applied load, followed by the solution for the fully unloaded crack geometry. The approach herein is not a rigorous analytical derivation due to the complex nature and geometry of elastic-plastic indentation, but rather the application/modification of existing stress intensity factor solutions [1]. Non-standard crack geometries in equilibrium with a complex three-

dimensional elastic-plastic loading environments are typically not analytically tractable and the numerical techniques used to solve for the stress intensity factor are outside the focus of this work [2].

The major assumption in the Palmqvist stress intensity factor derivation is that the influence of the elastic modulus is negligible due to the large amount of plastic deformation occurring at the contact periphery. In order to show that this assumption is valid, it is useful to normalize applied load, *P*, and crack length, *c*, measured from the center of the indent to the crack tip, by the hardness, *H*, and the fracture toughness, K_{Ic}. Doing this leads to a non-dimensional load, $\hat{P}$, given by:

$$\hat{P} = \frac{PH^3}{K_{Ic}^4}, \tag{6.1}$$

and a non-dimensional crack length, $\hat{c}$, given by:

$$\hat{c} = \frac{cH^2}{K_{IC}^2}. \tag{6.2}$$

Note that neither of these non-dimensionalizations involves elastic parameters.

Evidence for this choice of normalization is provided in Figs. 6.2, 6.3, 6.4, and 6.5. Loads and crack lengths measured during **loading** of a Vickers indenter in materials (Poisson's ratio = 0.10) exhibiting the Palmqvist geometry are plotted in Fig. 6.2. The same l**oading** data are plotted as non-dimensional parameters in Fig. 6.3 (log-log scale). Crack length results, separated by Poisson's ratio, after complete **unloading** are plotted in Figure 6.4 as a function of the maximum applied load. Non-dimensionalized crack lengths and loads for the **unloaded** state are plotted in Fig. 6.5. The data clearly collapse for both loading and unloading even though elastic modulus varies between 100 GPa and 400 GPa.

Physically, one interpretation of this is that the contact geometry in the high elastic modulus to hardness ratio regime (*E/H* > 30) is approaching that which would occur in a rigid-plastic material, and thus elastic influences are minimal. From a fracture mechanics view, the driving force can then be thought

of as a centrally loaded penny-crack where the force is distributed over the plastic zone. Because the indentation geometry is nearly independent of *E/H*, the geometry of the plastic zone only depends on the applied load and the hardness. Strictly speaking, the rigid-plastic limit has not been reached as stress gradients exist around the hardness impression. In addition, crack growth at the surface occurs upon unloading of the indenter. However, the unique results shown in Figs. 6.3 and 6.5 helps in understanding equilibrium crack growth in the Palmqvist regime and aids development of a stress intensity factor solution.

The assumptions in the derivation of the following stress intensity factor models are as follows:

1. The indentation geometry including the crack, contact size, plastic zone, and surface profile are independent of the ratio of *E/H* and only scale with applied load [3].
2. The model utilizes penny-shaped crack stress intensity factor solutions with a constant that accounts for the free surface, see, for example, Tada [1] on a half-penny crack at a free surface.
3. During loading, the stress intensity factor is the sum of a positive residual component stemming from plasticity and a negative elastic component due to elastic contact stresses from the indenter.
4. Upon unloading, only the residual component of the stress intensity factor is present.

6.2. Stress Intensity Factor on Loading

In typical linear-elastic fracture toughness geometries, stresses in the body scale with increased loading while the geometry remains relatively constant. In direct contrast to that statement, during indentation the stresses remain constant with increased loading due to geometric self-similarity of the elastic-plastic indentation while the size of the contact and crack length increase. A few observations help in identifying the form of the stress intensity factor solution required to describe the indentation crack during loading:

1. A centrally loaded penny-shaped crack gives rise to a stable crack with increasing load, but does not allow for a length scale such as the plastic zone, does not allow for a threshold load for cracking, and requires infinite crack opening displacement at the center which is physically unreasonable.
2. A penny-shaped crack with a constant uniform stress acting over the crack surface results in an unstable crack with increased crack size.
3. The crack mouth opening displacement idea from the previous section is not applicable in the Palmqvist regime as the stress intensity factor is derived from elastic resistance to rigid wedge opening. As shown in Fig. 6.3, the solution should be independent of the elastic modulus.
4. During loading, a compressive elastic component exists that restricts crack growth. Unloading the indenter results in increased crack length, e.g., Fig. 4.6.

Given the above observations, we approach the problem by modifying the mode I stress intensity factor, K_I, solutions 24.5 and 24.6 in Tada's stress analysis of cracks handbook [1], pictured in Fig. 6.6a and Fig. 6.6b, respectively. Solution 24.5 applies a line load, p, at a radial distance, x, from the center of a penny-shaped crack with a length of c ($b < c$). Solution 24.6 applies a uniform stress, σ_{avg}, acting on the crack surface outside of the radial distance x. Crack opening loads and stresses act normal to the crack plane and occur in the z direction shown in Fig. 6.6. Superposition of the two solutions yields:

$$K_I = \frac{2p}{\sqrt{\pi c}} \frac{x}{\sqrt{c^2 - x^2}} + \frac{2\sigma_{avg}}{\sqrt{\pi c}} \sqrt{c^2 - x^2}. \tag{6.3}$$

Henceforth, we choose to drop coefficients in the equations noting that the ≈ symbol reads "varies as" in this work under the assumption that any corrections from the standard geometry to the indentation geometry are constants. Letting the radius of the plastic zone be denoted by b and assuming that the indentation hardness, H, is uniformly distributed over the plastic zone, integration of the first term in Eq. 6.3 with respect to x from 0 to b yields:

$$K_I \approx \frac{H}{\sqrt{c}}\left[-\sqrt{c^2-b^2}+c\right]+\frac{\sigma_{avg}}{\sqrt{\pi c}}\sqrt{c^2-b^2}. \quad (6.4)$$

The geometries described by the first and second parts of Eq. 6.4 are pictured in Fig. 6.7a and Fig. 6.7b, respectively.

Feng has provided an analytical solution to the stress field around a conical indenter hardness impression in an elastic-plastic material. During loading the elastic compressive stress acting normal to the crack plane, $\sigma_{\theta\theta}$, at the surface outside of the contact is a function of applied load, P, and radial distance, r, and can be estimated from:

$$\sigma_{\theta\theta} = -(1-2\upsilon)\frac{P}{2\pi r^2}. \quad (6.5)$$

Assuming that this stress is relatively independent of angle with respect to the surface, the average stress acting over the region from the plastic zone to the crack tip is given by:

$$\sigma_{avg} = -(1-2\upsilon)\frac{P}{bc}. \quad (6.6)$$

Substitution of Eq. 6.6 into Eq. 6.4 yields:

$$K_I \approx \frac{H}{\sqrt{c}}\left[-\sqrt{c^2-b^2}+c\right]-(1-2\upsilon)\frac{P}{\sqrt{c}}\frac{\sqrt{c^2-b^2}}{bc}. \quad (6.7)$$

It is of great importance to analyze some limits of Eq. 6.7 in terms of their physical meaning. In the limit that the crack length is equal to the plastic zone radius, the condition for a crack threshold or the point at which crack can be observed experimentally, and noting that the applied load, P, is given by $P \approx Hb^2$ due to geometric self-similarity, the stress intensity factor becomes:

$$K_I \approx H^{0.75}P^{0.25}. \quad (6.8)$$

Rearranging and assuming equilibrium crack growth by setting the stress intensity factor equal to the fracture toughness, K_{Ic}, yields:

$$P \approx \left.\frac{K_{Ic}^4}{H^3}\right|_{c=b}. \quad (6.9)$$

Equation 6.9 is an important result for two reasons. First, the chosen stress intensity factor predicts a crack threshold load that is a function of the materials

fracture toughness and hardness in a way that is surprisingly consistent with Lawn and Swain's analysis (see Chapter II) given the differences between the two approaches. Lawn and Swain derive a stress intensity factor model that grows is a function of the size of the contact and "searches" for a flaw of the right orientation and shape that gives rise to crack extension. Secondly, the exponents on the toughness and hardness are consistent with the non-dimensional parameters in Eqs. 6.1 and 6.2. The cohesive finite element simulations in this work are not suited to describing short cracks, as is the case in the threshold load cracking. However, advances in in-situ indentation testing could provide useful information on material behavior in this limit.

A first order series expansion of Eq. 6.7 yields the solution when the crack length, *c*, is slightly greater than the plastic zone size, *b*, as is the case of the indentation crack:

$$K_I \approx \frac{Hb^2}{c^{1.5}} - \frac{P}{b\sqrt{c}} \approx \frac{P}{c^{1.5}} - \left(\frac{HP}{c}\right)^{0.5}. \tag{6.10}$$

Note, however, that the magnitude of the stress intensity factor given in Eq. 6.10 is dependent on the magnitudes of each term. For example, non-dimensional crack lengths are plotted in Fig. 6.8 as a function of non-dimensional loads for both the finite element data (Poisson's ratio = 0.10) and those calculated from Eq. 6.10 assuming that the coefficients of each term are equivalent. The data in figure 6.8 comes from the same set of data in Figs. 6.3 and 6.4 for Poisson's ratio of 0.10. Clearly, Eq. 6.10 does not accurately describe the results from the finite elements. However, decreasing the magnitude of the coefficient of the elastic term shifts the model toward the finite element data suggesting that the plastic term is dominant in the regime explored in the finite elements, consistent with the argument that plasticity dominates the contact response in the Palmqvist regime. Equation 6.10 may be useful in the Palmqvist cracking regime when crack lengths can be measured in-situ, something that has not been greatly explored to date.

6.3. Stress Intensity Factor on Unloading

Of greater importance for post-test measurements of crack lengths is the solution for the stress intensity factor of a fully unloaded indentation crack in the Palmqvist regime. Examination of the finite element simulations confirmed that no further plastic deformation occurred during unloading in the Palmqvist regime. In addition, removal of the load did not cause a large change in geometry (see Chapter IV). Given that, the condition for an equilibrium crack of an unloaded indent from a maximum load of P_{max} in the Palmqvist regime is given by the removal of the elastic contribution in Eq. 6.10, which, under conditions of equilibrium crack growth, simplifies to:

$$K_{Ic} \approx \frac{P_{max}}{c^{1.5}}. \tag{6.11}$$

The result is an amazingly simple relationship between crack length, applied loads, and fracture toughness that is independent of elastic moduli and indentation hardness. Note, though, that Eq. 6.11 must be applied under the conditions where plastic deformation dominates the indentation response. Interestingly, Tanaka [4] derived a similar expression, and Harding [5] showed that Tanaka's equation described a large material data set best with the cube-corner indenter wherein plasticity dominates the indentation response.

Shetty et al. [6] derived a stress intensity factor solution in the Palmqvist regime as:

$$K_{Ic} \approx \sqrt{\frac{HP_{max}}{l}}, \tag{6.12}$$

where l is the crack length measured from the corner of the indentation impression to the crack tip, or approximately $l=c-b$. Shetty's solution written in terms of non-dimensional variables is given by:

$$\hat{l} \approx \hat{P}, \tag{6.13}$$

where the non-dimensional crack length is, $\hat{l}=lH^2/K_{Ic}^2$.

The third geometrical dimension of importance to visualizing the model for crack length as a function of load for the Palmqvist regime is the size of the plastic zone, *b*, which in dimensionless form scales as:

$$\hat{b} \approx \sqrt{\hat{P}}. \tag{6.14}$$

Figure 6.9 is a log-log plot of the current model results (Eq. 6.11) fit to Vickers finite element results after complete unload for non-dimensional crack lengths $\hat{c}$, and $\hat{l}$, and the non-dimensional length of the plastic zone $\hat{b}$ on the surface near the threshold load for cracking (i.e., when *l* is greater than *b*). While the slope of the non-dimensional crack length $\hat{l}$ continuously changes, it has a magnitude of ~1.0 at a non-dimensional load of $1x10^6$, which corresponds well with Shetty's prediction (Eq. 6.13). The slope of the plastic zone size is 1/2 due to geometric self-similarity of the indenter and the slope of crack length *c* is 2/3. The results of Eq. 6.11 are consistent with previous derivations of the stress intensity factor for Palmqvist cracks and experimental observations. Furthermore, the model is consistent with the finite element data over the range of elastic modulus and yield strength examined (see Fig. 6.4).

The novelty of the model (Eq. 6.11) derived herein lies in its simplicity with respect to other derivations. Recognizing that plasticity drives crack growth and that elastic deformation is nearly negligible combined with a simple stress intensity factor solution allows for a straightforward, if not purely analytical, estimation of fracture toughness in the Palmqvist indentation cracking regime . The applicability of Eq. 6.11 will be tested in the following section where the results from a number of cohesive finite element simulations of indentation cracking in the Palmqvist will be added to the Vickers indenter results.

6.4. Conclusions

A stress intensity factor solution has been developed for an indentation crack in the Palmqvist regime. The total stress intensity factor is composed of a positive residual component stemming from the severe plastic deformation around the contact and a negative elastic component due to the contact stresses induced by the indenter. Upon unloading, only the residual component is active. The result is an extremely simple relationship between crack lengths, applied loads, and fracture toughness under the condition of equilibrium crack growth.

References

1. Tada, H., P.C. Paris, and G.R. Irwin, *The stress analysis of cracks handbook*. 1973: Del Research Corp.
2. Anderson, T.L., *Fracture Mechanics: Fundamentals and Applications*. 2005: Taylor & Francis.
3. Feng, G., et al., *An analytical expression for the stress field around an elastoplastic indentation/contact.* Acta Materialia, 2007. **55**(9): p. 2929-2938.
4. Tanaka, K., *Elastic/plastic indentation hardness and indentation fracture toughness: The inclusion core model.* Journal of Materials Science, 1987. **22**(4): p. 1501-1508.
5. Harding, D.S., *Craking in Brittle Materials During Low-Load Indentation and its Relation to Fracture Toughness.* PhD Thesis, Rice University, 1995.
6. Shetty, D.K., et al., *Indentation fracture of WC-Co cermets.* Journal of Materials Science, 1985. **20**(5): p. 1873-1882.

APPENDIX 6.1.

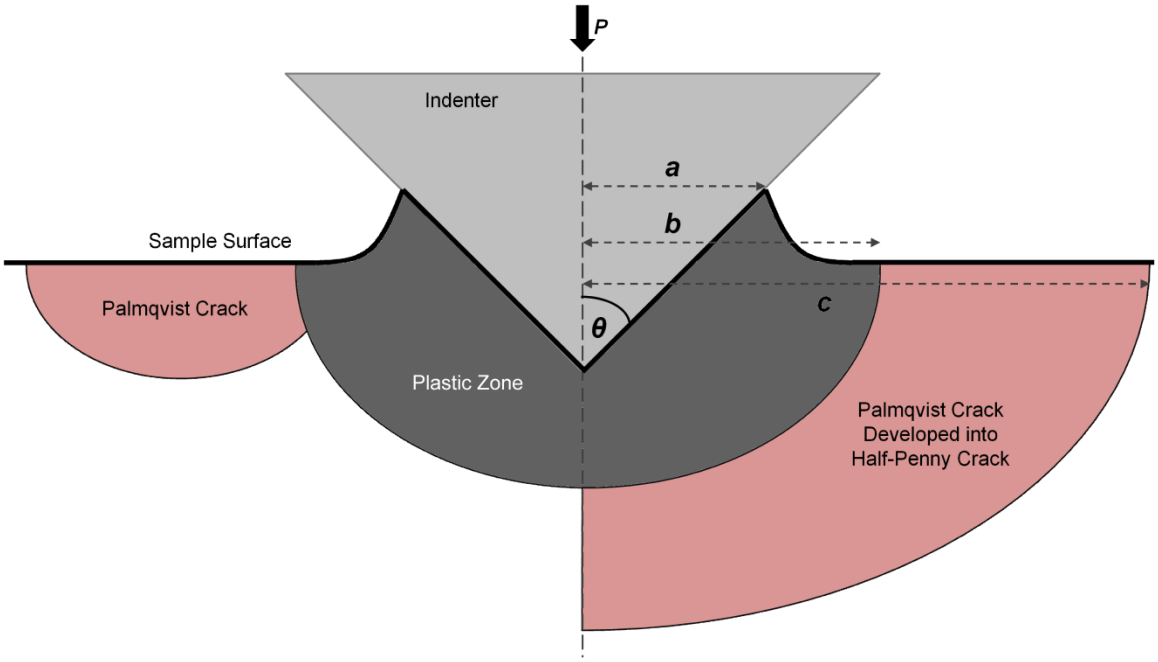


Figure 6.1. An idealized subsurface Palmqvist indentation cracking geometry during Vickers indentation.

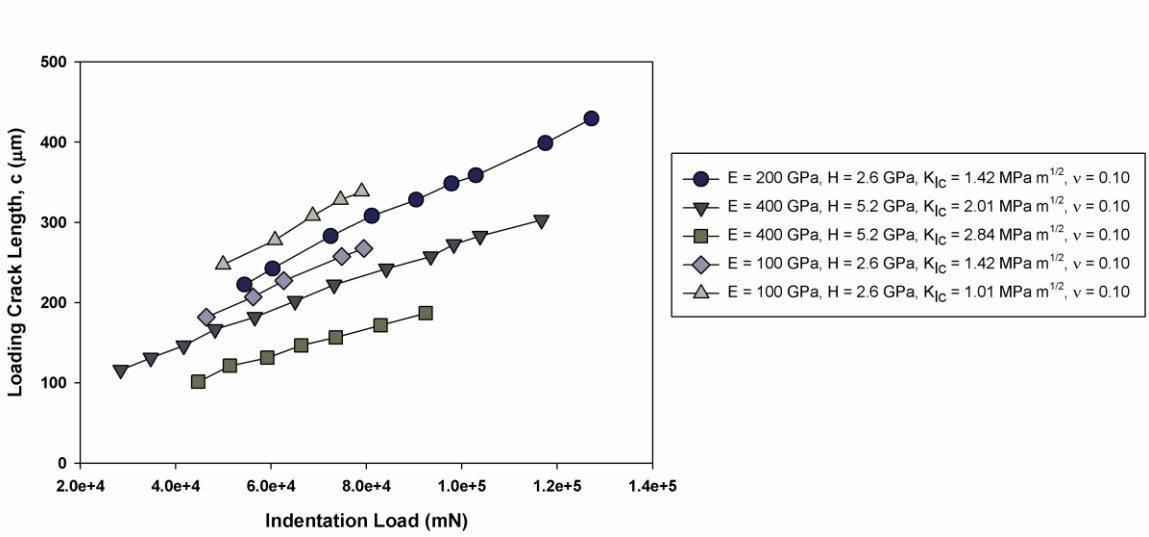


Figure 6.2. Vickers indentation crack lengths versus load for Palmqvist cracks during loading (Poisson's ratio = 0.10).

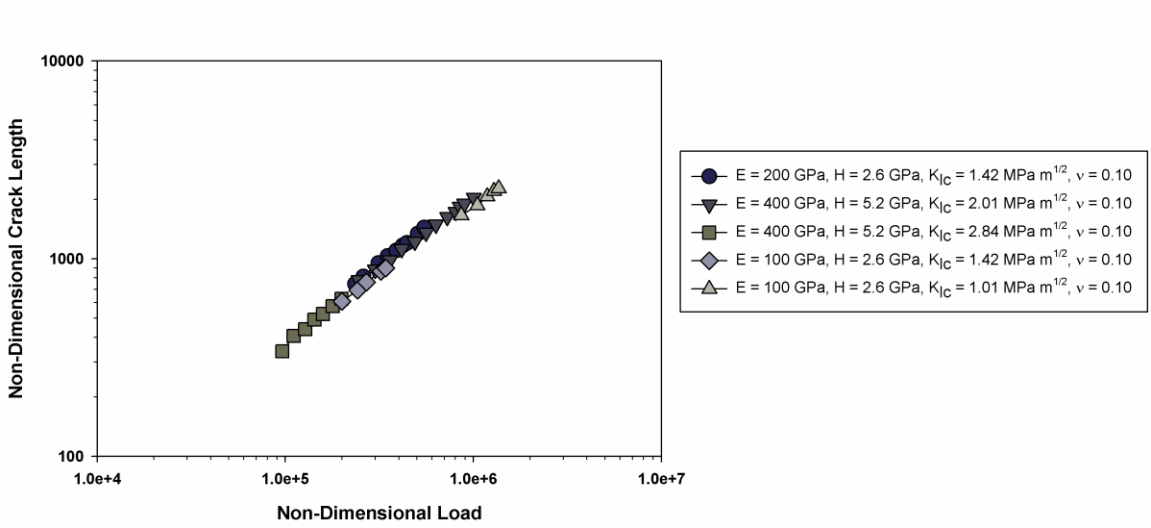


Figure 6.3. Non-dimensional loads and crack lengths for Palmqvist cracks during loading (Poisson's ratio = 0.10).

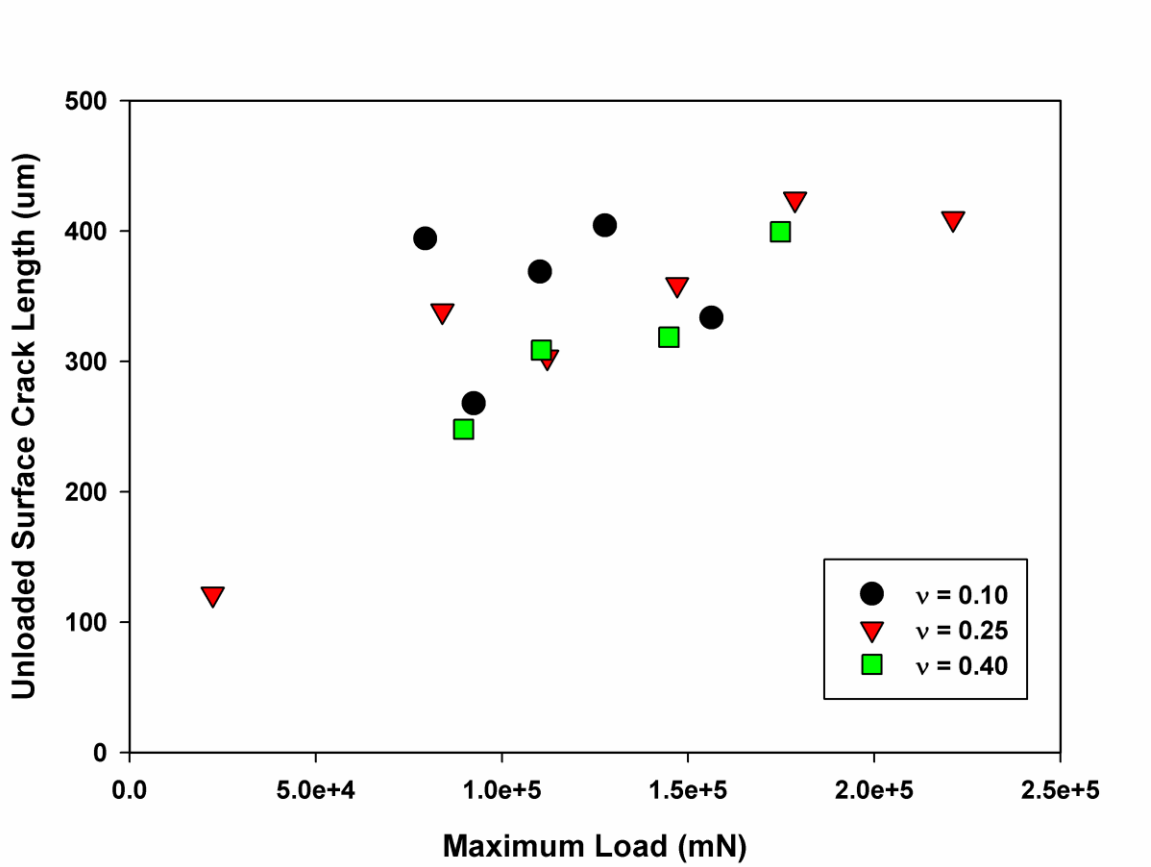


Figure 6.4. Unloaded surface crack lengths of Vickers indentation simulations in the Palmqvist regime.

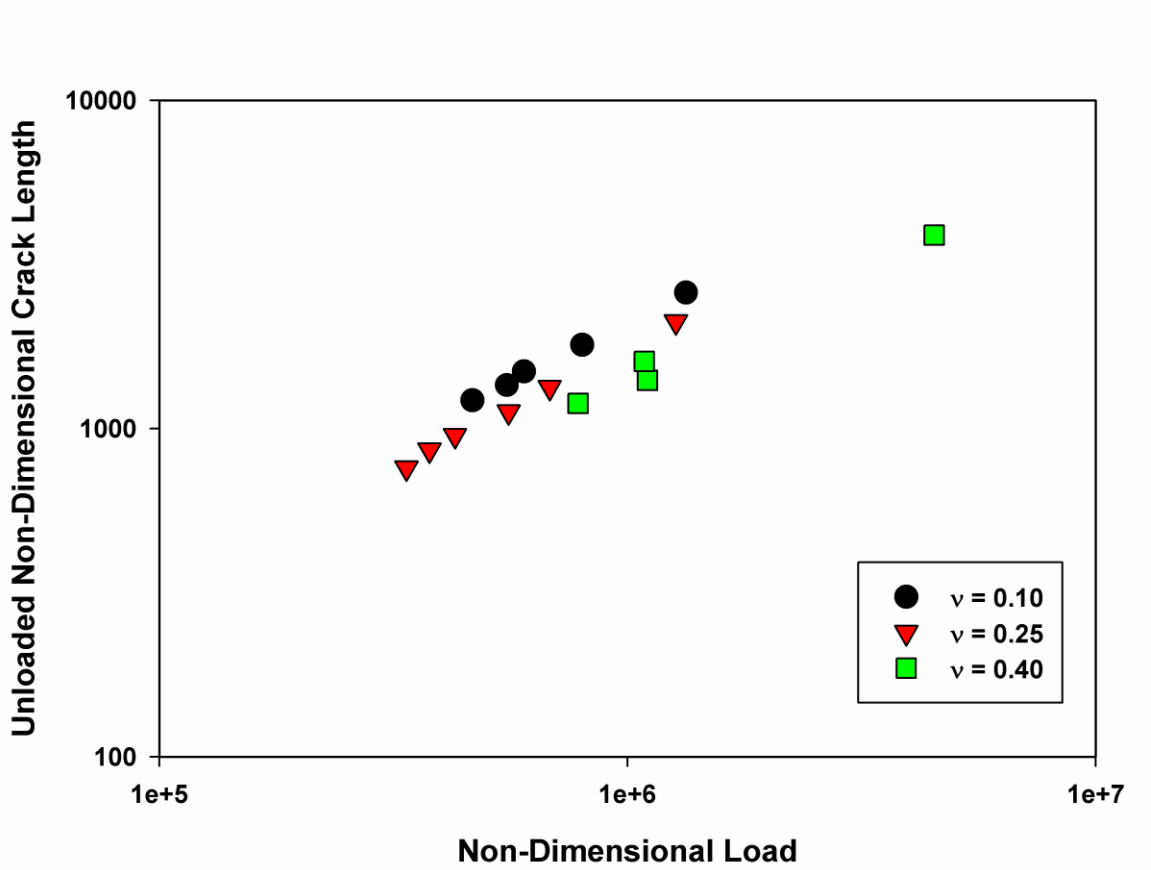


Figure 6.5. Non-dimensional loads and crack lengths for Palmqvist cracks after complete unload.

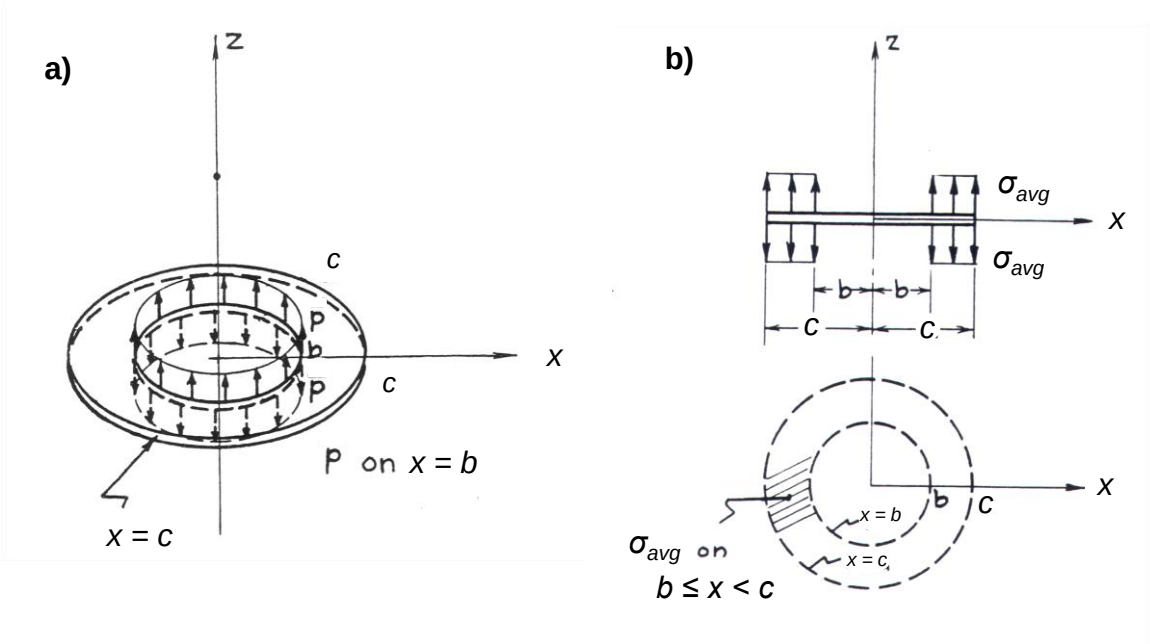


Figure 6.6. Stress intensity factor geometries 24.5 (a) and 24.6 (b) from the stress analysis of crack handbook [1].

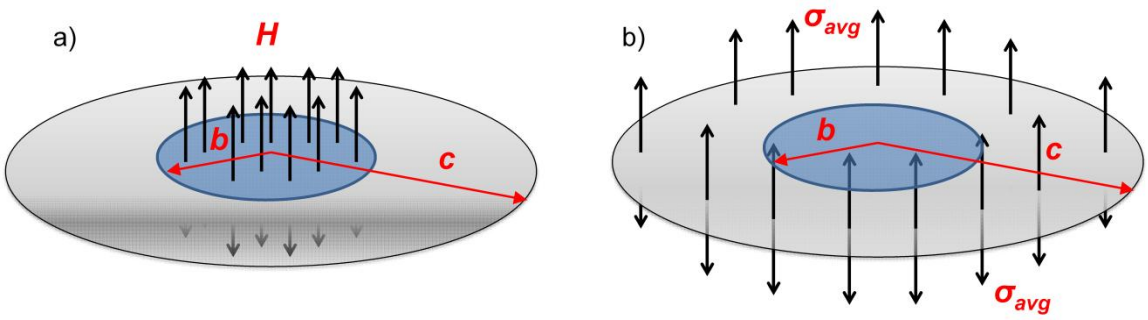


Figure 6.7. Schematics of the stress intensity factor geometries used to describe indentation cracking.

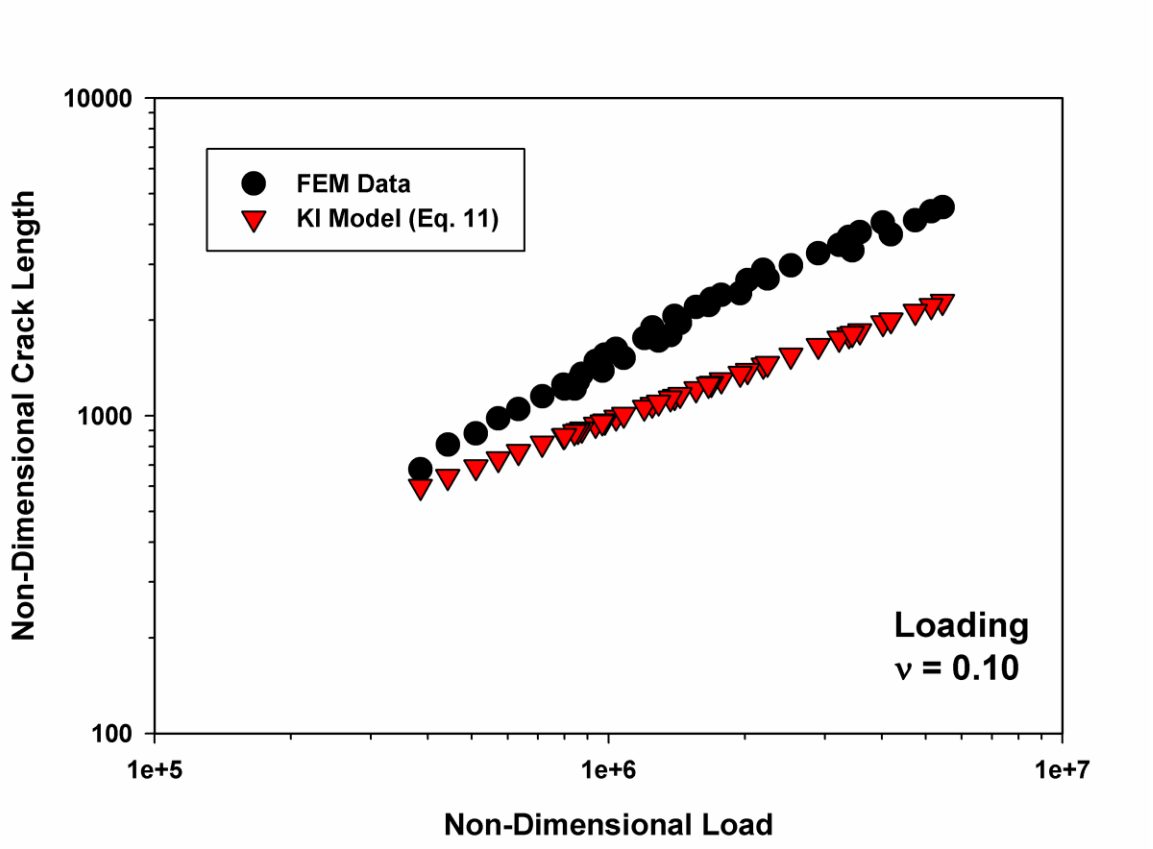


Figure 6.8. Comparison between the finite element results and the stress intensity factor model for loading given by Eq. 6.10.

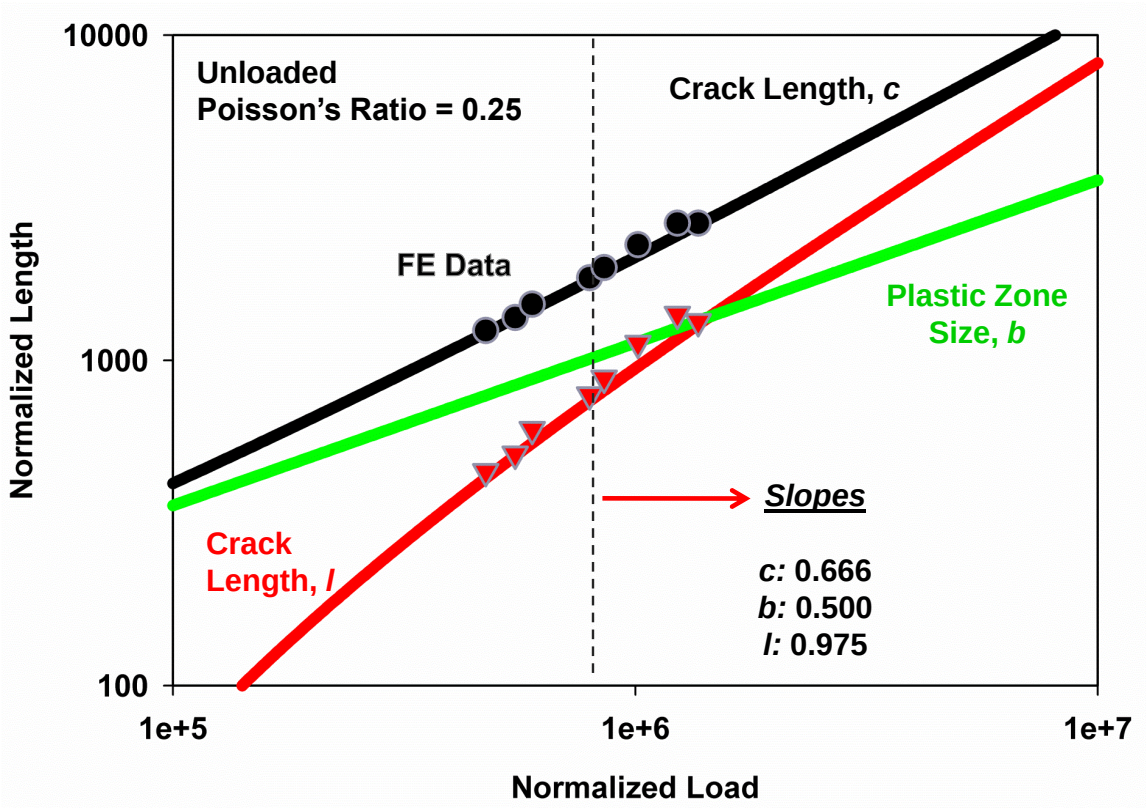


Figure 6.9. Predicted scaling behavior of non-dimensional crack lengths *c* and *l* as well as non-dimensional plastic zone size, *b*, in the Palmqvist regime. Finite element results have been superimposed on the plot.

CHAPTER VII

EXPLORING INDENTER GEOMETRY EFFECTS IN INDENTATION CRACKING WITH COHESIVE ZONE FINITE ELEMENTS

Abstract

Cohesive zone finite element simulations of indentation cracking were carried out to examine the influence of indenter geometry on cracking behavior. Simulations of the three-sided pyramidal Berkovich indenter along with three-sided indenters with various centerline-to-face angles were used for comparison with the Vickers indenter results and stress intensity factor solutions shown in previous chapters. In addition, the influence of the number of corners on an indenter was explored and compared to experimental results. It was found that the simulations of Berkovich indentation cracking gave rise to crack lengths that were approximately ten percent greater than a Vickers indentation on the same material and applied load. This result was consistent with experimental results from Harding and Dukino and Swain in addition to validating the use of Ouchterlony's stress intensity factor solution to account for the number of indenter corners. More importantly, the results herein substantiated the stress intensity factor solutions in Chapters V and VI. Furthermore, it was found that the indentation cracking response could be tailored such that plastic deformation dominates by using indenters with smaller centerline-to-face angles like the cube-corner geometry. This tailoring has important ramifications to accurately measuring fracture toughness with indentation cracking. Experiments and simulations in the *Palmqvist* regime compared extremely well with the fracture toughness relationship developed in Chapter VI where the influence of material properties and indenter angle were negligible.

7.1. Introduction

The cracking that occurs in brittle materials during indentation with pyramidal indenters and subsequent relationship between material properties, applied loads, and crack geometry is complex and fraught with nuances. In previous sections of this dissertation, we have focused on the role of material properties in indentation cracking with a Vickers pyramidal indenter, specifically, elastic moduli, hardness, and fracture toughness. A primary result of that work was the identification of a transition in cracking behavior as the contact moves from elastic-plastic to plasticity dominated as the ratio of elastic modulus to hardness increases. This section aims to provide some insight into the effects of the pyramidal indenter geometry, e.g., the number of corners on the indenter, and the indenter centerline-to-face angle. Indentation cracking with a 3-sided Berkovich indenter has importance in nanoindentation with the ability to produce results at small scales without the effect of a tip defect inherent to the 4-sided Vickers indenter. The work pertaining to the effect of the number of corners is motivated by the results from Harding [1], Pharr and Harding [2], and Dukino and Swain [3], while indenter angle effects have been previously described by the pioneering work of Lawn and coworkers [4].

Harding [1] and Dukino and Swain [3], working over a range of brittle materials, found that the Berkovich indenter produces crack lengths that are approximately 10% greater those resulting from a Vickers indenter for the same load. Harding's results are summarized in Fig. 7.1 where crack lengths for a Vickers indenter are plotted against crack lengths from a Berkovich indenter with equivalent maximum loads [1]. Both Harding and Dukino and Swain utilized Ouchterlony's stress intensity factor solution for a two-dimensional star-shaped through crack [5] to explain for the differences observed between the two indenters. Harding modified Ouchterlony's solution such that the driving force was distributed among the number of cracks. Dukino and Swain arrived at a similar observation having used Ouchterlony's solution, however incorrectly derived. The ratio of Ouchterlony's stress intensity factors of a 3-star crack and a

4-star crack would result in a value of 0.93, not the value of 1.07 arrived at by Dukino and Swain. With experimental evidence limited by available indenter geometries, cohesive finite element simulations provide a unique opportunity to assess the influence of the number of cracks or viewed another way the number of corners on a pyramidal indenter.

The additional indenter geometry descriptor of interest is the indenter centerline-to-face angle. Lawn, Evans, and Marshall provided an indenter angle dependence in their indentation cracking model derivation [4]. Their result of a $cot^{2/3}\theta$ dependence stems from the assumption that the volume of the indent gives rise to an equivalent change in plastic zone volume. Thus, sharper indenters, i.e., those with a greater volume to contact area ratio, will provide a greater crack driving force. However, as shown in previous chapters of this work, the LEM model does not take into account pile-up or sink-in of material at the contact periphery, which, in their derivation, may result in changes to the influence of indenter angle. While an important topic of interest to the indentation cracking community is the threshold load for crack initiation as a function of indenter angle, such events are ill described with cohesive finite elements in the framework that we have set in this study (see Chapter II). The focus of the simulations, as in other chapters of this dissertation, remains on analyses in the limit of large cracks in comparison to the process zone size.

This work provides cohesive finite element simulation analyses of the influence of indenter geometry on indentation cracking. Specifically, the three primary goals are:

1. to examine the differences in indentation cracking results between the Berkovich, Vickers, and conical indenter geometries.
2. to examine the dependency on the number of cracks and number of corners in light of experimental observations.
3. to document the influence of the indenter centerline-to-face angle on indentation cracking results for three-sided pyramidal indenters.

The results presented here in combination with the information from previous indentation cracking simulations give rise to a more complete description of the relationship between material properties, indenter geometry, applied loads, and indentation crack lengths. The result is an improved ability to estimate fracture toughness with pyramidal indenters.

7.2. Finite Element Simulations

The finite element software package ABAQUS was used to simulate indentation cracking with cohesive finite elements. The details of the three-dimensional meshes and application of cohesive finite elements to indentation cracking of brittle materials has been detailed in previous chapters. Specifically, ABAQUS bi-linear traction-separation based cohesive element (COH3D8) inputs included an initial stiffness of $1x10^{4}$ GPa, a viscosity of $1x10^{-6}$ s^{-1}, an onset of debonding criterion of MAXS (mode I loading), and an energy based criterion for complete separation [6]. A large initial stiffness, compared to the elastic modulus of the material, ensured that any additional compliance due to the presence of cohesive elements was negligible. Viscous regularization facilitated convergence during the separation process [7]. A maximum cohesive strength of 0.30 GPa was used in all simulations for consistency in the size of the process zone, noting that the tensile stresses on prospective crack planes near the hardness impression are a function of indenter geometry.

As previously described, the maximum tensile stress during indentation of elastic-perfectly plastic materials is limited by the yield strength, and a cohesive strength set at theoretical strengths would never result in the onset of cracking. In addition, nucleation of a crack cannot be accurately described by the cohesive element formulation in this work. The energy of separation, G_{Ic}, is used to compute fracture toughness, K_{Ic}, only in the limit that the crack is greater than ten times the size of the process zone, noting that the choice of cohesive strength and shape of the cohesive traction-separation curve does not influence long crack behavior. Post-processing confirmed that output traction-separation

cohesive behavior of matched the input behavior and no overloading of the cohesive elements occurred due to the use of viscous regularization.

ABAQUS solid elements (C3D6 and C3D8) were used in simulating materials with an elastic-perfectly plastic constitutive behavior having inputs of elastic modulus, E, Poisson's ratio, v, and yield strength, Y. Elastic modulus varied from 100 GPa to 400 GPa, while Poisson's ratio was held to 0.25 for all simulations. Yield strength varied from 1 GPa to 10 GPa. Hardness, H, was calculated from a maximum load, P_{max}, and contact area, A_c, as measured from simulation results. The combinations of E and Y resulted in a range of E/H that spans ceramic materials as well as brittle metals. A rigid element, fixed in all but the indentation direction, was used for the indenter that was in frictionless contact with the material surface.

Most current structural ceramics lie in an E/H regime of ~10 and the dominant cracking mode observed in experiments with Vickers indenters is median cracking during loading followed by crack extension at the surface during unloading [4]. Thus, in examining the effect of the number of cracks/corners we have chosen to work with an elastic-perfectly plastic material with an E/Y ratio of ~20, Poisson's ratio of 0.25, and a fracture toughness, K_{Ic}, of 1.0 MPa $m^{1/2}$. This combination of elastic modulus, Poisson's ratio, and yield strength resulted in a E/H ratio of ~10, a typical value for ceramic materials. In addition to the conical, Berkovich, and Vickers indenters, 5-sided, and 6-sided indenters have been simulated. While indenters with a number of sides greater than 4 may be experimentally impractical, such simulations provide insight into their influence on indentation crack growth. For consistency between indenters an area function, i.e., the relationship between contact area, A_c, and contact depth, h_c, of $A_c=24.5h_c^2$ was used. This relationship is the same area function for ideal Berkovich and Vickers indenters and has an equivalent cone half-included angle of 70.3 degrees. The chosen area function additionally results in an equivalent volume to depth ratio. The mesh symmetry changed depending on the number of cracks and number of corners simulated, e.g., a simulation of the 4-sided

Vickers indenter in a 2-crack system has a 4-fold symmetric mesh while a simulation with a 5-sided indenter in a 5-crack system has a 10-fold symmetric mesh. An example of the 5-crack, 5-sided indenter mesh is shown in Fig. 7.2.

The influence of indenter angle was explored using 3-sided pyramidal indenters with centerline-to-face angles of 45°, 55°, 65.3°, and 75° as a function of *E/H*. Note here, that as the indenter became sharper, i.e., the centerline-to-face angle decreased, finite element artifacts became more prominent due to difficulties in contact convergence. While these artifacts could not be eliminated, care was taken to minimize their influence on the results. Cube corner indenter simulations (θ = 35°) would have been ideal for comparison to experiments, but it was found that too many artifacts existed in the contact given the mesh formulation used in these indentation cracking simulations. The material properties and simulations have been summarized in Table 1. Note that the effects of contact friction and work-hardening have not been examined in this study; both of which have significant influence on the deformation behavior beneath the indenter and depend on the indenter angle.

7.3. Results

The results from the cohesive finite element simulations of indentation cracking are split into three sections corresponding to the three goals outlined in the introduction. First, comparisons between Vickers and Berkovich indenter geometries are presented. Second, results are shown from the effect of number of cracks and interpreted in terms of Ouchterlony's stress intensity factor solution. Third, the influence of indenter angle is shown as a function of the ratio of *E/H*.

The comparison between the Vickers and Berkovich indenters is divided into the median cracking regime and Palmqvist cracking regime in light of the results described in the Vickers indentation cracking section of this dissertation. For the median cracking regime (*E/H* < ~30) the dimensionless cracking parameter, $K_{Ic}c^{3/2}/P_{max}$, a measure of a materials susceptibility to indentation

crack extension, is plotted as a function of *E/H* (semi-log) for both the Vickers and Berkovich indenters in Fig. 7.3. In this regime, the crack geometry is subsurface median during loading followed by propagation at the surface on unloading for both indenters. The Berkovich results almost mirror the Vickers results, i.e., the dimensionless cracking parameter is linear with *log E/H*. In addition, Berkovich crack morphologies mimic Vickers geometries with the exception that the Berkovich cracks are quarter-penny where the Vickers cracks are half-penny. This was explained in terms of the symmetry in the finite element simulations in Chapter II. The transition from median type cracking to Palmqvist type cracking in the Berkovich indenter also occurs at an *E/H* of ~ 30. The primary difference between the two indenters is found in the magnitude of the dimensionless cracking parameter. The Berkovich indenter consistently produces greater values of $K_{Ic}c^{3/2}/P_{max}$ as compared to the Vickers indenter.

In order to more closely compare the Berkovich and Vickers geometries in the median cracking regime, the ratios of $c^{3/2}/P_{max}$ (fixed fracture toughness) for the two indenters are plotted against each other in Fig. 7.4. Note that the ratio of $c^{3/2}/P_{max}$ is plotted instead of just crack lengths because the simulations are run with the indenter in displacement control while loads are measured. The slope of the linear best fit is 1.19 and when raised to the power of 2/3 results in a Berkovich to Vickers crack length ratio of 1.12, remarkably close to the values obtained from Harding [1] and Dukino and Swain [3].

Above an *E/H* value of ~30, Berkovich indentation cracking takes on the Palmqvist geometry, consistent with the results from the Vickers indenter. In this regime the scaling relationship between crack length, maximum load, and fracture toughness changes in accordance with the change in crack morphology/development (see Chapter VI). Comparison between Vickers and Berkovich indenters in the Palmqvist regime is shown in Fig. 7.5, where the normalized load is given by $P_{max}H^3/K_{Ic}^4$ and normalized crack length is given by cH^2/K_{Ic}^2. Not only does the Berkovich indenter follow the same scaling as the Vickers indenter, but the Berkovich indenter results in consistently greater values

of cH^2/K_{Ic}^2 than the Vickers indenter for a given material and applied load. A similar analysis to that applied to the median cracking regime results in a Berkovich to Vickers crack length ratio of ~1.09 in the Palmqvist regime. A Berkovich indenter would produce greater crack lengths than the Vickers indenter independent of the value of *E/H* and independent of the crack geometry. This result is of great importance to the development of fracture toughness estimations from indentation cracking.

Results from the indentation cracking simulations of conical indenter and 3,4,5,6-sided pyramidal indenters for a fixed material with an *E/Y* ratio of ~20, Poisson's ratio of 0.25, and a fracture toughness, K_{Ic}, of 1.0 MPa $m^{1/2}$ which exhibited median type cracking are shown in Fig. 7.6, where $K_{Ic}c^{3/2}/P_{max}$ has been plotted as a function of the number of cracks in the simulation. Taking advantage of symmetry, 2,4-crack simulations were run for the 4-sided indenter (Vickers) while 2,3,6-crack simulations were run for the 6-sided indenter. In addition, a simulation with the Berkovich indenter in a 3-crack system was run with the face normal of the indenter aligned with the crack plane instead of the corner. First and foremost, there is a clear dependence of the number of cracks on the relationship between load, crack length, and fracture toughness. Secondly, the influence of corners on an indenter is negligible after 4-sides when the pyramidal indenter result converges to the conical result. Finally, based on the observations of the 3-sided indenter, misalignment between the crack plane and corner of the indenter appears to drastically reduce the driving force for crack extension.

Indentation cracking geometries resulting from the finite element simulations of the 45°, 55°, and 75° 3-sided indenters are shown in Figs. 7.7, 7.8, and 7.9, respectively. Figure 7.7 highlights loaded (7.7b,c) and unloaded (7.7d,e) states for *E/Y* values of 50 and 12.5, respectively, which corresponded to the limiting cases examined in this study (Poisson's ratio = 0.25). Figure 7.8 highlights the 55° results for loaded (7.8b,c) and unloaded (7.8d,e) states for *E/Y* values of 50 and 10, respectively, which corresponded to the limiting cases

examined in this study (Poisson's ratio = 0.25). Figure 7.9 highlights the 75° results for loaded (7.9b,c) and unloaded (7.9d,e) states for *E/Y* values of 50 and 12.5, respectively, which corresponded to the limiting cases examined in this study (Poisson's ratio = 0.25). Values of $K_{Ic}c^{3/2}/P_{max}$ were not dependent on load above a crack lengths that was ~10 times greater than the process zone size. In fact, $K_{Ic}c^{3/2}/P_{max}$ remained constant whether or not a Palmqvist crack remained at the surface or developed into a median/radial crack, as depicted in Fig. 2.11 in Chapter II.

Results from indentation cracking simulations of 3-sided pyramidal indenters having different centerline-to-face angles is shown in Fig. 7.10, where $K_{Ic}c^{3/2}/P_{max}$ is plotted as a function of *E/H*. At low values of *E/H*, sharper indenters produce greater crack lengths for a given load and fracture toughness than the more blunt 65.3° and 75° indenters, consistent with the greater indentation volume to depth ratio. However, as *E/H* increases, this trend no longer holds and the sharper indenters lose their driving force compared to the 65.3° and 75° indenters. Just as the change in scaling behavior in Berkovich and Vickers indentation is associated with a change in crack morphology, the explanation for this transition can be found in the transition from median cracking to Palmqvist cracking as *E/H* increases, which is a strong function of indenter angle. For the materials examined in this study, which are representative of the *E/H* range in which ceramic materials lie, the 45° and 55° indenter simulations exhibited only Palmqvist type cracking while angles blunter than the Berkovich resulted only in median type cracking. The amount of crack growth on unloading was also dependent on indenter angle. Very little crack growth occurred on unloading with the 45° and 55° indenters (see Fig. 7.7), consistent with the large amount of plastic deformation, while a significant amount of crack growth occurred on unloading during the highly elastic deformation of the 75° indenter. More will be discussed in the following section.

7.4. Discussion

The cohesive finite elements simulations of indentation cracking herein have shown that indenter geometry effects play an important role that must be taken into account in the development of methods for estimating fracture toughness. In light of that, the results will be discussed in terms of accounting for the effects of the number of corners/cracks for pyramidal indenters as well as the influence of indenter centerline-to-face angle. This information combined with previous results in a more complete equation for indentation fracture toughness than previous attempts.

The similar behavior and equivalent transition with *E/H* from median to Palmqvist cracking between the Berkovich and Vickers indenters is consistent with their identical volume to depth relationship. However, the Berkovich indenter consistently produces crack lengths that are ~10% greater than the Vickers indenter for a given load and material, independent of the crack morphology. One possible explanation of this increased crack length could be based purely on the geometry of the indenters. For a given contact area, the contact dimension, i.e., the projected distance from the center of the indent to the corner, is larger for a Berkovich compared to a Vickers, which in turn is larger than a conical indenter. Figure 7.11 shows contact outlines for equivalent contact areas of a 70.3° cone, Berkovich, and Vickers indenter where the corners of the pyramidal indenters have been aligned to the x-axis. The contact dimension of the Berkovich indenter is ~1.24 times larger than the Vickers, which may explain the longer crack lengths. However, evidence against the geometric explanation comes in comparison between pyramidal and conical indenters in cases greater than 3-crack systems, e.g., the Vickers and conical indenter results for the 2-crack system in Fig. 7.6, which are virtually identical. Thus the more pronounced cause for the difference between the Berkovich and Vickers crack lengths is then the number of cracks and the distribution of the driving force over those cracks.

Both Harding and Dukino and Swain utilized Ouchterlony's stress intensity factor solution for a two-dimensional (2D) star-shaped through crack to account for difference between the Berkovich and Vickers indenters. Harding modified Ouchterlony's solution to distribute the driving force over the number of cracks, *n*. Assuming that the 2D solution is applicable to the three-dimensional (3D) solution, the resulting pre-factor, *k(n)*, for a given material, i.e., *E/H*, the modified fracture toughness equation has the following form:

$$\frac{K_{Ic}c^{3/2}}{\alpha P_{max}} = k(n) = \frac{1}{n}\sqrt{\frac{n/2}{1 + n/2\pi\, sin\left(2\pi/n\right)}}, \tag{7.1}$$

where *α* is a constant for a given value of *E/H*. While Harding and Dukino and Swain could only compare the Berkovich and Vickers geometries, the simulation data herein allows for the evaluation of Harding's modified solution over a wider range of number of cracks. Figure 7.12 shows a comparison between *k(n)/k(4)*, arbitrarily chosen, and the conical indenter simulation ratio of $K_{Ic}c^{3/2}/P_{max}$ for a given value of *n* and $K_{Ic}c^{3/2}/P_{max}$ result from the 4-crack system as a function of the number of cracks. Harding's modified stress intensity factor solution provides an excellent description of the data except in the case of a 2-crack system, which is physically not important when working with pyramidal indenters. Based on results from previous sections of this dissertation, one consideration for the driving force for crack extension is based on the plastic zone volume controlling displacements at the crack mouth. Physically, the plastic deformation of the indentation creates a fixed amount of material available for wedging open the crack and from a symmetry viewpoint, this volume must be distributed equally among the cracks.

With an understanding of the correction factor that needs to made for the number of cracks, the discussion now turns to examining the influence of indenter angle on indentation cracking with 3-sided indenters with a focus on developing an equation for measuring fracture toughness. Keeping in line with the pile-up theme, Johnson plots constraint factor versus *E/Htanθ* , where *θ* is the centerline-to-face angle, as a way to include indenter angle, noting that his

derivation is for blunt angles. Previous results indicate two regimes of indentation cracking: first, a low *E/H* regime where both the elastic and plastic stresses play an important role in developing a half-penny crack geometry; and second, a high E/H regime (*E/H* > ~30) for the Berkovich and Vickers indenters) where plasticity dominates the development of Palmqvist cracks.

The two regimes have different scaling relationships between load, crack length and material properties. From previous cohesive finite element simulations, the low *E/H* (median cracking) regime for the Vickers indenter exhibits the following empirical scaling relationship:

$$\frac{K_{Ic}c^{3/2}}{P_{max}} = Aln\left[\frac{E}{H} - B\right], \tag{7.2}$$

where *A* is a constant. The value of *B* is a result of the fact that *E/H* is not zero for a purely elastic material wherein no surface cracking occurs after complete unloading of the indenter. *E/H* for an elastic material is dependent on indenter angle and can be estimated via Sneddon's solution for contact of an elastic material with a rigid conical indenter [8]:

$$B \approx \frac{E}{H}\Big|_{elastic} = \frac{2(1-\upsilon^2)}{\cot\theta}. \tag{7.3}$$

Values of *B* from the finite element simulations for the 65.3° and 75° indenters were found to be 3.9 and 7.8 respectively, while Sneddon's equation results in values of 4.0 and 7.0, respectively. Note that hardness in this work is measured from the contact area at peak load and not from the conventional measurement of area of the residual impression. Conventional hardness would be infinite for an elastic material and *E/H* would then be zero.

A complex analytical solution to the stress intensity factor for the high *E/H* regime (Palmqvist cracking) was developed in previous sections of this dissertation for the Vickers indenter. However, the solution can be approximated through the following empirical scaling relationship:

$$\frac{cH^2}{K_{IC}^2} = \beta\left(\frac{P_{max}H^3}{K_{IC}^4}\right)^m, \tag{7.4}$$

where β is a constant and the exponent, m, lies between ~0.60 to ~0.80. A closer inspection of the results from the indenter angle study show that the 75° indenter exhibits median cracking while the 45° and 55° degree indenters exhibit Palmqvist cracking. These results are physically consistent with Johnson's ideas as well as a number of other results wherein decreasing the indenter angle increases the amount of pile-up at the contact periphery, i.e., sharper indenter angles decrease the value of E/H at which the contact transitions from elastic-plastic to plastic dominated .

Lawn, Evans, and Marshall derived an indenter angle dependence of $\cot^{2/3}\theta$ for the median cracking regime. Plots of $K_{Ic}c^{3/2}/P_{max}\cot^{2/3}\theta$ for the 65.3° and 75° indenters as a function of the right hand side of Eq. 7.2 are shown in Fig. 7.13. Good agreement is found, and the results are only slightly sensitive to the value of the angle exponent. It would be nice to have a larger dataset to evaluate the exponent, but the range of indenter angles that result in median cracking in these types of simulation was limited to angles of ~60° to 80°.

Figure 7.14 shows the results of plotting the normalized load and normalized crack length for the 45° and 55° degree indenters, as well as the results from Berkovich indentation cracking simulations in the Palmqvist regime. The influence of indenter angle is found to be negligible as results for all three of the indenters are collinear. Plasticity blunts the effects of indenter angle.

Incorporation of the two indenter geometric dependencies described above into Eqs. 7.2 and 7.4 leads to the most complete description of the relationship between material properties, indenter loads, indenter geometry, and crack length. Additionally, the constants in Eqs. 7.2 and 7.4 can be estimated from fits to the finite element data. For the median cracking regime, fracture toughness can be estimated with the following equation:

$$\frac{K_{Ic}c^{3/2}}{P_{max}\,cot^{2/3}\theta} = 0.15k(n)ln\left(\frac{E}{H} - \frac{2(1-v^2)}{\cot\theta}\right). \tag{7.5}$$

Fracture toughness for the Palmqvist cracking regime is insensitive to indenter angle and can be estimated from:

$$\frac{cH^2}{K_{IC}^2} = 0.78\left(k(n)\frac{P_{max}H^3}{K_{IC}^4}\right)^{0.62}. \quad (7.6)$$

While Eqs. 7.5 and 7.6 are results of empirical fits to the finite element data, previous sections of this dissertation have provided strong physical evidence for both the form of the equations and reasoning for the transition from one to the other depending on the crack and contact geometries. It is also important to note here that these equations do not include Poisson's ratio effects, which are not accounted for in this chapter. Interestingly, an exponent of 2/3 on the right hand side of Eq. 7.6 would result in a fracture toughness relationship similar to the one proposed by Tanaka [9, 10] where the relationship between P_{max} and $c^{3/2}$ is only determined by the fracture toughness and not the ratio of elastic modulus to hardness, E/H. The empirical fit to the finite element data results in an exponent of 0.62 which is close to the value of 2/3.

Harding generated experimental indentation cracking results with a 3-sided pyramidal indenter having a centerline-to-face angle of 35° (cube corner indenter) for soda-lime glass, pyrex, silicon (100) and (111), fused quartz, germanium (111), sapphire (111), spinel (100), and silicon carbide SA. For purposes of this work, it is assumed that Harding's results lie in the Palmqvist regime due to the sharpness of the indenter. Harding's results are plotted alongside Vickers and Berkovich finite element results from the Palmqvist regime as well as the 45° and 55° finite element results in Fig. 7.15. The FE data and experimental data are in remarkable agreement considering Harding's data includes single crystal, polycrystalline, and amorphous materials [1].

Finally, the results from this work can be summarized in terms of the utility of measuring fracture toughness with pyramidal indenters. The choice of indenter angle allows for tailoring the response of the material, i.e., sharper indenters will force the plasticity dominated Palmqvist regime, while blunt indenters will result in the elastic-plastic median cracking regime. While empirical formulas have been generated for both the median and Palmqvist cracking regimes, working in the Palmqvist regime has a number of advantages:

First, the threshold load for cracking is much lower for sharper indenters as compared to blunt indenters; Second, much smaller indents can be made allowing for estimation of material properties at smaller length scales; Third, working in the Palmqvist regime does not require accurate knowledge of the elastic modulus, a result that may prove beneficial to measuring fracture toughness in anisotropic materials.

7.5. Conclusions

Cohesive finite element simulations of indentation cracking with pyramidal indenters have been used to study the effects of indenter geometry on the relationships between material properties, applied loads, and crack lengths. Specifically, the influences of the number of corners/cracks and indenter centerline-to-face angle have been accounted for and empirical relationships with physical origins have been developed from the finite element data. Additionally, the results herein are in remarkable agreement with experimental indentation cracking data over a wide range of materials. The important conclusions that can be drawn from this work are as follows:

1. Experimental results of Berkovich indenter crack lengths ~10% greater than Vickers indenter crack lengths for the same load and material are mirrored in the cohesive finite element simulations.
2. Ouchterlony's modified stress intensity factor solution for a 2D star shaped though crack accurately explains the difference between the Berkovich and Vickers crack lengths.
3. In the median cracking regime (low *E/H* and blunt indenters), indenter angle has a $cot^{2/3}\theta$ dependence, consistent with the derivation of Lawn, Evans, and Marshall.
4. Indenter angle effects are negligible in the Palmqvist cracking regime (high *E/H* and sharp indenters) where plastic flow at the surface during contact blunts the influence of indenter angle.

5. Finite element results from simulations of three-sided pyramidal indnters having centerline-to-face angles of 45° and 55° exhibit Palmqvist type cracking over an *E/H* regime that encompasses most brittle ceramic materials. Simulations of a 75° indenter exhibited median type cracking over the same regime of *E/H*.
6. The results from this work have been used to incorporate and account for material properties and indenter geometry into relationships meant for estimating fracture toughness from indentation cracks (Eqs. 7.5 and 7.6).

References

1. Harding, D.S., *Craking in Brittle Materials During Low-Load Indentation and its Relation to Fracture Toughness.* PhD Thesis, Rice University, 1995.
2. Pharr, G.M., D.S. Harding, and W.C. Oliver, *Measurement of Fracture Toughness in Thin Films and Small Volumes Using Nanoindentation Methods.* 1993: p. 449-461.
3. Dukino, R.D. and M.V. Swain, *Comparative Measurement of Indentation Fracture Toughness with Berkovich and Vickers Indenters.* Journal of the American Ceramic Society, 1992. **75**(12): p. 3299-3304.
4. Lawn, B.R., A.G. Evans, and D.B. Marshall, *Elastic-Plastic Indentation Damage in Ceramics - the Median-Radial Crack System.* Journal of the American Ceramic Society, 1980. **63**(9-10): p. 574-581.
5. Ouchterlony, F., *Stress Intesnity factors for the Expansion Loaded Star Crack.* Engineering Fracture Mechanics, 1976. **8**: p. 447-448.
6. Simulia, *ABAQUS User's Manual*. 2008: Simulia Co.
7. Gao, Y.F. and A.F. Bower, *A simple technique for avoiding convergence problems in finite element simulations of crack nucleation and growth on cohesive interfaces.* Modelling and Simulation in Materials Science and Engineering, 2004. **12**(3): p. 453-463.
8. Sneddon, I.N., *The relation between load and penetration in the axisymmetric boussinesq problem for a punch of arbitrary profile.* International Journal of Engineering Science, 1965. **3**(1): p. 47-57.
9. Tanaka, K., *Elastic/plastic indentation hardness and indentation fracture toughness: The inclusion core model.* Journal of Materials Science, 1987. **22**(4): p. 1501-1508.
10. Tanaka, M., *Fracture toughness and crack morphology in indentation fracture of brittle materials.* Journal of Materials Science, 1996. **31**(3): p. 749-755.

APPENDIX 7.1.

Table 7.1. Material, indenter, and cohesive element input properties in the finite element simulations.

Simulation	**θ** (deg)	**E/Y**	**v**	**G_{Ic}** (GPa um)	**σ_c** (GPa)	**# of Cracks**	**# of Corners**
Vickers vs Berkovich	70.3	10-400	0.25	0.01	0.30	4 and 3	4, 3
Number of Cracks	70.3	20				2-6	3-6
Indenter Angle	45, 55, 65.3, 75	20				3	3

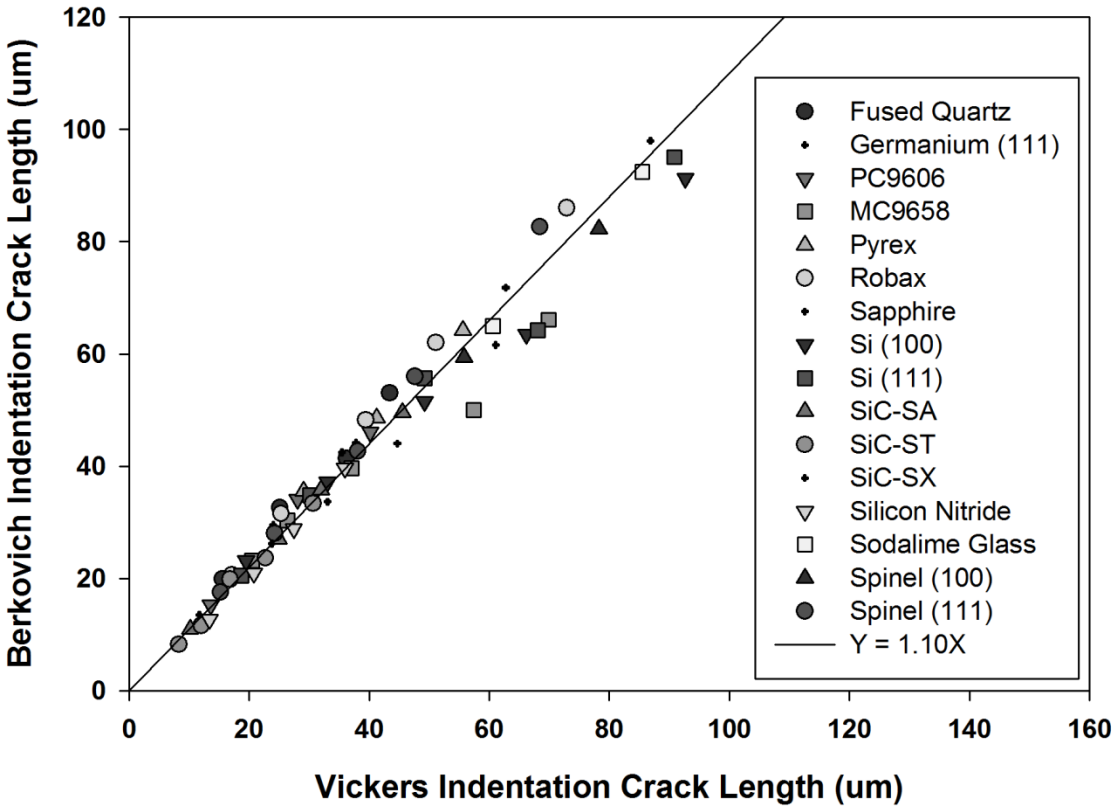


Figure 7.1. Harding's experimental results on crack lengths measurements from Vickers and Berkovich indentations at the same load in a number of brittle materials.

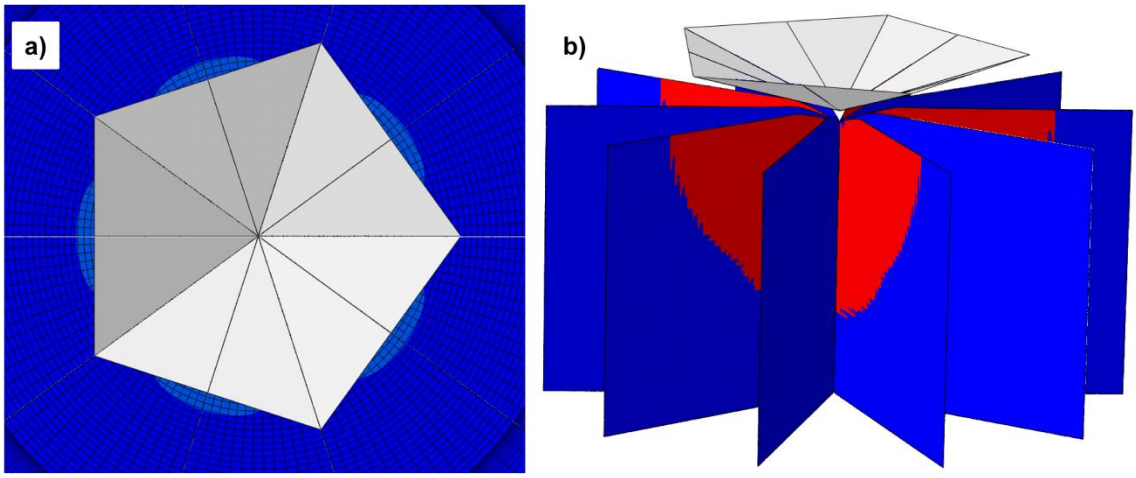


Figure 7.2. Example finite element model of a multi-sided pyramidal indenter: (a) top down view of a 5-sided indenter; and (b) resulting quarter-penny cracks occurring on planes aligned with indenter corners.

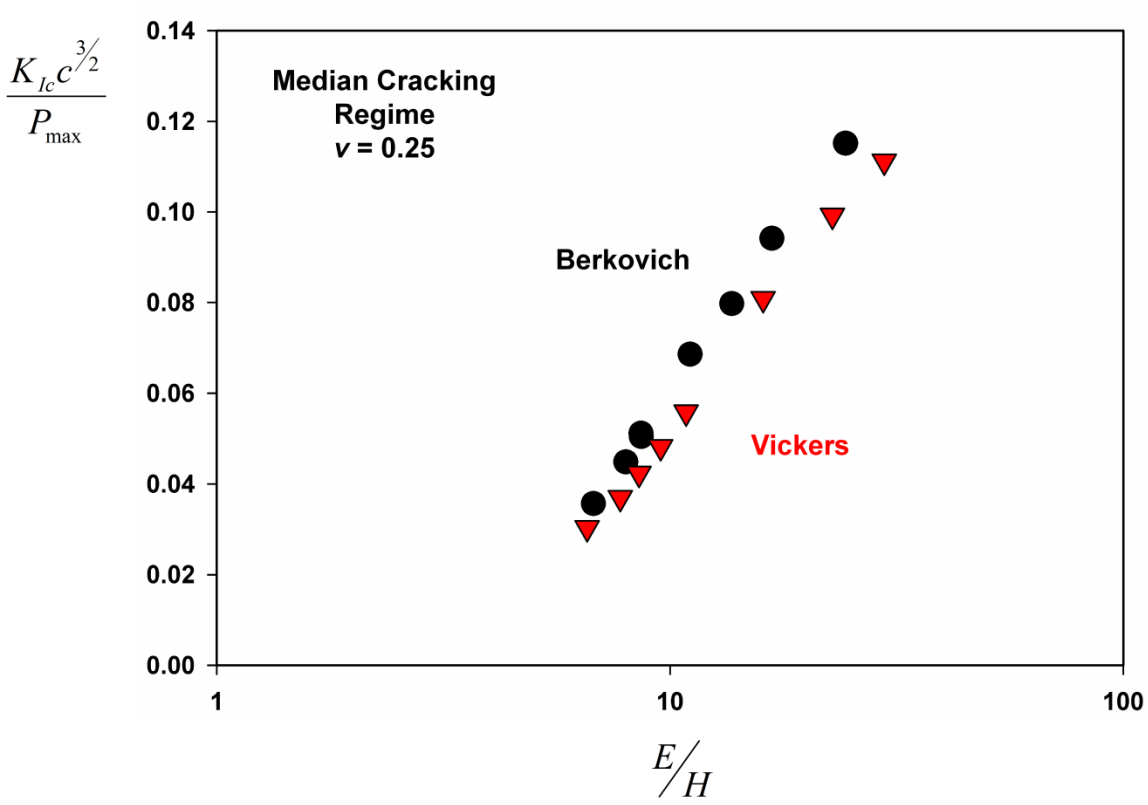


Figure 7.3. The non-dimensional cracking parameter, $K_{Ic}c^{3/2}/P_{max}$, plotted as a function of *E/H* (semi-log scale) for materials in the median indentation cracking regime.

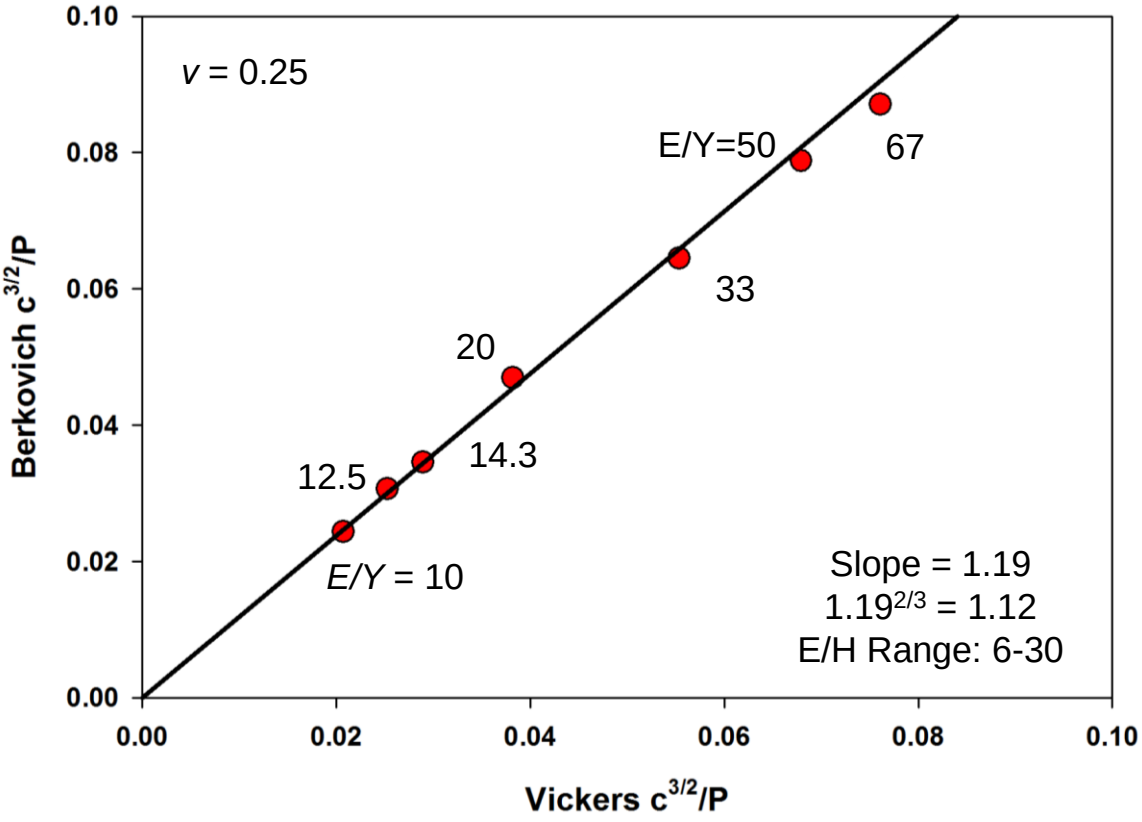


Figure 7.4. Berkovich results versus Vickers results for materials in the median cracking regime having a constant fracture toughness.

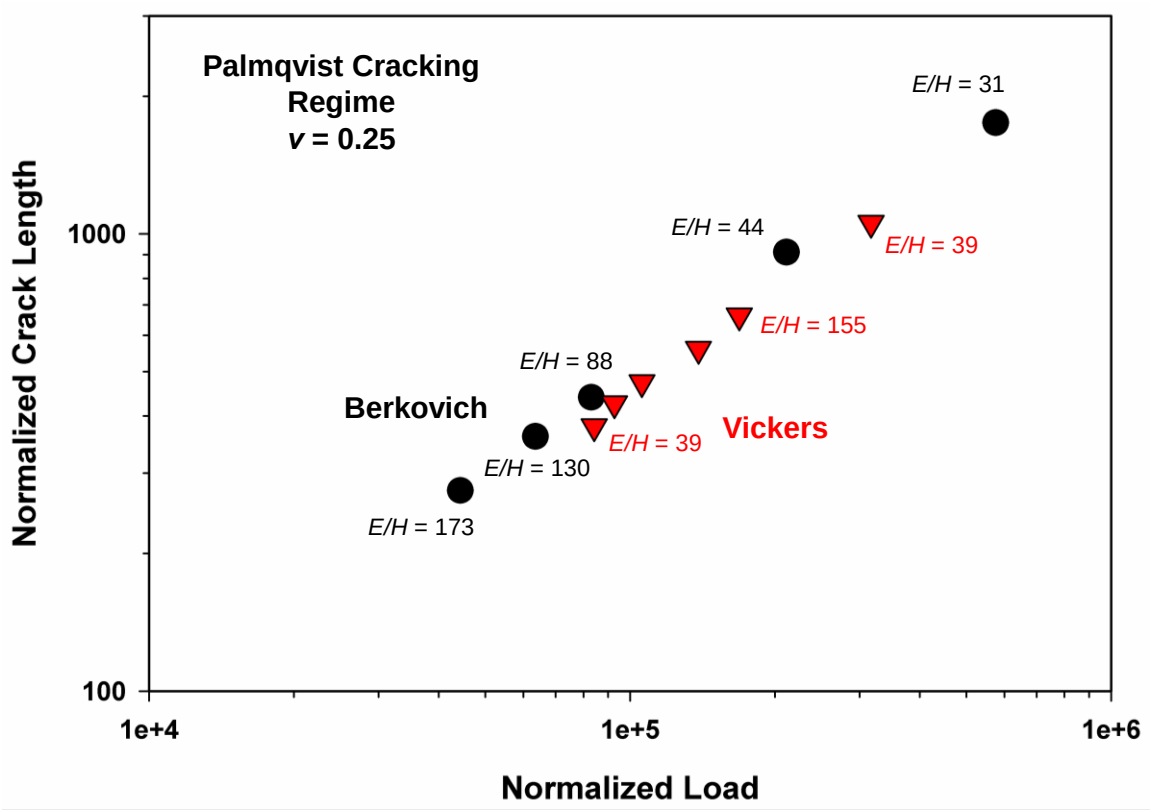


Figure 7.5. Normalized crack lengths plotted as a function of normalized load for Vickers and Berkovich indenters in the Palmqvist regime.

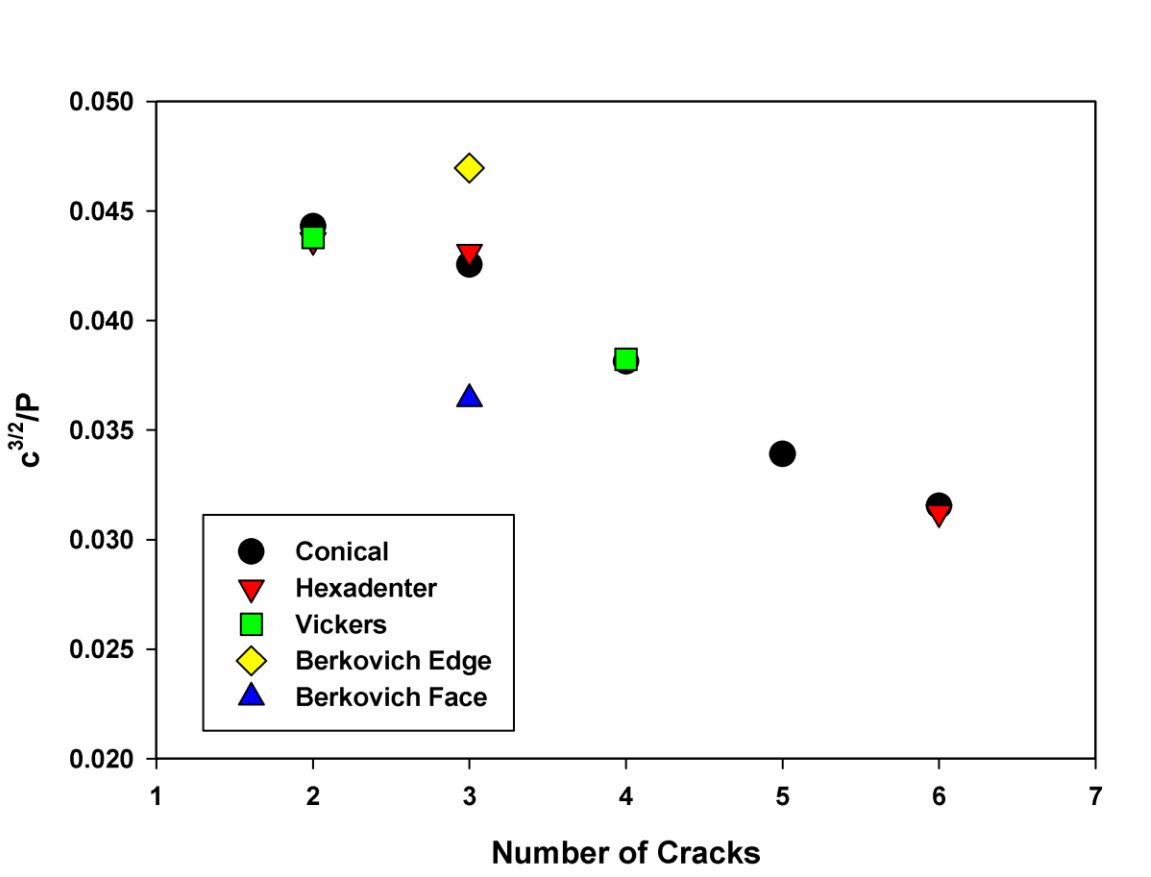


Figure 7.6. The non-dimensional cracking parameter plotted as a function of the number of cracks for pyramidal indenters having different sides.

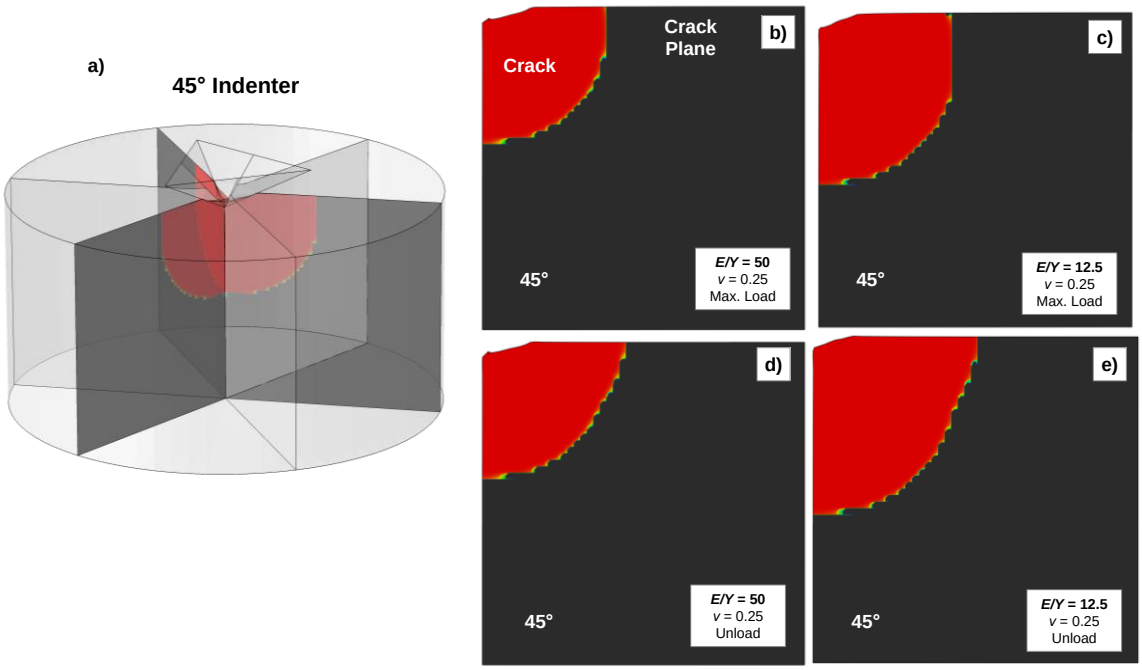


Figure 7.7. Indentation cracking geometries observed in simulations of a 3-sided indenter having a centerline-to-face angle of 45°: finite element model (a); geometries at maximum load for *E/Y* ratios of 50 and 12.5, respectively (b,c); and unloaded geometries (d,e).

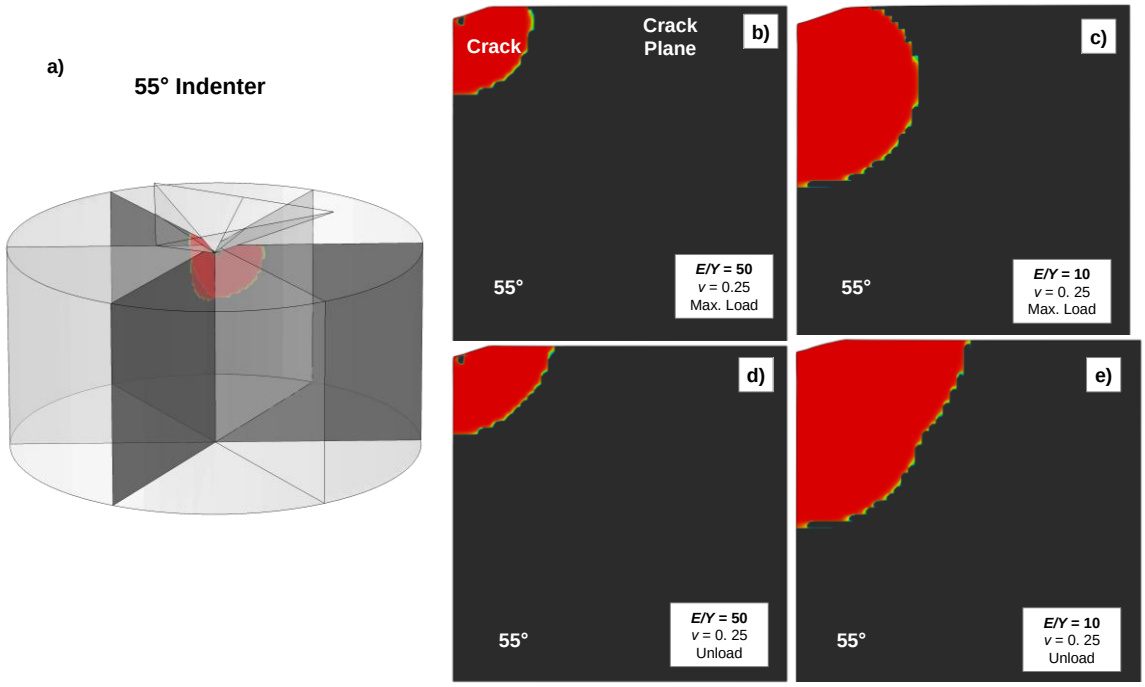


Figure 7.8. Indentation cracking geometries observed in simulations of a 3-sided indenter having a centerline-to-face angle of 55°: finite element model (a); geometries at maximum load for *E/Y* ratios of 50 and 10, respectively (b,c); and unloaded geometries (d,e).

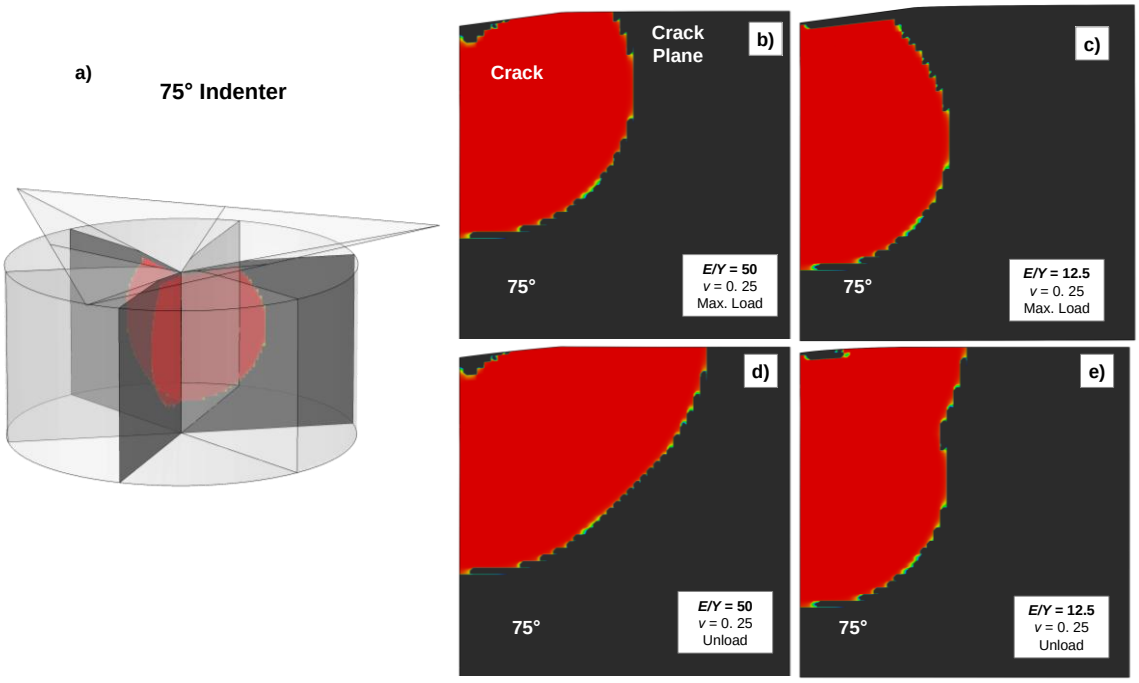


Figure 7.9. Indentation cracking geometries observed in simulations of a 3-sided indenter having a centerline-to-face angle of 75°: finite element model (a); geometries at maximum load for *E/Y* ratios of 50 and 12.5, respectively (b,c); and unloaded geometries (d,e).

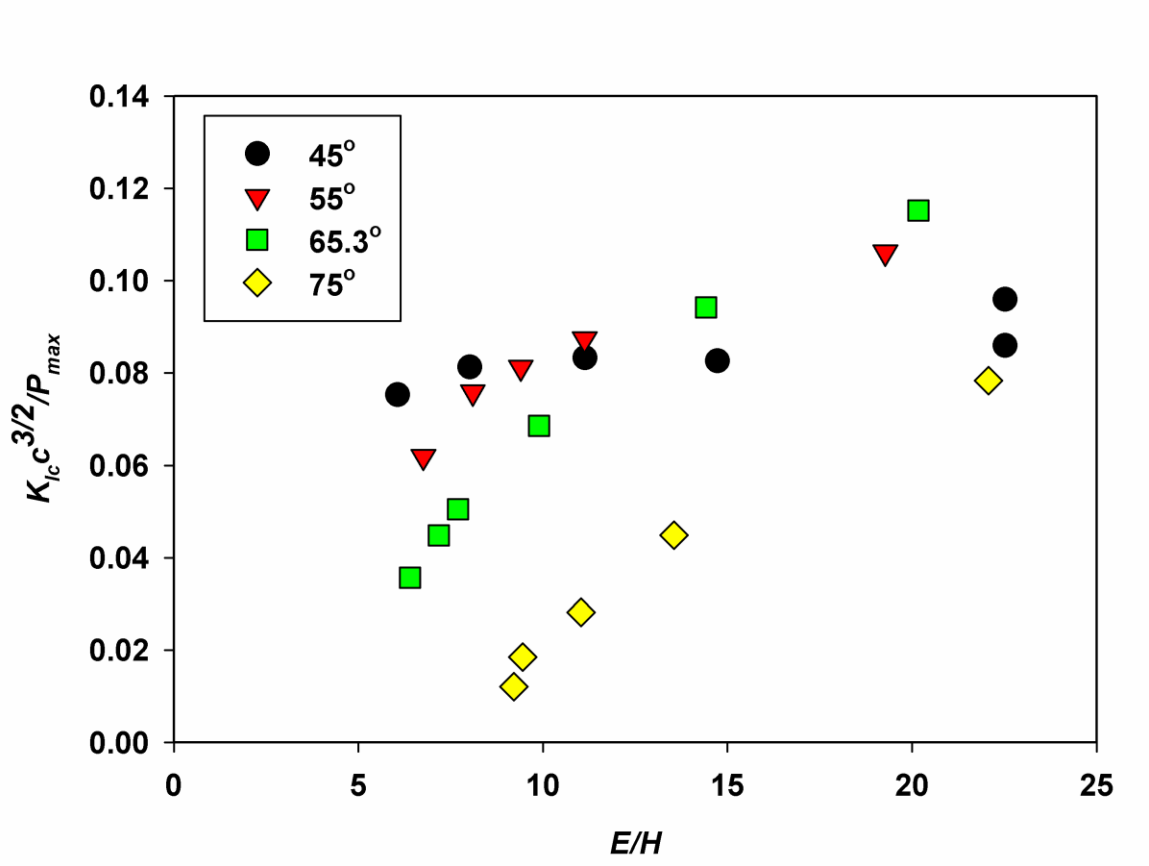


Figure 7.10. The non-dimensional cracking parameter plotted as a function of *E/H* for 3-sided indenters having different centerline-to-face angles.

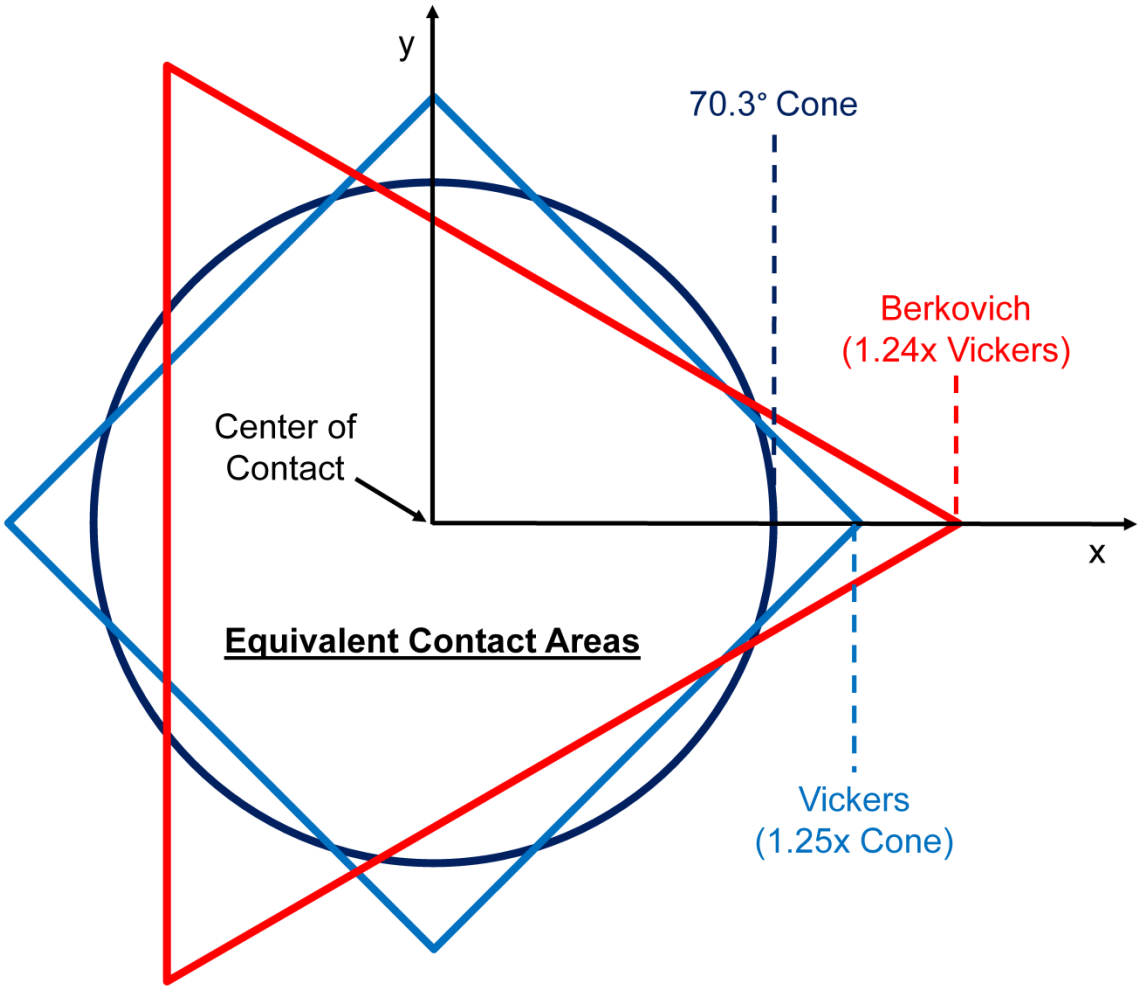


Figure 7.11. Equivalent contact area outlines for 70.3° cone, Vickers, and Berkovich indenters.

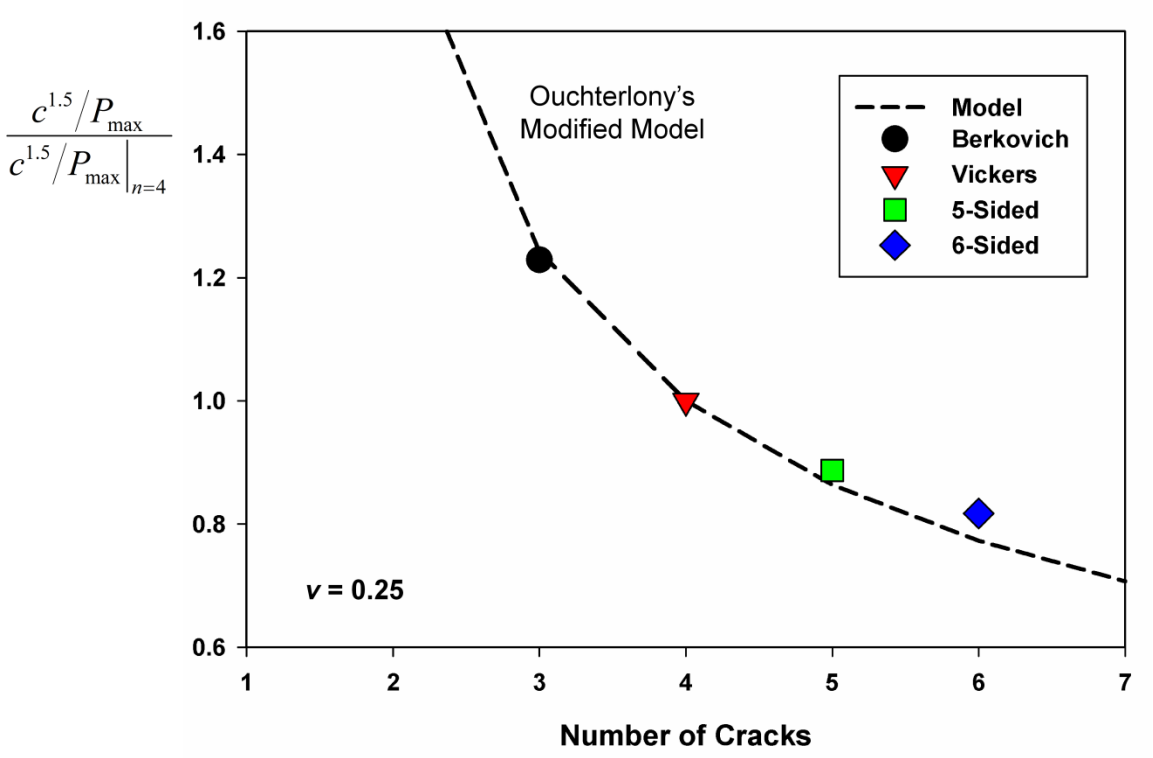


Figure 7.12. Ouchterlony's stress intensity factor model compared to results from indentation cracking simulations having different numbers of cracks.

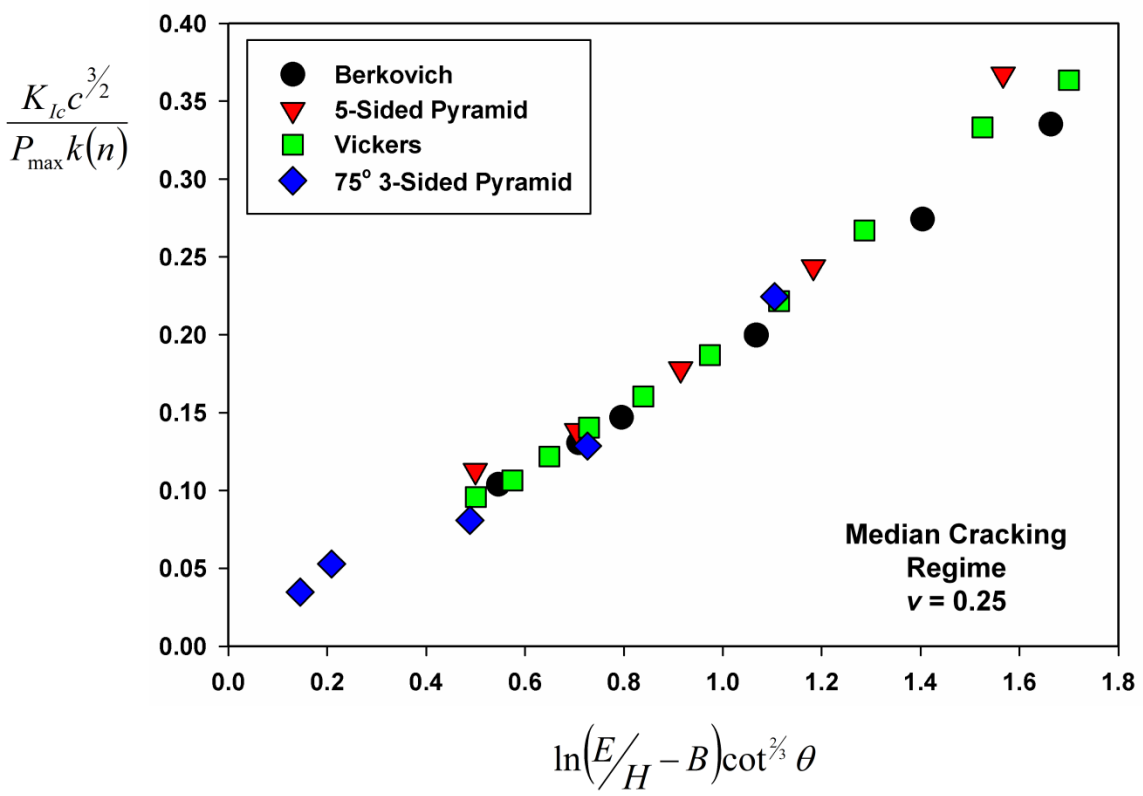


Figure 7.13. The entire simulation dataset in the median cracking regime plotted as a function of Eq. 7.5.

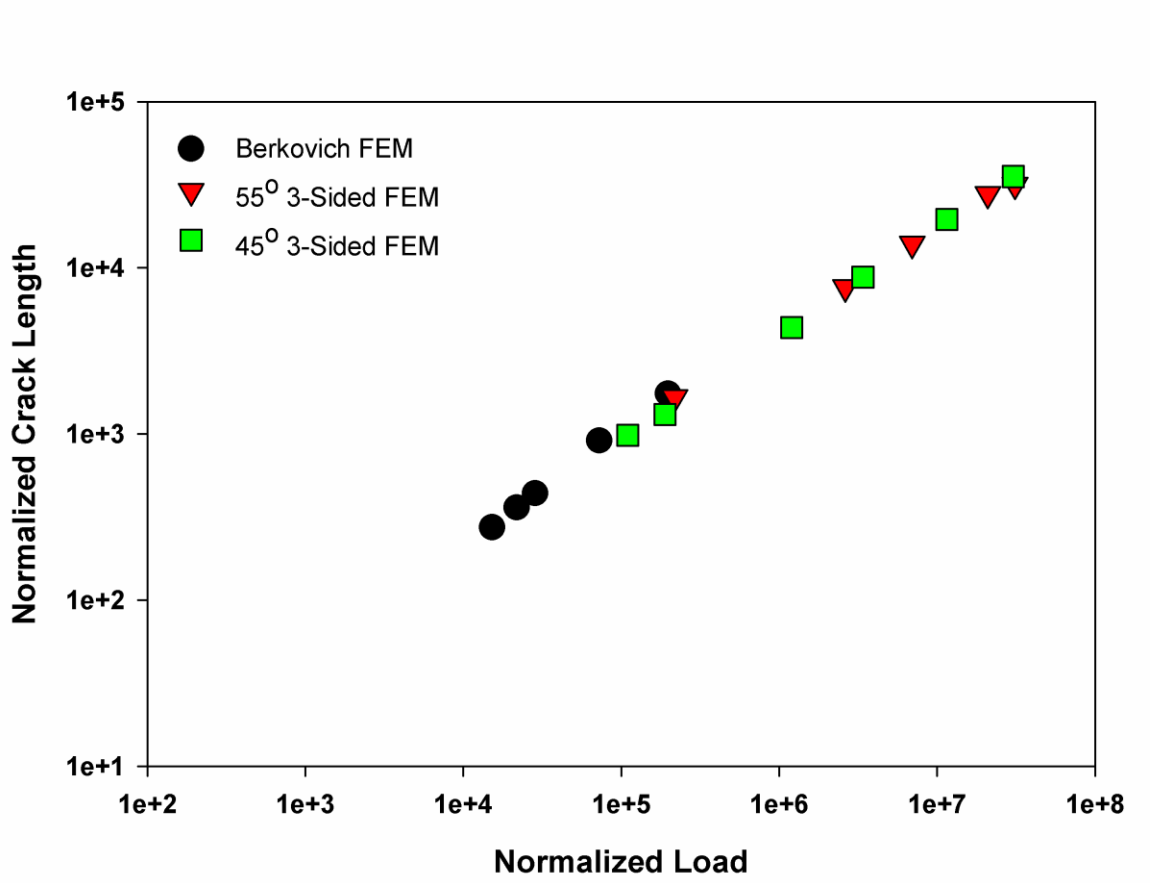


Figure 7.14. The entire simulation dataset in the Palmqvist regime plotted as a function of Eq. 7.6.

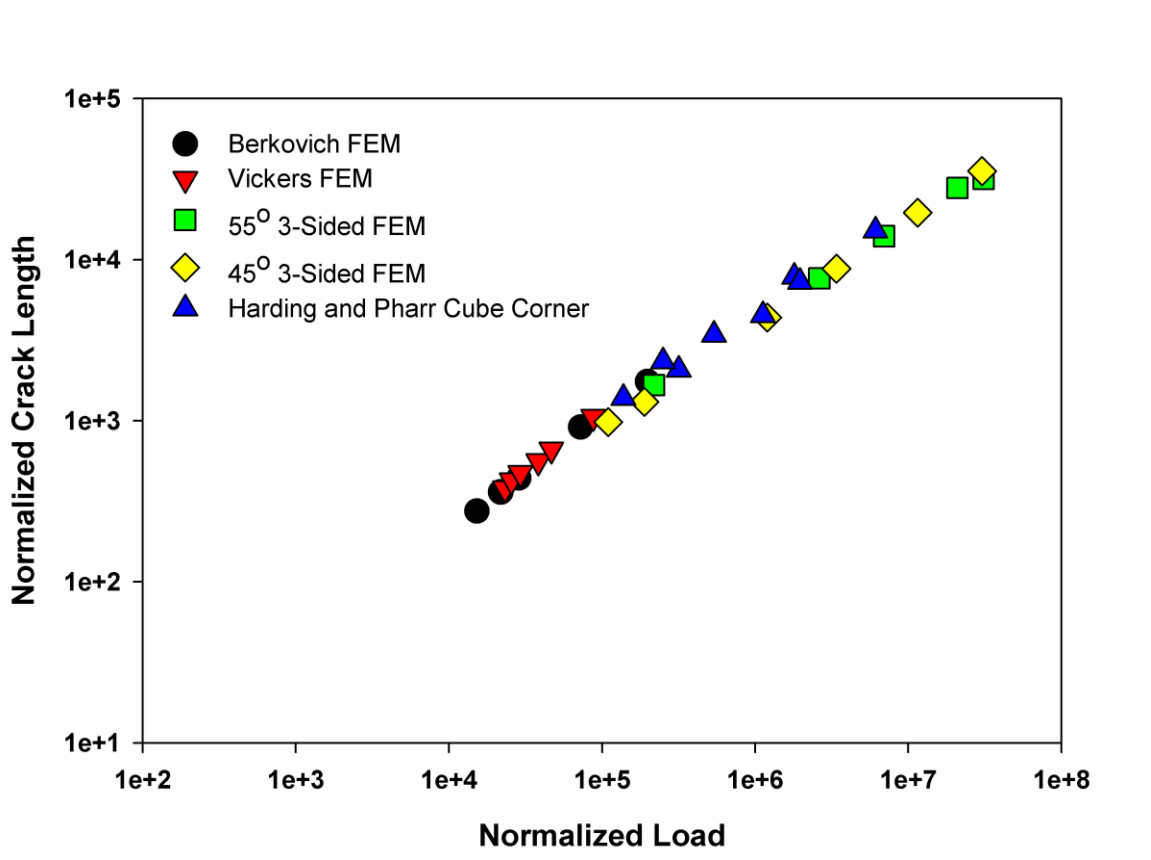


Figure 7.15. Harding's experimental cube-corner indentation cracking results plotted along with the finite element results.

CHAPTER VIII

SUMMARY AND CONCLUSIONS

Cohesive zone finite element simulations of pyramidal indentation cracking in brittle materials have been carried out in order to: (1) critically examine the Lawn, Evans, and Marshall model of indentation cracking that relates fracture toughness to indentation data; (2) determine the underlying physical mechanisms of indentation crack growth from a continuum view and their relationship to material properties; and (3) provide a platform from which future simulations can add more complex material behavior as well as guidance for experimental measurements of fracture toughness. The results and conclusions of the simulations were divided into six chapters in this dissertation that build upon one another.

Simulations of a standard fracture toughness test geometry were used in Chapter II to identify the regime in which cohesive zone finite element simulations could be used in combination with linear-elastic fracture mechanics. In addition, two-dimensional wedge, Vickers, and Berkovich indentation cracking geometries were simulated. It was found that a crack length of at least ten times the size of the process zone was required for linear-elastic fracture mechanics to be valid. Crack initiation during indentation was highly dependent on cohesive zone properties while crack extension in the long crack limit was only dependent on fracture toughness. Short crack behavior, i.e., cracks less than ten times the process zone size, was dominated by the process zone. Most importantly, the simulations resulted in *median* and *Palmqvist* crack geometries that were consistent with experimental observations.

Detailed simulations of two-dimensional wedge indentation cracking in elastic-perfectly plastic brittle materials were provided in Chapter III. The Lawn, Evans, and Marshall model was derived for the two-dimensional case and compared to simulation results over a wide range of material properties and indenter angles. It was found that the Lawn, Evans, and Marshall model's reliance on Hill's expanding cavity model limits its predictive capabilities over the range of materials examined in the simulations. The free surface had little to no influence on crack growth and crack growth did not occur on unloading as elastic

contact stresses on the median crack plane were minimal. Crack extension was found to follow a simple stress intensity factor solution where the driving force was crack mouth opening displacement caused by expansion of the plastic zone. The simple fracture toughness relationship accounted for the influence of elastic modulus, Poisson's ratio, hardness, and indenter angle. While the results from such two-dimensional relationships may not be experimentally practical, they help in understanding the physical mechanisms underlying indentation crack growth in a much simpler geometry than that of pyramidal indenters.

The crux of this work, Chapter IV, was three-dimensional simulations of the four-sided pyramidal Vickers indentation cracking geometry in elastic-perfectly plastic brittle materials. A critical examination of the Lawn, Evans, and Marshall model and assumptions therein was of primary interest. Two important conclusions were drawn from the Vickers simulations: (1) The Lawn, Evans, and Marshall model works well over a small range of the ratio of elastic modulus to hardness, a range where indentation behavior is consistent with Hill's expanding cavity model, but deviated significantly outside of this limited range; and (2) there was a dramatic change in indentation cracking behavior as the ratio of elastic modulus to hardness moved from more ceramic-like materials toward metallic-like materials. Materials with lower values of elastic modulus to hardness, where elastic deformation dominates, exhibited *median* like cracking behavior where surface cracking was only evident upon unloading of the indenter. More metallic-like materials, where plasticity dominates deformation, exhibited *Palmqvist* type cracking where surface crack extension occurred on loading and unloading. This transition in indentation cracking behavior was consistent with experimental observations in glass (*median*) and tungsten carbide (*Palmqvist*). To the best of our knowledge, this was the first report of the change in cracking behavior being linked to the way in which a material accommodates deformation during the indentation process.

Observations and numerical data from cohesive zone finite element simulations of Vickers indentation cracking were used to relate material

properties, applied loads, and crack lengths to simple stress intensity factor solutions in Chapter V. It was found that a stress intensity factor solution of the insertion of a rigid wedge, similar to the two-dimensional wedge result, was able to describe fracture toughness measurements in the *median* cracking regime. However, contrary to the two-dimensional wedge solution, the presence of the free surface was accounted for through material pile-up/sink-in at the contact periphery. Increasing the ratio of elastic modulus to hardness from 10 to 30 resulted in changes in pile-up deformation at the contact periphery giving rise to material behavior not considered in the Lawn, Evans, and Marshall model for median type cracks.

Significant error in fracture toughness was found when the derived solution from chapter V was applied to the *Palmqvist* regime, and a separate stress intensity factor solution was required and developed in Chapter VI. A stress-based solution was chosen for the Palmqvist regime where the fact that large changes in the ratio of elastic modulus to hardness resulted in nearly negligible changes in deformation behavior. The result was a remarkably simple relationship between fracture toughness, applied load, and crack length that was independent of material properties other than Poisson's ratio. Measurements of fracture toughness with the *Palmqvist* model were only valid when plastic deformation dominated the materials response to indentation.

Chapter VII reported results from cohesive zone finite element simulations of indentation cracking that focused on the influence of indenter geometry on cracking behavior. Simulations of the three-sided pyramidal Berkovich indenter along with three-sided indenters with various centerline-to-face angles were used for comparison with the Vickers indenter results and stress intensity factor solutions. In addition, the influence of the number of corners on an indenter was explored and compared to experimental results. It was found that the simulations of Berkovich indentation cracking gave rise to crack lengths that were approximately ten percent greater than a Vickers indentation on the same material and applied load. This result was consistent with experimental results

from Harding and Dukino and Swain in addition to validating the use of Ouchterlony's stress intensity factor solution to account for the number of indenter corners. More importantly, the results in chapter VII substantiated the stress intensity factor solutions in Chapters V and VI. Furthermore, it was found that the indentation cracking response could be tailored such that plastic deformation dominates by using indenters with smaller centerline-to-face angles like the cube-corner geometry. This tailoring has important ramifications to accurately measuring fracture toughness with indentation cracking. Experiments and simulations in the *Palmqvist* regime compared extremely well with the fracture toughness relationship developed in Chapter VI where the influence of material properties and indenter angle are negligible.

Ultimately, experimental measurements of fracture toughness using the ideas and results found in this dissertation are only useful when the assumptions and conditions of the cohesive zone finite element simulations are met. Anisotropy, grain size, deformation not consistent with Mises yielding, friction, hardening, short crack behavior, etc..., may have influence on indentation crack behavior not accounted for in these models. That being said, the observations provided by the simulation work create a platform for accounting for more complex material properties by considering deformation behavior and the ability to tailor a response by implementing different indenter geometries. Finally, the utility of indentation cracking is not limited to estimating fracture toughness. Plasticity at the contact, crack mouth opening displacements at the elastic/plastic boundary, and crack tip deformation provide ample opportunities to study intrinsic deformation behavior of materials. Furthermore, the volume of material over which this unique deformation occurs can be explored over different length scales with pyramidal indenters.

APPENDIX

This appendix details the meshing strategy and methods used during the course of the cohesive finite element simulations of indentation cracking. While the salient points of the mesh geometry and properties have been previously described for reproducibility, this section is intended to provide helpful information for those looking to generate meshes similar to the ones used in this work. This appendix is broken down into two sections:

1. Meshing strategy and mesh generation.
2. Example input file.

The meshing strategy herein is certainly not the only method for using cohesive elements in an indentation simulation, but one that has proven to be robust with a relatively simple implementation. All of the models have used input files for running simulations, however, the ABAQUS™ CAE software package could also be used for input.

Meshing Strategy

The following discussion refers to "cohesive elements" and "material" elements. Cohesive elements are those that comprise the crack and have the cohesive zone constitutive behavior. Material elements are those outside of the crack and have material behavior specified by the *ELASTIC and *PLASTIC commands in ABAQUS™.

The standard mesh for indentation simulations has nodes that are densely spaced at and near the contact where strains and strain gradients are most intense. This high density ensures that the contact conforms to the shape of the indenter in addition to ensuring accuracy in calculated loads and contact areas. For computational savings, the nodes become less dense further away from the contact. Simulations of indentation cracking have the same requirements with the added provision that the mesh be dense enough on the prospective crack path to accurately model cohesive zone behavior. Low density meshes may lead to inconsistencies with the input and output cohesive element constitutive behavior. A common misconception is that only the cohesive elements need be dense on the prospective crack path. However, the density of material elements

must also be fine enough to capture the strain and strain gradients at the crack tip as well as the tractions at the boundary of the cohesive zone. The requirement for mesh density at the contact as well as the crack path is not a problem in two-dimensional (2D) or axisymmetric problems, but can become an issue in three-dimensional (3D) problems where the number of elements, and thus computational requirements, may be limited by time or machine constraints.

The natural tendency to improve calculation accuracy while limiting calculation time is to take advantage of the symmetry that arises in indentation problems and boundary conditions become important. Symmetry boundary conditions need to be placed on both the material mesh and the indenter. The latter is accomplished by specifying displacement conditions on the reference node of the rigid indenter. The size of the mesh (e.g., height and width in 2D) must be large enough such the outer boundaries do not influence the strain field induced by the indenter. Once the mesh is large enough compared to the size of the contact, the difference between "roller" or "fixed" boundary conditions on the bottom of the mesh is irrelevant in most cases.

Further care must be taken when considering boundary conditions in indentation cracking simulations. Specifically, crack closure may occur due to the expansion of the indentation plastic zone along the crack path. For example, refer to Fig. 2.8 in Chapter 2 of this dissertation. Symmetry boundary conditions are only placed on the left nodes of the cohesive elements in the 2D wedge simulations, while the right nodes of the cohesive elements and the adjacent material nodes have no boundary conditions as they must be free to displace as the crack progresses. In the absence of crack closure (e.g., the center cracked tension panel simulations in Section 2) these boundary conditions accurately reflect the model. However, crack closure that occurs due to the compressive stresses of the indentation plastic zone results in negative material displacements perpendicular that are non-physical. The solution to the crack closure and symmetry problem was to place a rigid element along the symmetry plane that is in contact with the material elements. The contact formulation

prevents negative material displacements while maintaining symmetry. In order to verify that this strategy does not impose constraints that are invalid, 2D simulations of full meshes (i.e., both sides of the contact have been modeled) were run. The results (crack length, load, hardness, etc...) were nearly identical in all cases. Similar results were found in 3D simulations.

Note here, that symmetry conditions must be accounted for in calculating the value of fracture energy. Crack opening displacements are actually twice that of those measured from the model and thus fracture energy is doubled. In addition, because initial crack opening displacement is zero, the initial thickness of the cohesive elements is also zero. This means that the top and bottom nodes of the cohesive elements (referring to the opening direction) are in the same position. Applied boundary conditions must give rise to the same nodal displacements in the absence of cohesive element separation. The *EQUATION command in ABAQUS™ can be a useful way for implementing this condition.

Finally, it is worth mentioning that scaling and optimization of the size of the mesh can be difficult. The size of the contact, plastic zone, and crack tip must not be influenced by outer boundaries. In addition, under conditions of linear-elastic fracture mechanics, the size of the crack must be at least ten times greater than the size of the process zone. The relative sizes of the contact and the crack scale differently with applied load and one may take precedence over the other leading to a large number of either material or cohesive elements to maintain accuracy. Often, the contact strain field was the determining factor. Thus, in order to generate a general mesh that eliminated changes in systematic error from one mesh to another, a geometry that consisted of three sections was used in both 2D and 3D simulations. The first section contained the contact and crack plane and had the highest density of both material elements and cohesive elements. The second and third sections only contained material elements (i.e., cracks could not propagate into these sections) with a less dense mesh whose sole purpose was to provide a large enough mesh so that outer boundaries did not influence the contact. ABAQUS™ "tie" constraints were used to combine the

three sections. It was found that the tie constraint was nearly the same as a multi-point constraint (MPC) in the limit that strains and strain gradients were minimal at the boundaries between sections. The tie constraint has the added advantage that it is relatively simple to implement in the code.

Because crack lengths and contact sizes as a function of applied load and material properties is not known a priori, the most efficient method for optimizing mesh size was to run a simulation with a coarse mesh that provided approximate size information followed by a simulation with a much finer mesh of the appropriate size. Note that during the course of using cohesive elements, it was found that elements having opening faces of equivalent lengths throughout the mesh tended to work best (i.e., a square mesh).

Mesh Generation and Example Mesh Input File

Mesh generation was accomplished in the command file for 2D simulations while an external program was used to generate node coordinates and element connectivity for 3D simulations. The external program allowed for freedom in controlling mesh geometry/properties in a way that was more flexible than the standard ABAQUS™ software. Attached below is an example 2D wedge indentation cracking input file.

```
**
*HEADING
2D WEDGE INDENTATION - MEDIAN INITIATION
**
*PREPRINT, ECHO=YES
**
**
**********************************************
**  TARGET BLOCK NODE GENERATION
**********************************************
**
**
*NODE, NSET=TOP_LEFT
1, 0, 0
*NODE, NSET=TOP_RIGHT
101, 16.6, 0
*NODE, NSET=BOTTOM_LEFT
90301, 0, -50
*NODE, NSET=BOTTOM_RIGHT
90401, 16.6, -50
**
**
*NFILL, NSET=LEFT_NODES, BIAS=1.00
TOP_LEFT, BOTTOM_LEFT, 300, 301
**
*NFILL, NSET=RIGHT_NODES, BIAS=1.00
TOP_RIGHT, BOTTOM_RIGHT, 300, 301
**
*NFILL, NSET=INNER_NODES, BIAS=0.98
LEFT_NODES, RIGHT_NODES, 100, 1
**
**
**********************************************
**  COHESIVE NODE GENERATION
**********************************************
**
**
*NODE, NSET=COH_TOP_LEFT
500000, 0, 0
*NODE, NSET=COH_TOP_RIGHT
600000, 0, 0
*NODE, NSET=COH_BOTTOM_LEFT
501000, 0, -50
*NODE, NSET=COH_BOTTOM_RIGHT
601000, 0, -50
```

```
**
*NFILL, NSET=COHESIVE_NODES_2, BIAS=1.00
COH_TOP_LEFT, COH_BOTTOM_LEFT, 1000, 1
**
*NFILL, NSET=COHESIVE_NODES_1, BIAS=1.00
COH_TOP_RIGHT, COH_BOTTOM_RIGHT, 1000, 1
**
**
*****************************************
**  RIGHT BLOCK NODE GENERATION
*****************************************
**
**
*NODE, NSET=RB_TOP_LEFT
100001, 16.6, 0
*NODE, NSET=RB_TOP_RIGHT
100051, 1000, 0
*NODE, NSET=RB_BOTTOM_LEFT
105101, 16.6, -50
*NODE, NSET=RB_BOTTOM_RIGHT
105151, 1000, -50
**
*NFILL, NSET=RB_LEFT_NODES, BIAS=1.00
RB_TOP_LEFT, RB_BOTTOM_LEFT, 100, 51
**
*NFILL, NSET=RB_RIGHT_NODES, BIAS=1.00
RB_TOP_RIGHT, RB_BOTTOM_RIGHT, 100, 51
**
*NFILL, NSET=RB_INNER_NODES, BIAS=0.92
RB_LEFT_NODES, RB_RIGHT_NODES, 50, 1
**
**
*****************************************
**  LOWER BLOCK NODE GENERATION
*****************************************
**
**
*NODE, NSET=LB_TOP_LEFT
200001, 0, -50
*NODE, NSET=LB_TOP_RIGHT
200101, 1000, -50
*NODE, NSET=LB_BOTTOM_LEFT
205051, 0, -1000
*NODE, NSET=LB_BOTTOM_RIGHT
205151, 1000, -1000
```

```
**
*NFILL, NSET=LB_LEFT_NODES, BIAS=0.93
LB_TOP_LEFT, LB_BOTTOM_LEFT, 50, 101
**
*NFILL, NSET=LB_RIGHT_NODES, BIAS=0.93
LB_TOP_RIGHT, LB_BOTTOM_RIGHT, 50, 101
**
*NFILL, NSET=LB_INNER_NODES, BIAS=0.93
LB_LEFT_NODES, LB_RIGHT_NODES, 100, 1
**
**
******************************************
**  NODE SET GENERATION
******************************************
**
**
*NSET, NSET=BASE_NODES, GENERATE
90301, 90401, 1
**
*NSET, NSET=SURFACE_NODES, GENERATE
1, 101, 1
**
*NSET, NSET=LB_BASE_NODES, GENERATE
205051, 205151, 1
**
**
******************************************
**  ELEMENT GENERATION
******************************************
**
**
*ELEMENT, TYPE=CPE4
1, 1, 302, 303, 2
100000, 100001, 100052, 100053, 100002
200000, 200001, 200102, 200103, 200002
**
*ELEMENT, TYPE=COH2D4
500000, 500000, 500001, 600001, 600000
**
*ELGEN, ELSET=MATERIAL_ELEMENTS
1, 100, 1, 1, 300, 301, 300, 1, 1, 1
**
*ELGEN, ELSET=RB_MATERIAL_ELEMENTS
100000, 50, 1, 1, 100, 51, 50, 1, 1, 1
**
```

```
*ELGEN, ELSET=LB_MATERIAL_ELEMENTS
200000, 100, 1, 1, 50, 101, 100, 1, 1, 1
**
*ELGEN, ELSET=COHESIVE_ELEMENTS
500000, 1000, 1, 1
**
**
**********************************************
**  ELEMENT SET GENERATION
**********************************************
**
**
*ELSET, ELSET=SURFACE_ELEMENTS, GENERATE
1, 100, 1
**
*ELSET, ELSET=SIDE_ELEMENTS, GENERATE
1, 89701, 300
**
*ELSET, ELSET=RIGHT_ELEMENTS, GENERATE
100, 89800, 300
**
*ELSET, ELSET=BASE_ELEMENTS, GENERATE
89701, 89800, 1
**
*ELSET, ELSET=RB_LEFT_ELEMENTS, GENERATE
100000, 104950, 50
**
*ELSET, ELSET=RB_BASE_ELEMENTS, GENERATE
104950, 105000, 1
**
*ELSET, ELSET=LB_SURFACE_ELEMENTS, GENERATE
200000, 200100, 1
**
**
**********************************************
**  INDENTER GENERATION
**********************************************
**
**
*NODE, NSET=INDENTER_NODES
100000001, 0, 0.01
100000002, 107.22534602547793081781303955523, 50.01
**
*NODE, NSET=INDENTER_REF
900000001, 0.000000000, 1.000000000
```

```
**
*ELEMENT, TYPE=R2D2, ELSET=INDENTER_ELEMENTS
100000001, 100000002, 100000001
**
**
*****************************************
**  SIDE WALL GENERATION
*****************************************
**
**
*SURFACE, TYPE=SEGMENT, NAME=SIDE_WALL
START, 0.0, 0.1
LINE, 0.0, -50
*NODE, NSET=SIDE_WALL_REF
900000002, 0, 0.5
**
**
*****************************************
**  MATERIAL PROPERTIES
*****************************************
**
**
*RIGID BODY,  REFNODE=900000001, ELSET=INDENTER_ELEMENTS
**
*SOLID SECTION, ELSET=MATERIAL_ELEMENTS, MATERIAL=MATERIAL
*SOLID SECTION, ELSET=RB_MATERIAL_ELEMENTS,
MATERIAL=MATERIAL
*SOLID SECTION, ELSET=LB_MATERIAL_ELEMENTS,
MATERIAL=MATERIAL
**
*MATERIAL, NAME=MATERIAL
**
*ELASTIC
100, 0.25
**
*PLASTIC
5
**
**
*COHESIVE SECTION, ELSET=COHESIVE_ELEMENTS,
MATERIAL=C_MATERIAL, RESPONSE=TRACTION SEPARATION,
CONTROLS=CTRLS, THICKNESS=SPECIFIED
1.0
**
*SECTION CONTROLS, NAME=CTRLS, VISCOSITY=1E-5
```

```
**
**
*MATERIAL, NAME=C_MATERIAL
*ELASTIC, TYPE=TRACTION
10E3, 10E3, 10E3
**
*DAMAGE INITIATION, CRITERION=MAXS
0.5, 1E5, 1E5
**
*DAMAGE EVOLUTION, TYPE=ENERGY, SOFTENING=LINEAR
0.009375
**
**
********************************************
**  BOUNDARY CONDITIONS
********************************************
**
**
*BOUNDARY
COHESIVE_NODES_2, XSYMM
LB_LEFT_NODES, XSYMM
INDENTER_REF, 1, 1
INDENTER_REF, 6, 6
SIDE_WALL_REF, 1, 6
LB_BASE_NODES, 2, 2
TOP_LEFT, 1, 1
**
*EQUATION
2
COHESIVE_NODES_2, 2, -1, COHESIVE_NODES_1, 2, 1
**
**
********************************************
**  MODEL SURFACES
********************************************
**
**
*RIGID BODY,  REFNODE=900000002, ANALYTICAL SURFACE=SIDE_WALL
**
*SURFACE, TYPE=ELEMENT, NAME=TARGET_SURFACE_RIGHT
SURFACE_ELEMENTS, S4
**
*SURFACE, TYPE=ELEMENT, NAME=INDSURF
INDENTER_ELEMENTS, SPOS
**
```

```
*SURFACE, TYPE=ELEMENT, NAME=SIDE_SURFACE
SIDE_ELEMENTS, S1
**
*SURFACE, TYPE=ELEMENT, NAME=COHESIVE_SURFACE
COHESIVE_ELEMENTS, S3
**
**
*SURFACE, TYPE=ELEMENT, NAME=RB_LEFT_SURFACE
RB_LEFT_ELEMENTS, S1
**
*SURFACE, TYPE=ELEMENT, NAME=RIGHT_SURFACE
RIGHT_ELEMENTS, S3
**
*SURFACE, TYPE=ELEMENT, NAME=BASE_SURFACE
BASE_ELEMENTS, S2
**
*SURFACE, TYPE=ELEMENT, NAME=RB_BASE_SURFACE
RB_BASE_ELEMENTS, S2
**
*SURFACE, TYPE=ELEMENT, NAME=LB_UPPER_SURFACE
LB_SURFACE_ELEMENTS, S4
**
**
*****************************************
**  INTERACTION PROPERTIES
*****************************************
**
**
*SURFACE INTERACTION, NAME=CONTACT_INTERACTION_1
1.,
*FRICTION
0.00
**
*CONTACT PAIR, INTERACTION=CONTACT_INTERACTION_1,
TYPE=SURFACE TO SURFACE
TARGET_SURFACE_RIGHT, INDSURF
**
*CONTACT PAIR, INTERACTION=CONTACT_INTERACTION_1,
TYPE=SURFACE TO SURFACE
SIDE_SURFACE, SIDE_WALL
**
**
*TIE, NAME=COHESIVE_TIE
COHESIVE_SURFACE, SIDE_SURFACE
**
```

```
*TIE, NAME=FIRST_TIE
RB_LEFT_SURFACE, RIGHT_SURFACE
**
**
**TIE, NAME=FIRST_LB_TIE
**LB_UPPER_SURFACE_LEFT, BASE_SURFACE
**
**TIE, NAME=SECOND_LB_TIE
**LB_UPPER_SURFACE_RIGHT, RB_BASE_SURFACE
**
*TIE, NAME=FIRST_LB_TIE
RB_BASE_SURFACE, LB_UPPER_SURFACE
**
*TIE, NAME=SECOND_LB_TIE
BASE_SURFACE, LB_UPPER_SURFACE
**
**
**********************************************
**  STEP 1
**********************************************
**
**
*STEP, NLGEOM, INC=10000
*STATIC
.01, 5., 1.0E-10, .01
**
**
*BOUNDARY
INDENTER_REF, 2,, -4.00
**
**
*OUTPUT, HISTORY, VARIABLE=PRESELECT, FREQUENCY=50
*OUTPUT, FIELD, VARIABLE=PRESELECT, FREQUENCY=50
*OUTPUT, HISTORY
*ENERGYOUTPUT, ELSET=COHESIVE_ELEMENTS
**
*OUTPUT, HISTORY
*NODE OUTPUT, NSET=INDENTER_REF
RF1, RF2, U2
**
*EL PRINT, ELSET=COHESIVE_ELEMENTS, POSITION=CENTROIDAL,
SUMMARY=NO, FREQUENCY=5
SDEG, COORD2, COORD1, SP2
**
```

```
*EL PRINT, ELSET=SIDE_ELEMENTS, POSITION=CENTROIDAL,
SUMMARY=NO, FREQUENCY=10000
COORD2, SP3
**
*NODE PRINT, NSET=INDENTER_REF, SUMMARY=NO
RF1, RF2, U2
**
*CONTACT PRINT, NSET=SURFACE_NODES, SUMMARY=NO,
FREQUENCY=10000, MASTER=INDSURF
CAREA
**
*OUTPUT, FIELD, FREQUENCY=50
*ELEMENT OUTPUT, ELSET=COHESIVE_ELEMENTS
SDEG
**
*END STEP
**
```

VITA

Kurt Edward Johanns was born in Flint, MI on December 25th, 1982 to Pamela and David Johanns. They lived in Lakewood, CO for a number of years where his two sisters, Rebekke and Katti, were born. After Colorado, Coors Ceramics transferred David to Oak Ridge, TN and the family has lived in Knoxville, TN since. Kurt, having sworn to his dad that he would never work with ceramics, attended Tennessee Technological University in 2001 and graduated in 2005 with a bachelors of science in chemical engineering. Kurt married his wife, Sheena, in 2005 and started a post-bachelor internship with A. A. Wereszczak at Oak Ridge National Laboratory working on the indentation of ceramic armor. There he met G. M. Pharr and decided to pursue a PhD in materials science in 2006 at the University of Tennessee. Kurt and Sheena had a son, Erik, in 2010. In addition, Kurt has continuously worked on the mechanical properties of ceramic (and other) materials, proving that fate is fickle.